SEA SURFACE TEMPERATURE OF THE COASTAL ZONES OF FRANCE

HEAT CAPACITY MAPPING MISSION - HCMM
INVESTIGATION Nº 15
FINAL REPORT

P.Y. DESCHAMPS, R. FROUIN
Laboratoire d'Optique Atmosphérique - Université de Lille I

J. CASSANET, F. VERGER
Laboratoire de Géographie - Ecole Normale Supérieure

M. CREPON
Laboratoire d'Océanographie Physique - Muséum d'Histoire Naturelle

J.M. MONGET, L. WALD
Centre de Télédétection et d'Analyse des Milieux Naturels - Ecole des Mines

JUIN 1982

SEA SURFACE TEMPERATURE OF THE COASTAL ZONES OF FRANCE

HEAT CAPACITY MAPPING MISSION - HCMM
INVESTIGATION N° 15
FINAL REPORT

P.Y. DESCHAMPS, R. FROUIN
Laboratoire d'Optique Atmosphérique - Université de Lille I

J. CASSANET, F. VERGER
Laboratoire de Géographie - Ecole Normale Supérieure

M. CREPON
Laboratoire d'Océanographie Physique - Muséum d'Histoire Naturelle

J.M. MONGET, L. WALD
Centre de Télédétection et d'Analyse des Milieux Naturels - Ecole des Mines

JUIN 1982

SUMMARY

LIST OF ABREVIATIONS

AVHRR - Advanced Very High Resolution Radiometer on TIROS-N, NOAA-6 & 7 satellites

CCT - Computer Compatible Tape

CMS - Centre de Météorologie Spatiale

CTAMN - Centre de Télédétection et d'Analyse des Milieux Naturels

ENS - Ecole Normale Supérieure

HCMM - Heat Capacity Mapping Mission

HCMR - Heat Capacity Mapping Radiometer

LOA - Laboratoire d'Optique Atmosphérique

SST - Sea Surface Temperature

VHRR - Very High Resolution Radiometer on NOAA-1 to 5 satellites

1 - INTRODUCTION

The main objective of this investigation was to map the thermal gradients in french coastal zones for the period of one year in order to enable a coherent study of certain oceanic features detectable by the variations in the sea surface temperature field and their evolution in time. The phenomena examined were meso-scale thermal features in the English Channel, the Bay of Biscay, and the northwestern Mediterranean; thermal gradients generated by french estuary systems; and diurnal heating in the sea surface layer.

The investigation was conducted by the following researchers : Dr. P.Y.DESCHAMPS (Principal Investigator); and Dr.M.CREPON, Mr.J.M.MONGET, and Professor F.VERGER (Co-Investigators).

Appendix A gives related organizations and addresses.

2 - TECHNIQUES

2.1 - TECHNICAL ORGANIZATION OF THE INVESTIGATION

2.1.1. Documents

Every document received by the Principal Investigator from NASA and concerned with the HCMM investigation was duplicated in order to provide the Co-Investigators with individual copies. When necessary, feedback was requested from the Co-Investigators.

.../

2.1.2. Photographic products

Two negative transparencies were on standing order by the Principal Investigator. As they were received, one transparency was archived at L.O.A (Laboratoire d'Optique Atmosphérique, Université de LILLE) and the other at ENS (Ecole Nationale Supérieure) from which additional positive prints were made for each of the Co-Investigators.

2.1.3. Digital products

Request orders for CCTs were collected from the Co-Investigators and submitted by the Principal Investigator. When received, he both catalogued the CCTs and forwarded copies to the appropriate individuals.

2.2 - PHOTOGRAPHIC PRODUCT TECHNIQUES

The photographic products used within the investigation did not require any special developing techniques.

2.3 - DIGITAL PRODUCT TECHNIQUES

2.3.1. Digital product facilities

Most of the facilities used in the investigation are located at C.T.A.M.N. (Centre de Télédétection et d'Analyse des Milieux Naturels), Ecole des Mines, where the processing of remotely sensed data has been extensively developped for a variety of applications. The other investigators had the choice of using this main facility or their own smaller, in-house facilities.

2.3.1.1. Digital product facility at LOA (Laboratoire d'Optique Atmosphérique, Université de LILLE)

This facility is divided into the CII model IRIS 80 computer of the University with specific terminals located at LOA, and a communication link between the two locations. Main processing is done on the IRIS 80 computer.

Digital data may then be transferred and stored on floppy disks at LOA, each containing 6 small scenes of 256x256 pixels. A small scene may be displayed on a PERICOLOR-system color graphic device (256x256 pixels). An HP 9825 A calculator permits minor processing of the stored data. Additional outputs of the processed data may be obtained on a graphic plotter and/or in the form of printer listings.

2.3.1.2. Digital products facilities at CTAMN (Centre de Télédétection et d'Analyse des Milieux Naturels)

The CTAMN was equiped with a self contained computer system for image processing based on two HP 21 MX minicomputers. An improved computing facility, consisting of an array processor FPS (Floating Point System) has been implemented at CTAMN during the investigation.

This system is linked to specific output devices such as :

- a VERSATEC printer/plotter with special gray scale display software developped by CTAMN which allows cartography of satellite data using any given scale and cartographic projection,
- a BENSON ink-plotter with adequate software for mapping with various symbols and colors, as well as cartographic projection,
- a TEKTRONIX digitizer with associated graphics display for landmark acquisition and input capability for rectification or registration.

The main body of the CTAMN system is an interactive image processing system TRIM-CIT ALCATEL. This versatile equipment allows display and manipulation of images in a man-interactive loop. Image memory is 512 x 512 x 8 bits with an overlay graphical memory of 512 x 512 bits. A realtime processor allows color selection, pixel selection with cursor tracking, zooming, and lateral displacement of the image.

2.3.1.3. Digital product facility at ENS (Ecole Nationale Supérieure)

This facility is divided into :

- an IBM 370 main computer at CIRCE, the computer centre of CNRS (Centre National de la Recherche Scientifique), with special output devices :
  - . a VERSATEC printer plotter and a BENSON color printer plotter,
  - . a MODCOMP CLASSIC minicomputer located at ENS which is linked to CIRCE, in association with a TEKTRONIC 4013 graphic display.

2.3.2. Digital product interpretation

The three laboratories working on the present investigation had already developped appropriate interpretation techniques for the NOAA and LANDSAT satellites. As they are used for collaborative programs, there are many common points between the techniques they have implemented on each of their own digital systems.

2.3.2.1. Digital product interpretation at LOA

Digital data may be processed more or less routinely with the following options :

- radiometric calibration if necessary,
- resampling for uniform scaling if necessary,
- smoothing,
- stripes filtering.

Localization and display of a typical scene (containing 1024 x 1024 pixels) is usually done in the following procedure :

- Display is attained by reducing the whole scene to 256x256 pixels after sampling every n pixels and every n lines, or after averaging over an n x n pixel square,
- selection of a small scene (256 x 256 pixels) and visualization at full ground resolution,

- localization with reference to map locations and addition of coordinates on the color graphic display,
- mapping of surface isotherms or isocontours on the printer plotter after the necessary filtering.

Computation and display of a selected scene is possible using the following methods :

- histograms,
- spatial spectrum of temperature variance density,
- structure functions of temperature variations,
- spatial cross-correlation function between two different acquisition of the same area.

2.3.2.2. Digital product interpretation at CTAMN

Upon receiving the HCMM data on magnetic tapes, the processing was organized as follows :

- "Quick look" of available data, at a scale of 1 : 2 000 000, using a black and white printer plotter :
- transformation of data into surface temperature by using the calibration curve,
- destriping of imagery
- isotropic filtering, to reduce the noise level, This algorithm was constrained to local variance in order to leave untouched the strong gradients along the coastlines,
- geometric corrections in order to rectify the imagery at a specified projection (ex.: LAMBERT),
- display of sea-surface temperature as colored maps.

2.3.2.3. Digital product interpretation at ENS

The following programs were used to produce a convenient automatic cartography.

The FRALISET program performs a fast and low cost print-out visualization of a part of a given scene. The HCMR digital counts were converted to alphanumeric characters.

After selection by the operator, each printed character was associated to one or several pixels. The 1/500 000 scale appeared to be suitable for the HCMM applications in the Bay of Biscay. Isotropic filtering of the data could be applied once or several times. The additional legend was selected by the operators. Out-put was done on the BENSON plotter both in black and white and white 6 color prints.

2.4. GROUND TRUTH TECHNIQUES

Ground truth techniques were not assigned to this specific investigation. The necessary oceanographic and meteorological data was obtained either from routine observations or from dedicated oceanographic cruises conducted by the following organizations.

2.4.1. Routine observations

Periodical sea surface temperature measurements are performed by the "Reseau National d'Observation de la Qualité du Milieu Marin", in the french coastal and estuarine zones. As an exemple, six stations are sampled every week in the Loire estuary. Some of these measurements were simultaneous with the HCMM data (09/15/78 ; 05/28/79 ; 06/18/79).

The "Etablissement d'Etudes et de Recherches Meteorologiques" at the "Centre Océanologique de Bretagne", Brest, performs a statistical treatment of the sea surface temperature field from the routine observations of the merchant ships in the Bay of Biscay, the Celtic Sea and the Western English Channel. As result of this analysis, a thermal map (SST-GASC) is produced three times a month with a temperature accuracy of about 0,5°C.

Lighthouseboats also routinely measure sea surface temperature at several locations in the eastern British Channel and the southern North Sea. They report these measurements through the meteorological network.

2.4.2. Oceanographic cruises

In addition to these routine procedures, this investigation had access to data from several oceanographic experiments

conducted by various french organizations and complementary to the objectives of the HCMM experiment :

- LION 78 (June to September 1978), a summer experiment in the Gulf of Lions, Mediterranean Sea for the coastal upwellings.
- PHYGAS 78 (8 November 1978 to 2 December 1978) in the Bay of Biscay.
- A drifting buoy experiment in the Bay of Biscay, starting February 1979, for the study of ocean dynamics.
- PROLIFIC (5 to 24 March 1979), an experiment in the Ligurian Sea, to support remotely sensed data of sea surface temperature and ocean color.
- Several cruises in the British Channel to support remotely sensed data of sea surface temperature and ocean color :
  - . 19 to 29 June 1979, in the "Golfe de Saint Malo"
  - . 20 to 28 July 1979, in the "Golfe de Saint Malo"
  - . 4 to 14 September 1979, in the "Golfe de Saint Malo"
  - . SATIR 1, 17 to 27 July 1979, in the Celtic Sea
  - . SATIR 2, 3 to 22 September 1979, in the Celtic Sea.

No airbone temperature measurements were performed for the HCMM experiment since specific request for this type of data appeared within the investigation.

The major ommission in the ground truth data collection was due to the unavailability of BOHRA II, a french buoy previously anchored at a fixed station in the Mediterranean Sea, about 100 km south of Marseille. BOHRA II was removed prior to the AEM-A spacecraft launch for technical reasons. BOHRA II was intended to support the investigation by continuously recording the vertical thermal structure of the upper water layers. The absence of this instrument seriously restricted the scope of the studies relating to diurnal heating of the surface layer.

3 - ACCOMPLISHMENTS

3.1. - HCMR CALIBRATION - SEE APPENDIX B

Several comparisons were made between HCMR digital data and in situ measurements obtained in the Bay of Biscay - see Appendix B. HCMR radiometric temperatures were found to be 7°C less than in-situ measurements of the sea surface temperature. This difference is rather large and cannot be accounted for solely by the atmospheric correction of water vapor absorption for which the mean computed value was only a few °C (2 to 3°C). A HCMR calibration bias of several °C should probably have been added to the data in order to derive more accurate absolute temperatures. Still this calibration bias was not a severe problem for the objectives of the investigation, because it appeared rather constant, and because HCMR data were only used as relative temperatures.

3.2. - COMPARAISON OF HCMR TO VHRR AND AVHRR DATA - SEE APPENDIX C

Comparisons were made of radiometric data obtained over the same marine area at the same time by both HCMR and VHRR/NOAA-5, or by HCMR and AVHRR/TIROS-N. They demonstrate a definite improvement in the radiometric quality of the HCMR data over that of the VHRR, primarily in the area of radiometric resolution. The comparison between HCMR and AVHRR shows that these two instruments have similar improved radiometric performances. The higher repetitivity of data acquisition and the possibility of a multichannel (3.7 and 11 μm) atmospheric correction are in favour of the AVHRR experiment, while the HCMR experiment offered the unique advantage of delivering geometrically corrected photographic and digital products. The ground resolution of the HCMR instrument ($\simeq$ 500m) was better than the AVHRR experiment ($\simeq$ 1 km) but the value of this feature is limited to the studies of areas having a large surface temperature variability at small scales, typically the coastal marine areas and the sharp thermal fronts. While over some very homogeneous oceanic areas, the spatial variability of the SST field at scales below 5 km is too low to be detected by the two instruments.

Data from AVHRR onboard TIROS-N and NOAA-6 can now be directly transmitted to CMS, LANNION, FRANCE and it was this facility that did the processing for the HCMM experiment. An atmospheric algorithm has been implemented at CTAMN, which uses the equivalent radiometric temperatures T_3 and T_4 in AVHRR channels 3 and 4 (3.7 and 11 μm), to determine the actual sea surface temperature, T_0 :

$$T_0 = 1.054\ (1.42\ T_3 - 0.42\ T_4) + 1.13$$

(T_0, T_3 and T_4 in (°C).

This relation has been obtained by Mc CLAIN[1] from a comparison between AVHRR data and actual surface measurements over the Gulf Stream and is very close to the one predicted by DESCHAMPS and PHULPIN[2] from theoretical simulation :

$$T_0 = 1.48\ T_3 - 0.48\ T_4 + 2.02.$$

3.3. - HCMR PRODUCTS

HCMM photographic products with a suitable enhancement of the grey scale in the range of sea surface temperatures and a geometric correction were highly applicable to the objectives of the investigation because they enabled direct utilization of the data. In contrast, VHRR and AVHRR photographic products from meteorological satellites received at CMS, LANNION, FRANCE, have a standard enhancement for the meteorological needs in a large temperature range, which only permits the selection of cloudfree areas : consequently, the main body of the work is held up until after a heavy procedure of digital data processing has been completed.

---

(1) Mc CLAIN, E.P., 1980 - Multiple atmospheric-window techniques for satellite derived sea surface temperatures. COSPAR/SCOR/IUCRM Symp. "Oceanography from Space", Venice, ITALY, May 26-30 1980.

(2) DESCHAMPS P.Y., PHULPIN T., 1980 - Atmospheric correction of sea surface temperature using channels at 3.7, 11 and 12 μm.

In addition to providing a more extensive and accurate overview of the thermal features in the french coastal zones, facilitating initial detection and mapping of thermal eddies and fronts, etc.., the expediency provided by the HCMM photographic products allowed the investigators to conduct a preliminary assessment of the data in order to select the digital sets to receive processing and to recommend guidelines for further elaboration and analysis. This consequently allowed a more productive and efficient evaluation of the data by the oceanographic community prior to any computerized processing.

A more detailed description of the results achieved by the experiment is given in section 4 and corresponds to the following outline.

(1) During the period of investigation, May 1978, May 1979, HCMM photographic products used to make a qualitative analysis of certain persistent thermal features :

- thermal fronts in the western British Channel, and north of Balearic Islands, western Mediterranean Sea;
- large eddies north of the algerian and african coast;
- upwellings northwest of Portugal in the Gulf of Lions and in the western Mediterranean Sea.

(2) HCMM photographic products were used to obtain an assessment of the frequency of occurence of diurnal heating of the sea surface in the Mediterranean Sea. Prior to the HCMM experiment, the importance of frequent and extensive diurnal heating of the sea surface was unexpected, but its subsequent establishment leads to the conclusion that for oceanographic purposes, daytime satellite imagery should be used cautiously because the SST field may be interpreted erroneously.

(3) HCMM digital products were used to perform a statistical spectral analysis of the mesoscale variability of the SST field in the range of scales 3-30 km, thanks to the low noise level of the HCMR.

4 - SIGNIFICANT RESULTS

4.1. - MESOSCALE VARIABILITY OF THE SST FIELD - SEE APPENDIX D

Using VHRR and HCMR infrared digital data, a statistical analysis of the mesoscale variability of the SST field was performed in order to characterize the random properties of this field. The power law exponent, n, of the spatial spectrum of variance density, $E(k) \sim k^{-n}$ (k is wavenumber), was deduced from the computation of the structure function of the SST. When the study was first started on VHRR/NOAA-5, the range of scales was on the order of 40-100 km but HCMR data allowed an extension of the study down to a scale of 3 km. From an examination of 11 VHRR and 9 HCMR scenes, in the range of 3-100 km, n was found to vary from 1.5 to 2.3, with a mean value of 1.8. These values of n are on the order of those predicted by turbulence theories.

However a discrepancy exists and further advanced theories are needed to explain this experimental determination of the mesoscale SST variability.

The feasability of the spectral analysis in the range of scales 3-30 km was only made possible by the low noise level of the HCMR data.

4.2. - DIURNAL HEATING - SEE APPENDIX E

Daytime HCMR data occasionally exhibited warmer sea surface areas which extended over 10 to 100 km. The warming was of several °C and easily detected on photographic products because these warmer areas usually have graded margins that cannot be confused with the sharper boundaries of other oceanic thermal phenomena.

These warmer areas were interpreted as a large diurnal heating of the upper surface layer under low wind speed conditions. Evidence of this is supported by several arguments.

(1) Meteorological observations and analysis show that warmer areas are associated with low wind speed conditions - i.e. anticyclonic conditions or coastal breeze effects.

(2) Glitter - i.e. the portion of solar radiation reflected by the uneven sea surface directly toward the satellite sensor - has been used to derive an equivalent wind speed from the HCMR visible channel (feasible when observation is close to the specular reflexion of a flat sea). Warmer areasare always associated with changes in the glitter patterns and decreasing wind speeds.

(3) Warmer areas disappear on consecutive nightime HCMR data.

Under low wind speed conditions, turbulence induced in the sea surface by the wind stress is strongly reduced, and most of the solar radiation absorbed is stored in the surface layer without downward propagation. Theoretical simulations using a radiative and heat transfer model have been performed. They predict large heating rates in the upper metersand a maximum heating of several °C in the upper layer, and have been confirmed by in-situ measurements. Significant heating only occurs in the upper few ten centimeters of the surface and is very rapidly destroyed by the nightime cooling.

HCMR data allowed us to discover that diurnal heating of more than 1°C was affecting large areas. The frequency of occurence was relatively high in the western Mediterranean Sea where more than 10 % of marine surface was affected one day or an other, while large diurnal heating was very rarely observed in the North Sea (only one scene). In strongly affected areas, daytime satellite data could consequently yield misleading SST fields, leading to the conclusion that a less deceptive picture of the SST field is more likely to be obtained from observations restricted to nightime or early morning when the surface layer is more homogeneous.

4.3. - RESIDUAL FLOW THROUGH THE DOVER STRAIT - SEE APPENDIX C

The time sequence of HCMM scenes allowed us to outline the influence of meteorological conditions on the residual current which flows to the N.E., from the British Channel through the Dover Strait, and into the North Sea. Southwestern winds enhance this residual flow, and, as a result, the thermal effluent of the Rhine River is forced northward along the Dutch coast in a very narrow coastal band. Northeast winds oppose the residual flow, reduce its speed and deflected it toward the English coast allowing the Rhine thermal effluent ro expand seaward at a distance of up to 25 nautical miles. A close correlation exists between wind speed direction and the offshore spread of the effluent.

4.4. - TIDAL FRONTS IN THE WESTERN APPROACHES OF THE BRITISH CHANNEL - SEE APPENDIX C

Tidal fronts occur in shelf areas where the tidal currents are large enough to destroy the seasonal thermocline. In shallow depths, the tidal currents induce turbulence that mixes the water column. The warmer stratified and colder homogeneous waters are separated by a tidal front that appears as a surface thermal front on satellite imagery.

Tidal fronts in the western approaches of the British Channel were first detected with the VHRR. HCMM photographic products have since been used to further analyse the time and space variability of these thermal fronts during summer 78.

4.5. - UPWELLING AT THE CONTINENTAL SHELF BREAK IN THE BAY OF BISCAY - SEE APPENDIX C

HCMM data confirm the existence of a permanent upwelling phenomenon at the continental shelf break in the Bay of Biscay. The upwelling is outlined by the appearance of cold water in summertime. This has already been observed in previous VHRR data. From HCMM scenes, a more complete description and interpretation of the upwelling has been obtained.

(1) The upwelling is probably permanent, but is enhanced by colder upwelled water in summertime when a seasonal thermocline is formed. On one occasion, January 17, 1979, warmer water appeared in wintertime at the shelf break (HCMM scene A-A 0265 - 01090); this is probably an intermediate warmer water, possibly of Mediterranean, flowing out through the Gibraltar Strait, into the Atlantic, at a depth of several hundred meters.

(2) The upwelling is more pronounced after spring tides, which suggests that the basic mechanism for the upwelling is a tidal one. On two occasions after spring tides, August 25 and September 21, 1978, HCMM scenes (A-A 0121-13260 and A-A 0148-13320) show very similar patterns of cold water at the shelf break, with a maximum intensity between 48N-8E and 46.30N- 5E where the tidal currents are at a maximum.

4.6. - COASTAL STUDIES IN THE BAY OF BISCAY - SEE APPENDIX F

The action of tidal currents in shallow regions produces a turbulence that mixes the water column and destroys the seasonal thermocline. The resulting colder, homogeneous shelf water is separated from the warmer stratified offshore water by a zone where the thermal gradient is high. This phenomenon, unexpected prior to HCMM observations, is similar to the tidal fronts in the western approaches of the British Channel (section 4-4).

4.7. - WESTERN MEDITERRANEAN SEA TEST SITE

Results reported here are based on VHRR/NOAA-5 and HCMM data.

4.7.1. Results obtained with VHRR/NOAA-5

The region of Ligurian Sea between Corsica and the southern coast of France was studied in 100 VHRR/NOAA-5 images taken from the period 1975-79. The study revealed a cyclonic surface circulation quasi-permanent and emphasized by its thermal pattern.

Annual variations of the horizontal thermal gradient structure have been described and agree very well with previous in-situ measurements. Low frequency waves in the Ligurian Sea have been observed on time-series of VHRR/NOAA-5 in December 1977, with associated wavelength and phase velocity of 40 km and 0.18 $m.s^{-1}$. These waves are analysed in terms of large amplitude baroclinic waves as those discussed in the theory of baroclinic instability.

A similar study using VHRR/NOAA-5 was done for the Gulf of Lions, an area where coastal upwelling is common in summertime. The data shows strong evidence for a relation between the location of the upwelling and the contour of the adjacent coastline. The phenomenon is much more intense along straight coastal segments of 10 to 20 km in length than in the vicinity of capes and small bays. The whole imagery suggests that the associated circulation in the surface layer is strongly variable in space and time a fact verified by in-situ measurements and consistent with the very real presence of wind induced eddies in the surface layer.

The effect of the Mistral wind on the Ligurian current has been studied by using a time sequence of VHRR/NOAA-5 data. The Ligurian current flows along the french coast from the Ligurian Sea into the Gulf of Lions where a frontal zone separates the Ligurian current and colder water upwelled in the Gulf of Lions. It has been found that the surface flow associated with the current is stemmed by strong westerly winds and when the wind drops, the frontal zone moves westward at speeds up to 0.3 $m.s^{-1}$.

4.7.2. Results obtained with HCMM - see Appendix C and G

HCMM photographic products allowed us to capture several features of the large scale surface circulation in the northern part of the western Mediterranean sea (see Appendix C) :

- to study the seasonal variation of the mean location of the front formed north of Balearic Islands, at the juncture between the Atlantic current flowing from the Gibraltar Strait to the north-east and the Ligurian current flowing to the south-west along the southern coast

- to confirm previous observations of cyclonic circulation in the Ligurian sea and upwellings in the Gulf of Lions,

- to detect for the first time large anticyclonic eddies (≃ 100 km diameter) in the southern part of the Mediterranean Sea.

HCMM digital products were also used to make a statistical analysis of small cyclonic and anticyclonic eddies in the Ligurian sea (see Appendix G).

5 - PUBLICATIONS

Included in this section are all the materials published by the investigators on infrared remote sensing of the sea surface temperature. Publications which pertain more specifically to the HCMM experiment are marked with an asterisk.

5.1. - REVIEWS

- M.CREPON, P.Y.DESCHAMPS (1978) - La télédétection en océanographie - Oceanis, 4, 663-672.
- C.MILLOT (1979) - Wind induced upwellings in the Gulf of Lions - Oceanologica Acta, 2, 261-274.
- P.Y.DESCHAMPS, T.PHULPIN (1980) - Atmospheric correction of infrared measurements of sea surface temperature using channels at 3.7, 11 and 12 μm - Boundary-Layer Meteorology, 18, 131-143.
- P.Y.DESCHAMPS, R.FROUIN, L.WALD (1980) - Comments on the "Spatial variability of coastal surface water temperature during upwelling" - Journal of Physical Oceanography, 10, 1303.
- C.MILLOT, L.WALD (1980) - Some aspects of the Ligurian current along the Provence coasts - Oceanologica Acta, 3, 399-402.
- L.WALD, G.HIHOUS (1980) - Ligurian Sea : annual variation of the sea-surface thermal structure as seen by satellite NOAA-5 - Oceanologica Acta, 3, 465-469.

*- P.Y.DESCHAMPS, R.FROUIN, L.WALD (1981) - Satellite determination of the mesoscale variability of the sea surface temperature - Journal of Physical Oceanography, 11,864-870.

- M.CREPON, L.WALD, J.M.MONGET - Low frequency waves in the Ligurian Sea during December 1977 from satellite NOAA-5 - (to appear in) Journal of Geophysical Research.

*- P.Y.DESCHAMPS, R.FROUIN, M.CREPON - Sea surface temperature of the coastal zones of FRANCE observed by the HCMM satellite - (submitted to) Oceanologica Acta.

*- P.Y.DESCHAMPS, R.FROUIN - Large diurnal heating of the sea surface observed by the HCMM experiment - (submitted to) Journal of Physical Oceanography.

5.2. - PROCEEDINGS OF CONFERENCES

- M.ALBUISSON, J.M.MONGET, M.CREPON, C.MILLOT (1977) - Observation of transient upwellings in the Mediterranean sea with the NOAA VHRR imagery - in "Journées de Télédétection du GDTA", Saint Mandé, FRANCE, Septembre 1977, 85-95.

- P.Y.DESCHAMPS, M.VIOLLIER, P.LECOMTE (1977) - Observation à partir de l'espace de l'environnement marin côtier - in "Journées de Télédétection du GDTA", Saint Mandé, FRANCE, Septembre 1977, 119-125.

- P.Y.DESCHAMPS, T.PHULPIN (1978) - Correction atmosphérique des données obtenues par télédétection dans l'infrarouge - in "Utilisation pour l'océanologie des satellites d'observation de la terre", CNEXO, Actes de Colloques n°5, 123-131.

- M.ALBUISSON, J.M.MONGET (1978) - Méthodes et moyens utilisés pour la mise en forme de données de satellites de télédétection : application à la cartographie thermique - in "Utilisation pour l'océanologie des satellites d'observation de la terre", CNEXO, Actes de Colloques n°5, 181-202.

*- P.Y.DESCHAMPS (1978) - Présentation de l'expérience HCMM - in "Utilisation pour l'océanologie des satellites d'observation de la terre", CNEXO, Actes de Colloques n°5, 339-341.

- M.ALBUISSON, J.M.MONGET, G.NIHOUS, L.WALD (1979) - Sea surface temperature anomaly mapping using the NOAA satellite - in "Applications of remote sensing to fisheries research", ICES Remote Sensing Working Group Meeting, Valbonne, FRANCE, June 1979, 13-14.

- M.ALBUISSON, J.M.MONGET, G.NIHOUS, M.POISSON, L.WALD (1980) Seasonal variations of sea surface temperature in the Ligurian Sea - in "Coastal and marine applications of remote sensing", A.P.CRAKNELL Ed. The Remote Sensing Society, 17-19.

- T.PHULPIN, P.Y.DESCHAMPS (1980) - Estimation of sea surface temperature from AVHRR infrared channels measurements - in "Coastal and marine applications of remote sensing", A.P.CRAKNELL Ed., The Remote Sensing Society, 47-58.

- C.MILLOT, L.WALD (1981) - Infrared remote sensing in the Gulf of Lions - in 'Oceanography from Space", J.F.R.GOWER Ed., Marine Science n°13, Plenum Press, 183-188.

- L.PRIEUR, M.ALBUISSON, L.WALD, J.P.BETHOUX, J.M.MONGET (1981) - A comparison between infrared satellite images and sea truth measurements - in "Oceanography from Space", J.F.R. GOWER Ed., Marine Science n°13, Plenum Press, 159-167.

- C.MILLOT, L.WALD (1981) - Upwellings in the Gulf of Lions - in "Coastal Upwelling", F.A.RICHARDS Ed., A.G.U. (to appear).

5.3. - THESIS

- L.WALD (1980) - Utilisation du satellite NOAA-5 à la connaissance de la dynamique oceanique - Thèse de 3ème cycle, Université de PARIS VI, février 1980.

*- R.FROUIN (1981) - Contribution à l'étude de la température de surface de la mer par télédétection au moyen de l'expérience spatiale HCMM - Thèse de 3ème cycle, Université de LILLE 1, Janvier 1981, n°877.

6 - PROBLEMS

6.1 - HCMM DATA GEOMETRY

The geometric correction performed on HCMM data was partly disappointing. The accuracy with which it was performed on the day or night products was generally of several pixels. Occasionally, the vertical scale was different from the horizontal scale : when transferred on to map locations, there was a discrepancy between lines distances (500 m) and pixel distances (450 m), lacking correspondance to the nominal value (470-480 m).

Additional geometric correction of digital data for registering one HCMM scene to an other, was sometimes necessary in order to arrive at a better accuracy. In some cases, it would have been simpler to start from non geometrically corrected data.

Photographic were products without problems in geometry and were used to detect and map with sufficient accuracy most of the oceanic features.

6.2 - PERIODIC NOISE

A periodic signal of variable amplitude was present is the data when analysed by FOURIER transform or structure function, particularly along a line ; with a tropical period of 6 pixels. This was only a problem for the statistical analysis of the sea surface temperature at the smallest scales (less than 5 km).

6.3 - CONTRAST OF THERMAL IMAGERY

Some of the standard photographic products were not enough enhanced in the infrared channel, making it impossible to derive from these images any formation over the oceanic areas where temperature variations were small.

This mainly occured on the day-infrared photographic products when the grey scale was then extended over a large temperature range to adjust for the warm temperature of land surfaces. Specific enhancement for the purposes of oceanographic research would be very useful and is proposed as a recommendation (section 8).

7 - IMAGE QUALITY AND DELIVERY

7.1 - IMAGE QUALITY

Image quality was generally good except for those periods corresponding to high noise levels in the thermal channel. Another problem was the geometry of the images (see section 6-1). Defects occasionally occured : stripes, or anomalous lines, grids of periodic black or bright pixels, but did not seriously affect the objectives of the investigation.

7.2 - TEST SITES COVERAGE

A list of the received data, photographic and digital products, is given in Appendix H.

Coverage was generally good over all the test sites, and excellent in the Mediterranean Sea, as excepted from the cloud cover analysis.

The major lack of cloudfree data was for studies of estuarine thermal gradients during winter.

7.3 - DELIVERY

Photographic products started to arrive one year after launch on a erratic schedule. It would have been preferable to receive them in chronological order, e.g. as complete monthly data sets. This would have enabled a more efficient and definite selection of the request orders within a given period.

Some of the digital data on requested were received twice, some completely omitted. Most of the tapes received contained only one or two scenes, against a potential of 5 scenes at the very minimum. The amount of tapes was increased consequently : 200 tapes that were finally received were eventually copied onto only 35 tapes.

8 - RECOMMENDATIONS

The following recommendation is specific to oceanographic investigation of the SST field. It is our opinion that in would be better to study photographic products (infrared imageries) having a constant contrast temperature, i.e. a grey scale expanded over a constant range of temperature ($\simeq$10°C) around the mean climatological value of the SST.

9 - CONCLUSIONS

1° -HCMR and AVHRR data were comparable quality for oceanographic studies of SST. Both instruments show a large improvement over the VHRR, primarily due to a reduction in noise level. Repetitivity and multichannel atmospheric correction favour the AVHRR, while geometric correction performed on suitably enhanced HCMM photographic products is a great help to detection mapping oceanic features.

2° - Day and night infrared HCMM data were used in a number of studies of oceanic and coastal phenomena :

- the interaction of the residual flow through the Dover Strait with the Rhine River effluent,
- the tidal fronts in the western approaches of the British Channel,
- the upwellings at the shelf break in the Bay of Biscay,

- the formation of coastal cold water regions in the Bay of Biscay,
- the surface circulation and eddies in the Ligurian sea,
- the coastal upwellings in the Gulf of Lions,
- the thermal front north of the Balearic islands,
- large eddies associated with the Atlantic current north of Algeria,
- statistical analysis of the mesoscale variability of the SST.

3° - Day - night differences were used only for a study of diurnal heating of the surface layer of the sea during periods of low wind speed.

AKNOWLEDGEMENTS

Many thanks to the technical staffs of all investigators. We are particularly indebted to C.DEROO, L.GONZALES, J.M.PANHALEUX, Y.THEROUX for their assistance to the investigation. Supports were obtained from several french organizations :

- C.N.R.S., Centre National de la Recherche Scientifique,
- C.N.E.S., Centre National d'Etudes Spatiales,
- C.N.E.X.O., Centre National pour l'Exploitation des Océans,
- Ministère de l'Environnement,
- Etablissement Public Régional du Nord - Pas de Calais.

=======

Appendix A

Permanent adresses and organizations of the investigators

Dr. M. CREPON
Laboratoire d'Océanographie Physique
Muséum d'Histoire Naturelle
43, rue Cuvier
75231 PARIS Cedex 05 (France)

Dr. P.Y. DESCHAMPS
Laboratoire d'Optique Atmosphérique
Université des Sciences et Techniques
U.E.R. de Physique Fondamentale
59655 VILLENEUVE D'ASCQ (France)

Mr. J.M. MONGET
Centre de Télédétection et d'Analyse des milieux naturels
Ecole des Mines
Sophia-Antipolis
06560 VALBONNE (France)

Pr. F. VERGER
Laboratoire de Géographie
Ecole Normale Supérieure
1, rue Maurice Arnoux
92410 MONTROUGE (France)

Appendix B

GROUND TRUTH DATA and HCMR MEASUREMENTS

1) Periodical sea surface temperature measurements are performed by the " Réseau National de la Qualité du Milieu Marin " along the Atlantic shore. For example, in the Loire estuary, measure--ments are performed by the " Institut Scientifique et Technique des Pêches Maritimes ", Nantes, every week, at 6 stations. On 09/15/78 ; SST measurements were made simultaneously by the HCMM satellite and the I.S.T.P.M..
Results : for 2 stations A and B. Sea surface temperatures measured I.S.T.P.M. were 290°C. Calculated temperatures from calibrated count of HCMR were 283°C.. Thus, in this particuler case, the temperatures observed by the satellite were cooler than the ground truth by 2°C.

2) The "Etablissement d'Etudes et de Recherches Météorologiques" situated at the "Centre Océanologique de Bretagne", in Brest, performs a statistic treatment of sea surface temperature measurements in the Bay of Biscay, the west of Channel, and the southern region of the Irish sea (SST-GASC is the name of the processing). (Visualization of the results) are printed twice a day and a thermography in this area is produced three times a month...The range of precision of these measurements (obtained from merchant ships) is about ± 0.5°C.

From three HCMM scenes of good quality, comparisons were made between Satellite and SST-GASC measurements.

The following table presents results of this analysis.
For each station are given : temperature in °C from SST-GASC measurements, temperature in °C calculated from calibrated count of the HCMR, and difference between ground truth data and satellite measurement.

In each case, the satellite observed temperatures were cooler than the ground truth (about 7°C). These results are similar to R.N.O. observations.

STATIONS in Gulf of Biscay	06/10/78			09/15/78			10/28/78		
	SST-GASC	HCMM	ΔT	SST-GASC	HCMM	ΔT	SST-GASC	HCMM	ΔT
47°20N/03°30W	17,1°C	9,7°C	-6,4°C	17,9°C	10,1°C	-7,8°C			
47°00N/04°00W				17,8°C	10,5°C	-7,3°C			
47°00N/03°30W	17,0°C	10,1°C	-6,9°C	18°C	10,8°C	-7,2°C	14,9°C	8,3°C	-6,6°C
47°00N/03°00W	16,9°C	9,7°C	-7,2°C	18,2°C	11,2°C	-7,0°C	14,9°C	7,9°C	-7,0°C
46°40N/03°30W				18,1°C	10,8°C	-7,3°C	15,2°C	8,7°C	-6,5°C
46°40N/03°00W	16,8°C	9,5°C	-7,3°C	18,3°C	11,2°C	-7,1°C	15,1°C	8,7°C	-6,4°C

Appendix C

SEA SURFACE TEMPERATURES OF THE COASTAL ZONES OF FRANCE OBSERVED BY THE H.C.M.M. SATELLITE

P.Y. DESCHAMPS and R. FROUIN

Laboratoire d'Optique Atmcsphérique
Université de Lille I
Villeneuve d'Ascq - France

and

M. CREPON

Laboratoire d'Océanographie Physique
Museum National d'Histoire Naturelle
Paris - France

ABSTRACT

The HCMM (Heat Capacity Mapping Mission) experimental satellite was launched in April 1978 and provided data until 1980. Although the basic objective of the experiment was the measurement of diurnal temperature variations of the earth's surface for applications to geology and hydrology, the good performance of the HCMR (Heat Capacity Mapping Radiometer) on board the satellite recommended it for use in oceanographic studies. The data were acquired in the form of photographic products and magnetic tapes, and systematically utilized for evaluation of surface temperature in french oceanic regions according to an investigation accepted by NASA (National Aeronautics and Space Administration).

A comparison of the radiometric performances of the HCMR to those of the VHRR (Very High Resolution Radiometer) and AVHRR (Advanced Very High Resolution Radiometer) on board meteorological satellites is presented, demonstrating the decisive gain in quality of the HCMR over the VHRR for the observation of mesoscale structures in the ocean. The similarities between the radiometric properties of the HCMR and AVHRR are also discussed.

The utilization of photographic products proved very suitable since they had already been geometrically corrected and enhanced in the temperature range of the sea surface, consequently avoiding many of those cases requiring involved computer treatment. Examples of results obtained by photo interpretation of marine structures observed in the regions relevant to the investigation (North Sea, British Channel, Celtic Sea,

Bay of Biscay and western Mediterranean) are presented in this study. From these, conclusions have been drawn regarding several oceanic phenomena.

- The thermal effluent of the Rhine is affected by the tidal residual current of the North Sea. The extent of the offshore diffusion of the estuary system is influenced by winds from the NE and W which respectively retard or accelerate the residual current.

- Images showing cold water along the edge of the continental shelf strongly support the hypothesis of a mixing process due to internal waves generated by the action of tidal currents at the edge of the shelf.

- Large scale eddy structures detected during the summer in the western Mediterranean region around 6°E and 38°N may be linked to a phenomenon of barotropic - baroclinic instability.

- The presence of significant diurnal heating of the surface layer (several °C) is related to weak winds in the Mediterranean, leading to interpret with caution daytime SST (Sea Surface Temperature) satellite observations made during the summer period.

RESUME

L'expérience satellitaire H.C.M.M. a été lancée en avril 1978 avec pour objectif de mesurer les variations diurnes de la température de surface de la Terre, en vue d'applications en Géologie et en Hydrologie. Les bonnes performances du radiomètre H.C.M.R. à bord du satellite (NEDT de 0,3 °C, résolution au sol de 500 m) l'ont aussi désignée pour des études en Océanographie. Les données fournies par le satellite ont couvert la période allant de avril 1978 à juillet 1980. Ces données, sous forme de produits photographiques et de bandes magnétiques, ont été systématiquement utilisées pour l'observation de la température de surface des régions océaniques françaises, dans le cadre d'une investigation acceptée par la NASA.

Une comparaison des performances radiométriques du H.C.M.R. à celles du V.H.R.R. et du A.V.H.R.R. des satellites météorologiques de la NOAA est d'abord effectuée, mettant en évidence le gain de qualité décisif du H.C.M.R. sur le V.H.R.R. pour l'observation des structures à moyennes échelles en zone océanique, ainsi que la qualité radiométrique similaire du H.C.M.R. et du A.V.H.R.R..

L'utilisation du produit photographique, particulièrement bien adapté puisque corrigé géométriquement et augmenté en contraste dans la gamme des températures de surface de la mer, s'est avérée fructueuse, évitant dans la plupart des cas de procéder à un traitement informatique souvent lourd. Des exemples de résultats obtenus par photo-interprétation pour l'observation des structures marines dans les régions concernées par l'investigation (Mer du Nord, Manche, Mer Celtique, Golfe de Gascogne, Méditerranée occidentale) sont présentés. En particulier, des conclusions ont été

obtenues sur plusieurs aspects océanographiques :

- influence du courant résiduel à travers le Détroit du Pas de Calais sur l'effluent thermique du Rhin ; la plus ou moins grande diffusion de cet effluent à partir de la côte est associée à des vents de secteurs Nord-Est et Ouest qui respectivement freinent ou accélèrent le courant résiduel ;
- les images obtenues sur l'apparition d'eaux froides en été à la limite du plateau continental au large de la Bretagne soutiennent fermement l'hypothèse d'un mécanisme déclenché par les ondes internes générées par les courants de marée à la rupture de la pente ;
- la détection de structures tourbillonnaires de grande amplitude (100 km) en Méditerranée Occidentale dans la zone voisine de 6°E et 38°N en période estivale ;
- l'apparition d'échauffements superficiels diurnes importants (plusieurs °C) liés à des vents très faibles, en Méditerranée : cela doit conduire à utiliser avec suspicion les obsservations satellitaires de jour en période estivale.

INTRODUCTION

Examination of the earth's surface temperature field is now becoming a common practice. The first space experiments in this area were launched in the 60's, but it wasn't until the early 70's that the VHRR experiment on meteorological NOAA (National Oceanographic and Atmospheric Administration) satellites permitted a systematic and fairly precise observation of the temperature field of the earth's surface. Although a large number of ocean phonomena have been studied in this manner from space (see among other reviews, those by LEGECKIS, 1978, and Mc CLAIN, 1980), examination of even pronounced ocean structures has still been somewhat limited by the instrumental performances of the VHRR (Noise Equivalent Differential Temperature, NEDT of 0.5 to 1°C).

During 1978, radiometers of a new generation were installed on different satellites : the HCMR on HCMM ; the AVHRR on TIROS-N ; and secondarily, the CZCS (Coastal Zone Color Scanner) on NIMBUS-7. All included channels in the infrared, and permitted a hope of improved performance for observing the sea surface temperature field primarily by a notable reduction in instrumental noise.

The present study essentially concerns the HCMR experiment launched in April 1978, for which an investigation had been accepted by NASA. The materials provided by NASA consisted of both photographic products and magnetic tapes. The utilization of photographic products was particularly well adapted to the purposes of this oceanographic study since they were already geometrically corrected and enhanced in the sea surface temperature range. A description of the satellite experiment is first presented, then a comparison of the radiometric performances of the HCMR to the VHRR and AVHRR, followed by the results obtained through

photo interpretation of the marine features observed in the regions relevant to the investigation.

II - THE HCMM SATELLITE EXPERIMENT

The fundamental objective of the HCMM space experiment was the measurement of the diurnal temperature variation on the surface of the earth (solar heating during the day, radiative cooling at night) for applications to earth resources (geology, hydrology, etc...) For this, the HCMM satellite was placed at an altitude of 620 km in a sun-synchronous orbit, circular, quasi-polar, characterized by an inclination of 97.79° and a period of 97.2 minutes. The passage over the equator took place at approximatively 02 and 14 hours local time in order that data could be obtained near the minimum and the maximum of diurnal temperature variation. The radiometer onboard the satellite was a scanning radiometer that acquired data in 2 channels : the visible and near infrared (0.5 - 1.1 μm), and the thermal infrared (10.5 - 12.5 μm). Similar channels had already been used on previous meteorological satellites, but the purpose of the modified instrumentation of the HCMM experiment was :

(i) to significantly improve measurement in the thermal infrared by an NEDT of 0.3°C and a ground resolution of 0.5 km (as opposed to an NEDT between 0.5 and 1°C and a ground resolution of 1 km for the VHRR radiometer of NOAA satellites), and

(ii) to increase the possibility of obtaining maps of the day/night surface temperature differences at 12 and 36 hour intervals. The main objective of the HCMM experiment was to determine the thermal inertia of the earth's surface with the intentions of : measuring variations of

ground humidity and evapotranspiration of the vegetation ; discriminating different rock types and locating mineral beds ; and measuring the extent of snow covered areas for the purpose of forecasting runoff due to the melting of ice. Moreover, the good performance of the HCMR recommended it for studies in oceanography.

The data were available in the form of photographic products and digitalized magnetic tapes. Each scene covered an area 700 x 700 km^2 and contained the following information :

(i) diffuse albedo (or reflectance) from the channel in the visible ;

(ii) surface temperature from the channel in the infrared ; eventually

(iii) day/night temperature difference, and

(iv) thermal inertia.

III - COMPARISON BETWEEN DIFFERENT RADIOMETERS (HCMR, VHRR and AVHRR)

Radiometers of the same type as the HCMR have been operational for the past few years for measurement, on an observational basis, of the earth's surface temperature : the VHRR on NOAA satellites (NOAA 3 to 5) from 1972 to 1978 ; the AVHRR on TIROS-N and NOAA 6 in 1978 and 1979, and recently (April 1981) on NOAA 7 which replaced TIROS-N. The performances of these radiometers are compared to those of the HCMR and summarized in Table 1. Note that the HCMR and AVHRR exhibit respectively a gain in radiometric quality (product of NEDT by the ground resolution) by a factor of 3 and 5 times over the VHRR.

In order to demonstrate the gain in radiometric performances of the HCMR over the VHRR and to evaluate its impact on the measured tempe-

rature field, the HCMR data acquired 10 May 1978 at 2 h TU on the Bay of Biscay have been compared to those of the VHRR acquired 11 May 1978 at 8 h TU on approximatively the same area centered at 45°30' N - 4°30'W. An eddy $\sim$ 50 km wide is clearly visible in the HCMR data (Fig. 1-a) while it appears only weakly in the VHRR data (too noisy) (Fig. 1-b). The refined quality of the HCMR data has allowed the detection and study of even those structures having weak amplitudes (less than 1°C).

Fig. 2 gives the spatial spectrum of variance density of the sea surface temperature E(k) (where k is the wavenumber) for the same region (64 x 64 km^2) corresponding to the preceeding eddy, drawn from the data of the VHRR and HCMR and calculated in the direction of the satellite track. The E(k) spectra, which characterize the surface temperature variability in the study region, tend to a limit at high wavenumbers, equal to the variance of the noise divided by τ (when τ is the sampling rate of the data : 1 km in the case of the VHRR ; 0.5 km in the case of the HCMR). Consequently the observed noise level is 0.03 $(°C)^2$ in the case of the HCMR and 0.6 $(°C)^2$ in the case of the VHRR - i.e. 20 times more elevated for the VHRR. Note also in Fig. 2 that the physical information begins to be significant at wavenumbers greater than 1/40 (km^{-1}) in the case of the VHRR, and 1/5 (km^{-1}) in the case of the HCMR. This indicates that in such an area of weak variance, the analysis of the surface temperature field is limited, due to noise, to a scale greater than 40 km in the case of the VHRR and to 5 km in the case of the HCMR.

A similar comparison was made on data acquired almost simultaneously by the HCMR and the AVHRR, 17 july 1979 in the Bay of Biscay (12 h 45 TU for HCMR, 15 h 15 TU for the AVHRR). The AVHRR data were acquired by the receiving station LANNION, France, and were not geometrically correc-

ted. The figures 3-a and 3-b present an enhanced visualization of an eddy structure of amplitude greater than 100 km in the south eastern region of the Bay of Biscay. The comparison of Fig. 3-a and 3-b shows a similar quality in the restituted temperature field by the HCMR and AVHRR that is confirmed by spectral analysis (Fig. 4). The spatial spectrum of temperature variance density, E(k), corresponding to the western portion of the eddy structure, was calculated in the direction of the satellite track.

In this oceanic zone, it seems that the surface temperature field could be characterized by $E(k) \sim k^{-2}$. The determination is limited at high wavenumbers by the noise level of the radiometers : 0.02 $(°C)^2$ for the HCMR, and 0.01 $(°C)^2$ for the AVHRR. This dependence of the spectrum on wavenumber has not been explained by any turbulence theory (DESCHAMPS et al., 1981). Note also in Fig. 4 that for the two experiments, the physical information begins to be significant at a scale greater than 5 km. This indicates that the relation between noise level and ground resolution by the radiometers is not optimal for study of surface temperature in those oceanic zones where variance is weak, particularly in the HCMR case. A better compromise would be to have a variance of noise less than 0.01 $(°C)^2$ and a ground resolution on the order of 2 km.

This comparative study emphasizes the following conclusions.

(1) The quality of the radiometric performances of the HCMR (ground resolution and NEDT) as compared to those of the VHRR, shows a net improvement in the observation of sea surface temperature field and its application to oceanography.

2) The analysis of the spatial spectrum of temperature variance density shows that the interpretation of the data is generally limited by radiometric performances (noise level) at scales below 5 km in oceanic regions. One can also conclude from this analysis that a N E D T less than 0.1°C and a ground resolution of 2 km give more optimal radiometric performances for the study of surface temperature in oceanic regions.

3) The HCMR data has the potential of being very useful for the detailed analysis of the sea surface temperature field, particularly in coastal regions, due to a ground resolution of 500 m.

4) The HCMR/HCMM and AVHRR/TIROS-N, NOAA 6 have comparable radiometric performances. The repetitivity and the existence of a channel at 3.7 μm for atmospheric correction (DESCHAMPS and PHULPIN, 1980) are in favor of the AVHRR; however, the HCMR has the unique advantage of delivering the photographic products and digital data radiometrically and geometrically corrected, which enables direct utilization.

IV - OCEANOGRAPHIC PHENOMENA OBSERVED OFF THE FRENCH COAST

Due to the operational features of the VHRR experiment on board the NOAA satellites, it has been possible since the 70's to systematically observe from space the surface temperature of french oceanic regions. Direct reception of the data at CMS (Centre de Météorologie Spatiale) in LANNION, France, has been routinely employed, being limited only by the radiometric performances of the VHRR and by the presence of clouds in the instrument field of view. In regions of the British Channel and North Sea, submitted to a continual regime of atmospheric perturbances, the cloud cover has the effect of considerably reducing the quality of observation from space, however, the meteorological situation in the Mediterranean is much more favorable.

The utilization of channels in the visible for discriminating regions of clouds and the time scales of atmospheric perturbations (generally much shorter than comparable oceanic perturbances) has permitted effective observation even though the presence of clouds has often rendered difficult those dynamic studies requiring continual survey of the phenomena of interest.

An HCMR with improved radiometric performance was launched in April 1978 with the hope of providing more detailed observation of fine structure phenomena. The photographic products provided by NASA were particularly appropriate since prior geometric correction and enhancement in the temperature range of the sea enabled direct interpretation of the data.

From May 1978 to May 1979, the HCMR provided approximatively 1000 such images of french oceanic regions that have since been examined and analysed.

That which follows is a presentation of the work accomplished on 3 regions of study (figure 5) : the southern portion of the North Sea (zone 1) ; the western British Channel, the Celtic Sea, and the Bay of Biscay (zone 2) ; and the northwestern Mediterranean (zone 3). On the photo images, the darkest shades correspond to either the lowest temperature (thermal infrared channel) or to the lowest reflectance (visible channel).

ZONE 1

The Thermal effluent of the Rhine

Systematic observations of the effluent from the Rhine-Meuse-Escaut system have been obtained by the HCMM experimental satellite and

are presented in figures 6 and 7.

On entering the sea, the effluent is entrained by the circulation characteristic of the southern portion of the North Sea. The mean residual circulation (NIHOUL and RONDAY, 1975) is directed from the south west to the north east (fig. 8) and the current tends to flow in a straight line from the Dover Strait following the isobaths deeper than 30 m which are located at the center of the southern Bight. It moves off the dutch coastline at the level of the Rhine-Meuse-Escaut estuary system permitting the effluent to diffuse offshore-i.e. westward. At the Frisonnis archipelago the current more or less follows again the dutch coast.

The interaction of the effluent (warmer in summer, colder in winter) with the residual circulation is complex, but an examination of the photos shows that it can be separated into 2 parts :

- The southern portion of the effluent (Escaut and Meuse) has a tendancy to flow towards the southwest before being entrained by the residual current, forming a diffuse wedge-shaped plume along the belgian coast. This is particularly visible during the winter period shown in figure 7. A LANDSAT image (figure 9) reveals that sediments are transported southward in a similar manner. The southern region receives fresh water of lower density ejected by estuary system but the energetic action of tidal currents rapidly destroys and prevents stratification in the marine environment.

- The northern position of the effluent (Rhine principally) is generally entrained directly toward the northeast and forced along the dutch coast by the residual current (figure 6 during the summer). The effluent forms a pronounced offshore boundary separating the non stratified atlantic water in the center from the coastally stratified water. In northern section, stratification is made possible by the combined actions of transport of less dense fresh water and the higher values of the SIMPSON-HUNTER

parameter (NIHOUL, 1980) which governs the stability of stratification. Unlike NIHOUL's model, the one's developed by PINGREE (1978) does not indicate this tendency toward increased stratification along the dutch coast from the city of the Haye to Texel Island (Fig. 10).

An examination of the meteorological situation (mean wind speed direction and speed) for the period May-June 1978, reveals the interaction between the residual current and the thermal effluent. In the situation of winds dominating from the west (4-10 June), the northern portion of the plume is observed to extend along the dutch coast in the direction of the Frisonnis Islands (see the observations of 4 and 9 June). On the other hand, when winds were from the northeast (16-19 and 25-31 May, 14-20 June) a broad seaward dispersion of the plume (typically 40 km) is noted (observations of 18, 30 May ; 19-20 June). During 19-20 June, following relatively strong winds from the northeast, cold unstratified water, encountered offshore the Frisonnis Islands, penetrated southward along the dutch coast. The offshore transport of freshwater rapidly diffused and was then insufficient to maintain stratifacation near the coast, which is in agreement with the diminution of the SIMPSON-HUNTER parameter.

The diffusion system of the northern portion of the thermal effluent is interpreted as being connected to changes in the residual current that arise as a consequence of wind action. Western winds tend to create a wind driven current which contributes to intensify the residual current, particularly along the dutch coast (PINGREE and GRIFFITHS, 1980), where it forces the effluent shoreward while entraining it farther to the north. When the winds are from the northeast they counteract the flow of the residual current, reducing its speed and deflecting it toward the english coast, thus permitting a broad seaward diffusion of the thermal effluent and only

limited northward entrainment.

Observation of the thermal effluent of the Rhine-Meuse-Escaut system by photographic products of the HCMM enables the following conclusions to be drawn, which are also supported by results based on numerical simulation (NIHOUL and RONDAY, 1975) of the circulation in the southern Bight of the North Sea :

- The average circulation is directed from the southwest to the northeast away from the Dover Strait (NIHOUL and RONDAY, 1975).

- The western winds reinforces the residual current toward the dutch coast, whereas winds from the northeast oppose this current and deflect it toward the english coast (PINGREE and GRIFFITHS, 1980).

- Stratification is absent to the south of the Rhine-Meuse-Escaut estuary system, but present to the north along the dutch coast (NIHOUL, 1980) where it is maintained by the transport of freshwater from river outflow.

ZONE 2

A - TIDAL FRONTS WEST OF BRITTANY AND IN THE WESTERN BRITISH CHANNEL

Figures 12-a and 12-c show HCMR observations of tidal fronts in the western approaches of the British Channel, west of Brittany (Ushant front), near the cape of Cornwalls (front of Scilly Islands), and between Ireland and England (front of the Irish Sea). These fronts have been known for a long time (already observed by DIETRICH, 1950) and the mechanisms forming them have been studied by various authors (SIMPSON and HUNTER, 1974 ; FEARN-HEAD, 1975, PINGREE and GRIFFITHS, 1978 ; GARZOLI, 1979).

These fronts are produced by the action of tidal currents which mix the water column in the shelf region when the depth is shallow and the tidal current speed, U, is high, and eventually destroy the summer stratification. As a result, surface water is colder and a well-marked surface thermal front separates the regions of stratified and homogenous waters.

The stratification is governed either by the SIMPSON-HUNTER parameter, $S = \log_{10}(H/C_D U^3)$ (SIMPSON and HUNTER , 1974) or by the parameter $S' = H/U^2$ (GARZOLI, 1979) where C_D is the drag coefficient ($C_D \simeq 0.0025$). According to PINGREE and GRIFFITHS, when $S < 1$ (H/U^3 is expressed in $cm^{-2}\ s^3$) the medium is stable and stratified, and when $S > 2$ mixing occurs and the fluid becomes homogeneous. In the model of GARZOLI, $H/U^2 = 1\ cm^{-1}\ s^2$ is the critical value beyond which stratification no longer takes place. The thermal front appears at the boundary between the stratified and homogeneous waters.

Fig. 13 shows locations of the fronts predicted by FEARNHEAD (1975), and PINGREE and GRIFFITHS (1978). These positions, already captured by NOAA satellites (SIMPSON et al., 1978 ; PINGREE and GRIFFITHS, 1978), are confirmed by HCMM observations. Note also in fig. 12-a and 12-c that the Ushant front, though pronounced at the level of Ushant Island ($\sim$ 3°C), progressively disappears farther north. This is explained by the fact that the gradient of S or S' is weaker in the northern portion than around Ushant Island (weaker tidal currents and the slope less steep) rendering the separation between the stratified and homogeneous regions less distinct.

On the image of 25 August, and less clearly on that of 21 September, one can observe a phenomenon mentionned by PINGREE (1979) ; colder and more homogeneous water east of the front of Brittany diffusing westward in fingers perpendicular to the margin of the front. According to PINGREE, these intrusions

of cold water play an important role in the mechanism of expanding thermocline erosion which occured during this period (the end of the summer). As surface heat was reduced, the front progressed westward.

The positions of these fronts are subjected to changes due to a variety of factors.

- Variations of the tidal coefficient can double the amplitude of the tidal current.

- The evolution of energy and heat exchanges at the surface throughout the season can create conditions of different stratification.

- The wind can be a dominant factor in regions of weak tidal current (SIMPSON et al., 1978).

- The phenomenon of advection may play a role, advancing the front margin (GARZOLI, 1979).

HCMR observations show the evolution in the position of the Ushant front during May-September 1978 (Fig. 14). The position is very fluctuating. Note an eastward displacement, due to increased stability of the stratified water, is absent during May-September in contradiction to studies by PINGREE (1975) and GARZOLI (1979).

Moreover, in Fig. 14, the situation of May 21 is different from that of 26 May in that the front is displaced more than 100 km westward at 49°30' N. These observations occured before and after a period of strong tidal coefficients, the meteorological situation being the same during 15-26 May with relatively weak winds in the northern sector. These observations suggest the following hypothesis : the currents became more important between 21 and 26 May, and as S and S' parameters diminished, the stratification was progressively destroyed in the region where the front was localized on 21 May. In response to the diminution in the S and S' parameters, the thrust of the front advanced to greater depths (westward) until H was large enough to render ineffective

the tidal currents on the destruction of the stratification.

B - OBSERVATIONS ON THE EDGE OF THE CONTINENTAL SHELF

Summer satellite observations (PINGREE, 1979, DICKSON et al., 1980) show a band of cold water situated at the edge of the continental shelf, where the ocean bottom drops from 200 m to several 1000 m. This band of cold water (reported by PINGREE from VHRR data in 1976-1978) persisted from July to September between 5° and 10°W. DICKSON et al. Presented observations in May and June 1979 obtained from AVHRR data, in which the band of cold water followed the edge of the continental shelf from the south of Ireland (11°W) to the south of Brittany (4°W). The explanation for this phenomenon that appears as an upwelling remains uncertain. Based on the works of KILLWORTH (1978), DICKSON advances the hypothesis of an interaction between Kelvin waves and the shelf break, an interaction which is intensified by the presence of canyons. The theory proposed by KILLWORTH supposes winds dominate from the northwest, blowing parallel to the slope. HEAPS (1980) suggests an upwelling generated at the shelf break when winds dominate from the southwest. Note, however, that satellite observations generally correspond to a cloudfree situation associated with an anticyclone high over the Bay of Biscay and the British Isles, and that the resulting winds were frequently from the east. This is contrary to the preceeding theory unless one admits to a shift of a few days between meteorological forcing and the response of the sea.

During the period May 1978-1979, 10 HCMR images focussed on the edge of the continental shelf. These permitted a pinpointing of phenomena and enabled the following observations to be made.

1) The well established band of cold water corresponds to the local destruction of the thermocline under the action of a mixing process linked to the presence of the shelf limit. This band appears in May-June at the onset of

summer when the thermocline is formed, and disappears in the autumn (october) when the stratification is destroyed.

2) The phenomenon is more intense after spring tides, (Fig. 12-a from 25 August 1978, and Fig. 12-c from 21 September 1978), whereas during the period of neap tides, the band of cold water appears as a more diffuse feature (Fig. 12-b from 15 September 1978). The physical process provoking this upwelling of cold water has a possible a relation to the interaction of tidal waves with the edge of the shelf.

3) One can follow an evolution of phenomena during the course of the summer. Early in the season (a period of weak stratification) a narrow band of cold water (several 10ths of km) was observed on the edge of the armorican and celtic shelves from south of Ireland to 46°N - 4°W in the Bay of Biscay. At the end of the summer (a period of strong stratification), the band of water had expanded and was particularly intense between 5 and 9°W though not discernable on the segment oriented NW-SW at the edge of the shelf from 49°N - 11°W to 46°N - 4°W. The observations of 25 August and 21 September 1978 are typical of this. Both were obtained near the close of the sping tide period. The zones of more intense phenomena which correspond to the colder water are located in precisely the same regions for both documents. It is worth emphasizing that the part of the shelf edge between 5 and 9°W coincides whith the segment where the slope of the shelf break is larger (it varies between 0.05 and 0.1, whereas in the region farther north, the slope is less than 0.03) and where the tidal currents are stronger (1.5 knot during spring tide). This group of observations indicates a direct correlation between the presence of cold water along the edge of the continental shelf and the amplitude of the tidal current. MAZE (1980) has shown that the passage of a barotropic tide over the slope can generate an internal baroclinic wave (elevation of the thermocline) of an amplitude of the same order as the depth of the thermocline, thereby suggesting an explanation for the appearance of cold water

at the surface. The amplitude of the internal wave is increased by the speed of the current and the inclination of the shelf break. The appearance of cold water is restricted to the summer, i.e. when the thermocline is pronounced, and to areas where the strongest currents and steepest slopes are encountered, as in the situation along the coast of Brittany. The observation of 25 August 1978 shows clearly a complex system of internal waves of wavelengths approximating 50 km which correspond to those of internal waves (c_i = 1 m s^{-1}) having a tidal period. The stationary regime of the internal waves is occasionally visible between the south of Brittany and the shelf break where it seems to be in resonnance within the limited conditions constituted by the shape of the basin.

On one occasion observed in the winter (Fig. 12-e from 16 January 1979) a band of warm water along the slope was shown extending very shoreward into the Bay of Biscay. In the location of the cold upwelling usually present off northwest coast of the iberian peninsula, warm water is also observed, having the appearance of a warm upwelling. It is difficult to attribute the phenomenon to the resurfacing of Mediterranean water because its depth is on the order of 1000 m. The hypothesis of a mechanism of advection linked to wind induced circulation in the Bay of Biscay can be equally advanced. This would imply current values (on the order of 1 m. s^{-1}) established over an extended time (on the order of a week).

C - COOLING ON THE CONTINENTAL SHELF DURING THE AUTUMN PERIOD

Starting in September, the surface layer begins to cool and become homogeneous to progressively greater depths. The mechanism is more rapid and abrupt in shallow areas, such as coastal zones ($h < 20$ m). At the end of September,

cold water that began to appear at several localized points along the southern coast of Brittany to Gironde (Fig. 12-c), had, by the end of October, formed a continuous coastal band extending to the 50 m isobath (Fig. 12-d). Note that when the thermocline is in complete erosion, cold water spans the entire shelf and extends seaward as successive intrusions with the characteristic scale of 20-50 km. Observations in the winter period of 16 January and 27 February 1979 (Fig. 12-e and 12-f) show a persistant band of cold homogeneous coastal water that extended to the 100 m isobath forming a distinct front of several °C, south of Brittany.

ZONE 3

A - NORTH BALEARIC FRONT

Figs 15-a, 15-b and 15-c provide observations of the north balearic front on 11, 16 July and 12 August 1978. This front results from circulating waters in the western Mediterranean which are characterized by a substantial surface current (LACOMBE and TCHERNIA, 1972) (extending to a depth of approximatively 150 m) of atlantic water and which flows eastward along the algerian coast in leaving the alboran Sea (Fig. 16). West of Algeria, the current stems and divides into 2 branches ;

- One continues in the eastward direction along the african coast to the strait of Sicily where it penetrates into the eastern Mediterranean.

- The other curves northeast, merges with the Ligurian current, and follows along the southern coast of France and Spain. This circulation forms two cyclonic rings, one in the Ligurian Sea and another trapped around Balearic Islands which generates the north balearic front.

In Fig. 15-a, 15-b and 15-c, one can detect two major oscillations in the front ; the first along the coast of Spain around 4°30' E and the second around 8°E and 42°N. The average position of the front during the summer of 1978 can be seen in Fig. 17. Note the southward displacement at 7°E, from May to August which can be related to wind action dominating from the NW that produces upwellings along the coast of Gulf of Lions and entrains the circulation to the south (MILLOT and WALD, 1981).

Aside from this general form, the north balearic front induces small scale meanders (typically 10-20 km) in response to baroclinic instability in the frontal zone (radius of deformations ; several km). Equally notable is an anticyclonic ring near the coast of the french-spanish border, which corresponds to the deviation of the Ligurian current by the Cape of Creux.

B - LARGE SCALE EDDIES OFFSHORE THE ALGERIAN COAST

On the observations of 11, 16 and 21 July (Fig. 15-a, 15-b and 15-c), two large anticyclonic eddies, having dimensions approximating 100 km, are clearly visible. They are practically stationary and centered at 38°N - 7°E. A weak propagation E - NE is noted. These eddies are revealed by the entrainment of colder water derived either from upwelling on the algerian coast (cape Bougaroun) or by cold water flowing along the sardinian coast. Although they have been systematically observed by satellite photos during the summer period, their origin still remains unclear. They could be linked to experiments made in a rotating tank (GRIFFITHS and LINDEN, 1981) in which similar undulations were attributed to a combination of barotropic and baroclinic instabilities. The horizontal scale L_E (100 km), of the ocean eddy is in partial agreement with the theory of baroclinic instability :

$$L_E \simeq \Pi R_H$$

with R_H, the radius of deformation :

$$R_H = \frac{1}{f} (gh \frac{\Delta\rho}{\rho})^{1/2} \simeq 20 \text{ km}$$

where H ≃ 150 m is the depth of the surface layer of the atlantic water ; $\frac{\Delta\rho}{\rho} \simeq 3.10^{-3}$ is the relative difference in density between the surface water and deep water ; $f \simeq 0.9(10^{-4})$ s^{-1} is the Coriolis parameter at the latitude in consideration ; and g is acceleration due to gravity. Fig. 15-c of 21 July seems to support the following. From eddies forming along the algerian coast at 3°E, there seems to be an amplification developing into rings from 5°E. Elsewhere, between 5°E and 9°E, anticyclonic eddies seem to induce smaller cyclonic rings along the algerian coast.

The observation of 16 July reveals a remarkable phenomenon between Balearic and Sardinia Islands around 40°N. The surface temperature field is very inhomogeneous. Structures more or less organized in bands 5 to 10 km wide give the surface temperature field a filamentious appearance for which the following explanation is proposed. From 5-8 July, a violent wind from the northwest, the Mistral, blew on the Gulf of Lions, entraining the thrust of the north Balearic front toward the south (particularly pronounced on the image of 11 July). Then just prior to 16 July, the winds were extremely weak resulting in minimum surface agitation and the cold water entrained southward to 40°N mixed with atlantic surface water in a series of warm and cold pockets, elongating in the direction of the current. During such a period, the direction of warm and cold fingers of water can be considered as an indication of the direction of the surface currents ; this being equally evident in the region of the large scale eddies on 16 July (38°N).

C - THE LIGURIAN CURRENT AND UPWELLINGS IN THE GULF OF LIONS

The situation in the liguro-provencal basin is well illustrated in Fig. 15-e, 12 August 1978. A cold water mass is located in the center of the basin bounding by a contrastingly warm water circulation that follows along the coast of Corsica, Italy and France (WALD and NIHOUS, 1980). The interface between the central water and the coastal current exhibits a series of deformations having an anticyclonic tendency and wavelengths of $\sim$ 50 km, particularly in the northern portion. This process has been outlined by CREPON et al. (1980), and is analogous to deformations in the polar front of the atmosphere and due to a phenomenon of baroclinic instability.

After flowing along the french coast, the Ligurian current penetrates into the Gulf of Lions, where it encounters coastal summer upwellings produced by strong gusts of winds from north (Mistral) and west (Tramontane) (Fig. 15-d, of 22 July and 15-e, of 12 August 1978). The image of July 22 gives a clear view of the extent of these upwellings created by the strong winds of the preceding days (17-21 July). Colder water appeared on the coast in diverse locations (MILLOT, 1979) : cape of Adge, mouth of the Rhone, cape Sicié and, in spreading seaward , was deflected to the right of the wind as a consequence of Coriolis acceleration.

The southward expansion of the cold upwelling extends to 100 km south of Marseille and is an important feature. The LANDSAT image of September 1976 (Fig. 18) confirms the mechanism that at the time of the upwelling, coastal sediments were entrained offshore at the cape of Adge and tended to describe an anticyclonic circuit. Only the western border of the upwelling generated at the mouth of the Rhone, is visible, but significant entrainment of suspended material farther south is apparent.

These phenomena have been numerically modelled by HUA and THOMASSET (1982), and good agreement has been obtained between the satellite observations and the results of the model.

Following release from the upwelling, the Ligurian current flows along the slope of the continental shelf of the Gulf of Lions and entrains towards the southwest those masses of cold water upwelled east of Marseilles (Fig. 19, for 12 August 1978).

5 - IMPORTANT DIURNAL HEATING DETECTED BY THE HCMR IN CONDITIONS OF WEAK WINDS

During the period extending from May 1978 to August 1978, a large amount of data acquired daily on the Mediterranean by the HCMR revealed marine zones of similar spatial structures in both visible and thermal infrared channels. Fig. 20 shows an example of these features ; one located in the area between Corsica and the southern coast of France, and the other in the area near the eastern coasts of Corsica and Sardinia. One observes higher temperatures in the infrared channel (Fig. 20-b) and at the same time, important changes in the reflectance in the visible channel (Fig. 20-a). These structures have been identified as significant heating of several degrees, of the first few centimeters of the surface layer during periods of weak wind (DESCHAMPS and FROUIN, 1982).

The changes in reflectance observed in the visible channel are interpreted as variations in "glitter", -i.e. in the specular reflection of direct solar radiation of the agitated sea surface. During the period around the summer solstice, the geometric conditions of observation were favorable for the detection of glitter phenomenon in the western portion of the scenes. Glitter is usually pronounced when the sea is relatively calm, and a maximum in reflectance occurs when the direction of satellite observation is near that of the specular reflection of the sunlight. One such patch of uniform brightness is noticeable in southwestern portion of Fig. 20-a. In the case of a very calm sea, the reflection of the surface becomes almost specular and a reduction of reflectance can usually be noted, because it is very improbable that the angle of the satellite observation would be aligned exactly in the direction of the specular reflection.

Fig. 20-a illustrates this reduction in reflection : two phenomena are presented with the more or less brilliant areas corresponding respectively to weak and zero winds. The fact that the change in sea surface agitation can produce an increase or reduction of the observed reflectance has already been mentionned by Mc CLAIN and STRONG (1969), and LA VIOLETTE et al. (1980).

When the surface agitation due to wind stress decreases, the heating of the surface layer increases (HASSE, 1971). In the absence of wind, the gain in temperature is almost entirely determined by the local absorption of solar radiation. The effect is that the diffusivity in the upper layer tends towards the limit value given by the thermal molecular diffusivity which, on a scale of several hours, is insufficient for distributing the heat to deeper layers. Thus one can observe substantial diurnal heating of several degrees in the surface layer.

The meteorological observations (Fig. 20-d) are in good agreement with the fact that the zones of weak winds correspond to zones of weak reflectance and strong diurnal heating.

Radiative cooling during the night rapidly destroys most of the diurnal heating at least in the upper surface layer. The evidence of diurnal heating can then be established by making a comparative analysis of successive day/night observations Fig. 20-c gives the difference between day and night temperatures at 12-hour interval, corresponding to the day time image shown in Fig. 20-b and furnished by NASA : the warm anomalies are always present yet very well correlated to variations in reflectance in the visible channel.

From May 1978 to August 1978, approximatively 60 images were obtained on the western Mediterranean, among 34 of which it has been possible to identify several marine regions showing significant diurnal heating of more than 1°C and involving surface areas of dimensions ranging from 10 to 100 km. The frequency of these events is therefore of consequence in the Mediterranean. Diurnal heating seems much weaker in the near Atlantic and the North Sea where the authors have been able to observe only one scene possessing this phenomenon. Because regions such as the Mediterranean can be strongly affected by diurnal heating, the measurement of the sea surface temperature field obtained by daytime satellite observation may be without any oceanographic significance and should be restricted to night or early morning when the surface layer is more homogeneous.

6 - CONCLUSIONS

In this study, photographic products and numerical data provided by the HCMM experiment have been systematically utilized. Two types of conclusions

can be drawn from this. The first bears on the adequacy of the experiment itself and the pictorial documents provided for the aim of the research : observation of the sea surface temperature field. The other conclusions put in evidence some results of oceanographic interest.

The comparison of the radiometric performances (product of ground resolution by resolution in temperature, NEDT) between the HCMR and the VHRR indicates a gain by a factor of 7 in favor of the HCMR, a gain similar to that of the AVHRR which makes them comparable for selected operations. This gain is decisive and essential for observation of mesoscale structures (10-100 km) in the ocean. Evidence has been provided as much by the study of the spatial spectrum of temperature variance density as by certain original observations which can be found in section 4 (large scale eddies in the western Mediterranean).

The photographic products provided by NASA, already geometrically corrected and enhanced in the sea surface temperature range, greatly facilitated the interpretation of the data obtained. It avoided heavy computer treatment that is necessary with certain meteorological satellites (data of the VHRR and AVHRR). It also greatly improved the amount and quality of possible interpretations through an economy of means and by facilitating a more rapid and wider dissemination to the community of involved and interested oceanographers. A similar treatment of AVHRR data, furnishing operational items of similar photographic products corresponding to the needs of oceanographers, would certainly enable the use of satellite data complementary to in-situ measurements, to progress more rapidly.

Even though the HCMR and AVHRR have potentially comparable radiometric performances, the AVHRR of TIROS-N and NOAA-6 has certain advantages : increased repetitivity that is essential for eliminating the effect of cloud coverage, correction of atmospheric emission by means of a channel centered at 3.7µm, and operational character of the experiment until the mid 80's.

The analysis of the HCMR photographic products has permitted conclusions to be drawn on several aspects of oceanography :

- the influence of the residual current, as it passes through the Dover Strait, on the thermal effluent of the Rhine, and the rather broad offshore diffusion of the effluent associated with winds from the northeast or west which respectively retard or accelerate the residual current,

- the analysis of images obtained revealing the presence of cold water in the summer along the edge of the continental shelf to the west of Britanny firmly supporting the hypothesis of an upwelling mechanism produced by the action of tidal currents over the slope of the shelf break,

- the detection of large scale eddy structures (100 km) in the western Mediterranean around 6 E - 38° N during the summer, probably due to a phenomenon of instability of the baroclinic - barotropic type,

- the frequent appearance of significant diurnal surface heating (several °C) linked to weak winds in the Mediterranean, that should lead one to use with caution the daytime observations of the summer season.

The results presented here reflect upon a fairly restricted period : May 1978 to May 1979. It is evident that in the coming years, the infrared images of the AVHRR satellite will continue to be of broad interest to the oceanographic community by offering systematic and repetitive observations and by, for example, filtering cloud cover for the study of temporal changes in ocean-atmosphere phenomena.

ACKNOWLEDGMENTS

The authors are greatly indebted to NASA for providing them HCMM data as a support to HCMM Investigation No 15. Thanks to V.L. Vasek for her aid in the translation. Support for this work has been obtained from the following French agencies : CNRS (Centre National de la Recherche Scientifique) and CNES (Centre National d'Etudes Spatiales).

- REFERENCES -

DICKSON R.R., GURBUTT P.A., PILLAI V.N., 1980 : Satellite evidence of enhanced upwelling along the european continental slope. J. Phys. Oceanogr., 10, 813-819.

DIETRICH G., 1950 : Die anomale jarheschankung der warmeihalts in Englishen kanal, the ursachen und auswirkungen.Dtsch. Hydrogr.Z.

FEARNHEAD P.G., 1975 : On the formation of fronts by tidal mixing around the British Isles. Deep-Sea Res., 22, 311-321.

GARZOLI S., 1979 : Contribution à l'étude de la formation et de l'évolution du front thermique sur le plateau continental breton. Ann. Hydrogr., 5ème série, vol. 7, 2, 5-25.

HEAPS, N.S., 1980 : A mechanism for local upwelling along the European continental slope. Oceanol. Acta, 3, 449-454.

KILLWORTH P.D., 1978 : Coastal upwelling and kelvin waves with small longshore topography. J. Phys. Oceanogr., 8, 188-205.

LACOMBE H., TCHERNIA P., 1972 : Caractères hydrologiques et circulation des eaux en Méditerranée. Dans "The Mediterranean Sea, Stanley D.J., Ed., Dowden, Hutchinson et Ross,Stroudsberg, 26-36.

LA VIOLETTE, P.E., PETEHERYCH S., GOWER J.F.R., 1980 : Oceanographic implications of features in NOAA satellite visible imagery. Bourdary-Layer Meteorol., 18, 159-175.

LEGECKIS R., 1978 : A survey of worldwide sea surface temperature fronts detected by environmental satellite. J. Geophys. Res., 83, 4501-4522.

MADELAIN F., 1967 : Etude hydrologique au large de la péninsule ibérique. Cahiers Océanogr., 19 (2), 125-136.

MAZE M.R., 1980 : Formation d'ondes internes stationnaires sur le talus continental. Application au Golfe de Gascogne. Ann. Hydrogr., n° 754 , 45-58.

Mc CLAIN E.P., 1980 : Passive radiometry of the ocean from space-an overwiew. Boundary-Layer Meteorol., 18, 7-24.

Mc CLAIN E.P., STRONG A.E., 1969 : Dark patches in satellite viewed sunglint areas. Montl. Weather Rev., 97, 875-883.

MILLOT C., 1979 : Wind induced upwelling in the Gulf of Lion. Oceanol. Acta, 2, 261-274.

NIHOUL J.C.J., 1980 : Résidual circulation, long waves and mesoscale eddies in the North Sea. Oceanol. Acta, 3, 309-316.

NIHOUL J.C.J., RONDAY F.C., 1975 : The influence of the tidal stress on the residual circulation. Tellus, 29, 484-490.

PINGREE R.D., 1975 : The advance and retreat of the thermocline on the continental shelf. J. Mar. Ass. U.K., 55, 965-974.

PINGREE R.D., 1979 : Baroclinic eddies bordering the Celtic Sea in late Summer. J. Mar. Biol. Ass. U.K., 59, 689-698.

PINGREE R.D., GRIFFITHS D.K., 1978 : Tidal fronts on the shelf seas around the British Isles. J. Geophys. Res., 83, 4615-4622.

PINGREE R.D., GRIFFITHS D.K., 1980 : Currents driven by a steady uniform wind stress on the shelf seas around the British Isles. Oceanol. Acta, 3, 227-236.

SIMPSON J.H., ALLEN C.M., MORRIS H.C.G., 1978 : Fronts on the continental shelf. J.Geophys.Res.83,4607-4614.

SIMPSON J.H., HUNTER J.R., 1974 : Fronts in the Irish Sea. Nature, London, 1250, 404-406.

WALD L., NIHOUS G., 1980 : Ligurian Sea : Annual variation of the sea surface thermal structure as detected by satellite NOAA 5. Oceanol. Acta, 3, 465-469.

CREPON M., WALD L., MONGET J.M., 1982 : Low frequency waves in the ligurian Sea during December 77. J. Geophys. Res., 87, 595-600.

LEGEND OF ILLUSTRATIONS

1. - Satellite observations in the thermal infrared of the Bay of Biscay region around 45°N and 4°30'W (a) by the VHRR, 10 May 1978 at 8h TU and (b) by the HCMR, 11 May 1978 at 2h TU. Each grey shade corresponds to (a) 0,1°C and (b) 0,3°C. In the center of these images one notes the presence of an eddy approximating 50 km in diameter, basely visible on the VHRR image due tho instrumental noise get clearly distinguishable on the HCMR image.

2. - Density spectrum of variance of the surface temperature field for the same region (64 x 64 km^2) in the Bay of Biscay obtained from HCMR and VHRR data. The direction of analysis corresponds to that of the satellite track.

3. - Satellite observations in the thermal infrared of the Bay of Biscay 17 July 1979 (a) by the HCMR at 12h45 TU and (b) by the AVHRR at 15h15 TU. Each grey stade corresponds to (a) 0,2°C and (b) 0,1°C. One notice the presence of a large eddy structure approximately 300 km wide.

4. - Density spectrum of variance of the surface temperature field for the same region (64 x 64 km^2) in the Bay of Biscay obtained respectively from HCMR and AVHRR data. The direction of analysis corresponds to that of the satellite track.

5. - French oceanic regions : southern portion of the north sea (zone 1), the British Channel, the Celtic sea, and Bay of Biscay (zone 2), the north-western mediterranean (zone 3).

6. - HCMM observations of the thermal effluent of the Rhine-Meuse-Escaut system during the summer season. Significant offshose diffusion on images (a), (b), (e) and (f) (A-A 0022-12470, A-A 0034-13110, A-A 0054-12470 and A-A 0055-02030), effluent abutting the coast on images (c) and (d) (A-A 0039-13050 and A-A 0044-12570).

7. - HCMR observation A-A 0263-01320 of thermal effluent of the Rhine-Meuse-Escaut system during the winter reason (14 January 1979 at 2h TU). The southern position of the effluent flows toward the southewast forming a diffuse, wedge-shaped plume along the belgium

8. - Residual circulation in the southern position of the north sea, according to NIHOUL and RONDAY (1975). Stream lines in 10^4 m^3/s^{-1}

9. - Landsat image of 12 June 1975 showing the transport of sediment (clear shades) from the Meuse-Escaut system toward the southwest along the belgian coast.

10.- Value of the SIMPSON-HUNTER parameter, S, in the southern portion of the North Sea : (a) according to the model of PINGREE and GRIFFITHS (1978), and (b) according to the model of NIHOUL (1980). The S values greater than 2 correspond to a stratifield medium; value less than 1, to a homogeneous medium; and values of 1.5 to a system in transition where thermal fronts can be encountered.

11.- Mean wind speed and direction on the surface in the southern position of the North Sea for the periods of (a) 8-31 May 1978, and (b) 1-20 June 1978.

12.a - HCMM observation A-A 0121-13260 in the thermal infrared channel for 25 August 1978 at 13h26 TU. Tidal fronts at the entrance of the Manche. Relatively cold water at the shelf break and offshore of Brittany.

12.b - HCMM observation A-A 0142-13190 in the thermal infrared channel for 15 September 1978 at 13h19 TU. Following a period of weak tidal coefficients, the band of cold water at shelf break and offshore Brittany is less distinct.

12.c - HCMM observation A-A 0148-13320 in the thermal infrared channel for 21 September 1978 at 13h31 TU. Tidal fronts at the entrance of the Manche, near Cape of Cornwalls, and between Ireland and England. Relatively cold water at the shelf break offshore of Brittany. Upwelling along the coast of Spain.

12.d - HCMM observation A-A 0185-13180 in the thermal infrared channel for 28 October 1978 at 13h18 TU. Cooling on the continental shelf in the autumn season. Note the characteristic structure corresponding to turbulent offshore diffusion of cold coastal water.

12.e - HCMM observation A-A 0265-02090 in the thermal infrared channel for 14 January 1979 at 2 h 09 TU. Relatively warm water at the limit of the continental shelf southeast of Brittany, in the Bay of Biscay along the coast of Spain.

12.f - HCMM observation A-A 0307-01530 in the thermal infrared channel for 21 February 1979 at 1 h 53 TU. Note the band of cold water along the french coast.

13.- Tidal fronts in the summer season at the entrance of the Manche and in the Celtic Sea as predicted by the models of (a) FEARNHEAD (1975) and (b) PINGREE and GRIFFITHS (1978).

14.- Evolution of the tidal front position at the entrance of the British Channel during the period of May through September 1978, deduced by HCMR observations.

15.a - HCMM observation A-A 0076-01590 in the thermal infrared channel for 11 July 1978 at 1 h 59 TU. North Balearic front. Large scale eddies offshore of the african coast.

15.b - HCMM observation A-A 0081-01510 in the thermal infrared channel for 16 July 1978 at 1h51 TU. Apart from the large scale eddies offshore of the Algerian coast, note the irregularity of the surface temperature field between Baleares and Sardinia.

15.c - HCMM observation A-A 0086-01450 in the thermal infrared channel for 21 July 1978 at 1 h 45 TU. Eddies forming along the Algerian coast and expanding toward the coast.

15.d - HCMM observation A-A 0087-02020 in the thermal infrared channel for 22 July 1978 at 2 h 02 TU. Coastal upwelling in the Gulf of Lion.

15.e - HCMM observation A-A 0108-01510 in the thermal infrared channel for 12 August 1978 at 2 h 02 TU. Coastal upwelling in the Gulf of Lion. Liguro-Provençal Current.

16.- Summer surface circulation in the Mediterranean, according to LACOMBE and TCHERNIA (1972).

17.- Seasonal positions of the North Balearic front during the summer of 1978.

18.- LANDSAT image of September 1976. Upwellings in the Gulf of Lion. Coastal sediments entrained offshore and very much to the south in the case of the upwelling produced at the mouth of the Rhone.

19.- Diagram illustrating the situation on 12 August 1978 (Fig.15.c). After driving various masses of cold upwelling ligurian water the progression of the current is interrupted by a later upwelling released near the Cape of Sicily.

20.- Diurnal heating in the western Mediterranean (a) HCMM observation A-A 0038-12440 in the visible channel on 3 June 1978 at 12h44 TU. Note bright patches (high reflectance) to the coast and west of Corsica and Sardinia. (b) idem (a), but in the thermal infrared channel. Note the warmer water to the east and west of Corsica and Sardinia. (c) Day/night temperature difference from HCMM observations obtained on 3 June 1978 at 1h50 TU (night) (A-A 0038-01500) and 12h44 TU (day). The darker shades correspond to cooler diurnal temperatures. (d) Meteorological situation on 3 June 1978 at 12 h TU.

21.- Diurnal heating in the North Sea. (a) HCMM observation A-A 0034-13120 in the thermal infrared channel on 30 May 1978 at 13 h 10 TU. Note the warm patch east of Scotland in the center of the dark (cold) field. (b) HCMM observation A-A 0035-02280 in the thermal infrared channel on 31 May 1978 at 2h30 TU. The warm patch has disappeared during the night. (c) Meteorological situation on 30 May 1978 at 12 h TU.

Table 1 - Performances of the different radiometers on board the satellites :

	NEDT (300 K)	Ground Resolution	Repetitivity
VHRR/NOAA	0.5 to 1K	1 Km	2/day
AVHRR / TIROS-N NOAA-6	0.1	1	4/day
HCMR/HCMM	0.3	0.5	1/day

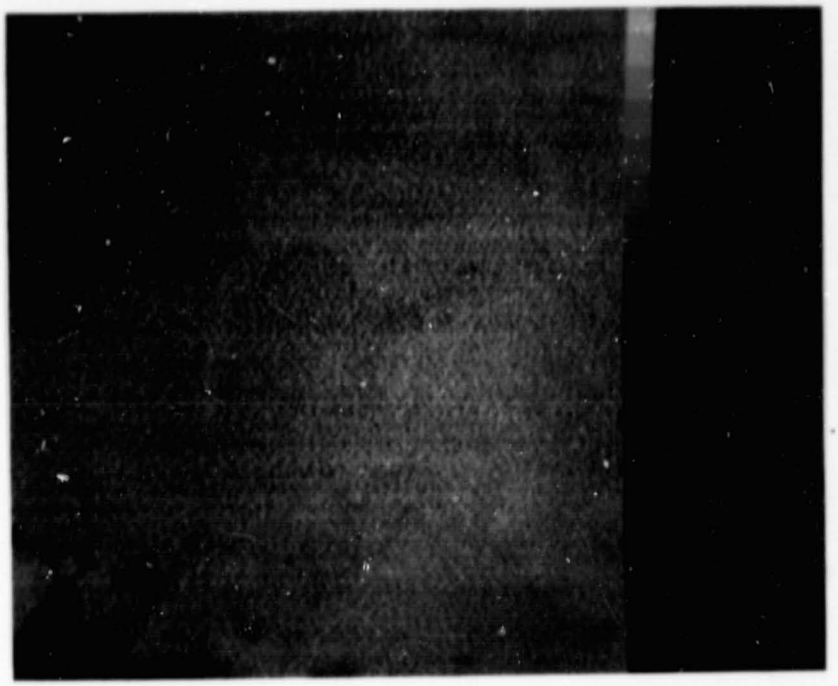

(a)

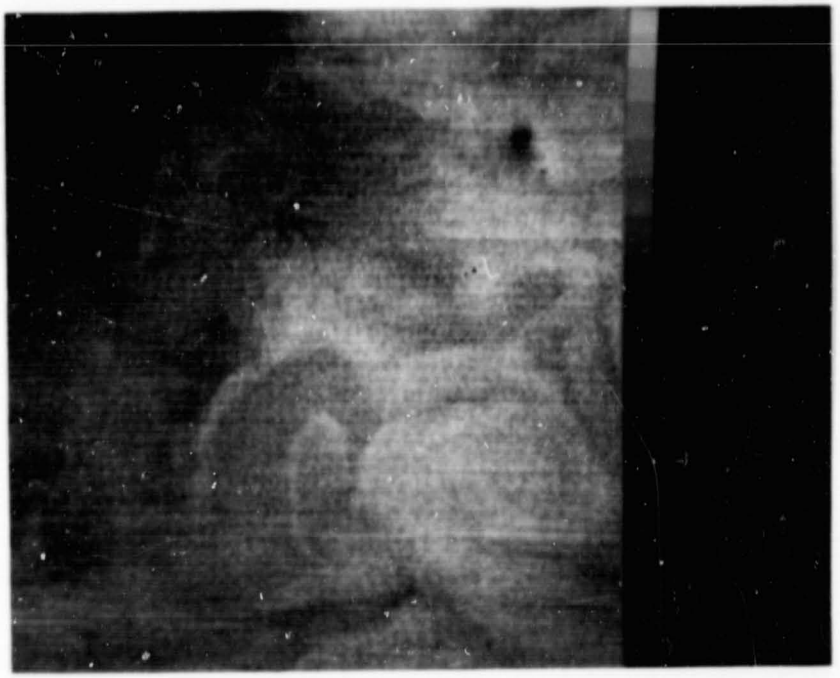

(b)

1. - Satellite observations in the thermal infrared of the Bay of Biscay region around 45°N and 4°30'W (a) by the VHRR, 10 May 1978 at 8h TU and (b) by the HCMR, 11 May 1978 at 2h TU. Each grey shade corresponds to (a) 0,1°C and (b) 0,3°C. In the center of these images one notes the presence of an eddy approximating 50 km in diameter, basely visible on the VHRR image due tho instrumental noise get clearly distinguishable on the HCMR image.

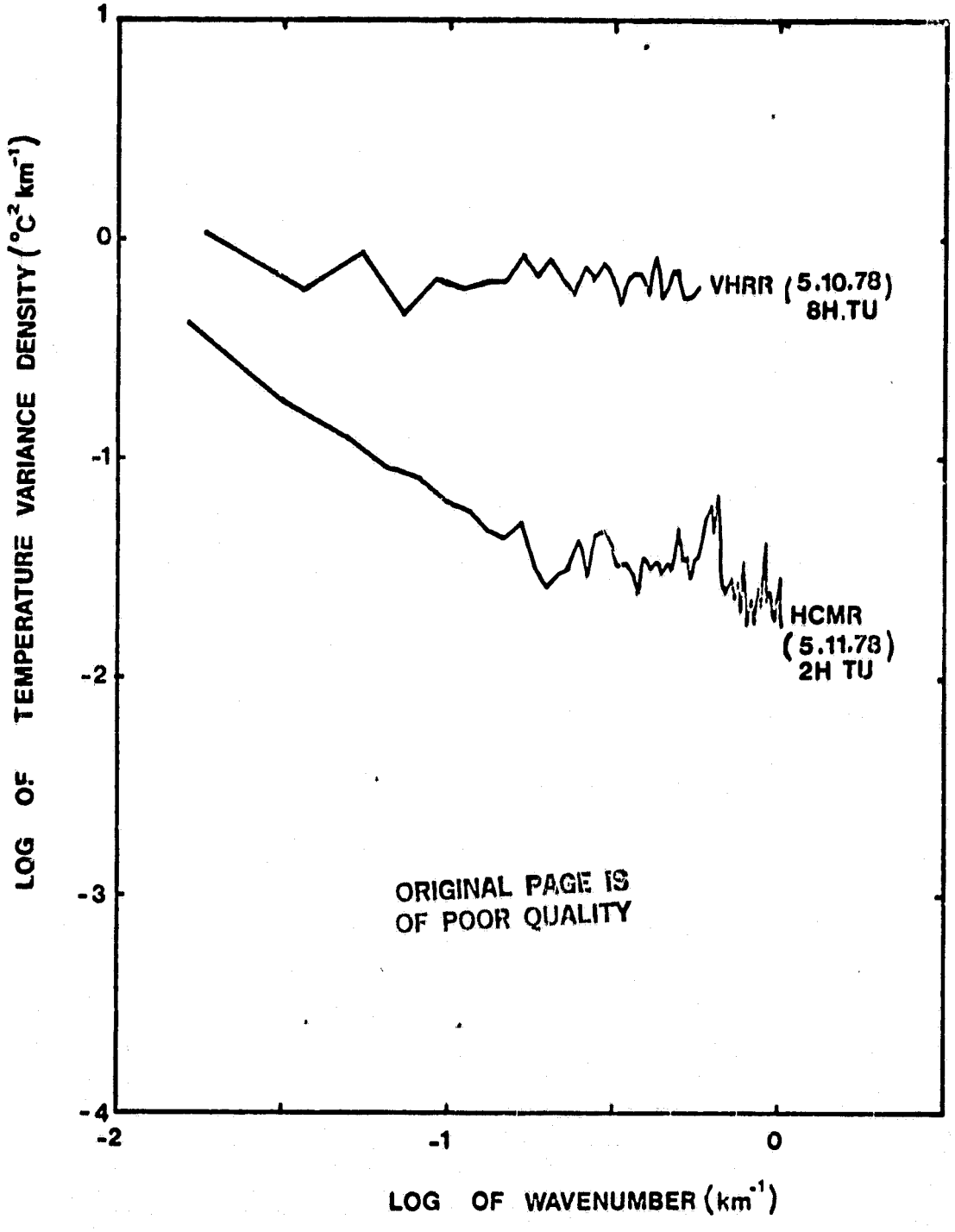

2. - Density spectrum of variance of the surface temperature field for the same region (64 x 64 km^2) in the Bay of Biscay obtained from HCMR and VHRR data. The direction of analysis corresponds to that of the satellite track.

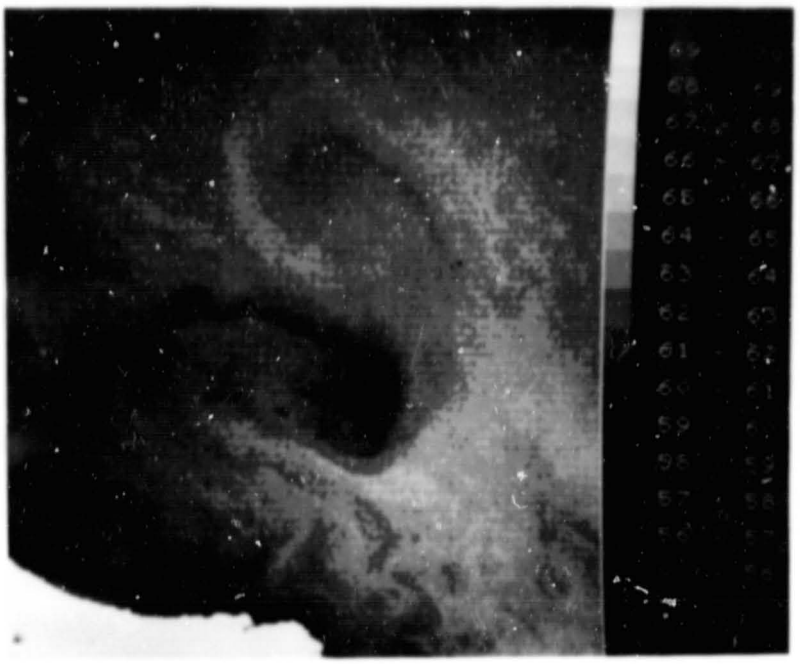

(a)

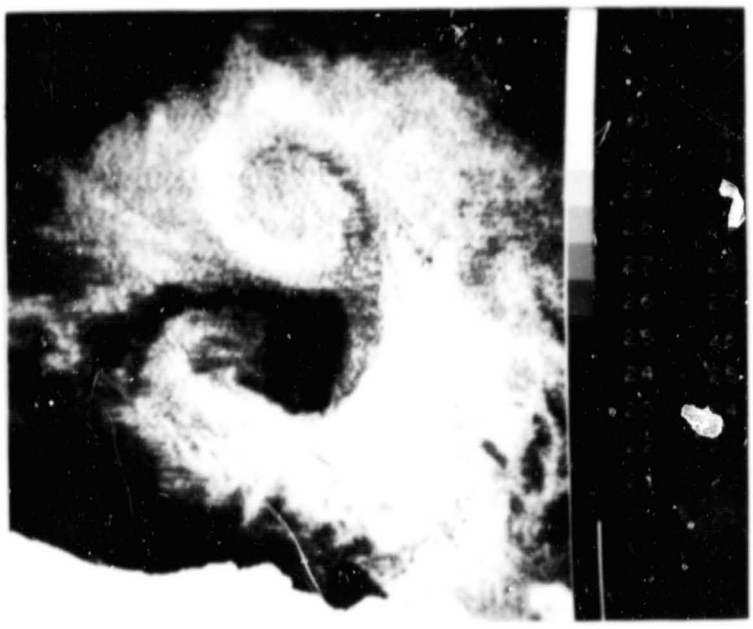

(b)

3. - Satellite observations in the thermal infrared of the Bay of Biscay 17 July 1979 (a) by the HCMR at 12h45 TU and (b) by the AVHRR at 15h15 TU. Each grey stade corresponds to (a) 0,2°C and (b) 0,1°C. One notice the presence of a large eddy structure approximately 300 km wide.

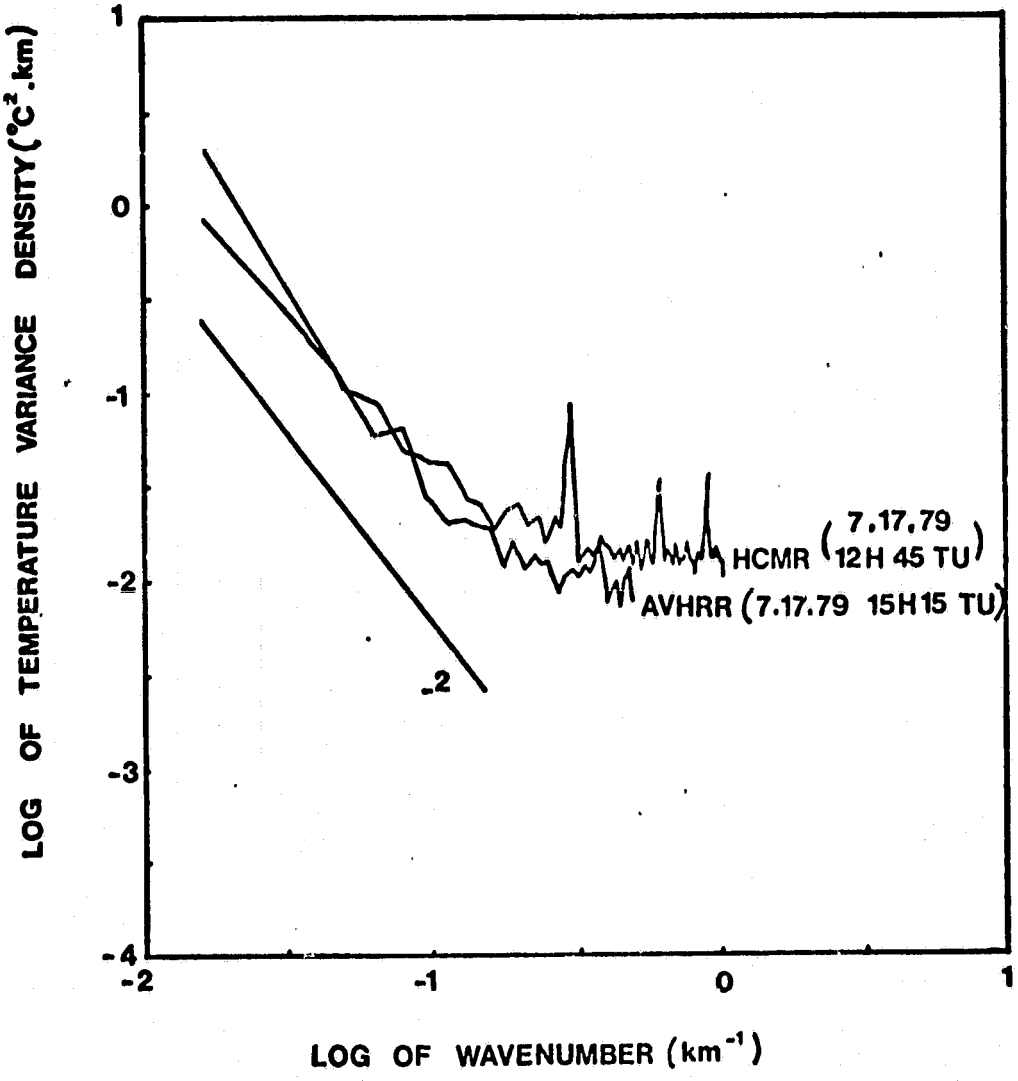

4. - Density spectrum of variance of the surface temperature field for the same region (64 x 64 km^2) in the Bay of Biscay obtained respectively from HCMR and AVHRR data. The direction of analysis corresponds to that of the satellite track.

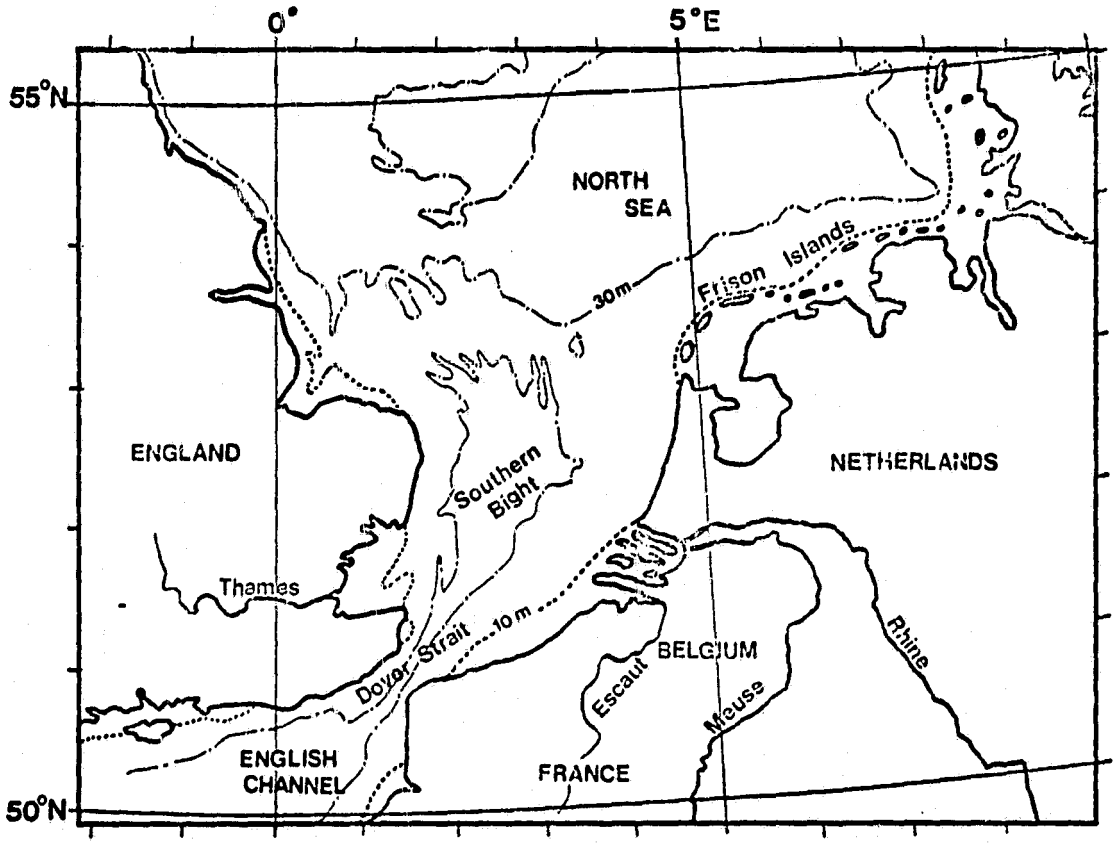

5. - (zone 1) : Southern portion of the north sea

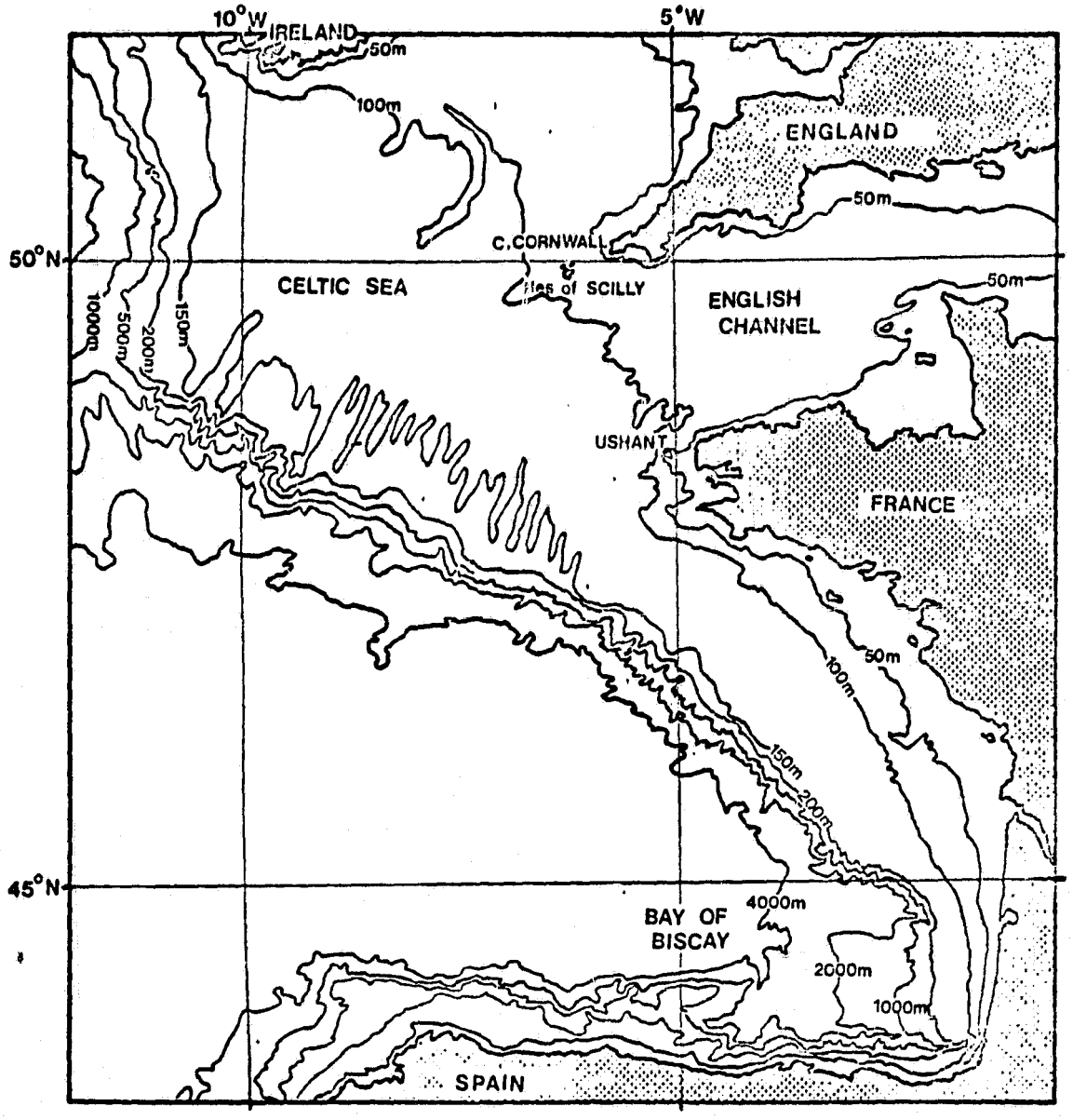

5. - (zone 2) : The British Channel, the Celtic sea, and Bay of Biscay

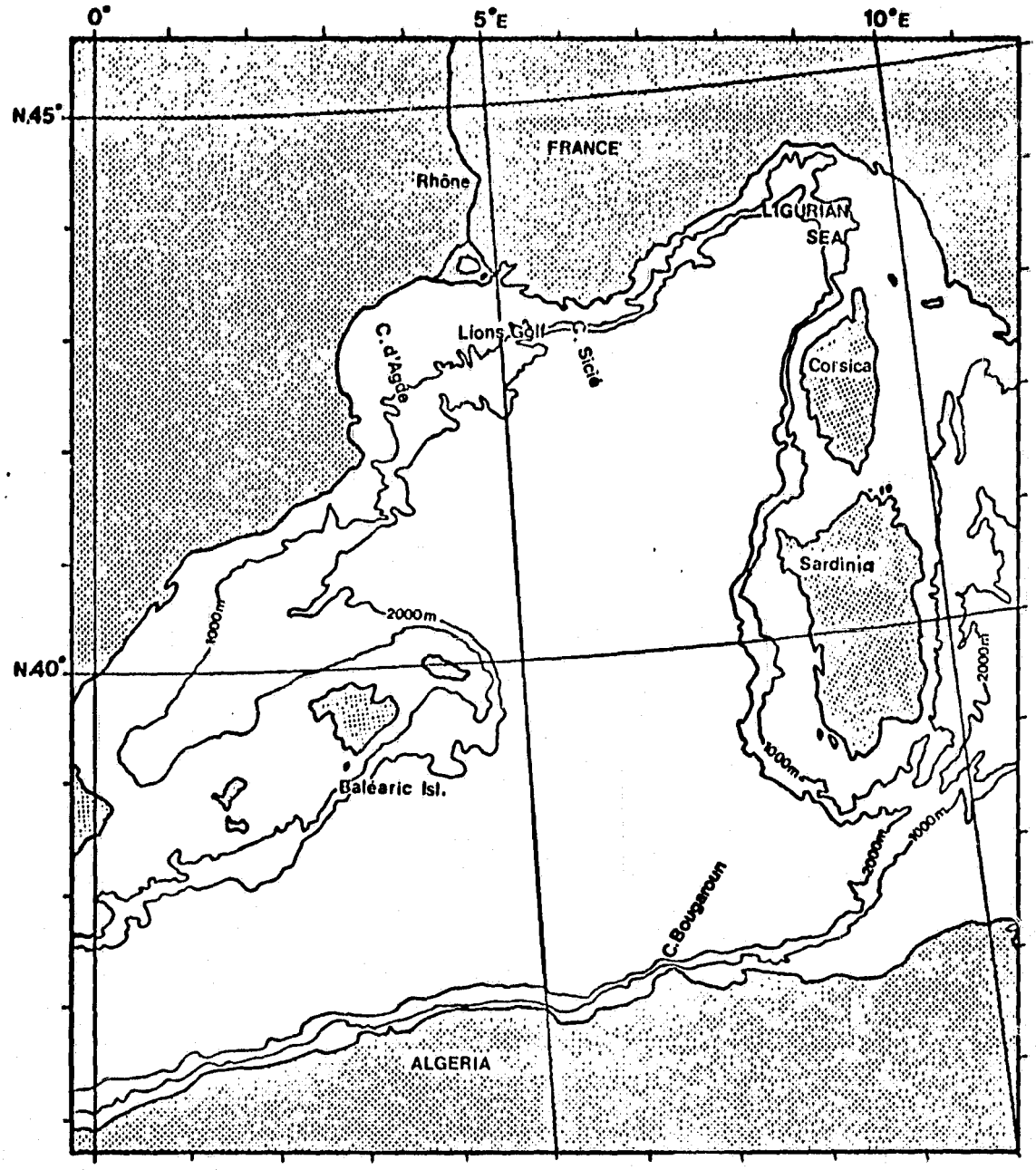

5, - (zone 3) : The north-western mediterranean.

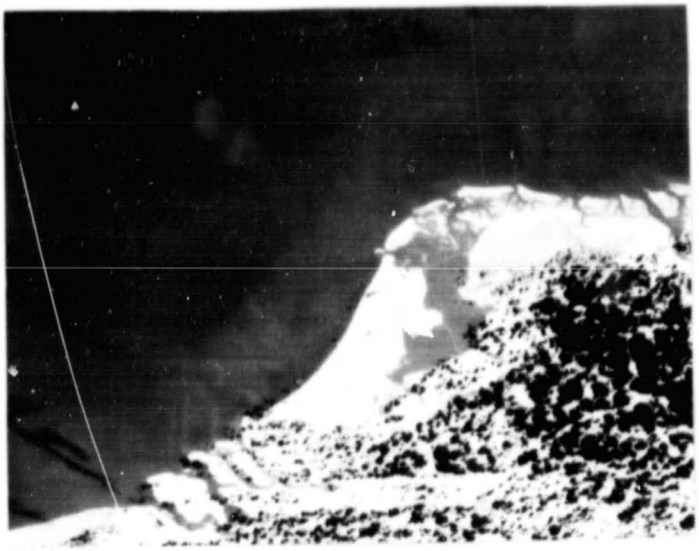

(a) : 18 may 78, 2h30 TU

(b) : 30 may 78, 13h11 TU

6. (a), (b) - HCMM observations A-A 0022-12470 (a) and A-A 0034-13110 (b) of the thermal effluent of the Rhine-Meuse-Escaut system during the summer season. Significant offshore diffusion.

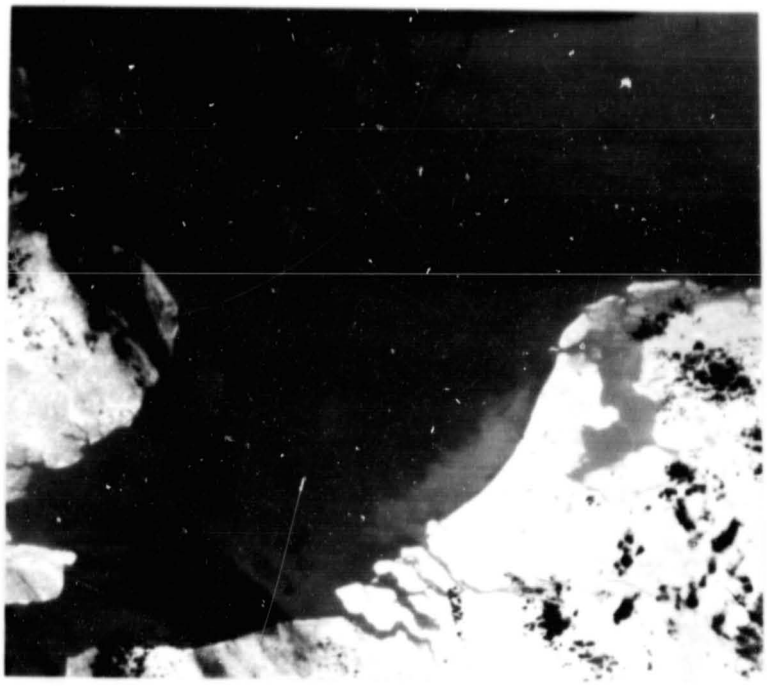

(c) : 4 june 78, 13h05 TU

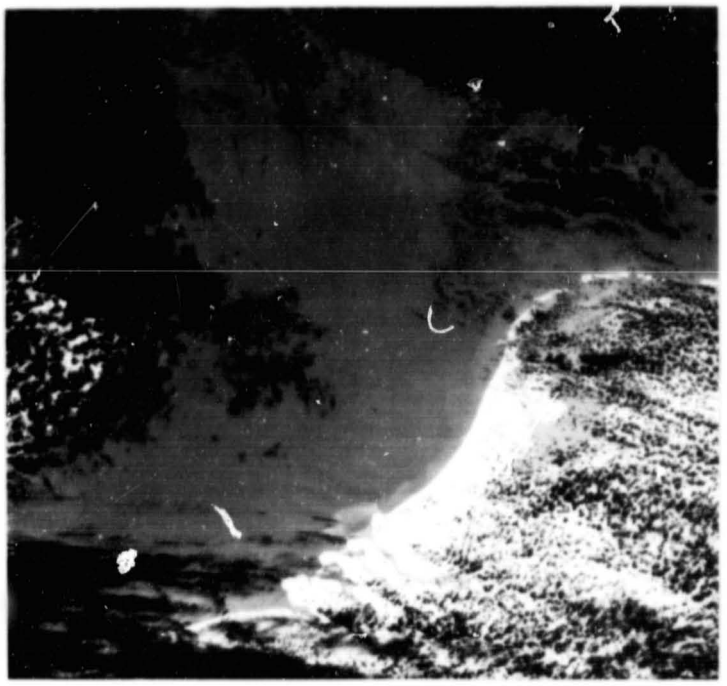

(d) : 9 june 78, 12h57 TU

6. (c), (d) - HCMM observations A-A 0039-13050 (c) and A-A 0044-12570 (d) of the thermal effluent of the Rhine-Meuse-Escaut system during the summer season. Effluent abutting the coast.

(e) : 19 june 78, 12h47 TU

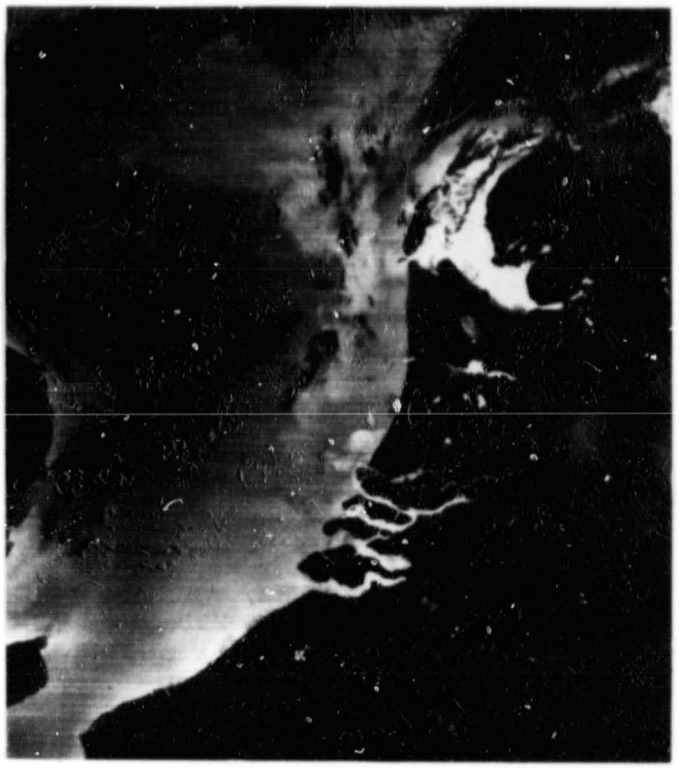

(f) 20 june 78, 2h03 TU

6. (e), (f) - HCMM observations A-A 0054-12470 (e) and A-A 0055-02030 (f) of the thermal effluent of the Rhine-Meuse-Escaut system during the summer season. Significant offshore diffusion.

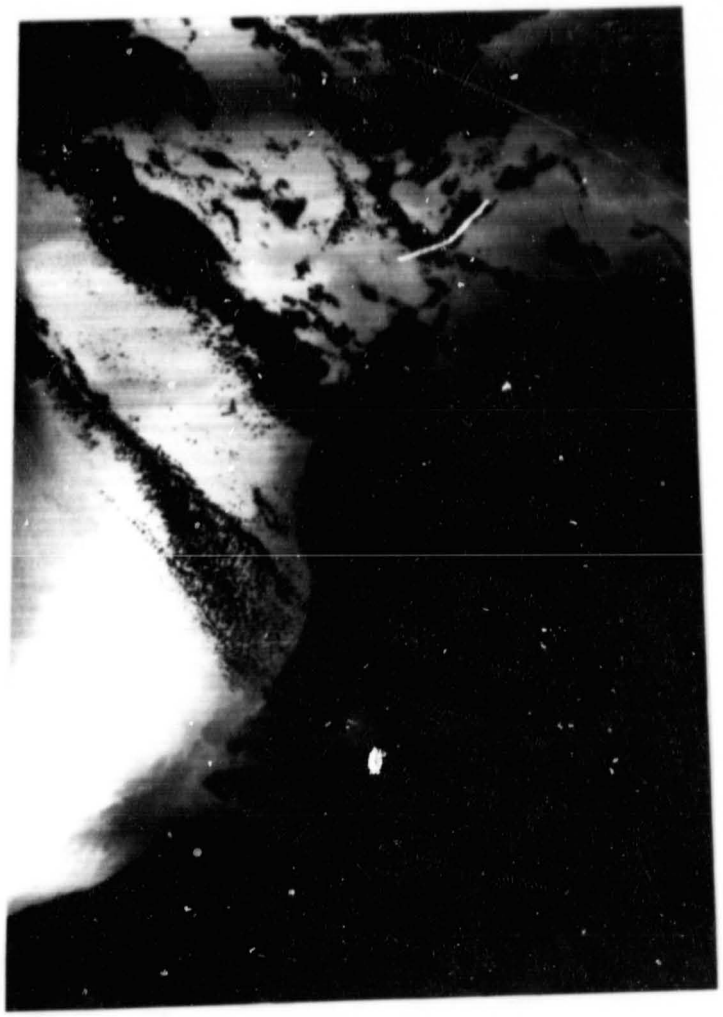

7. - HCMR observation A-A 0263-01320 of thermal effluent of the Rhine-Meuse-Escaut system during the winter reason (14 January 1979 at 2 h TU). The southern position of the effluent flows toward the southewast forming a diffuse, wedge-shaped plume along the belgium coast.

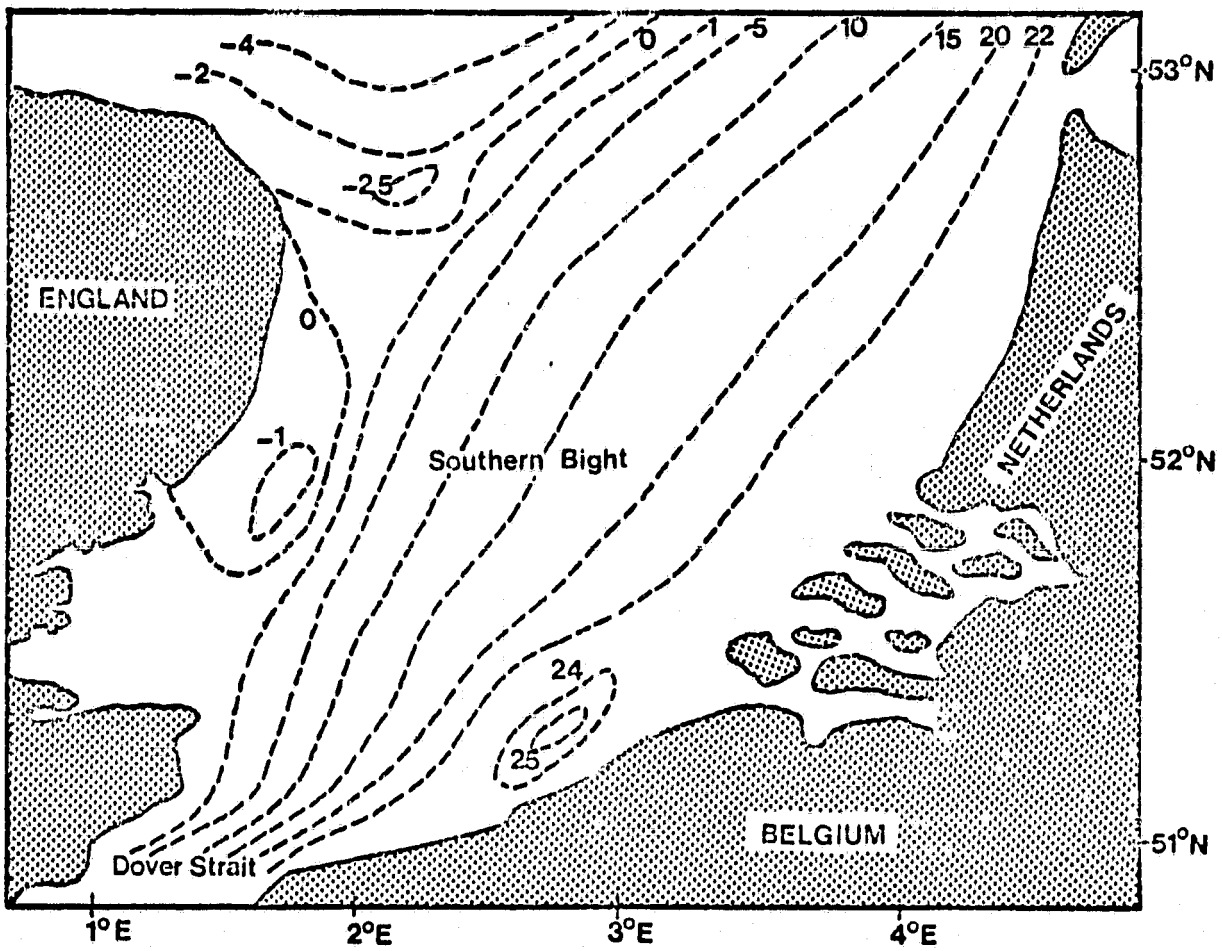

8. - Residual circulation in the southern position of the north sea, according to NIHOUL and RONDAY (1975). Stream lines in 10^4 m^3/s [1]

9. - Landsat image of 12 June 1975 showing the transport of sediment (clear shades) from the Meuse-Escaut system toward the southwest along the belgian coast.

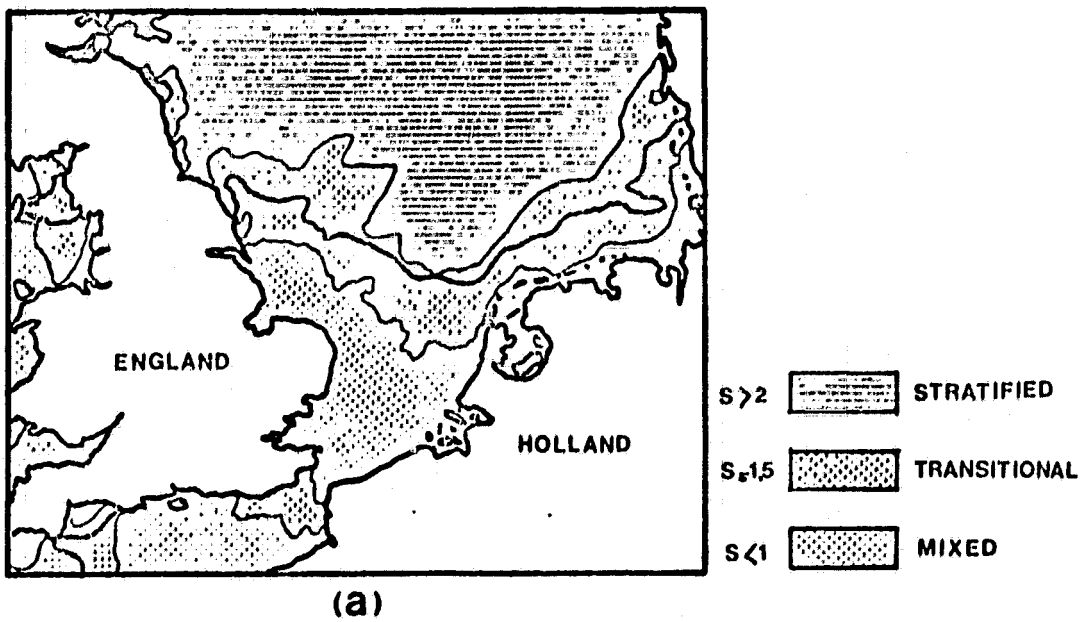

10.- Value of the SIMPSON-HUNTER parameter, S, in the southern portion of the North Sea : (a) according to the model of PINGREE and GRIFFITHS (1978), and (b) according to the model of NIHOUL (1980). The S values greater than 2 correspond to a stratificld medium; value less than 1, to a homogeneous medium; and values of 1.5 to a system in transition where thermal fronts can be encountered.

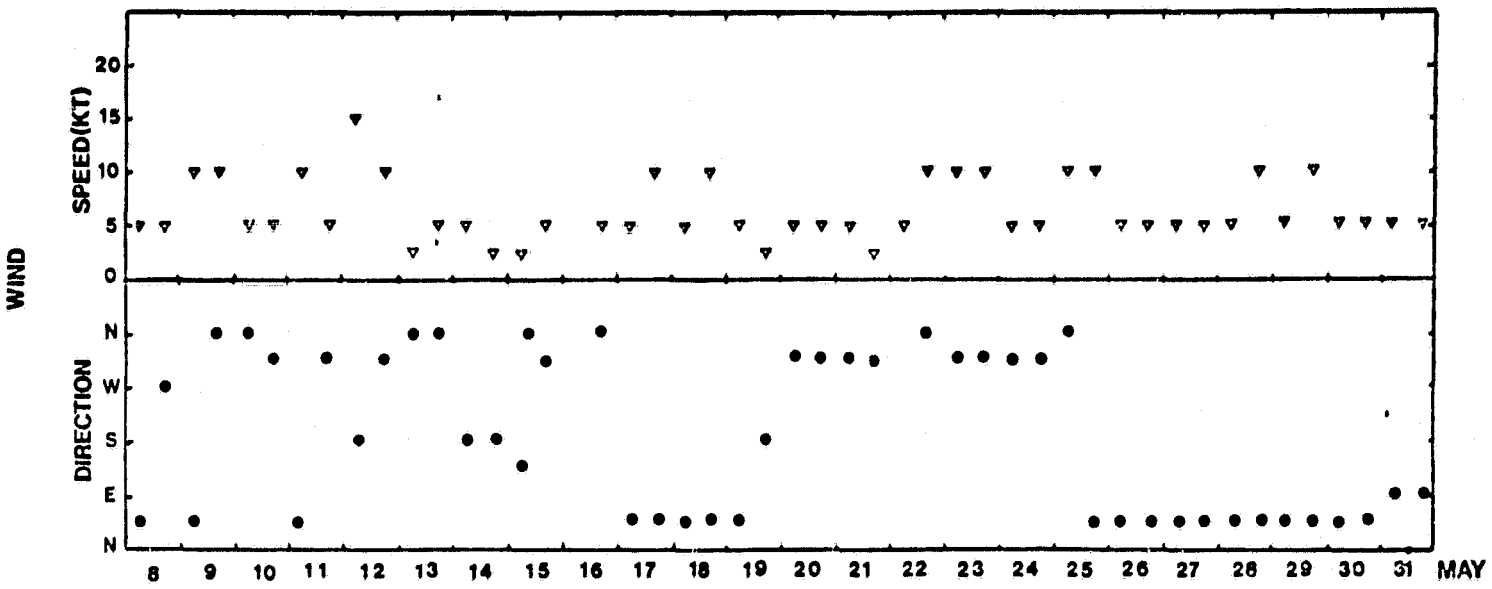

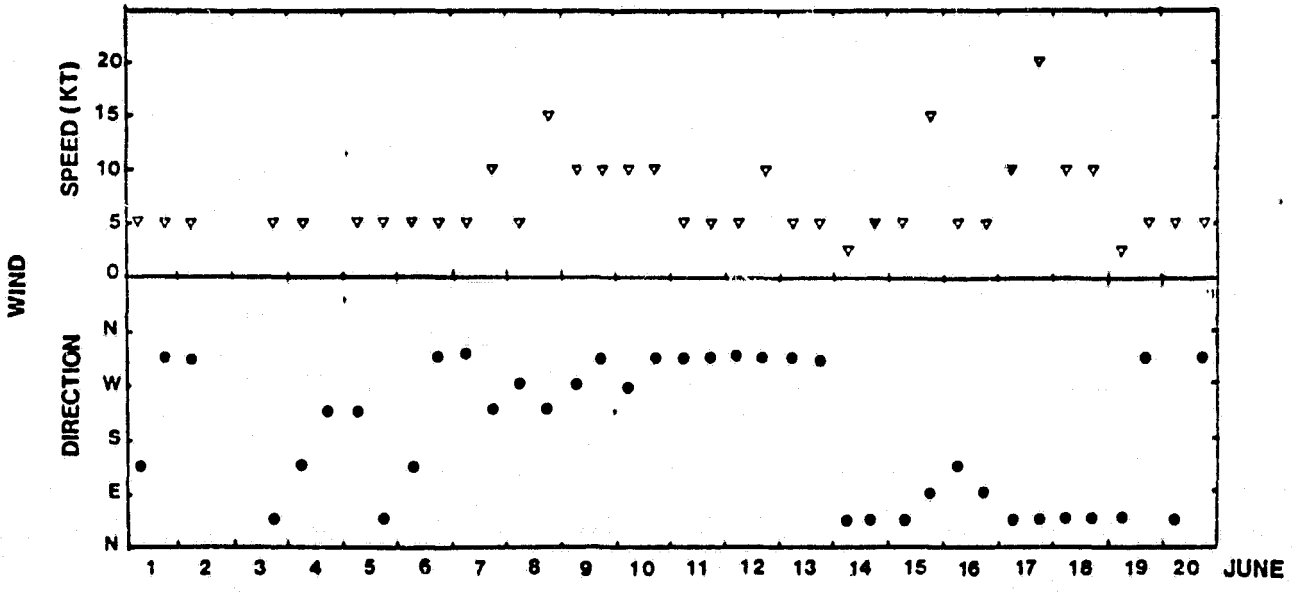

11.- Mean wind speed and direction on the surface in the southern position of the North Sea for the periods of (a) 8-31 May 1978, and (b) 1-20 June 1978.

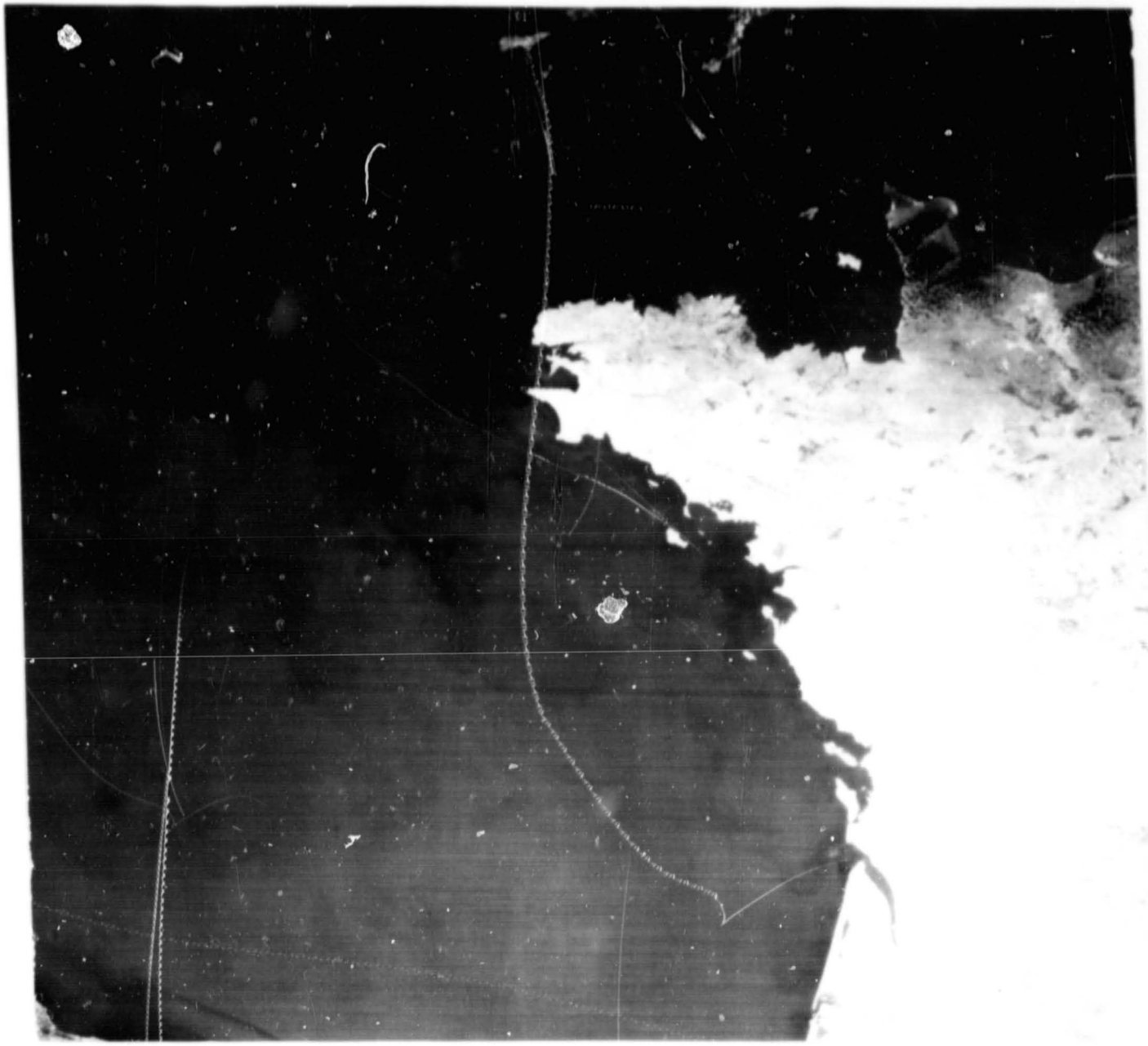

12.a - HCMM observation A-A 0121-13260 in the thermal infrared channel for 25 August 1978 at 13h26 TU. Tidal fronts at the entrance of the Manche. Relatively cold water at the shelf break and offshore of Brittany.

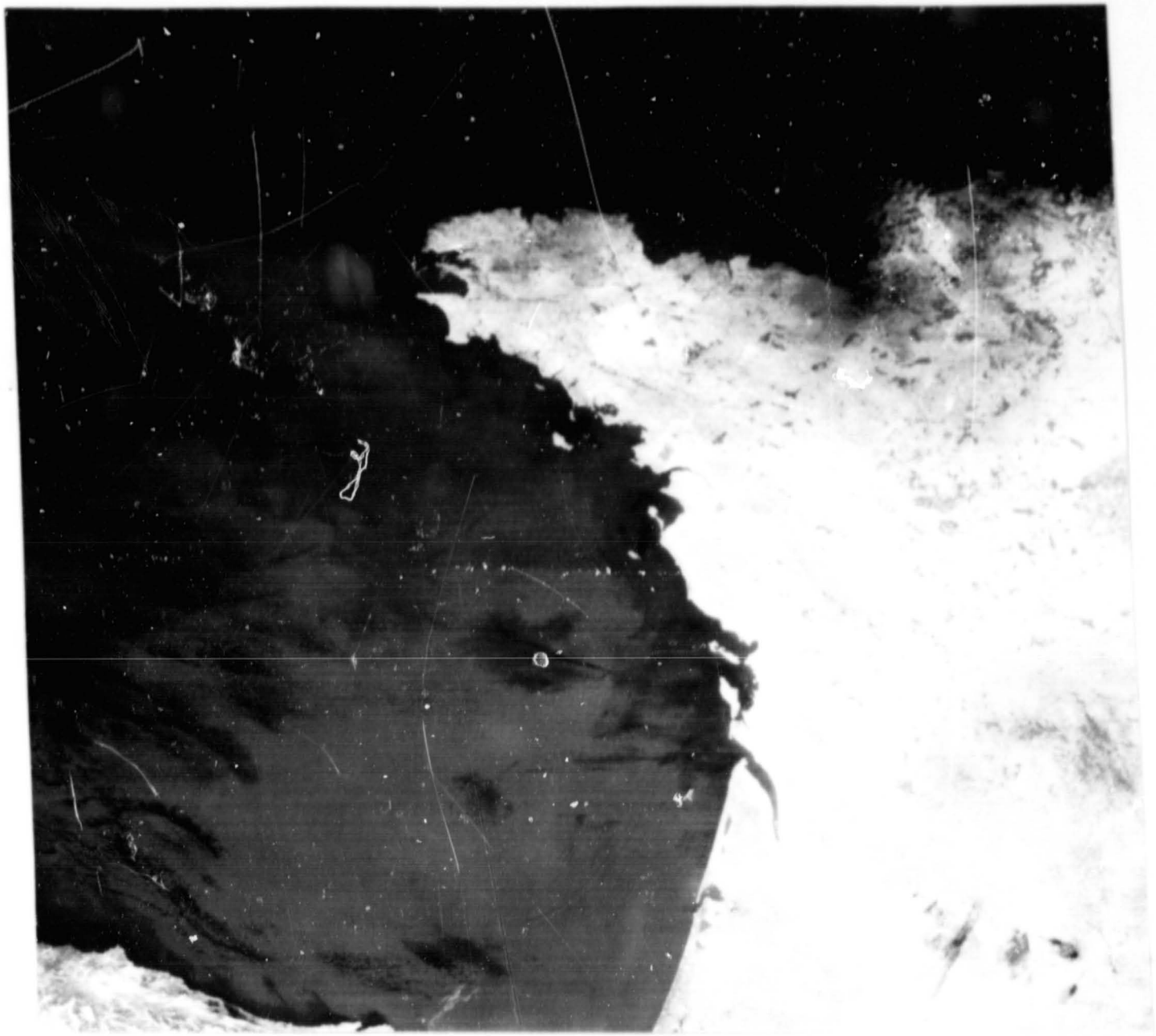

12.b - HCMM observation A-A 0142-13190 in the thermal infrared channel for 15 September 1978 at 13h19 TU. Following a period of weak tidal coefficients, the band of cold water at shelf break and offshore Brittany is less distinct.

12.c - HCMM observation A-A 0148-13320 in the thermal infrared channel for 21 September 1978 at 13h31 TU. Tidal fronts at the entrance of the Manche, near Cape of Cornwalls, and between Ireland and England. Relatively cold water at the shelf break offshore of

12.d - HCMM observation A-A 0185-13180 in the thermal infrared channel for 28 October 1978 at 13h18 TU. Cooling on the continental shelf in the autumn season. Note the characteristic structure corresponding to turbulent offshore diffusion of cold coastal water.

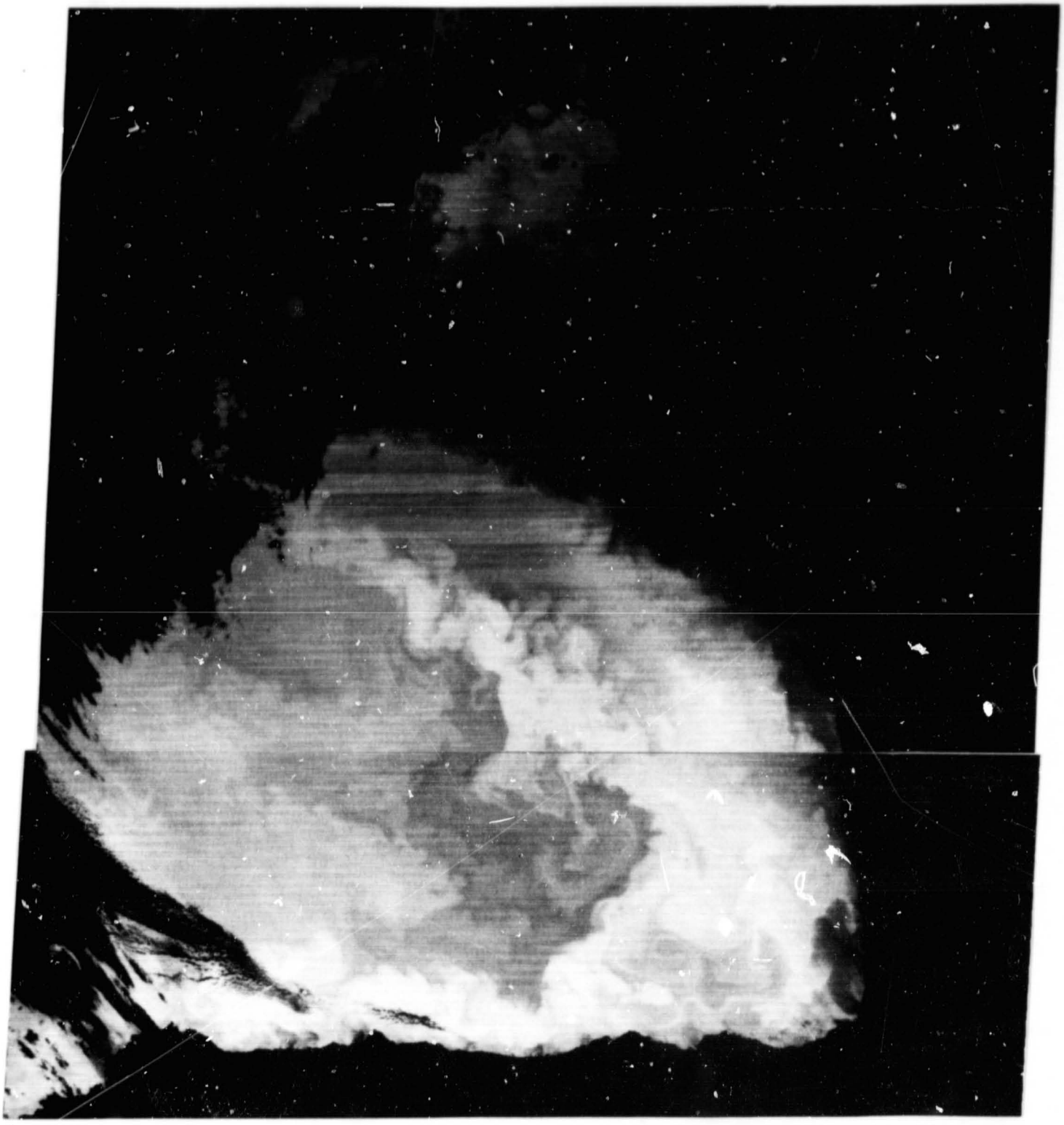

12.e - HCMM observation A-A 0265-02090 in the thermal infrared channel for 14 January 1979 at 2h09 TU. Relatively warm water at the limit of the continental shelf southeast of Brittany, in the Bay of Biscay along the coast of Spain.

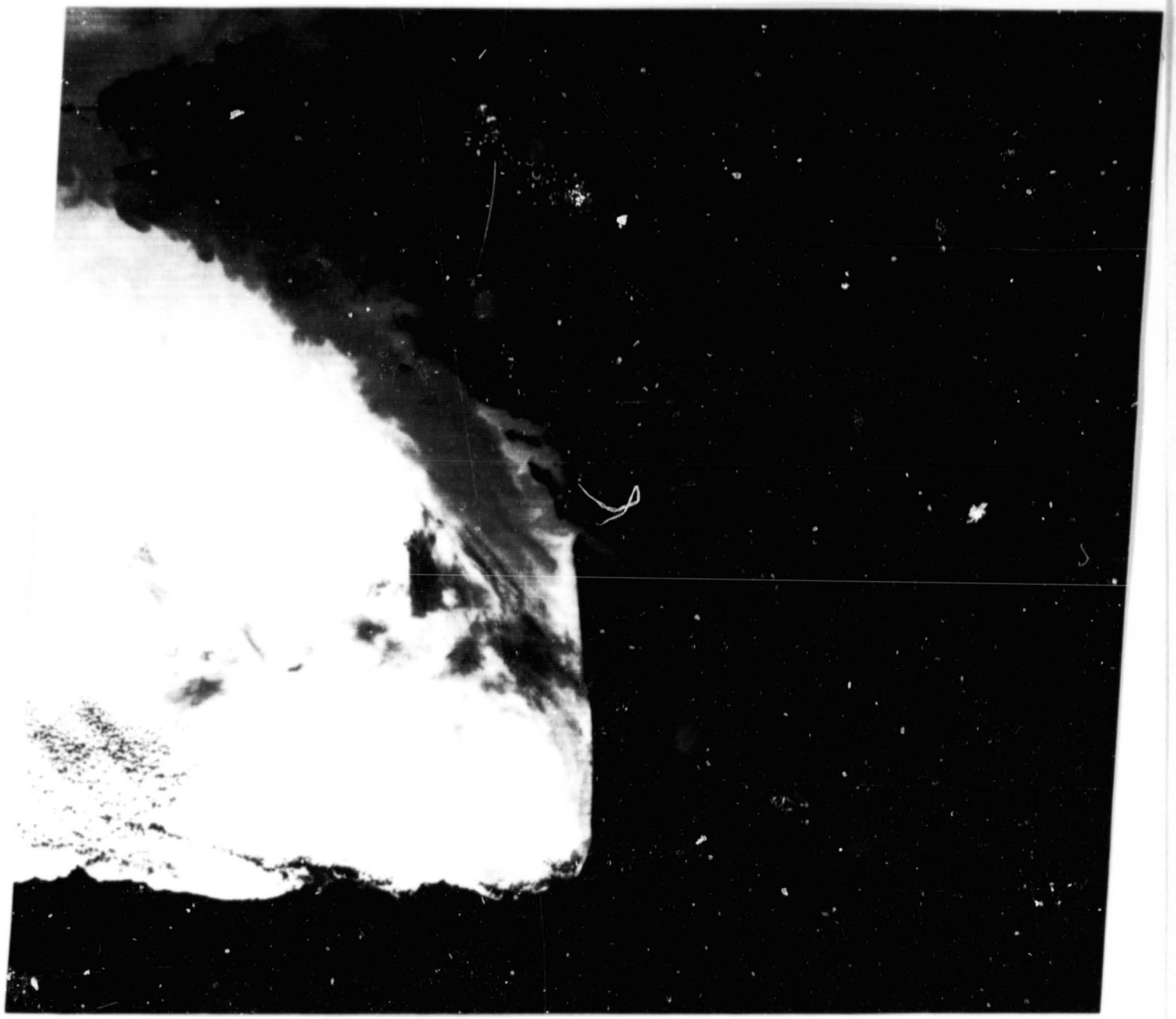

12.f - HCMM observation A-A 0307-01530 in the thermal infrared channel for 21 February 1979 at 1h 53 TU. Note the band of cold water along the french coast.

Fig. 13

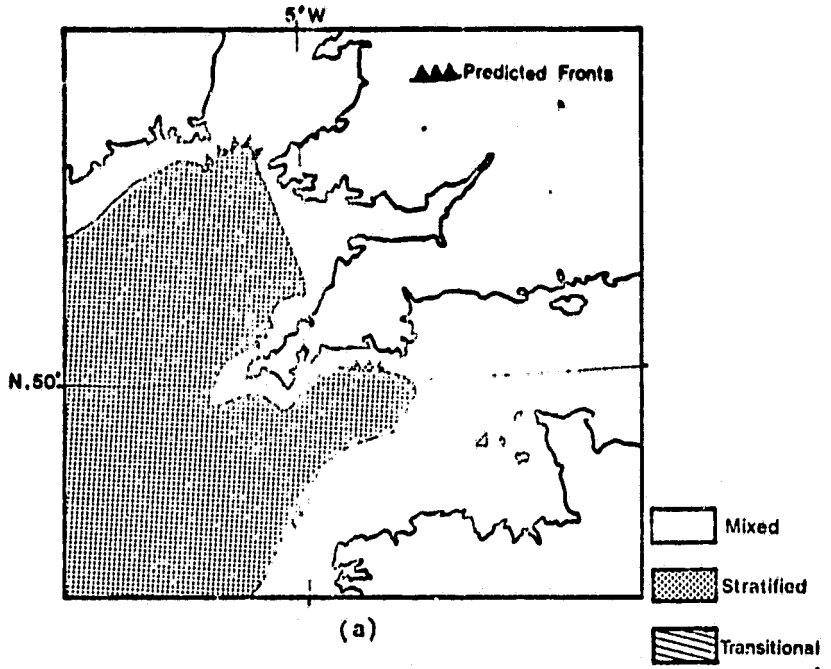

(a)

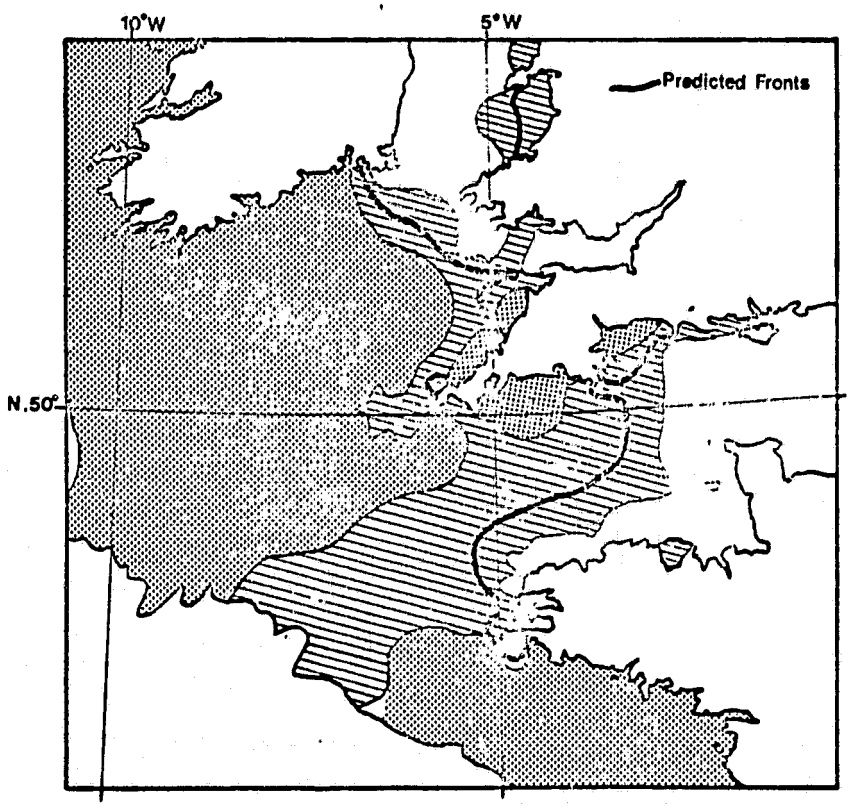

(b)

13.- Tidal fronts in the summer season at the entrance of the Manche and in the Celtic Sea as predicted by the models of (a) FEARNHEAD (1975) and (b) PINGREE and GRIFFITHS (1978).

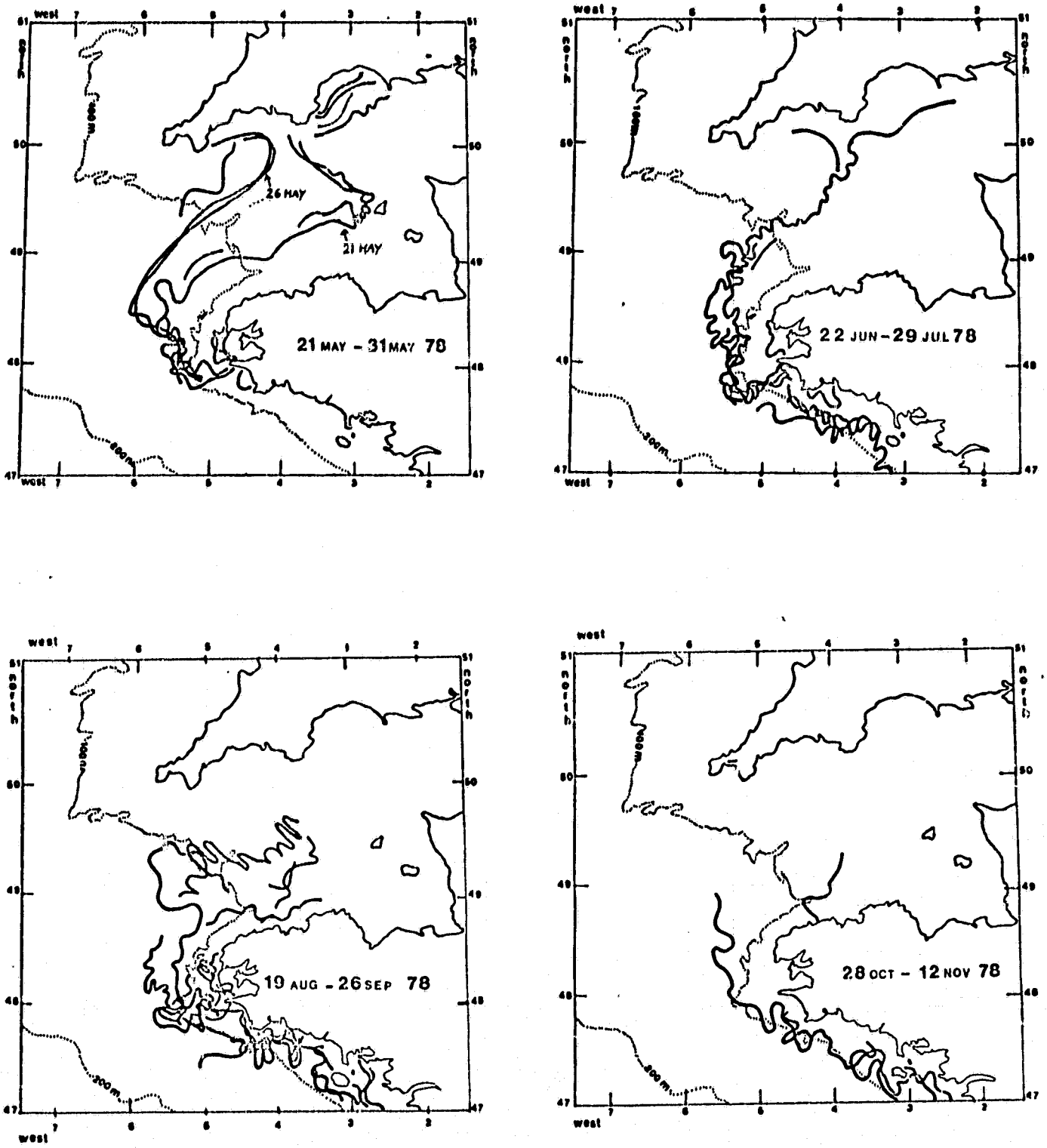

14.- Evolution of the tidal front position at the entrance of the British Channel during the period of May through September 1978, deduced by HCMR observations.

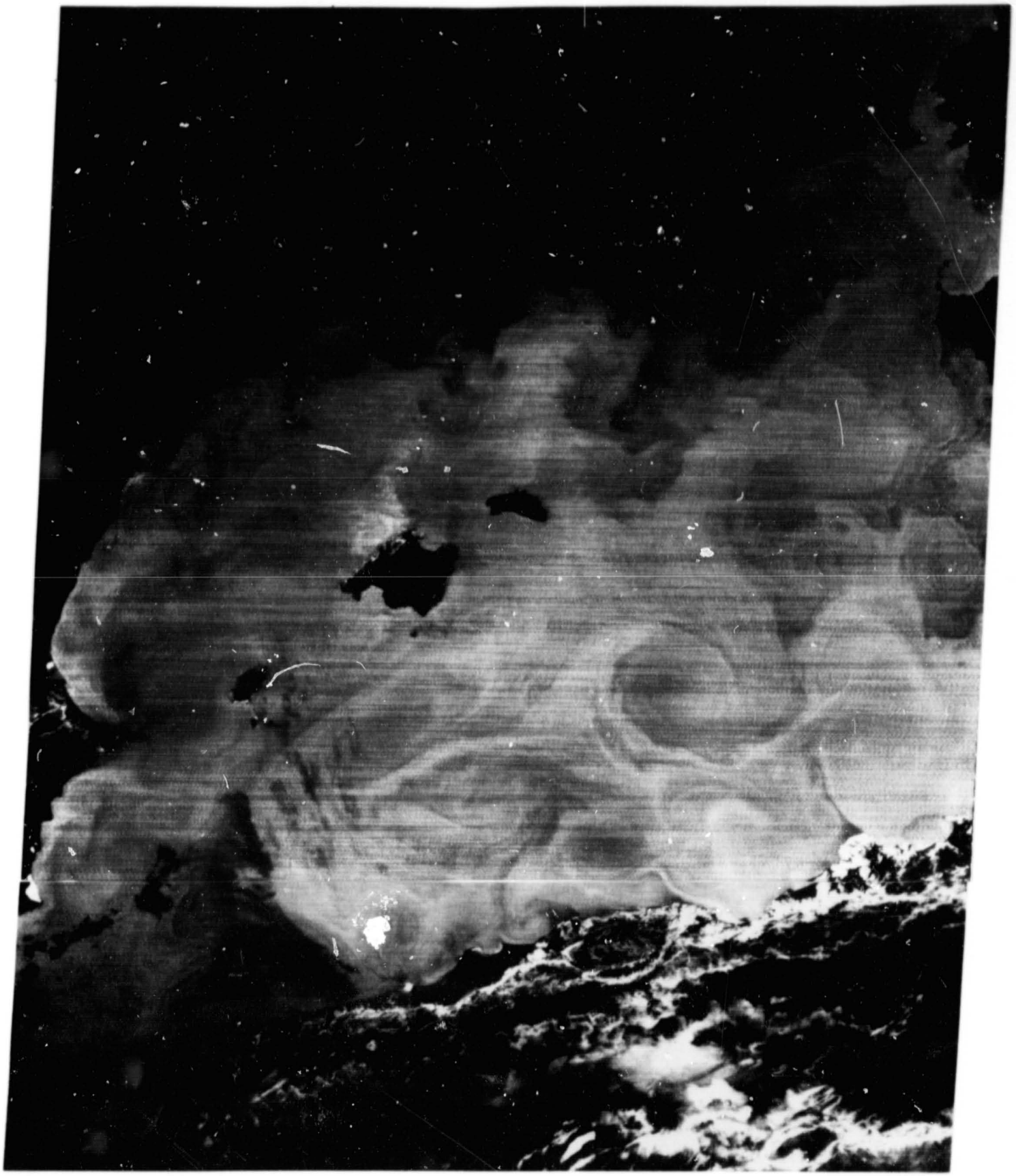

15.a - HCMM observation A-A 0076-01590 in the thermal infrared channel for 11 July 1978 at 1h59 TU. North Balearic front. Large

15.b - HCMM observation A-A 0081-01510 in the thermal infrared channel for 16 July 1978 at 1h51 TU. Apart from the large scale eddies offshore of the Algerian coast, note the irregularity of the surface temperature field between Baleares and Sardinia.

15.c - HCMM observation A-A 0086-01450 in the thermal infrared channel for 21 July 1978 at 1h45 TU. Eddies forming along the Algerian coast and expanding toward the coast.

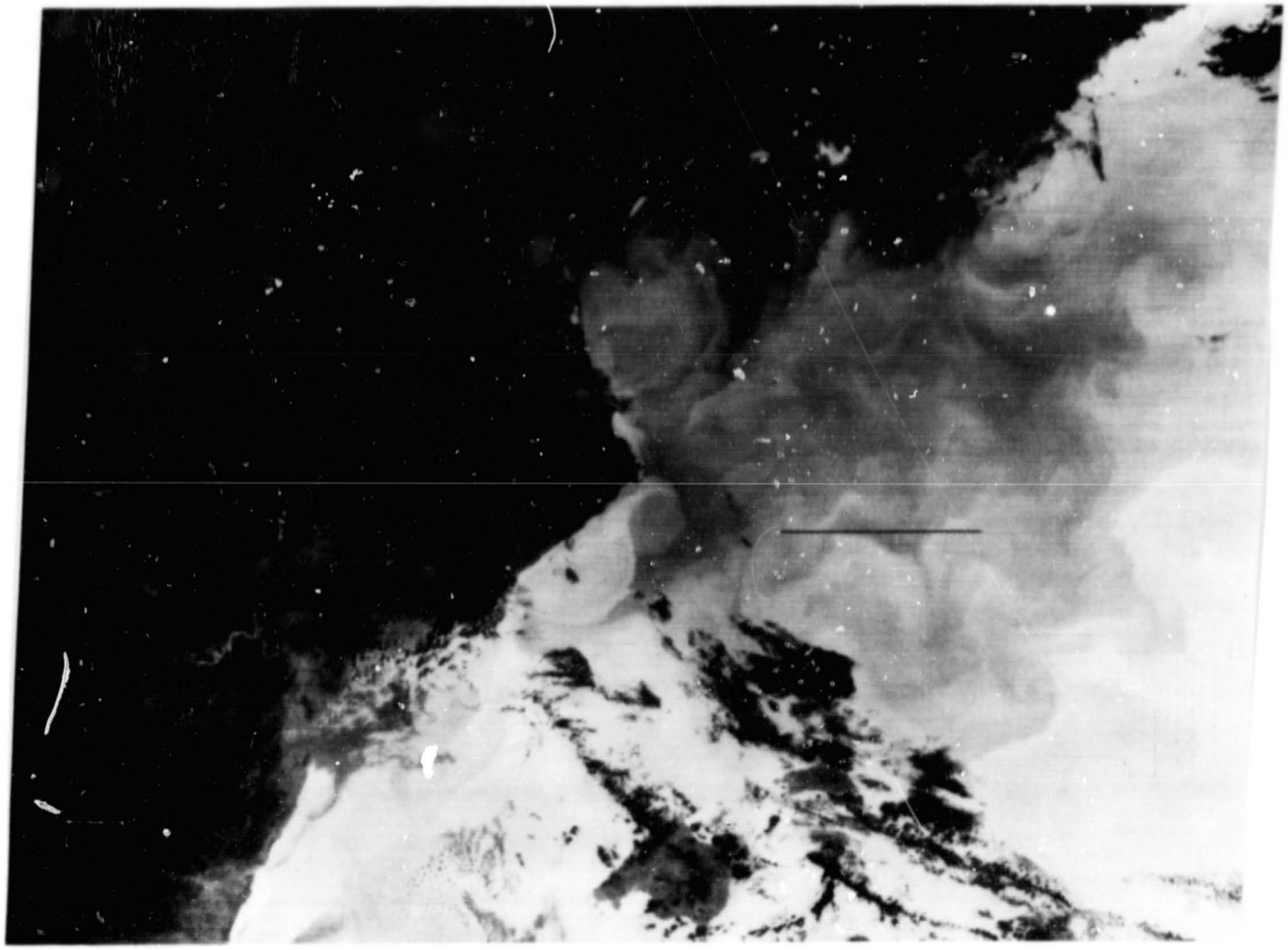

15.d - HCMM observation A-A 0087-02020 in the thermal infrared channel for 22 July 1978 at 2 h02 TU. Coastal upwelling in the Gulf of Lion.

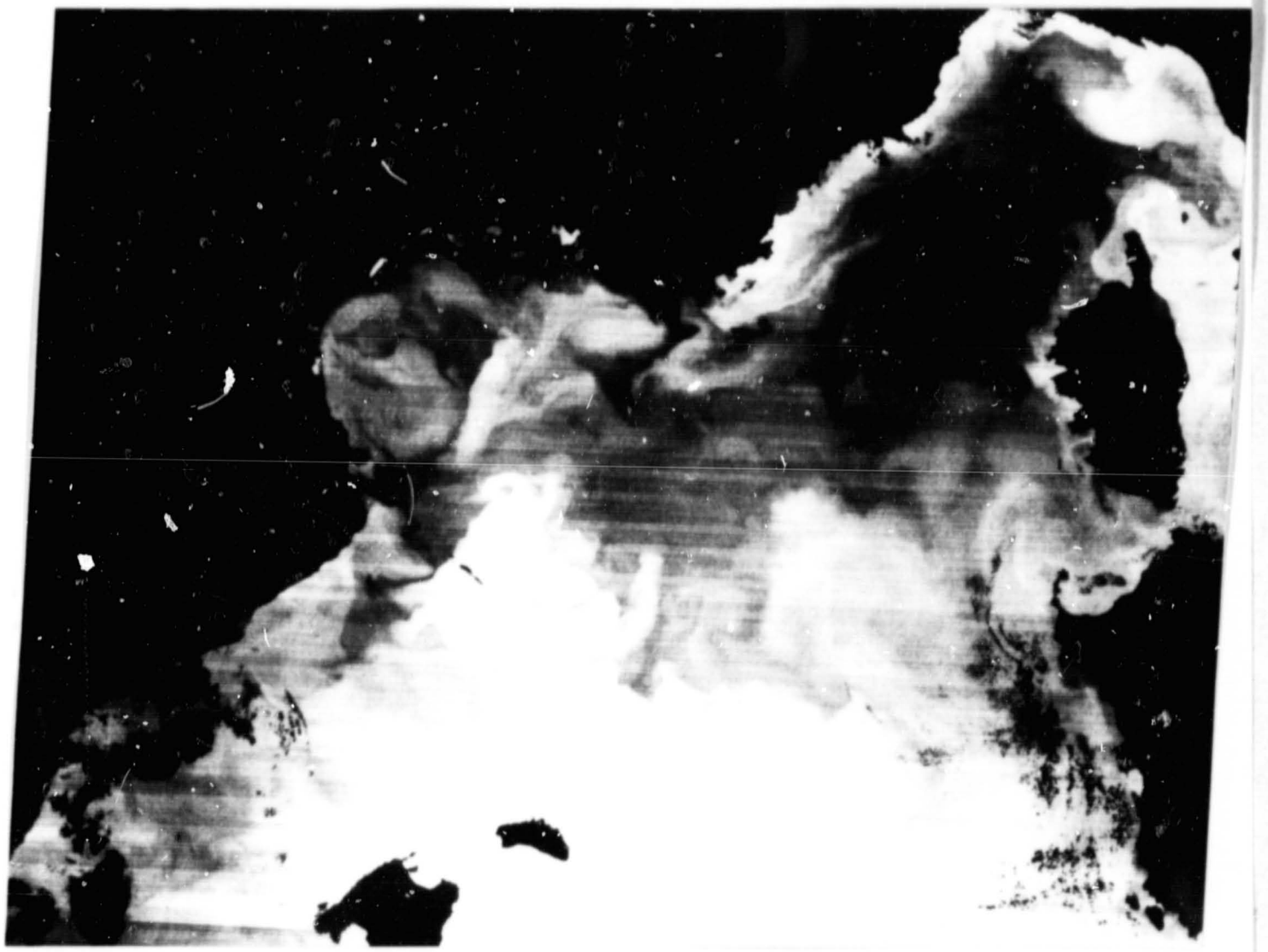

15.e - HCMM observation A-A 0108-01510 in the thermal infrared channel for 12 August 1978 at 2h 02 TU. Coastal upwelling in the Gulf of Lion. Liguro-Provençal Current.

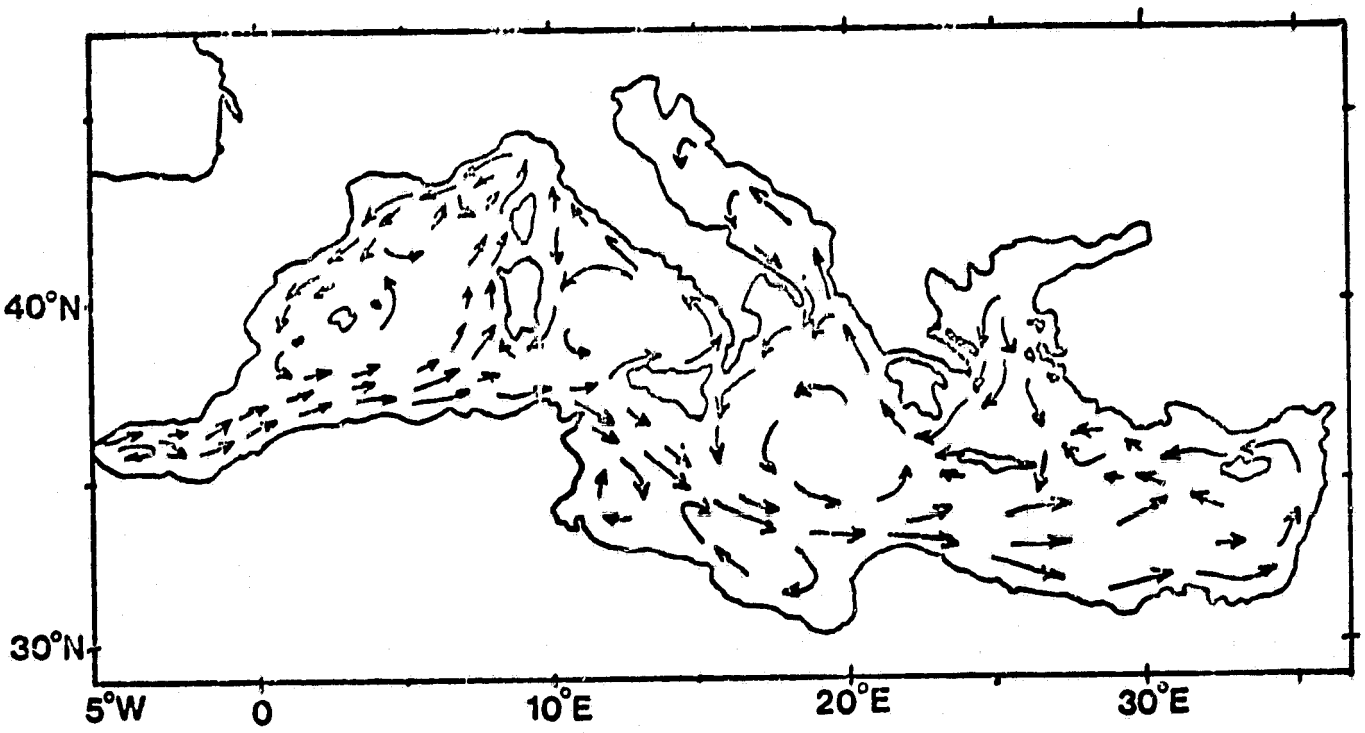

16.- Summer surface circulation in the Mediterranean, according to LACOMBE and TCHERNIA (1972).

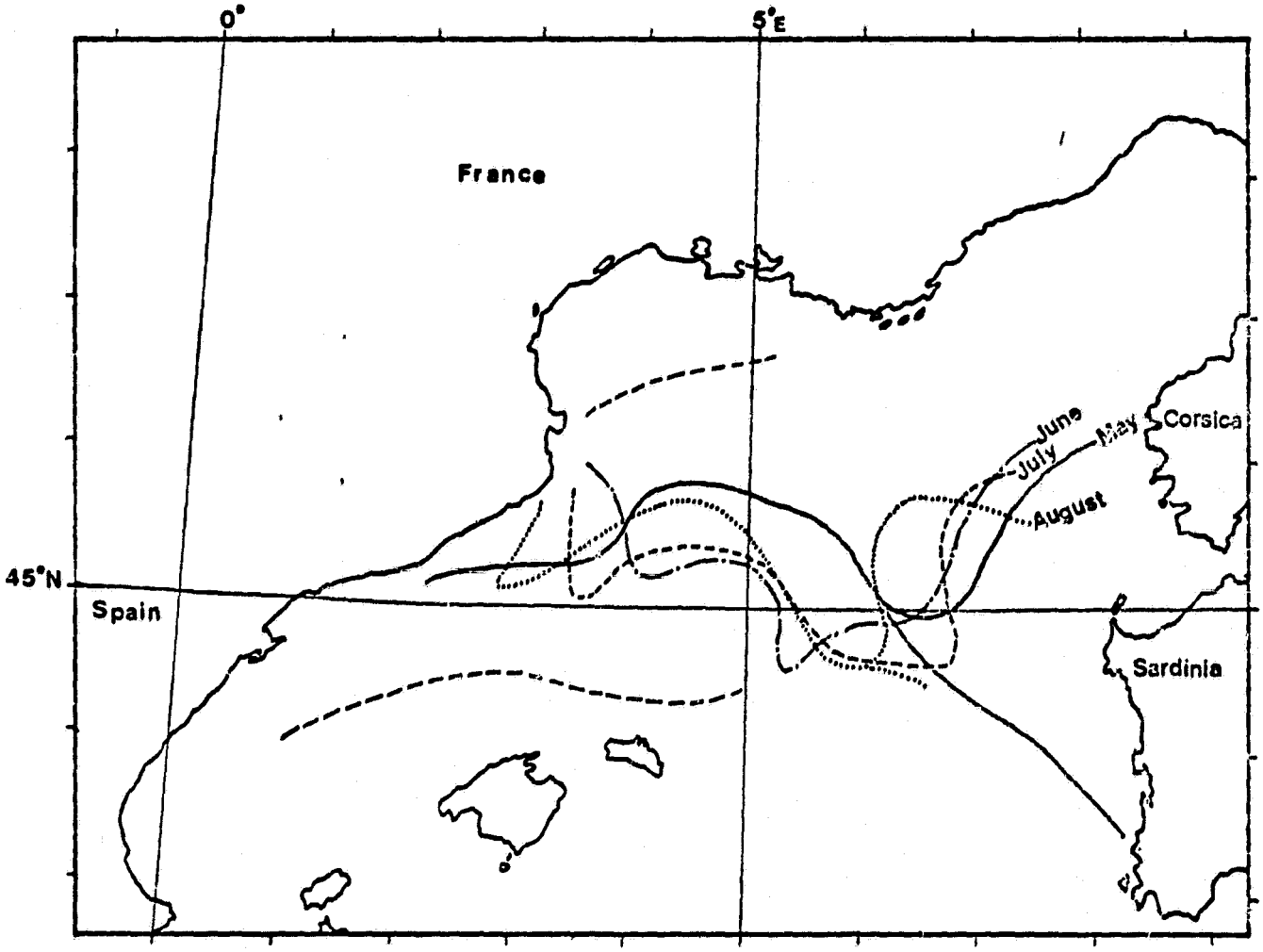

17.- Seasonal positions of the North Balearic front during the summer of 1978.

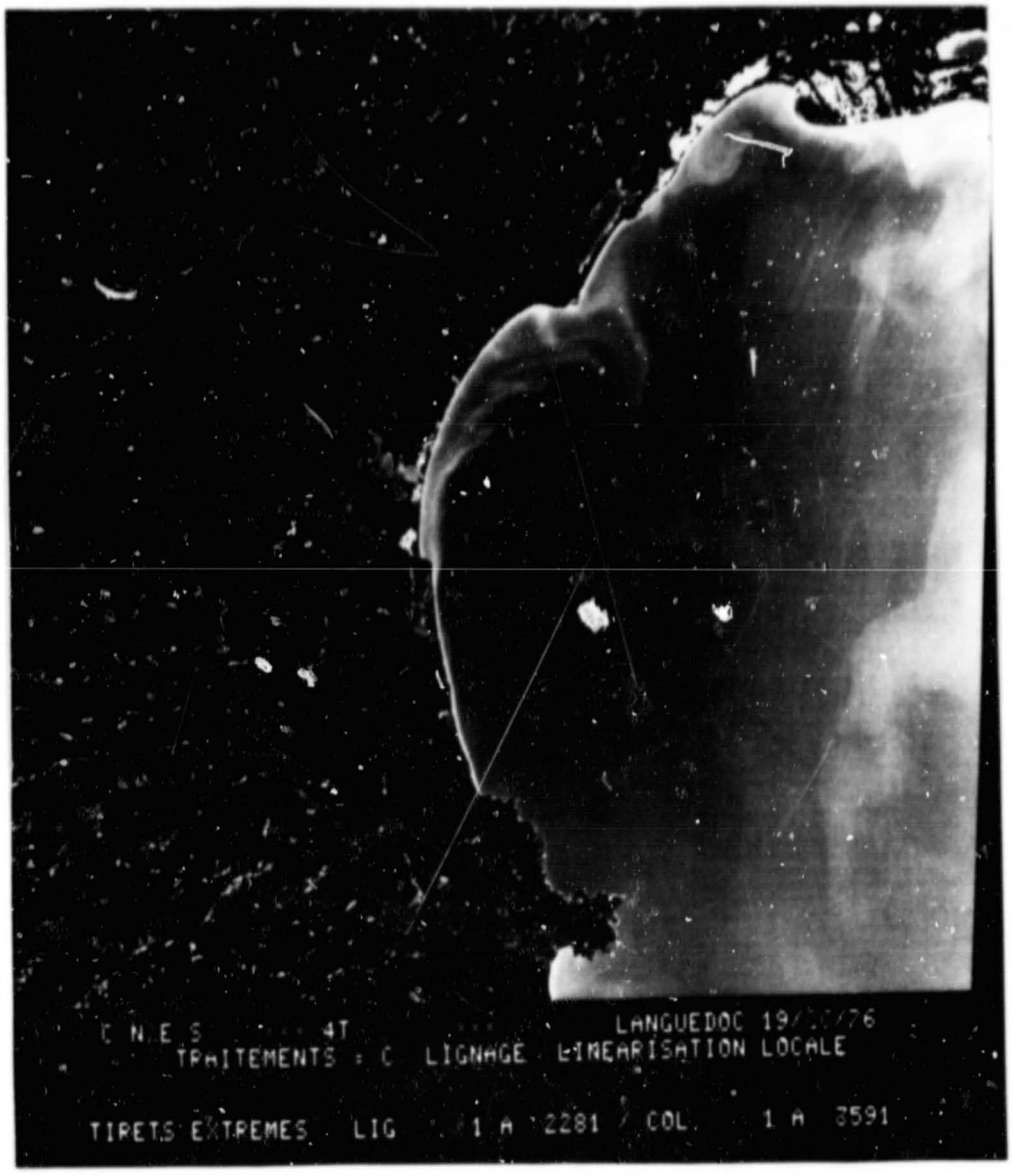

18.- LANDSAT image of September 1976. Upwellings in the Gulf of Lion. Coastal sediments entrained offshore and very much to the south in the case of the upwelling produced at the mouth of the Rhone.

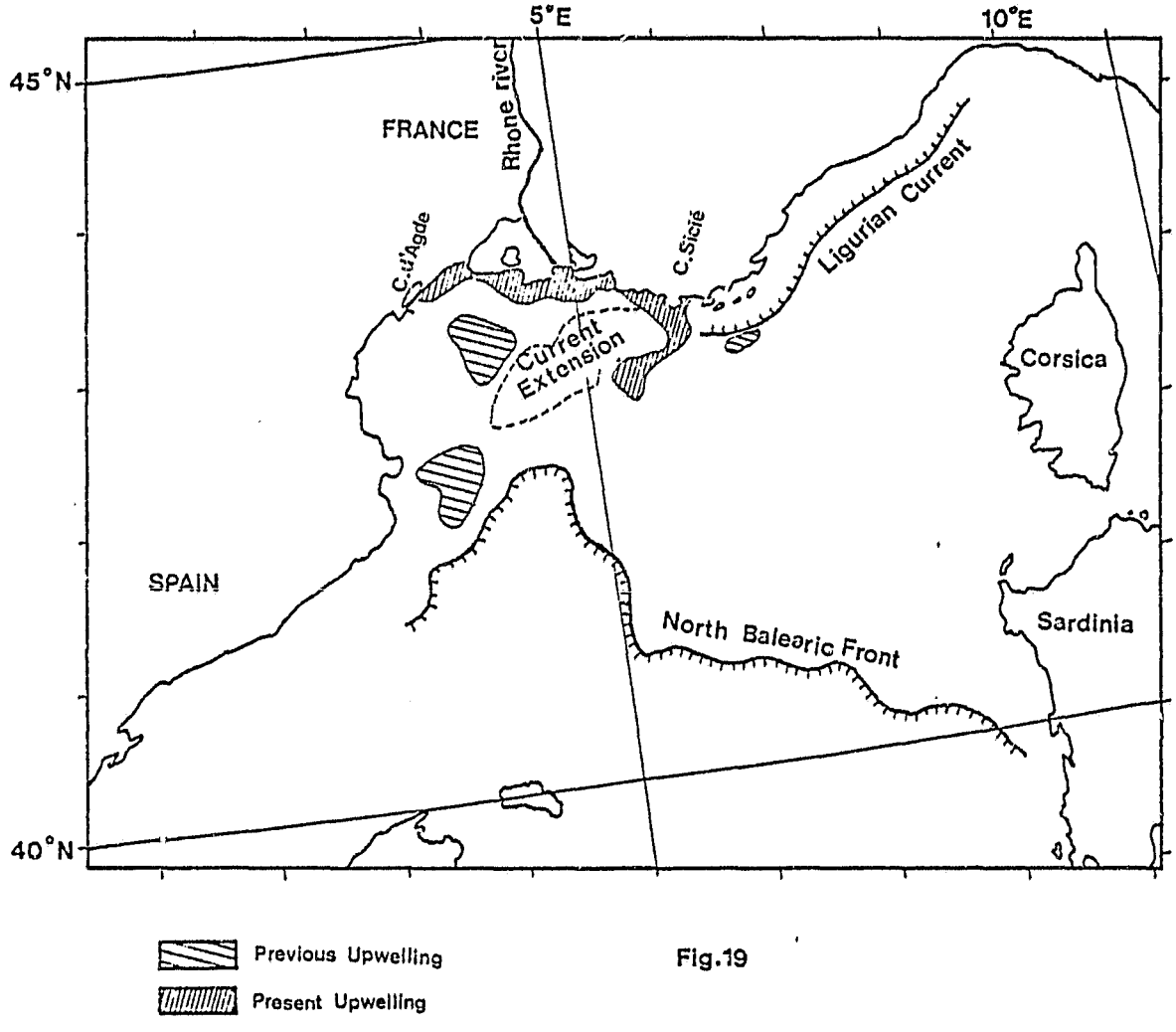

Fig.19

19.- Diagram illustrating the situation on 12 August 1978 (Fig.15.c). After driving various masses of cold upwelling ligurian water the progression of the current is interrupted by a later upwelling released near the Cape of Sicily.

C - 2

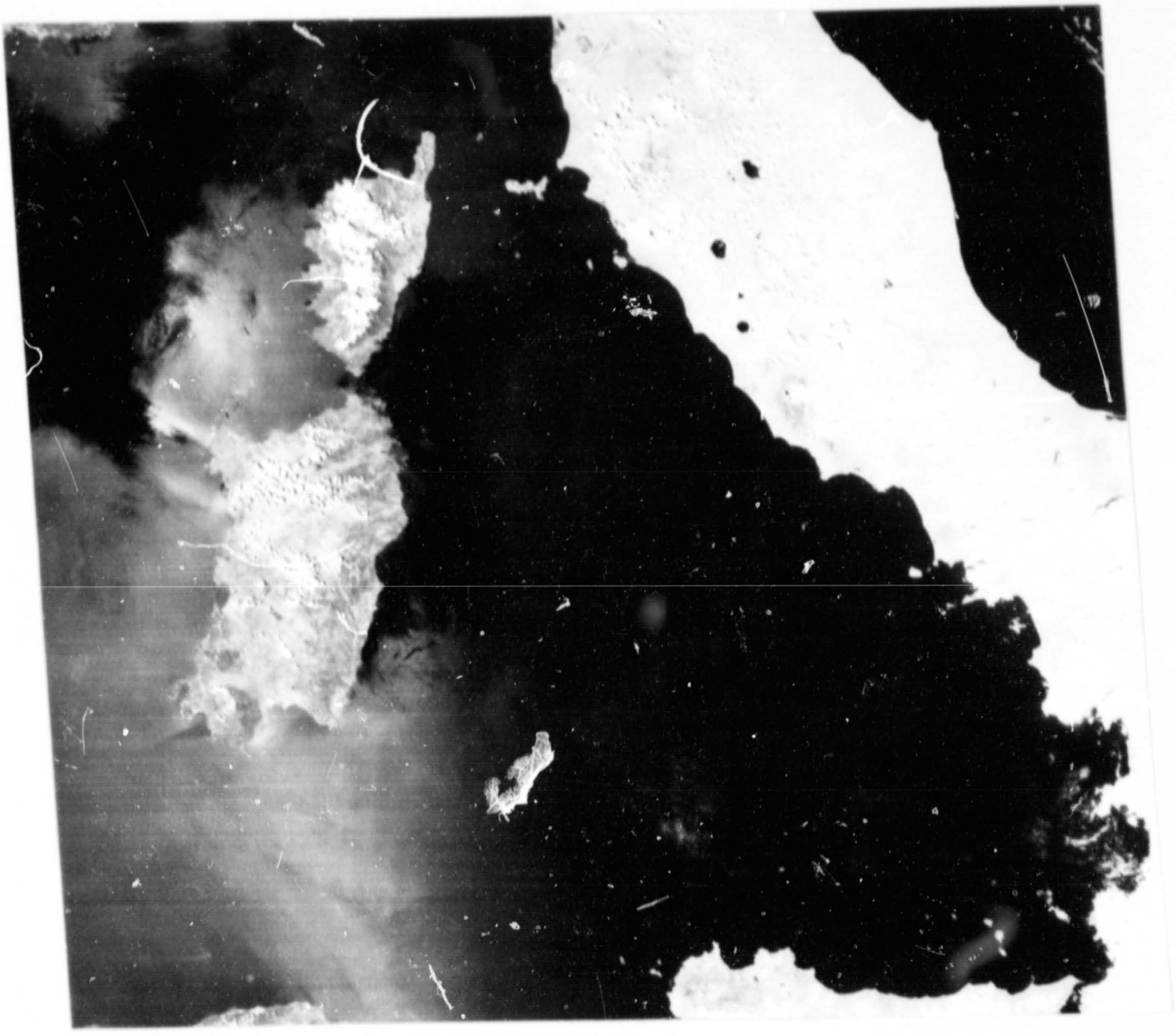

20. - (a) : HCMM observation A-A 0038-12440 in the visible channel on 3 June 1978 at 12 H.44 TU. Note bright patches (high reflectance) to the coast and west of Corsica and Sardinia.

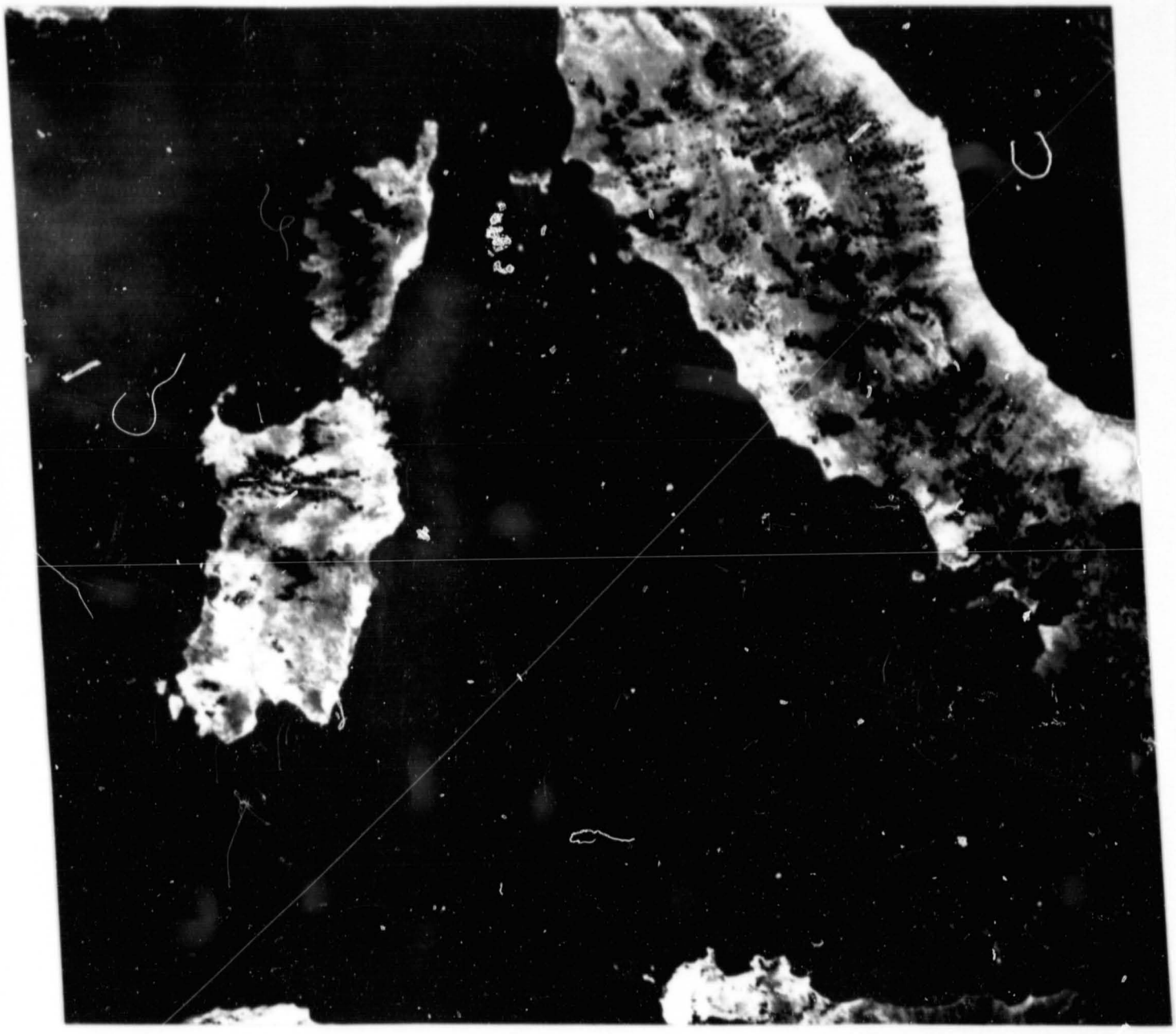

20. - (b) : Idem (a), but in the thermal infrared channel. Note the warmer water to the east and west of Corsica and Sardinia.

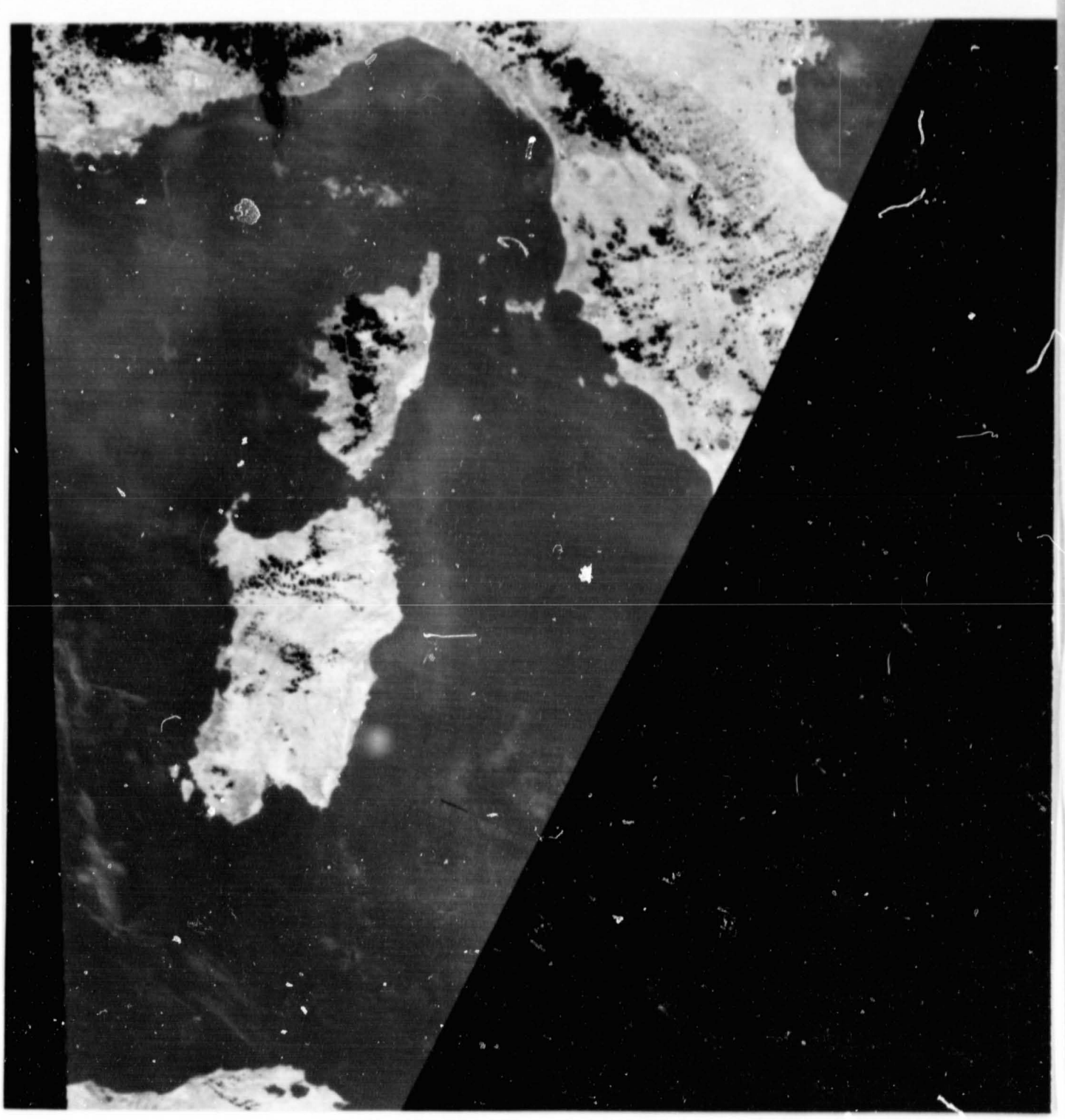

20. - (c) : Day/Night temperature difference from HCMM observations obtained on 3 June 1978 at 1 H.50 TH (night) (A-A 0038-01500) and 12 H.44 TU (day). The darker shades correspond to cooler diurnal temperatures.

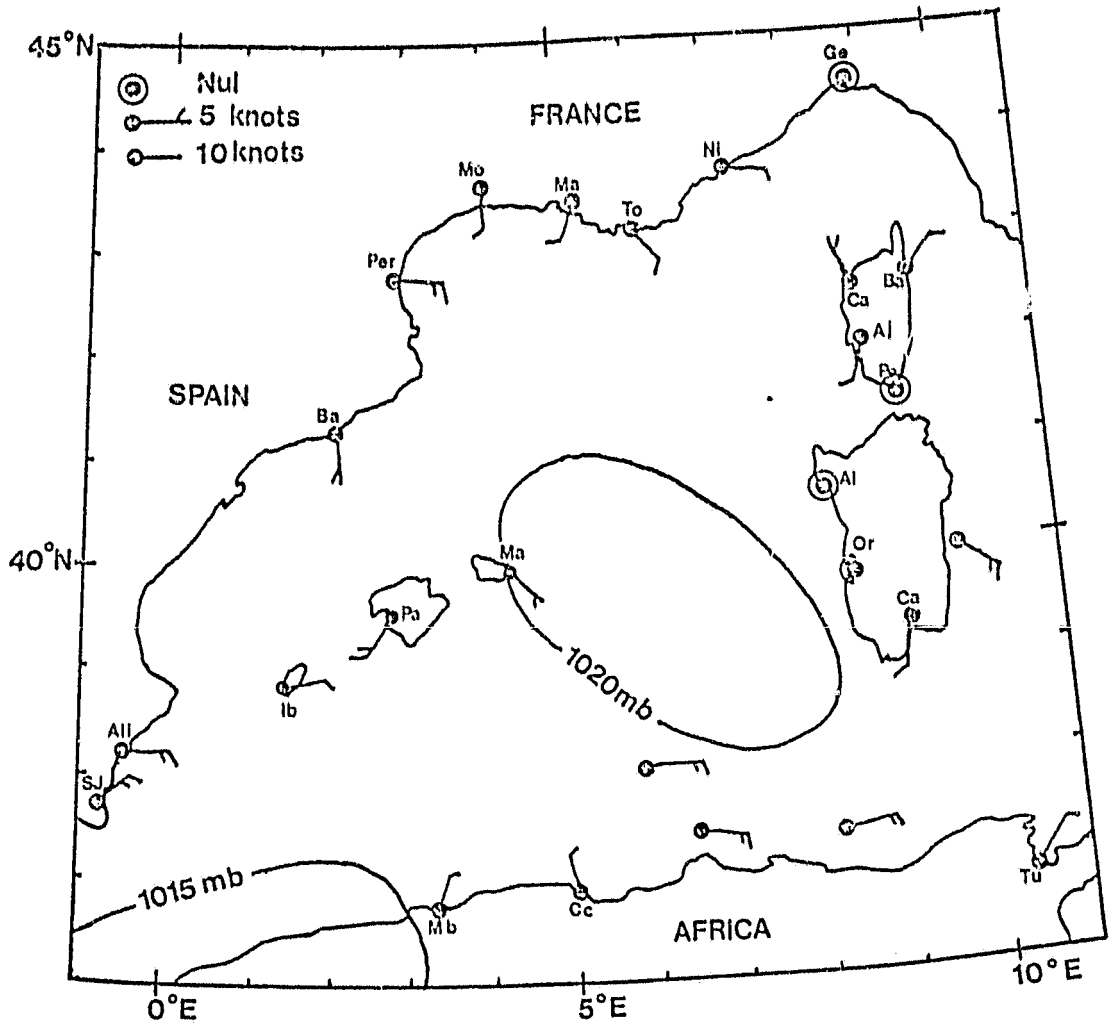

20. - (d) : Meteorological situation on 3 June 1978 at 12 H TU.

Appendix D

SATELLITE DETERMINATION OF THE MESOSCALE VARIABILITY OF THE SEA-SURFACE TEMPERATURE

P.Y. DESCHAMPS[1], R. FROUIN[1], L. WALD[2]

(1) Laboratoire d'Optique Atmosphérique, Equipe associée au C.N.R.S., Université des Sciences et Techniques de Lille, 59655 Villeneuve d'Ascq Cédex, France.

(2) Centre de Télédétection et d'Analyse des Milieux Naturels, Ecole Nationale Supérieure des Mines de Paris, Sophia-Antipolis, 06560 Valbonne, France.

Reprinted from JOURNAL OF PHYSICAL OCEANOGRAPHY, Vol. 11, No. 6, June 1981
American Meteorological Society
Printed in U. S. A.

Satellite Determination of the Mesoscale Variability of the Sea Surface Temperature

P. Y. DESCHAMPS AND R. FROUIN

L. WALD

Satellite Determination of the Mesoscale Variability of the Sea Surface Temperature

P. Y. DESCHAMPS AND R. FROUIN

Laboratoire d'Optique Atmosphérique, Equipe associée au C.N.R.S., Université des Sciences et Techniques de Lille, France

L. WALD

Centre de Télédétection et d'Analyse des Milieux Naturels, Ecole Nationale Supérieure des Mines de Paris, 06560 Valbonne, France

(Manuscript received 5 September 1980, in final form 11 February 1981)

ABSTRACT

Satellite infrared data have been used to investigate the mesoscale variability of the SST (sea surface temperature) field. A statistical analysis of the SST field has been performed by means of the structure function. Results give the equivalent power-law exponent n of the spatial variance density spectrum $E(k) \sim k^{-n}$. The exponent n was found to vary from 1.5 to 2.3 with a mean value of 1.8 in the range of scales 3–100 km which is in agreement with previous one-dimensional analysis from shipborne and airborne measurements. These observed values of n are discussed and compared with the values predicted by turbulence theories.

1. Introduction

Present-day satellite infrared radiometers permit the determination of the mesoscale SST (sea surface temperature) field on an operational basis thanks to their improved radiometric performances, which typically are of a few tenths of °C for a nadir resolution of 1 km². This gives a potential tool for a systematic investigation of mesoscale thermal features such as thermal fronts, eddies and plumes which have been already observed and studied by means of IR pictures or derived SST maps. In addition to these observable features, a part of the SST field must be considered as random and containing some other information which can only be retrieved by a statistical analysis—e.g., the spectral density of variance.

Attempts to compute the spatial spectrum of the SST have previously been made by McLeish (1970), Saunders (1972a) and Holladay and O'Brien (1975), from airborne infrared measurements along an aircraft track. Examples of mesoscale spectra have also been determined from shipborne measurements (Voorhis and Perkins, 1966; Fieux *et al.*, 1978). Satellite observations give a unique opportunity to investigate the mesoscale variability of the SST field, down to scales of 1 km, at any given time, with a frequency which is limited only by the cloud cover. In the present study, we intend to demonstrate the feasability of using satellite data to obtain statistical parameters of the mesoscale SST field.

2. Statistical analysis of the SST field

Studies of the variability of the temperature (or any scalar) field usually make extensive use of spectral methods, i.e., the computation of the density spectrum of the scalar variance by means of Fourier transformation or autocorrelation function, to obtain a typical power law which characterizes the variability of the temperature field and which can be related to turbulence theories. In the present study, the structure function has been employed in order to more accurately determine the power-law exponent in the presence of the large noise level found in satellite infrared data.

a. Structure function

If the SST field is considered as being an isotropic random process with homogeneous increments (at least locally), the structure function can be computed as

$$D_{TT}(h) = \tfrac{1}{2}\overline{[T(x + h) - T(x)]^2}, \qquad (1)$$

where $T(x)$ is the temperature at x, h the spatial scale, and an overbar denotes an average operator. In the following, k denotes the wavenumber of the form $k = h^{-1}$.

The main advantage of the structure function $D(h)$ when compared with the spectrum of the variance density $E(k)$ or with the autocorrelation function $B(h)$ is that its experimental determination is more accurate and much less affected by random variations because only increments are taken into account (Panchev, 1971). An example is given in Fig. 1 where both $E_T(k)$ and $D_{TT}(h)$ have been computed and are shown for the same sample of the SST field, measured by the AVHRR (Advanced Very High-Resolution Radiometer) experiment on board the TIROS-N

0022-3670/81/060864-07$05.75

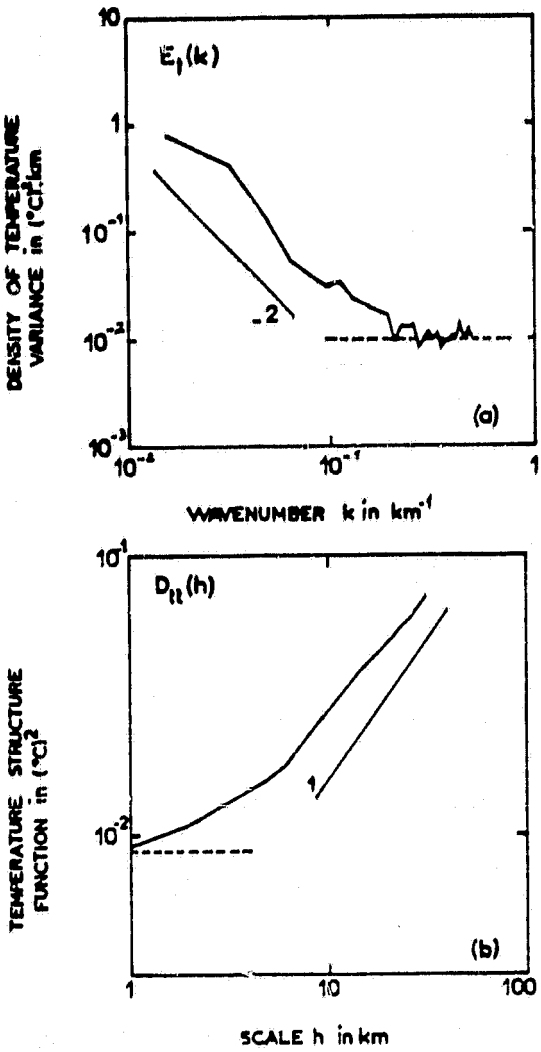

FIG. 1. Comparison between the (a) density of temperature variance $E_T(k)$ and (b) the structure function $D_{TT}(h)$, computed from AVHRR data, 17 July 1979, over the Bay of Biscay (45°30'N, 4°30'W). The dashed line indicates the radiometer noise level.

satellite. This example shows clearly that the structure function is more regular than the spectrum, allowing an easier determination of the characteristic parameters, e.g., the power-law exponent given by the slope when using logarithmic coordinates.

b. *Interpretation of the structure function*

The structure function $D(h)$ represents the statistical influence of a point upon other points at distance h. For a homogeneous and isotropic random process, $D(h)$ and $B(h)$ are linked by

$$D(h) = [B(0) - B(h)]. \tag{2}$$

As $B(h)$ and $E(k)$ are the Fourier transformations of each other, $D(h)$ may thus be related to $E(k)$ (Panchev, 1971):

$$D(h) = \int_0^\infty (1 - \cos 2\pi kh) E(k)\,dk, \tag{3}$$

for a one-dimensional analysis.

In the inertial range, the spectrum is usually characterized by

$$E(k) \sim k^{-n}, \tag{4}$$

From (3), it can be shown that the structure function may then be written as

$$D(h) \sim h^{-p}, \tag{5}$$

where

$$n = p + 1 \tag{6}$$

when $n > 1$ in order to respect the convergence of the integral (3) at small scales. The exponent n of the spectral density thus can be alternately determined from the structure function using (6), if the field under study is homogeneous.

Two kinds of error may affect the satellite-based determination of the SST field—instrumental data noise and atmospheric effects.

Although the structure function has the advantage of being much more regular than the spectrum, the study of the structure function and of its shape is generally limited by the noise level at the smallest scales. This effect is illustrated in Fig. 1b, where the observed slope giving the power law exponent of the structure function decreases from ~1 at large scales to zero at the smallest scales.

In the particular case of random fluctuations due to an instrumental white noise, both the spectral density and the structure function reduce to constants E_n and D_n, with $E_n = \sigma_n/k_0$, $D_n = \sigma_n$, where σ_n is the noise variance and k_0 the upper wavenumber limit of the spectral analysis. This noise constant adds to the actual structure function of the SST, which restricts the exponent determination at the largest scales where the noise constant may be neglected [$D_n \ll D(h)$]. When necessary, a suitable spatial smoothing may reduce the noise, with a corresponding degradation of the ground resolution.

Smoothing also introduces a bias in the determination of the structure function. If $D_F(h)$ is the structure function of the smoothed field, and Q is the convolution square of the smoothing function F it may be shown (Matheron, 1970), that

$$D_F(h) = D * Q - A, \tag{7}$$

where $*$ is the convolution operator and A is a constant, i.e.,

$$A = \int_{-\infty}^{+\infty} D(u)Q(u)\,du. \tag{8}$$

When F is the spatial average in a square of side a, $A = D(a)/3$ for $p = 1$. As with the noise constant, the influence of the bias introduced by smoothing rapidly decreases when h increases, and is less than 10% at $h > 3a$. Above this scale, the influence of smoothing can then be neglected [$A \ll D(h)$].

The atmospheric transmittance τ, in the 10.5–12.5 μm channel generally used on satellites, mainly depends on the atmospheric water vapor content and typically varies between 0.9 and 0.3 (Kneizys *et al.*, 1980). The radiometric temperature T_B measured from space must thus be expressed as

$$T_B = \tau T_W + (1 - \tau)T_a, \tag{9}$$

where T_W is the water temperature and T_a an appropriate mean air temperature. From (9) it is obvious that the structure function computed from satellite data depends not only on the variations of T_W, but also of T_a and τ. Atmospheric variability generally is assumed to be at larger scales than oceanic variability, so that atmospheric fluctuations could be neglected at scales < 100 km. Nevertheless, the satellite determination of the structure function may on some occasions be partially contaminated by air temperature and water vapor variations, but it is very unlikely that this would occur over the open sea where it can be assumed that atmospheric parameters are stable within the scale range. A further study involving satellite and surface measurements along the same track would have been necessary in order to resolve this problem. Assuming a constant atmosphere,

$$T_B(x + h) - T_B(x) = \tau[T_W(x + h) - T_W(x)] \tag{10}$$

$$D_{T_B T_B}(h) = \tau^2 D_{T_W T_W}(h), \tag{11}$$

where the influence of the atmosphere affects only the determination of the structure function amplitude, and not the determination of the power-law exponent p. Because the atmospheric transmittance cannot be accurately determined over the oceans, only one parameter of the structure function can be determined from a satellite; this is the power-law exponent p obtained from the slope of the curve in a log-log plot.

The hypothesis of the homogeneity of the random field must be verified, otherwise erroneous determinations of the exponent could be obtained. For example, a frontal zone would have a spectrum $E_T(k) \sim k^{-2}$, but $D_{TT}(h) \sim h^2$. Since these exponents are close to the physically expected values, it is necessary to carefully check the homogeneity of the SST field and to remove the existing trend if necessary. When the mean horizontal SST gradient $\partial T/\partial x$ is small, it is sufficient to take

$$(\partial T/\partial x)^2 h^2 \ll D(h) \tag{12}$$

over the study range of scales; otherwise, the standard procedures must be applied to detrend the data.

TABLE 1. Radiometer performances of the satellite experiments used in this study.

Satellite experiment	Ground resolution at nadir (km²)	Noise equivalent temperature difference (°C)
VHRR/NOAA-5	1	0.8
HCMR/HCMM	0.25	0.3
AVHRR/TIROS-N	1	0.1

3. Results

The results of two independent but complementary studies are hereby presented. The first study deals with data obtained from the VHRR (Very High-Resolution Radiometer) on board NOAA-5, and was limited to the range of scales 40–100 km because of the large level of instrumental noise. The improved radiometric performances of the HCMM (Heat Capacity Mapping Mission) data,—i.e., a nadir resolution of 0.5 km and NEDT = 0.3 K (see Table 1)—allowed us to extend the study down to scales of 3 km. The visible channel was used to select cloud-free study areas in the northeastern Atlantic Ocean and the Mediterranean Sea. Only areas in which no large-scale specific features were viewed on fully enhanced images were considered homogeneous and used in this study.

Locations are shown in Fig. 2 and dates are given in Table 2. At each location, the one-dimensional structure functions were computed in four directions, $\theta = 0$ (across the satellite track, i.e., approximately east to west), $\pi/4$, $\pi/2$ (along the satellite track) and $3\pi/4$.

Examples of the computed structure functions are given in Fig. 3 for VHRR/NOAA-5 and in Fig. 4 for HCMM. The results generally show that the SST field is not exactly isotropic. Nevertheless, the structure functions, if not equal, are roughly parallel on a log-log plot, so that the anisotropy is confined in the amplitude $A(\theta)$, i.e.,

$$D_{TT}(\theta, h) = A(\theta)h^p \tag{13}$$

but the slope p remains very nearly isotropic.

Values of p from 0.5 to 1.3 have been observed in this study with an estimated accuracy of ~0.1. Using VHRR/NOAA-5 data, 44 estimations of p were made in the range of scales 40–100 km, and HCMM data were used to make 37 estimations in the range of scales 3–30 km. The corresponding histograms of the observed p are given in Figs. 5a and 5b. The most frequent values are 0.9–1.0 and the mean values are 0.8 (3–30 km) and 0.9 (40–100 km) with a standard deviation of ~0.2. About 90% of the observed values are distributed between 0.5 and 1.1. The results correspond to a mean value of the power-law exponent of the spectrum n of 1.8 in the wavenumber range 0.01–0.3 km^{-1}.

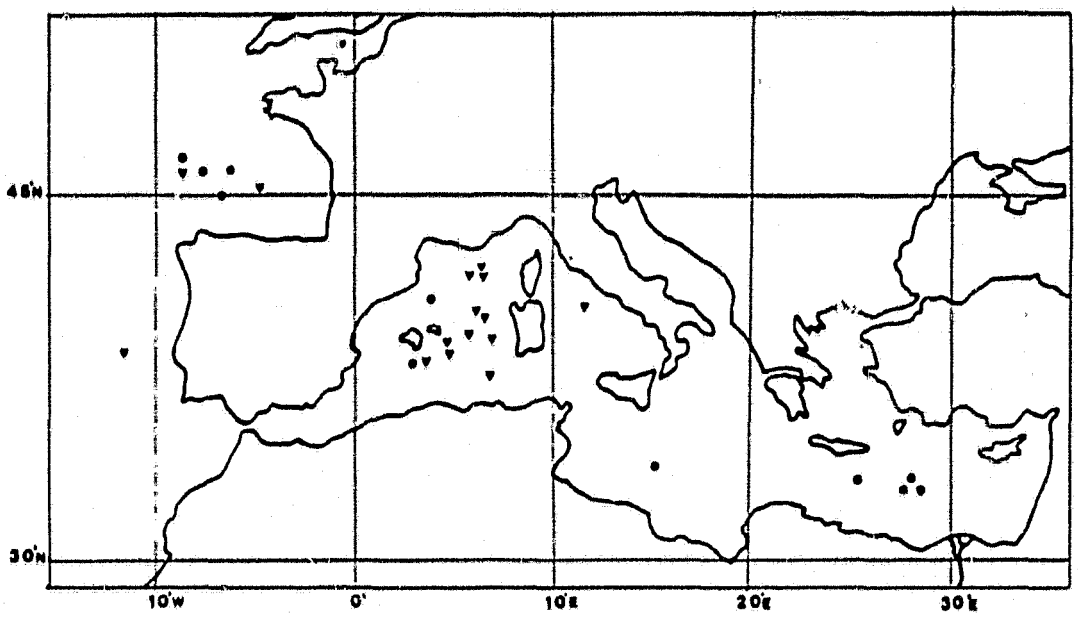

FIG. 2. Geographical locations of the different study areas for HCMM data (triangles) and VHRR data (circles).

The amplitude of the structure functions varied from 10^{-2} to 10^{-1} $(°C)^2$ at $h = 40$ km. Even after spatial smoothing, it was noted that the noise level tended to slightly reduce the estimated values of p because the structure function of the noise is a constant ($p = 0$). This is particularly true when the noise level (5×10^{-3} $(°C)^2$ for the HCMM data, 3×10^{-2} $(°C)^2$ for the VHRR/NOAA-5 after smoothings) is of the same order as the structure function (see Fig. 1). Whenever possible, the estimates of p were corrected for this effect, but the effect could partly explain the lowest values of p.

On the other hand, a mean horizontal thermal gradient would give $D(h) \sim h^2$. The areas studied were carefully selected to avoid the existence of thermal gradients which would increase the estimate of p toward larger values; nevertheless some influence on the data could remain. Both of these effects, noise level and horizontal thermal gradients, could partly but not totally explain the spread of the results around the mean value, between 0.5 and 1.3, which remains significant. There is no evidence of correlation between the estimates of p and the corresponding geographical locations or seasons but, nevertheless, we would guess that it is probably necessary to involve physical processes in the explanation of the observed p values.

4. Discussion

Using (6) and the results from this structure function analysis, we obtain a spectral density power exponent with a range of $1.5 < n < 2.3$. This agrees fairly well with the previous results reported by several authors either from shipborne measurements (Fieux *et al.*, 1978), or from airborne measurements (Saunders, 1972a), for the one-dimensional temperature spectra (see Table 3). Holladay and O'Brien (1975) attempted to reconstruct the two-dimensional SST field from the tracks of the aircraft survey and found $n = 3$ for the isotropic part of the two-dimen-

TABLE 2. Summary of the different areas studied.

Area	Date	Location	Experiment
Eastern Mediterranean Sea	19 Mar 1978	33°00'N, 28°00'E	VHRR
	05 May 1978	34°00'N, 15°00'E	VHRR
	08 May 1978	33°00'N, 29°00'E	VHRR
	14 May 1978	33°30'N, 28°30'E	VHRR
	17 May 1978	33°30'N, 26°00'E	VHRR
Western Mediterranean Sea	29 Sep 1977	41°00'N, 04°00'E	VHRR
	29 May 1978	39°05'N, 07°15'E	HCMM
	29 May 1978	40°05'N, 06°55'E	HCMM
	11 Jul 1978	38°55'N, 04°50'E	HCMM
	11 Jul 1978	41°55'N, 06°55'E	HCMM
	26 Jul 1978	39°20'N, 06°15'E	HCMM
	28 Jul 1978	38°15'N, 03°45'E	HCMM
	28 Jul 1978	38°35'N, 05°05'E	HCMM
	28 Jul 1978	37°40'N, 07°25'E	HCMM
	14 Aug 1978	38°30'N, 03°00'E	VHRR
	14 Sep 1978	40°25'N, 06°30'E	HCMM
	14 Sep 1978	40°35'N, 11°55'E	HCMM
	14 Sep 1978	41°40'N, 06°45'E	HCMM
Northeastern Atlantic Ocean	11 Sep 1977	46°00'N, 06°30'W	VHRR
	14 Sep 1977	45°00'N, 07°00'W	VHRR
	06 Jan 1978	46°30'N, 09°00'W	VHRR
	10 May 1978	46°00'N, 08°00'W	VHRR
	11 May 1978	45°15'N, 04°40'W	HCMM
	11 May 1978	38°35'N, 11°45'W	HCMM
	18 Jun 1978	46°00'N, 08°35'W	HCMM

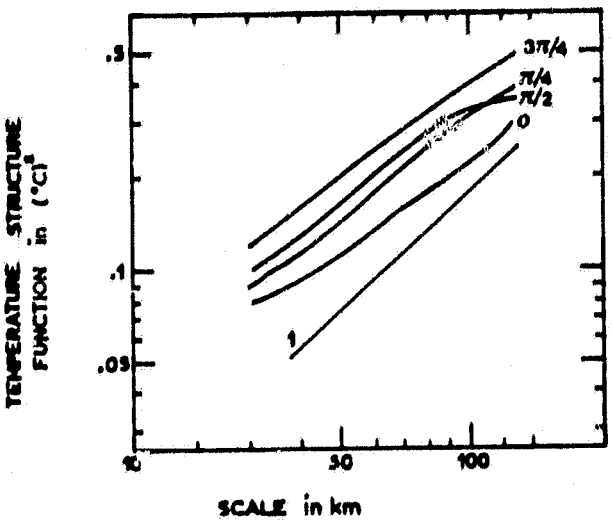

FIG. 3. Example of structure functions computed from VHRR data.

sional spectrum, which probably is an overestimation of the value due to the smoothing of high wavenumbers produced by the SST mapping procedure.

The experimental values, $1.5 < n < 2.3$, must be compared with those given by turbulence theories. All of the theories assume the existence of an inertial range, i.e., that the considered scales are far from the energy sink and source scales. It is not evident that the range of scales 3–100 km in the ocean is an inertial one. The scales of input and sink of energy remain puzzling [see a review in Rhines (1977) or Woods (1977)]. The final energy dissipation occurs at molecular scales but larger scales play a role via internal and surface wave breaking. These waves may also generate motion at larger scales via non linear processes (Hasselman, 1971). The interactions between internal waves and mesoscale eddies are uncertain. Müller (1974) predicts that internal waves gain energy from eddies, while the critical-layer absorption theory of Ruddick (1980) suggests the opposite. The typical scales of internal waves are to the lower limit of the studied range and interactions may occur.

Input of kinetic energy related to wind is found at scales of the same order as the wind waves (100 m), and the meteorological systems (1000 km or more). Energy inflow due to thermodynamic forcing is found at even large scales. All of these scales are one or two orders of magnitude smaller or greater than those studied. At some locations, interior processes such as baroclinic instability may also play an important role in converting energy through nonlinear mechanisms. The scales of these phenomena are on the order of one to six times the internal radius of deformation, depending on the physics of the problem. This radius is of approximately 50 km in the open ocean and 7 km in the Mediterranean sea. If these physical processes are of importance in the area studied, the 3–100 km range is not an inertial one. In fact, we cannot specifically determine whether or not the 3–100 km range is an inertial one from our observations: by looking at Fig. 3 and 4, one can notice that the structure functions do not exhibit any peak characterizing a very energetic scale in the range we deal with, but this may only mean that the energy inputs are from outside the studied range.

In the range of scales 3–100 km, horizontal scales are larger than vertical ones, and the observed variability may be considered a quasi two-dimensional process. Therefore the observations can be related to the n values predicted by the theories of two-dimensional turbulence (Kraichnan, 1971) and of geostrophic turbulence in the atmosphere (Charney, 1971). These theories take into account either the conservation of energy and of enstrophy (half of the mean square of the vorticity) in the case of Kraichnan's theory, or the conservation of energy and of the pseudo-potential enstrophy (Charney). Both of these theories agree when predicting the power law of the kinetic energy spectrum: $E_K(k) \sim k^{-3}$. But the relations between current and temperature are not obvious and the different mechanisms involved lead to drastically different theoretical power laws for the temperature variance spectrum. Kraichnan's theory, considering that temperature is a passive contaminant implies that $E_T(k)$ only depends on k and on the dissipation rates of enstrophy and temperature variance. Then, from a dimensional analysis, $E_T(k)$ must follow a k^{-1} power law. Charney made use of the perfect gas law and of the hydrostatic relation to compute a relation between the temperature and the streamfunction and he found the same law for $E_T(k)$ as for $E_K(k)$, i.e., $E_T(k) \sim E_K(k)$

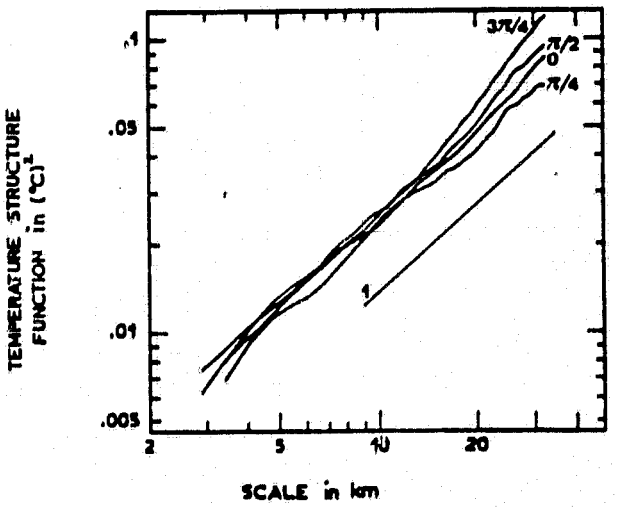

FIG. 4. Example of structure functions computed from HCMM data.

$\sim k^{-3}$. Also, assuming $E_\lambda(k) \sim k^{-3}$, Saunders (1972b) deduced a temperature variance spectrum $E_T(k) \sim k^{-5}$, by the use of the thermal wind equation. These examples demonstrate how results may be very different according to various authors. In this study, the mean observed value of 1.8 for n is far from the assessment ($n = 5$) made by Saunders but falls between the Kraichnan and Charney predictions ($n = 1$ and 3). This discrepancy may be due to the fact that the conditions of the theories have not been fully met and namely that the study range is not an inertial one.

Three-dimensional theories of turbulence (Kolmogorov, 1941; Bolgiano, 1962) or space-time variability theories of internal waves (Garrett and Munk, 1972, 1975) report values of n close to those found in our study (1.7, 1.4 and 2, respectively), but the physical basis of their hypothesis can hardly be extended to the mesoscale range.

We may also notice that several experimental studies of air temperature variability mention values of n in agreement with our study at similar range of scales (100–1000 km). See reviews by Gage (1979) and Panchev (1971). Some of these results are obtained by using spectral analysis on time-series data and equivalent wavenumbers are computed by using Taylor's relation. As the validity of this relation is dubious for such scales, these time-series results must be viewed skeptically. But as for the oceanographic observations, there is no atmospheric theory to explain the observed results.

In summary, the power law exponent n of the spectral temperature variance observed in the range of scales 3–100 km is nearly 2. This is very discordant with the values predicted by turbulence theories which are widely spread around this value. Results and conclusions from the present study are very similar to the experimental results published by Saunders (1972a) nearly a decade ago but it is emphasized that further advanced theories are still needed in order to explain the experimental determination of the mesoscale SST variability.

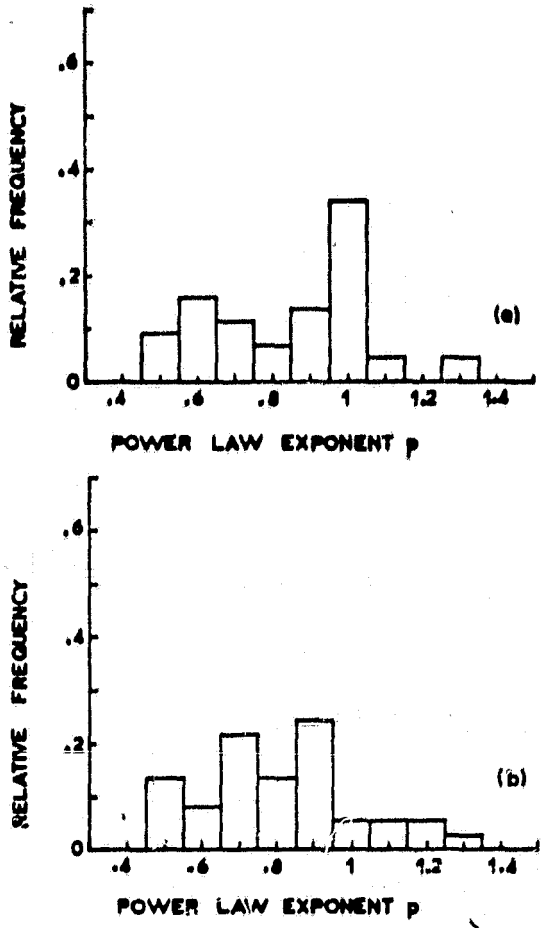

FIG. 5. Histograms of the observed values of the power-law exponent p of the structure function in the range of scales (a) 40–100 km and (b) 3–30 km.

5. Conclusion

This study has proven that it is feasible to estimate the random properties of the SST field in the mesoscale range 3–100 km from satellite infrared data. As compared with previous analysis of ship-borne and airborne observations, the use of satel-

TABLE 3. Summary of observed mesoscale SST variability.

Authors	Range of scales (km)	Power-law exponent n	Comments
Saunders (1972)	3–100	2.2 ± 0.1	one-dimensional, surface temperature, airborne infrared sensor
Holladay and O'Brien (1975)	3–20	3	two-dimensional, SST maps from aircraft surveys
Fieux *et al.* (1978)	1–64	2	one-dimensional, surface temperature, ship-towed sensors
This study	3–100	$1.5 < n < 2.3$; $\bar{n} = 1.8$	two-dimensional, surface temperature, satellite data

lite data allowed us to perform more systematic study, including the isotropy of the SST field. Using the structure function, the power-law exponent n of the SST field variance density spectrum can be retrieved with good accuracy (± 0.1). A mean value of 1.8 and a standard deviation of 0.2 have been found in the range of scales 3–100 km, and extreme values of 1.5 and 2.3 have been observed.

The results give rise to several questions: 1) Is the range of scales 3–100 km an inertial one? 2) If yes, is there any turbulence theory which would explain the spectrum power law observed? 3) If not, at which scales are the inputs of energy and to which processes are they related? At the present time, further investigations, both theoretical and experimental, are needed to interpret the physical mechanisms and parameters involved in the mesoscale variability of the SST field.

Acknowledgments. The authors are indebted to the receiving station of the Meteorologie Nationale at Lannion, France, for providing them the infrared data from meteorological satellites. HCMM data have been received from NASA as a support to HCMM Investigation No. 15. They wish also to acknowledge the helpful advice of J. M. Monget and the fruitful suggestions of Dr. Crepon. Thanks to L. F. Martin for his aid in the translation. Support for this work has been provided by the following French agencies: CNRS (Centre National de la Recherche Scientifique), CNES (Centre National d'Etudes Spatiales) and CNEXO (Centre National pour l'Exploitation des Océans).

REFERENCES

Bolgiano, R., 1962: Structure of turbulence in stratified media. *J. Geophys. Res.*, **67**, 3015–3023.

Charney, J. G., 1971: Geostrophic turbulence. *J. Atmos. Sci.*, **28**, 1087–1095.

Fieux, M., S. Garzoli and J. Gonella, 1978: Contribution à la connaissance de la structure spatiale des courants superficiels au large du golfe du Lion. *J. Rech. Oceanogr.*, **3**, 4, 13–26.

Gage, K. S., 1979: Evidence for a $k^{-5/3}$ law inertial range in mesoscale two-dimensional turbulence. *J. Atmos. Sci.*, **36**, 1950–1954.

Garrett; C., and W. Munk, 1972: Space time scales of internal waves. *Geophys. Fluid Dyn.*, **3**, 225–264.

——, and ——, 1975: Space time of internal waves: A progress report. *J. Geophys. Res.*, **80**, 291–297.

Hasselman, K., 1971: On the mass and momentum transfer between short gravity waves and larger scales motions. *J. Fluid Mech.*, **50**, 189–205.

Holladay, C. G., and J. J. O'Brien, 1975: Mesoscale variability of sea surface temperature. *J. Phys. Oceanogr.*, **5**, 761–772.

Kneizys, F. X., E. P. Shettle, W. O. Gallery, J. H. Chetwynd, Jr., W. L. Abreu, J. E. A. Selby, R. W. Fenn and R. A. McClatchey, 1980: Atmospheric transmittance radiance: Computer Code LOWTRAN 5. Environ. Res. Pap. No. 697, Air Force Geophysics Laboratory, 233 pp.

Kolmogorov, A. N., 1941: The local structure of turbulence in incompressible viscous fluid for very large Reynolds numbers. *Dokl. Akad. Nauk. SSSR*, **30**, 301–305.

Kraichnan, R. H., 1971: Inertial-range transfer in two and three-dimensional turbulence. *J. Fluid Mech.*, **47**, 3, 525–535.

McLeish, W., 1970: Spatial spectra of ocean surface temperature. *J. Geophys. Res.*, **75**, 6872–6877.

Matheron, G., 1970: *La Théorie des Variables Régionalisées et ses Applications.* Cahiers due Centre de Morphologie Mathématique de Fontainebleau, École des Mines de Paris, 212 pp.

Müller, P., 1974: On the interaction between short internal waves and larger scale motion in the ocean. *Hamb. Geophys. Einzelschr.*, No. 23.

Panchev, S., 1971: *Random Functions and Turbulence.* Pergamon Press, 444 pp.

Rhines, P. B., 1977: The dynamics of unsteady currents. *The Sea*, Vol. 6, Wiley Interscience, 189–318.

Ruddick, B., 1980: Critical layers and the Garrett-Munk spectrum. *J. Mar. Res.*, **38**, 135–145.

Saunders, P. M., 1972a: Space and time variability of temperature in the upper ocean. *Deep-Sea Res.*, **19**, 467–480.

——, 1972b: Comments on "Wavenumber-frequency spectra of temperature in the free atmosphere." *J. Atmos. Sci.*, **29**, 197–199.

Voorhis, A. D., and H. T. Perkins, 1966: The spatial spectrum of short-wave fluctuations in the near surface thermocline. *Deep-Sea Res.*, **13**, 641–654.

Woods, J. D., 1977: Parametrization of unresolved motions. *Modelling and Prediction of the Upper Layers of the Ocean*, E. B. Kraus, Ed., Pergamon Press, 118–140.

Appendix E

LARGE DIURNAL HEATING OF THE SEA SURFACE OBSERVED BY THE HCMM EXPERIMENT

P.Y. DESCHAMPS AND R. FROUIN

Laboratoire d'Optique Atmosphérique,
Equipe Associée au CNRS n° 466,
Université des Sciences et Techniques de Lille,
59655 Villeneuve d'Ascq Cédex, France

ABSTRACT

ORIGINAL PAGE IS
OF POOR QUALITY

Day-night surface temperature differences measured in the infrared (10.5-12.5 μm channel) by the HCMM satellite experiment frequently show large diurnal heating (several °C) of the upper layer of the ocean during summer months in the Mediterranean Sea, when the wind speed is low. When observed in the 0.5-1.1 μm channel, glitter reflectance - i.e. direct solar radiation specularly reflected towards the sensor - correlates with diurnal heating. Glitter reflectance has been modeled to retieve an equivalent wind speed, and observed diurnal heatings, ΔT, rapidly decrease from their maximum value of about 5 °C as the wind speed, U, increases. A mean diurnal heating of nearly 1 °C is calculated for the marine coastal areas of southern France in summer time. During this period, satellite observations should be restricted to night and early morning orbits, or to periods of high wind speed ($U > 5$ m.s^{-1}) at noon and during the afternoon.

I - INTRODUCTION

A daily variation in the temperature of the surface layer of the oceans is known to be produced by diurnal heating due to absorbed solar radiation. The amplitude of the daily temperature variation is usually small because of turbulent mixing which usually prevails over the molecular thermal diffusivity. A solar irradiance of 1000 $W.m^{-2}$, when absorbed in a mixed layer of 10 m, would give a heating rate of only 0.1 °C per hour, and a daily variation of less than 0.5 °C. If the turbulent mixing is reduced and the mixed layer is less than 1 m thick a heating rate of 1 °C per hour may be expected and daily variations of several °C should be observed. With the exception of very shallow waters, large diurnal surface temperature variations in open oceans correspond to low wind speeds because turbulence in the upper surface layer is mainly induced by the surface wind stress.

From a theoretical simulation of radiative and heat transfer in the upper ocean layer, HASSE (1971) predicted that the deviation of the sea surface temperature (SST) T_o from the bulk temperature T_{10} taken at 10 meter depth should vary as :

$$T_o - T_{10} = C_2 \, Q \, U^{-1} \qquad (1)$$

where Q is the solar irradiance, U, the wind speed, and $C_2 = 3.5\ 10^{-3}$ when Q is expressed in $W.m^{-2}$, U in $m.s^{-1}$. According to HASSE, Eq. (1) is only valid for $U \geq 2\ m.s^{-1}$, but the evidence that the SST diurnal variations increase when U decreases is supported by several observations : ROMER (1969), STOMMEL et al (1970) occasionaly found diurnal variations of more than 1 °C at very low wind speeds - i.e. for $U < 2\ m.s^{-1}$. These observations were nevertheless restricted to a single location and were isolated events.

Satellite infrared radiometers offer the opportunity to more systematically investigate such large diurnal variations of the SST. The first satellite experiment to provide adequate capability for this purpose was the HCMR (Heat Capacity Mapping Radiometer) experiment launched in late April 78 with an improved temperature resolution (0.3 °C) and a nearly noon overpass. Results from this experiment are hereby reported in order (i) to investigate large diurnal SST variations at low wind speeds (ii) to give an assessment of the relative frequency of such an event and its impact on the determination of the SST field in such areas as the Mediterranean Sea where diurnal heating is frequent.

II - OBSERVATIONS OF DIURNAL HEATING FROM HCMR SATELLITE DATA

II-1 - The HCMR experiment

The basic objective of the HCMR experiment is the measurement of variations of the earth surface temperature for applications to earth resources (geology, hydrology...). For this purpose, the satellite is sun-synchronous and crosses the equator at about 2 a.m and 2 p.m local time so that surface temperature data are obtained close to the minimum and the maximum of the diurnal variation. Satellite altitude is 620 km, and orbit inclination is 98.87°. The HCMR consists of a two-channel scanning/imaging radiometer, with a 0.5-1.1 µm spectral bandwith in the visible and 10.5-12.5 µm in the thermal infrared. Similar channels have been used on previous meteorological satellites, but the interests of the HCMR experiment are (i) a large improvement of the radiometric performances in the thermal infrared channel for which the temperature resolution is 0.3 °C and the nadir ground resolution is 500 m as compared with 0.5 to 1 °C and 1 km for the previous VHRR/NOAA satellites, (ii) the new ease with which the user can obtain differential surface temperature maps between day and

night at 12 or 36 hour intervals. The HCMR experiment was originally designed to produce thermal inertia data for soil and geology applications but the very good performances of HCMR are also suitable for oceanographic studies. Data were received from NASA (National Administration for Space Research) through an investigation concerned with sea surface temperatures of the coastal zones of France.

Available HCMR data are photographic or digital products covering a 700 x 700 km square scene. The following information is displayed :
(1) diffuse surface albedo or reflectance in the visible channel (day only),
(2) surface temperature from the infrared channel,
(3) surface temperature difference between day and night,
(4) thermal inertia, which was not used in the present study. About 1000 scenes covering the coastal zones of France were received during the May 1978 - May 1979 period. Examples of the photographic products are given for two areas in the Western Mediterranean Sea (Fig. 1) and in the North Sea (Fig. 2)) where large diurnal variations of the SST were observed.

II-1 - Diurnal heating and glitter (sun glint) patterns

A large number of the data received for the Mediterranean Sea during May, June, and July of 1978 exhibited very interesting and concordant features in both the visible and the infrared channels, as shown in Fig. 1 between the Island of Corsica and the Southern coast of France, and also close to the east coasts of Corsica and Sardinia. Warmer areas in the thermal channel are associated with brightness changes in the visible.

The observed brightness changes in the visible are identified as glitter or sunglint patterns - i.e. specular reflexion of direct solar radiation by the wavy sea surface. During the concerned time period around the summer solstice, the observation angle of the HCMR imagery was very close to the angle of the specular reflexion of direct solar radiation in the western part of the scenes. This favors the observation of glitter patterns. Glitter generally increases when the wind decreases and the sea surface becomes calmer and more specular. The surface exhibits a maximum brightness when the observation angle is close to that of the specular reflexion of solar radiation : a homogeneous bright area is thus noted in the south-west part of Fig. 1-a. For very calm seas, the surface reflexion becomes nearly specular, and a brightness decrease may be observed, because it is very unlikely that the observation angle be strictly in line with the specular reflexion. Both processes are present in the northwest part of Fig. 1-a, where bright and dark areas respectively correspond to weak and nul wind speeds. The fact that smoothing of the surface could produce either an increase or a decrease of the glitter brightness was previously mentionned by LA VIOLETTE et al (1980). A physical and detailed description is given in the Appendix, to aid in a further quantitative analysis of the data. The dark patterns in a mean bright glitter can thus be clearly interpreted as nul wind and calm sea areas, which obviously favour greater diurnal heating of the upper layer of the ocean because the heat transfer to deeper ocean layers is limited by reduced turbulent mixing and thermal diffusivity.

II-3 - Meteorological observations

Evidence of a large diurnal heating corresponding to low wind speed conditions is also given by correlative meteorological observations. Surface observations are presented in Fig. 1-b for the case of the Mediterranean Sea, and in Fig. 2-c for another case found in the North Sea where, due to higher latitudes, glitter is almost always unobservable. On Fig. 2-a a large warm

spot was detected by HCMR in the middle of the North Sea which was coincident with the center of an anticyclone high where nul wind speed was reported. Warmer areas observed in the Mediterranean Sea on Fig. 1-b are also coincident with low or nul wind speeds, but the observed wind field is much more complicated because most of the reporting coastal weather stations are affected by some breeze effects which are superimposed upon an anticyclone high. Cloudfree satellite SST observations are frequently acquired during similar anticyclonic situations with moderate wind speeds. It must be outlined that satellite estimations of SST may thus be systematically affected by diurnal heating, and a tentative statement of this is discussed in section III-4.

II-4 - Day-Night observations

At least in the upper layers, heat loss during the night very rapidly destroys most of the diurnal heating, which was produced during day time. Evidence of a diurnal heating may thus be found from a comparative analysis of two successive day and night observations at 12 hour intervals. For the two cases given in Fig. 1-b and 2-a, the corresponding night observations (Figs. 1-c and 2-b) show a much more constant SST fiels and the warmer features noted during day time disappear.

Figure 1-d gives the result of the computed day-night temperature differences after the proper calibration algorithms have been applied by NASA. These differences present the advantage of being independent of the mean mesoscale SST field and allow enhancement of the diurnal heating, which again closely correlates with glitter patterns in the visible channel. Day-night temperature differences are used in the following for a more quantitative analysis of diurnal heating.

III - DEPENDENCE OF DIURNAL HEATING ON SEA STATE AND WIND SPEED

The observed diurnal heatings were further quantified by analysis to derive their relationship with the sea state and the wind speed. Day-night temperature differences were correlated to the reflectance of the 0.5-1.1 µm channel. This reflectance, mostly due to sun glitter, is related to the surface slope variance and to a mean wind speed using the statistical model of COX and MUNK (1954).

III-1 - Diurnal heating and glitter reflectance

Day-night temperature differences (Fig. 1-d) - i.e. SST diurnal variations - show patterns similar to the glitter patterns (Fig. 1-a), on June 3, 1978. Fig. 3 gives the result of the correlation obtained when the diurnal heating, ΔT, is plotted as a function of the glitter reflectance, ρ_g, in a small study area east of Sardinia. It is evident that a close correlation exists and ΔT rapidly decreases when ρ_g increases. To further interpret that fact, ρ_g has to be related to the wind speed, or more exactly to the statistics of surface slopes.

Using the statistical distribution of surface slopes from COX and MUNK (1955), a model was developped to relate the glitter reflectance to the wind speed. This model is detailed in the Appendix. Results indicate that ρ_g could either increase or decrease with wind speed : ρ_g presents a maximum value for a given wind speed value, both of which depend on solar and observation angles through Θ_n ($tg\ \Theta_n$ is the surface slope allowing specular reflection toward the sensor). Fig. 4 gives the relationship between ρ_g and the wind speed, U, for $\Theta_n = 8°$, 10°, and 12°, corresponding to the area previously studied for $\Delta T = f(\rho_g)$. In this case ρ_g increases rapidly at the lower wind speeds and then is rather constant for $U > 3\ m.s^{-1}$ so that U can be estimated with a good accuracy from ρ_g, only when $U < 3\ m.s^{-1}$. The study has thus to be limited to this

wind speed range. It should also be noted that ρ_g is physically linked to the surface slope variance, and only statistically to the wind speed. Local anomalies may thus occurs, in particular when the fetch of the wind over the sea is variable. Keeping precautions in mind these, we may now transform $\Delta T(\rho_g)$ into $\Delta T(U)$ which is given in Fig. 5.

III-2 - Diurnal heating and the wind speed

The first point to be noted on Fig. 5, which gives the diurnal heating as a function of the wind speed, is that ΔT rapidly decreases from several °C to 1 °C when U increases up to 2 $m.s^{-1}$. The scatter of observations $\Delta T(U)$ on Fig. 5 is remarkably less than $\Delta T(\rho_g)$ on Fig. 3, because the variations of ρ_g with changes of observation angles within the study area have been eliminated. A fit of $\Delta T(U)$ on Fig. 5 would give :

$$\Delta T = 0.4\ U^{-1} + 0.5 \qquad (2)$$

(in °C for U in $m.s^{-1}$)

Some uncertainties related to the model $\rho_g(U)$ have previously been outlined. Additional errors may be due to armospheric effects on the measured radiances. An aerosol atmospheric reflectance of about 0.02 was estimated from the minimum reflectance within the scene ($\rho_g \simeq 0$) and substracted in the 0.5-1.1 µm channel. Day-night temperature differences have not been corrected for atmospheric emission in the infrared. This approximation would be valid only if the atmosphere were to remain the same between the two satellite overpasses, but a bias due to a change of atmospheric parameters - i.e temperature and water vapor concentration - could have occured which would possibly change the 0.5 °C constant found in (2). Lastly, the observed ΔT are certainly under-

estimated by a factor τ, the atmospheric transmittance in the 10.5-12.5 µm band, for which τ typically equals 0.7 for a midlatitude summer atmosphere.

The results may be compared to the values predicted by HASSE (1971). Using a mean solar irradiance at sea level $Q = 900\ W.m^{-2}$ in (1), ΔT is found to vary as $1.5\ U^{-1}$ (U in $m.s^{-1}$). This formula is shown in Fig. 5 and when compared to HCMM observations, gives a systematic overestimation of the diurnal heating fo $U < 3\ m.s^{-1}$. Elsewhere, the HASSE formula does not respect a limit value of ΔT when $U = 0$. As pointed out by HASSE, the results of the model given in (1) can not be applied to the lower wind speed range because the model used by HASSE refers to a steady state assumption not respected by scales of a few hours.

III-3 - Limit value of the diurnal heating

Fig. 5 and other HCMM scenes with large diurnal heatings indicate that diurnal heatings do not exceed about 5 °C, and that a limit value should exist at low wind speed. This value may be obtained by solving the heat transfer equation :

$$\frac{d}{dz}\left(k(z)\ \frac{dT(z,t)}{dz}\right) + \frac{dF(z,t)}{dz} = \rho c\ \frac{dT(z,t)}{dt} \qquad (3)$$

for $k(z) = k_m$, the thermal molecular conductivity of seawater - i.e no turbulent diffusivity is assumed at $U = o$. Eq. (3) was solved using the following conditions :

$$F(z,t) = F(o,t)\ g(z) - F_o \qquad (4)$$

where F(o,t) is the solar irradiance at sea level, F_o the heat loss by the surface, and

$$g(z) = \sum a_i \exp(-k_i z) \qquad (5)$$

where a_i, k_i are given in Table 1 and were obtained from a fit of g(z) according to the work of PRUVOST (1975). g(z) is considered independent of time in (4) which is a rather good approximation since the underwater penetration of the direct solar radiation is close to the nadir even at low solar elevation angles. A homogeneous layer was assumed to exist just below the surface. The depth z_o of this layer is defined similarly to the model of KRAUS and TURNER (1967) : the variation of potential energy produced by solar radiation and surface heat loss is equal to the work of the wind stress on the sea surface, i.e. nul for this study case where we look for a limit value of ΔT at U = o. Under these conditions, ΔT variance correlated well with the net heat budget of the surface :

$$\Delta T_{max} = C \int_o^{t_o} (F(o,t) - F_o)\, dt \qquad (6)$$

where $C = 0.65.10^{-6}$ $K.J^{-1}$ m^2. For the HCMM observations or June 3, 1978, $\frac{1}{t_o}\int_o^{t_o} (F(o,t) - F_o)\, dt$ was estimated to be a mean value of about 600 $W.m^{-2}$, over a period of 4 hours (in fact a maximum value of 900 $W.m^{-2}$ at noon at satellite overpass) and we found :

$$\Delta T_{max} = 5.6\ ^{\circ}C \qquad (7)$$

This value is in agreement with the observations reported in Fig. 5. At the lower wind speed, the observed diurnal heating is widely scattered with in the range of $2 < \Delta T < 4$ °C, and thus below the estimated limit value. The large variations of the observed ΔT at $U \approx 0$ may be explained by the fact that Eq. 6 requires a nul wind speed during the entire heating period preceeding the observation, i.e. several hours, which is very unlikely. The scatter of the diurnal heating at $U \approx 0$ therefore is probably linked to the time variations of the local wind speed.

III-4 - Frequency of diurnal heating

From May 13 to August 28, 1978, 60 HCMM scenes taken over the Western Mediterranean Sea were examined of which about 34 scenes exhibited large (typically more than 1 °C) diurnal heating of particular areas of 10 to 100 km width. Relative frequency of the event is rather large, and is enhanced in some areas which are affected by a breeze effect and where the wind systematically becomes nul at some distance from the coast. Table 2 gives relative frequencies of low wind speeds ($U < 3$ m.s^{-1}) at some stations along the Coast of France during the summer months (from DARCHEN (1974)). The frequency of nul wind allowing a diurnal heating of more than 1 °C is between 10 and 30 %. The frequency of low wind speed ($1 < U < 3$ m.s^{-1}) is from 20 to 50 %, allowing a diurnal heating of about 1 °C. From these frequencies, N_1 and N_2, a mean heating $\bar{\Delta T}$ was calculated as

$$\bar{\Delta T} = 2.5\ N_1 + N_2 \qquad (8)$$

and is also given in Table 2. The mean diurnal heating ranges from 0.5 to 1.5 °C along the south coast of France with a maximum on the French Riviera (Cap Ferrat).

IV - CONCLUSION

The present investigation, using SST satellite observations from the HCMM experiment has shown a high frequency of large diurnal heatings (more than 1 °C) of the sea surface during summer months in such areas as the Mediterranean Sea where low wind speeds are very frequent. This shows that satellite observations made at noon and during the afternoon should be rejected, or at least checked to eliminate those corresponding to low wind speed ($U < 3$ m.s^{-1}). If not, a systematic bias could be introduced in the SST analysis of some areas, particularly the marine coastal areas affected by a sea-land breeze effect.

Using simultaneous observations of the glitter reflectance, the diurnal heating was correlated to the wind speed. Diurnal heatings of about 0.8 °C were found for $U \approx 2$ m.s^{-1}, which is two time less than the formulation given by HASSE (1971). A maximum diurnal heating of 5 °C is found for nul wind conditions, which is in agreement with the value calculated from the radiative and heat transfer equations assuming the thermal diffusivity is only molecular.

APPENDIX

Glitter refers to direct solar radiation reflected by the sea surface. This reflection is specular for a planar surface. When there is wind, the surface is agitated and consists of elements which are statistically distributed around the horizontal plane. This produces a more or less bright spot of variable dimensions which is commonly called glitter.

The radiance L_g reflected by the agitated sea surface can be expressed (COX and MUNK, 1956)

$$L_g = \frac{E_s}{4} \frac{R(\omega)}{\mu_v \mu_n^4} p \qquad \text{(A-1)}$$

and the equivalent reflectance ρ_g will be expressed as

$$\rho_g = \frac{\pi L_g}{\mu_s E_s} = \frac{\pi}{4} \frac{R(\omega)}{\mu_s \mu_v \mu_n^4} p \qquad \text{(A-2)}$$

where E_s is the direct solar radiation at sea level,

$R(\omega)$ is the reflection coefficient of water at a given indicence ω,

p is the probability of encountering a properly oriented surface element,

$\mu_v = \cos\theta_v$, $\mu_s = \cos\theta_s$, $\mu_n = \cos\theta_n$, respectively define the zenithal angles of the observation direction, the direction of incidence,

p is the probability of encountering a properly oriented surface element,

$\mu_v = \cos\theta_v$, $\mu_s = \cos\theta_s$, $\mu_n = \cos\theta_n$, respectively define the zenithal angles of the observation direction, the direction of incidence, and their bisector,

ϕ is the angle between the incidence and observation planes :

$$\mu_n = \frac{\mu_s + \mu_v}{2\cos\omega} \qquad \text{(A-3)}$$

$$\cos 2\omega = \mu_s \mu_v + \left(1-\mu_s^2\right)^{\frac{1}{2}}\left(1-\mu_v^2\right)^{\frac{1}{2}}\cos\varphi \qquad \text{(A-4)}$$

From a study of aerial photographs of glitter patterns, COX and MUNK (1954) developped p in a Gram Charlier series which in a first approximation is reduced to a gaussian distribution, with revolution symmetry :

$$p = \frac{1}{\pi\sigma^2}\ \exp -\frac{(\operatorname{tg}\Theta_n)^2}{\sigma^2} \qquad \text{(A-5)}$$

with $\sigma^2 = 0{,}003 + 5{,}12.10^{-3}U_{m.s^{-1}} \pm 0{,}004$ (A-6)

for $1 < U < 14\ m.s^{-1}$.

Figure 6 gives an example of the glitter spot ρ_g thus computed as a function of solar zenithal angle for different values of W, and for a nadir viewing ($\Theta_v = 0$). In accordance with the reciprocity principle, by permutation (Θ_s, Θ_v), Fig. 6 also gives ρ_g as a function of the observation angle, for a sun at the zenith ($\Theta_s = 0$). For a given angle ρ_g presents a maximum, ρ_{gm}, at a certain value of σ_m which is related to wind speed. σ_m and ρ_{gm} are given by :

$$\sigma_m^2 = \operatorname{tg}^2\Theta_n = \mu_n^{-2} - 1 \qquad \text{(A-7)}$$

$$\rho_{gm} = \frac{R(\omega)}{4\ \mu_s\mu_v\mu_n^2\ (1-\mu_n^2)} \qquad \text{(A-8)}$$

The dashed curve in Fig. 6 envelops the preceding curves and represents the maximum glitter ρ_{gm} as defined by (A-8).

ACKNOWLEDGEMENTS

HCMM data have been received from NASA as a support to HCMM Investigation No 15. Thanks to L.F. MARTIN for his aid in the translation. Support for this work has been provided by the following French agencies : C.N.R.S. (Centre National de la Recherche Scientifique) and C.N.E.S. (Centre National d'Etudes Spatiales).

REFERENCES

COX, C.S., and W.H. MUNK, 1954 : Measurement of the roughness of the sea surface from photographs of the sun's glitter. J. Opt. Soc. Amer., 44, 838-850.

COX, C.S., and W.H. MUNK, 1956 : Slopes of the sea surface deduced from photographs of sun glitter. Bull. Scripps Inst. Oceanogr., 6, 401-488.

DARCHEN, J., 1974 : Eléments climatologiques concernant les côtes de la France métropolitaine. Monographie n° 93, Météorologie Nationale (77 rue de Sèvres, 92100 Boulogne Billancourt, France).

HASSE, L., 1971 : The sea surface temperature deviation and the heat flow at the sea-air interface. Boundary-Layer Meteor., 1, 368-379.

KRAUS, E.B., and J.S. TURNER, 1967 : A one-dimensional model of a seasonal thermocline. II - The general theory and its consequences. Tellus, 19, 98-105.

LA VIOLETTE, P.E., S. PETEHERYCH and J.F.R. GOWER, 1980 : Oceanographic implications of features in NOAA satellite visible imagery. Boundary-Layer Meteor., 18, 159-175.

PRIVOST, P., 1975 : Etude du flux solaire et de l'echauffement radiatif dans la mer par temps clair. Ann. Hydrogr., 3, 25-34.

ROMER, J., 1969 : Variations de la température de surface de la mer au voisinage de la surface. Note EERM n° 262, Météorologie Nationale (77 rue de Sèvres, 92100 Boulogne Billancourt, France).

STOMMEL, H., K. SAUNDERS and J. COOPER, 1969 : Observations of the diurnal thermocline. Deep-Sea Res., Suppl. 16, 269-284.

FIGURE CAPTIONS

Figure 1 - Diurnal heating in the Western Mediterranean Sea :

(a) - Day HCMM scene A-A0038-12440 on June 3, 1978 at 12.44 TU. Image center is at 40.54°N, 011.04°E. Visible channel : darker tones are lower reflectances. Note the bright patterns East and West of Corsica and Sardinia.

(b) - Same as (a) but infrared channel : darker tones are colder surface temperatures. Note warmer waters East and West of Corsica and Sardinia.

(c) - Night HCMM scene A-A0038-01490 on June 3, 1978 at 1.49 TU. Infrared channel : darker tones are colder temperatures.

(d) - Day-night temperature differences between HCMM scenes obtained on June 3, 1978 at 1.49 TU (night) and 12.44 TU (day). Darker tones are smaller diurnal heatings.

(e) - Meteorological situation on June 3, 1978 at 12.00 TU.

Figure 2 - Diurnal heating in the North Sea :

(a) - Day HCMM scene A-A0034-13120 on May 30, 1978 at 13.12 TU. Image center is at 54.27°N, 00.01°E. Infrared channel : darker tones are colder waters. Note the warm (bright) spot between Scotland and the top right of the image where a thermal front is shown close to Norway.

(b) - Night HCMM scene A-A0035-02280 on May 31, 1978 at 2.28 TU. Image center is at 56.13°N, 03.00°E. Infrared channel : darker tones are colder waters. The warm spot disappeared during the night.

(c) - Meteorological situation on May 30, 1978 at 12.00 TU.

Figure 3 - Day-night temperature difference vs glitter reflectance on June 3, 1978, for a study area East of Sardina.

Figure 4 - Retrieved wind speed vs glitter reflectance for the study area.

Figure 5 - Day-night temperature difference vs retrieved wind speed for the study area. The solid-dashed line shows the diurnal heating obtained from HASSE (1971), which is valid only at $U < 2$ m.s^{-1}.

Figure 6 - Glitter reflectance vs zenithal viewing angle, for a sun at zenith, and several wind speeds from 0 to 15 m.s^{-1}. Maximum glitter reflectance is given by a dashed line.

Table 1 - Coefficients a_i, k_i in (5) for water penetration by solar irradiance.

	a_i	k_i (m^{-1})
i = 1	.041	3365.9
i = 2	.139	201.18
i = 3	.211	13.05
i = 4	.24	1.22
i = 5	.37	.07

Table 2 - Relative frequencies of low wind speeds :

N_1 : nul ; N_2 : Beaufort forces 1 and 2 ($1 < U < 3$ m.s^{-1}), during June, July and August in the French Mediterranean coastal area, (DARCHEN, 1974). An estimate of the mean diurnal heating $\bar{\Delta T}$ is given in column (3).

Station	N_1 %	N_2 %	$\bar{\Delta T}$ °C
Cap Bear	16.0	26.9	0.67
Sète	9.5	42.3	0.66
Panègues	21.3	26.8	0.80
Cap Camarat	10.8	46.6	0.74
Cap Ferrat	35.1	50.4	1.38
Cap Corse	18.4	35.5	0.82
Pertusato	6.4	21.0	0.37
42° N-6E	7.6	/	

ORIGINAL PAGE
BLACK AND WHITE PHOTOGRAPH

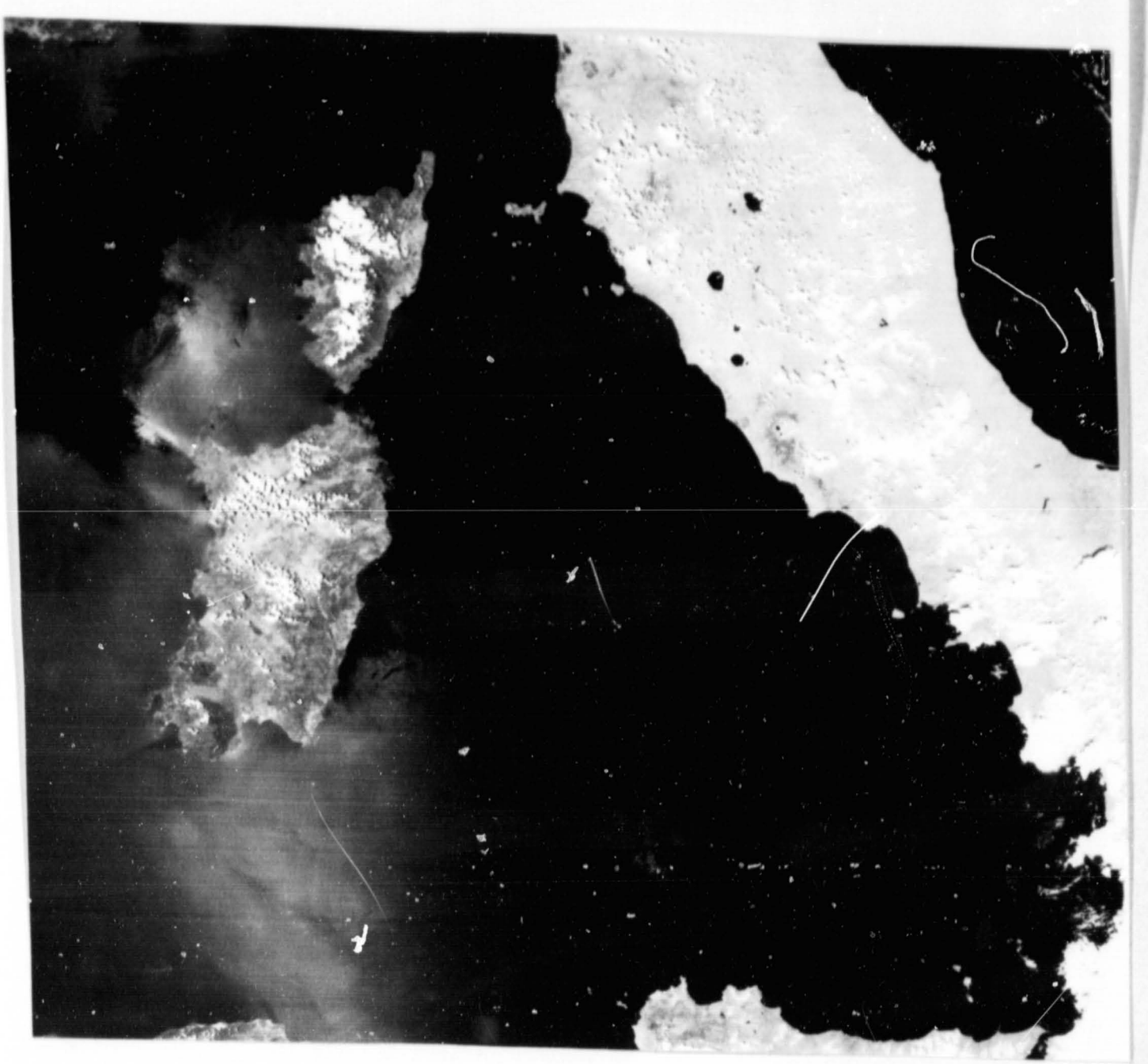

Figure 1 - (a) - Day HCMM scene A-A0038-12440 on June 3, 1978 at 12.44 TU. Image center is at 40.54°N, 011.04°E. Visible channel : darker tones are lower reflectances. Note the bright patterns East and West of Corsica and Sardinia.

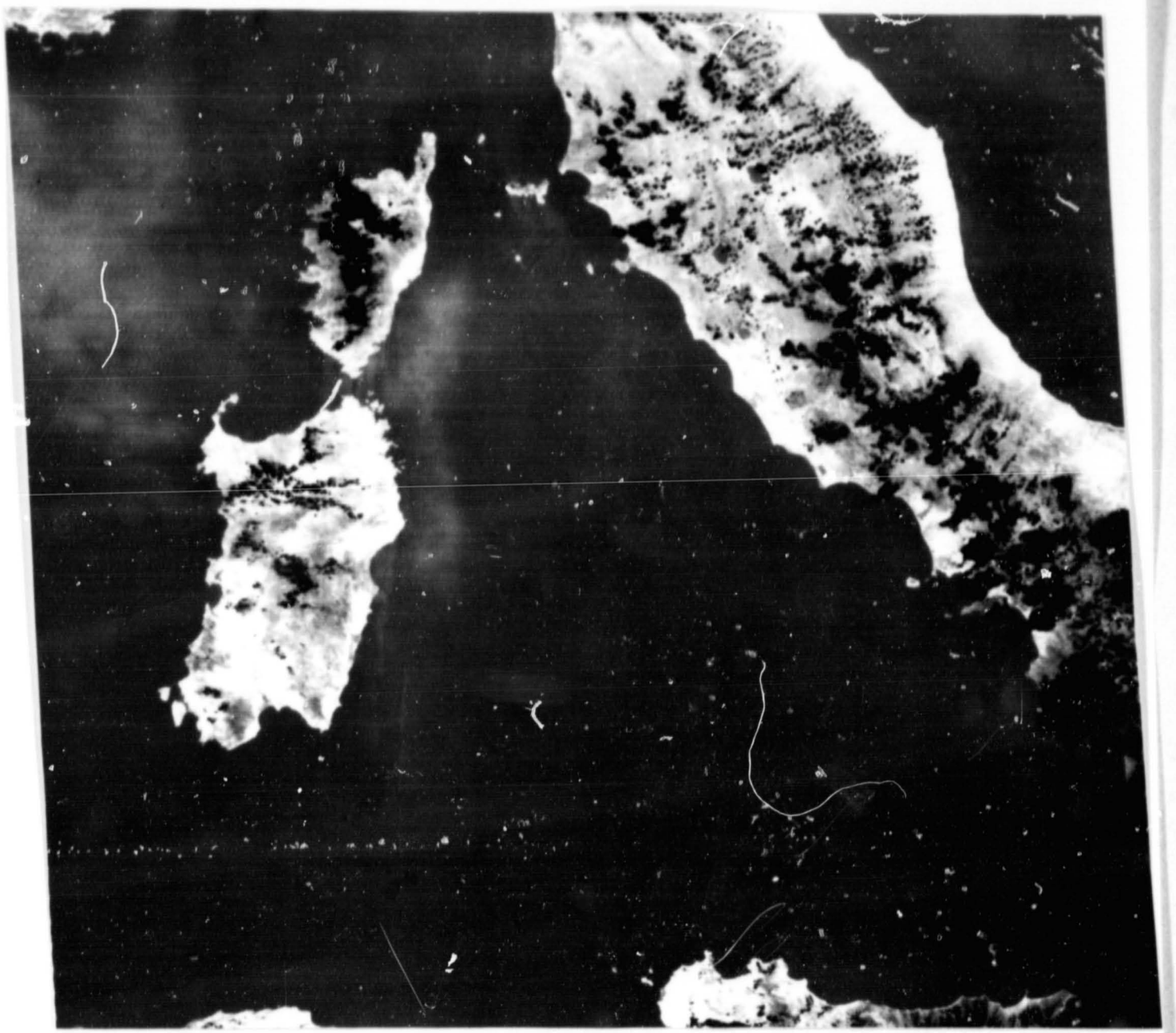

Figure 1 - (b) - Same as (a) but infrared channel : darker tones are colder surface temperatures. Note warmer waters East and West of Corsica and Sardinia.

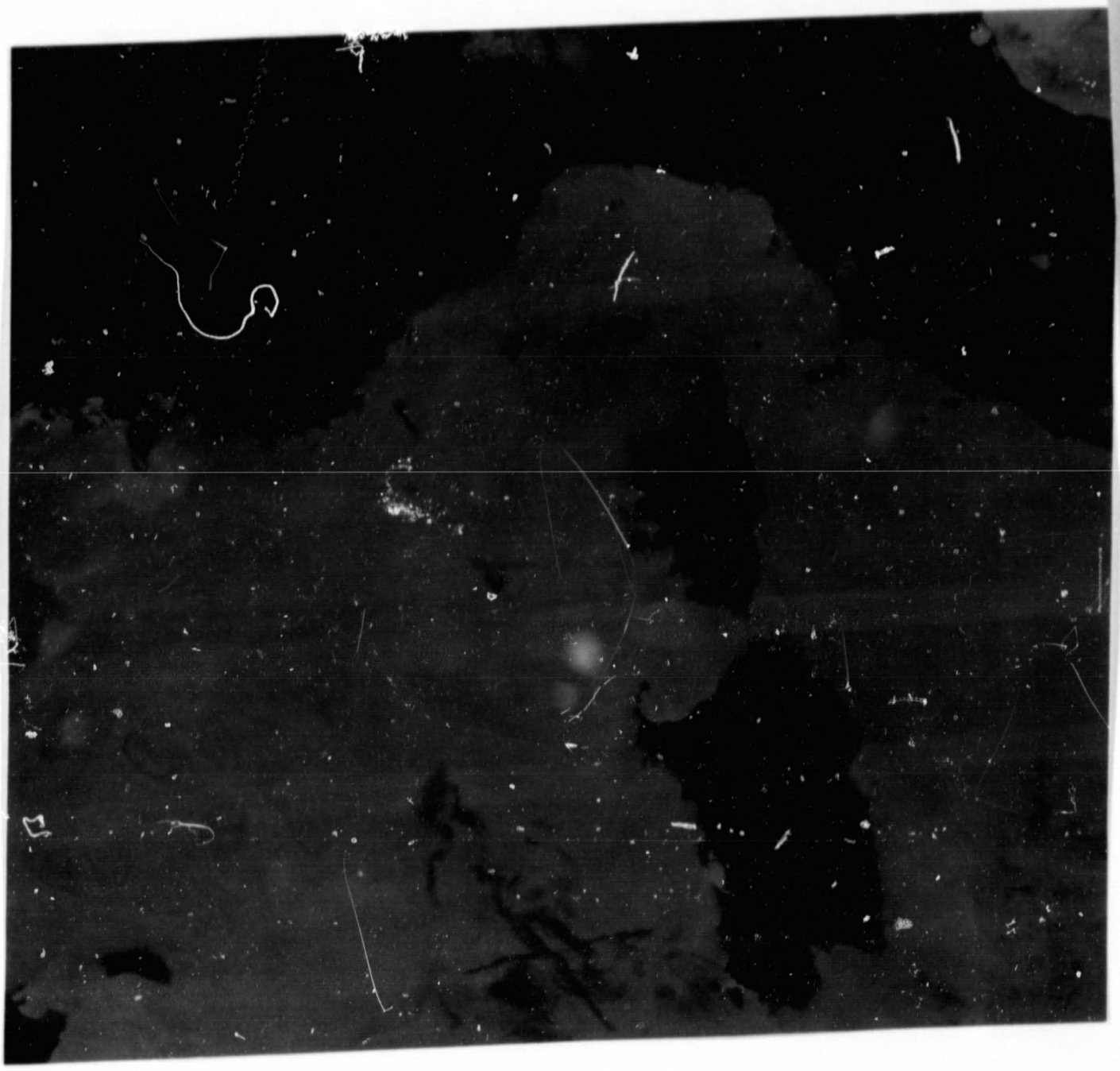

Figure 1 - (c) - Night HCMM scene A-A0038-01490 on June 3, 1978 at 1.49 TU.

Darker tones are colder temperatures.

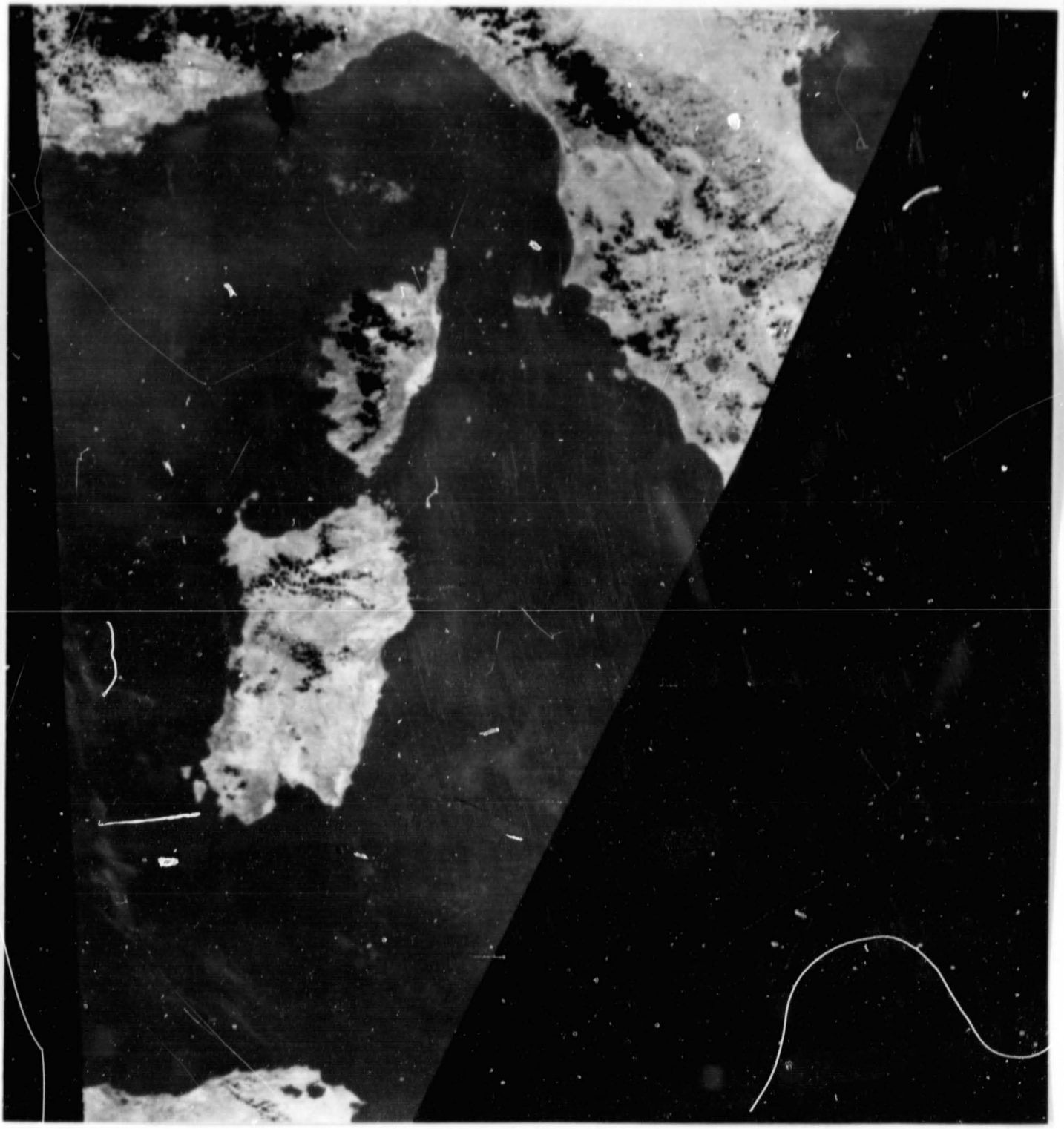

Figure 1 - (d) - Day-night temperature differences between HCMM scenes obtained on June 3, 1978 at 1.49 TU (night) and 12.44 TU (day. Darker tones are smaller diurnal heatings.

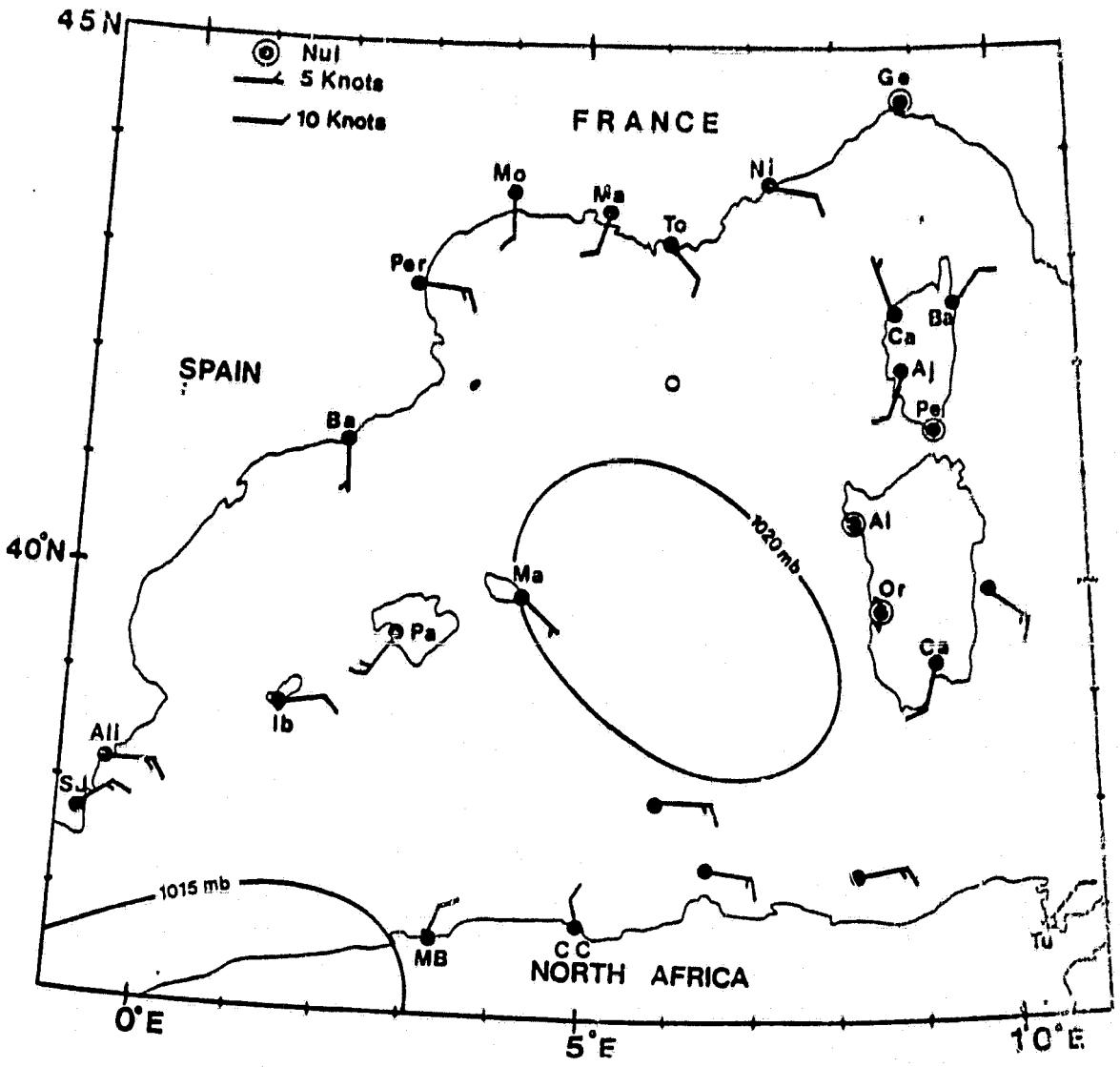

Figure 1 - (e) - Meteorological situation on June 3, 1978 at 12.00 TU.

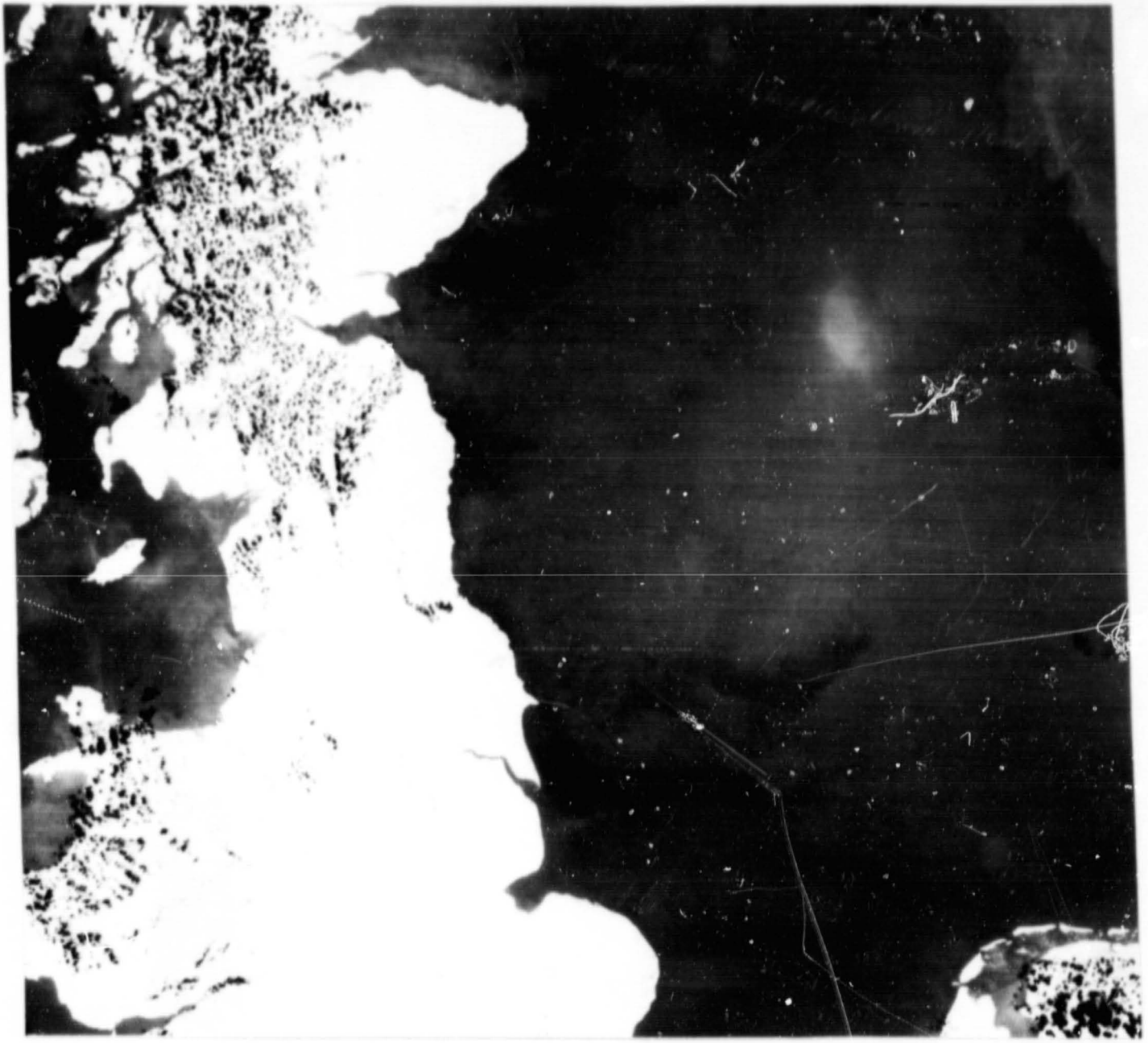

Figure 2 - (a) - Day HCMM scene A-A0034-13120 on May 30, 1978 at 13.12 TU. Image center is at 54.27°N, 00.01°E. Infrared channel : darker tones are colder waters. Note the warm (bright) spot between Scotland and the top right of the image where a thermal front is shown close to Norway.

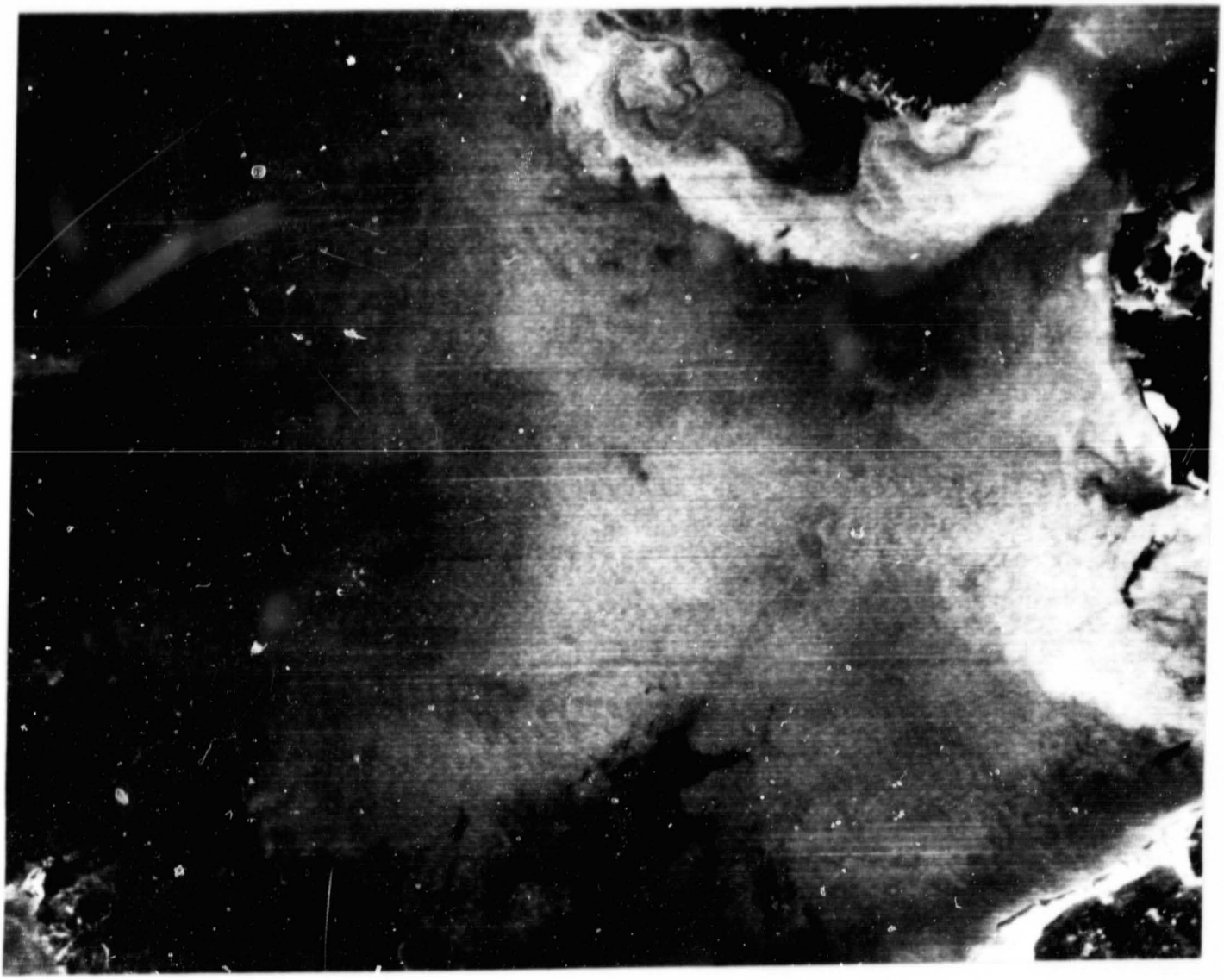

Figure 2 - (b) - Night HCMM scene A-A0035-02280 on May 31, 1978 at 2.28 TU. Image center is at 56.13°N, 03.00°E. Infrared channel : darker tones are colder waters. The warm spot disappeared during the night.

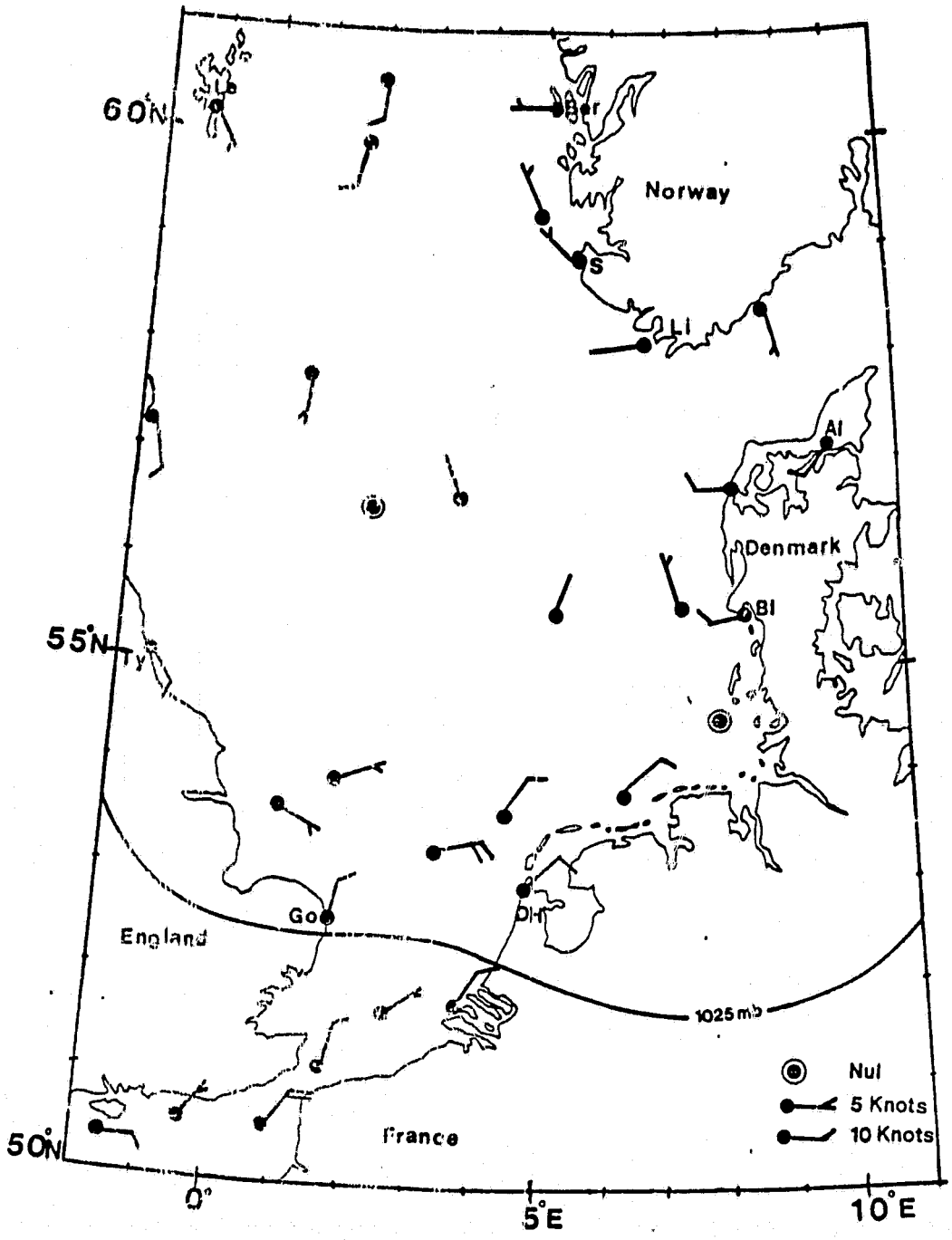

Figure 2 - (c) - Meteorological situation on May 30, 1978 at 12.00 TU.

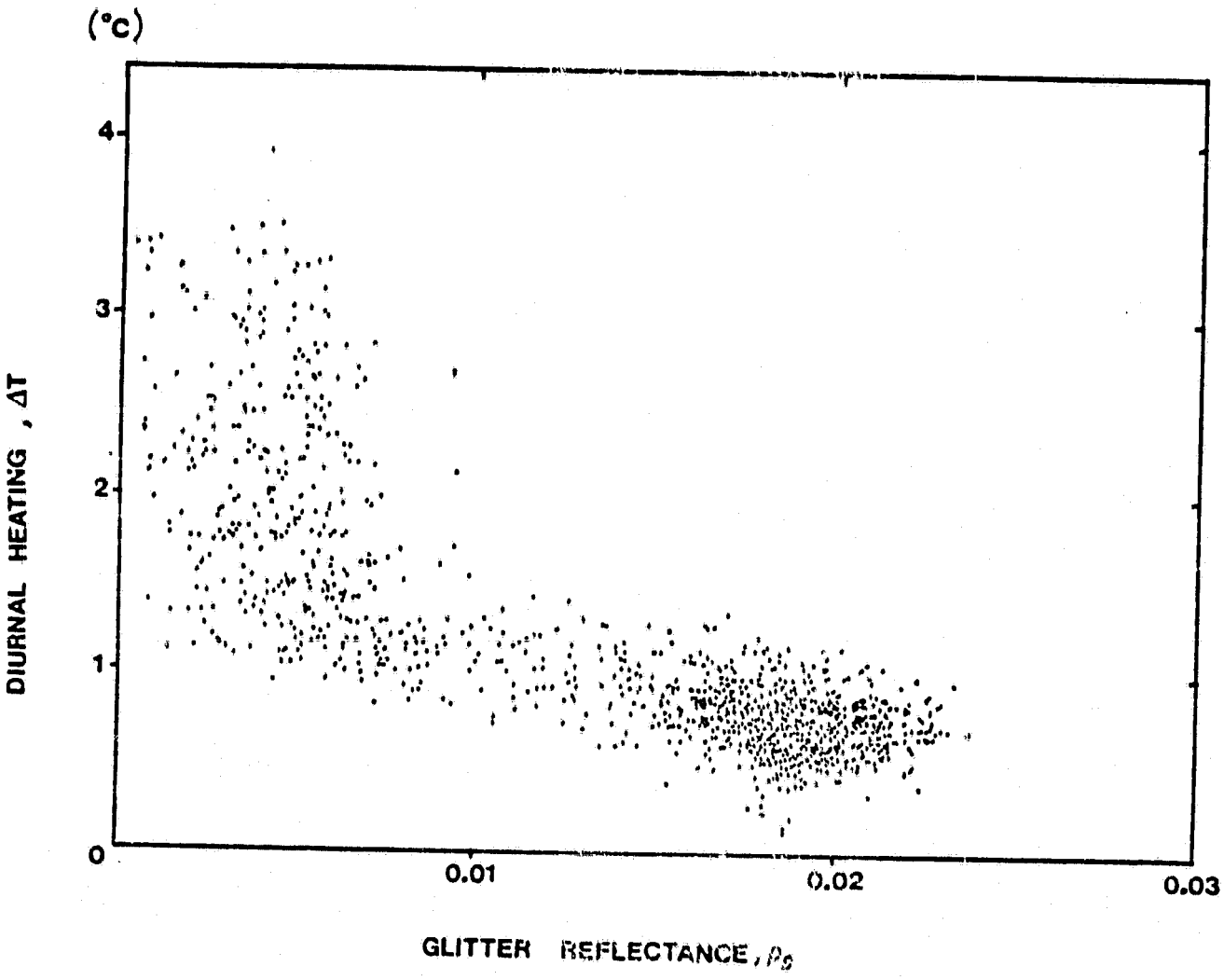

Figure 3 - Day-night temperature difference vs glitter reflectance on June 3, 1978, for a study area east of Sardinia.

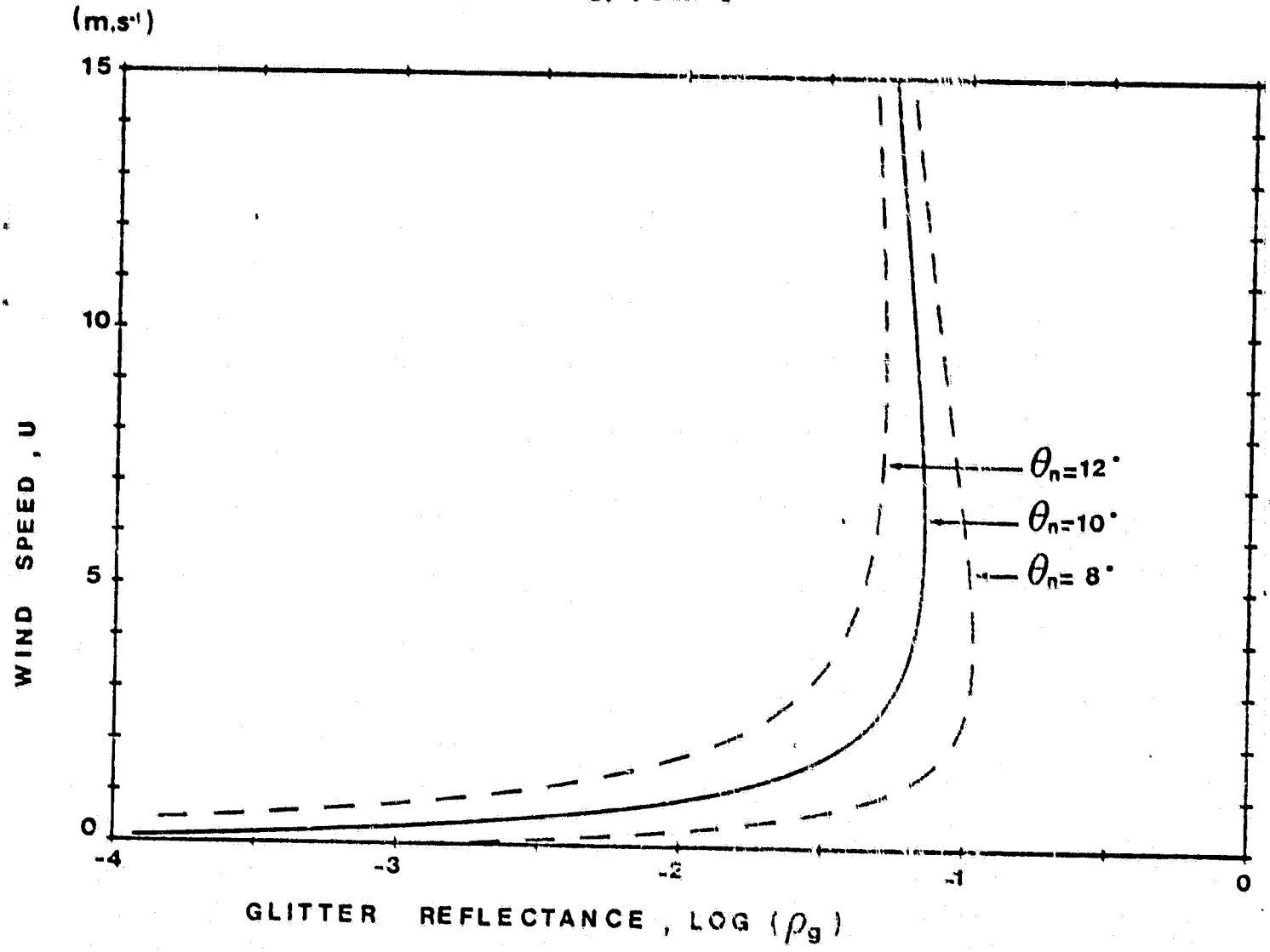

Figure 4 - Retrieved wind speed vs glitter reflectance for the study area.

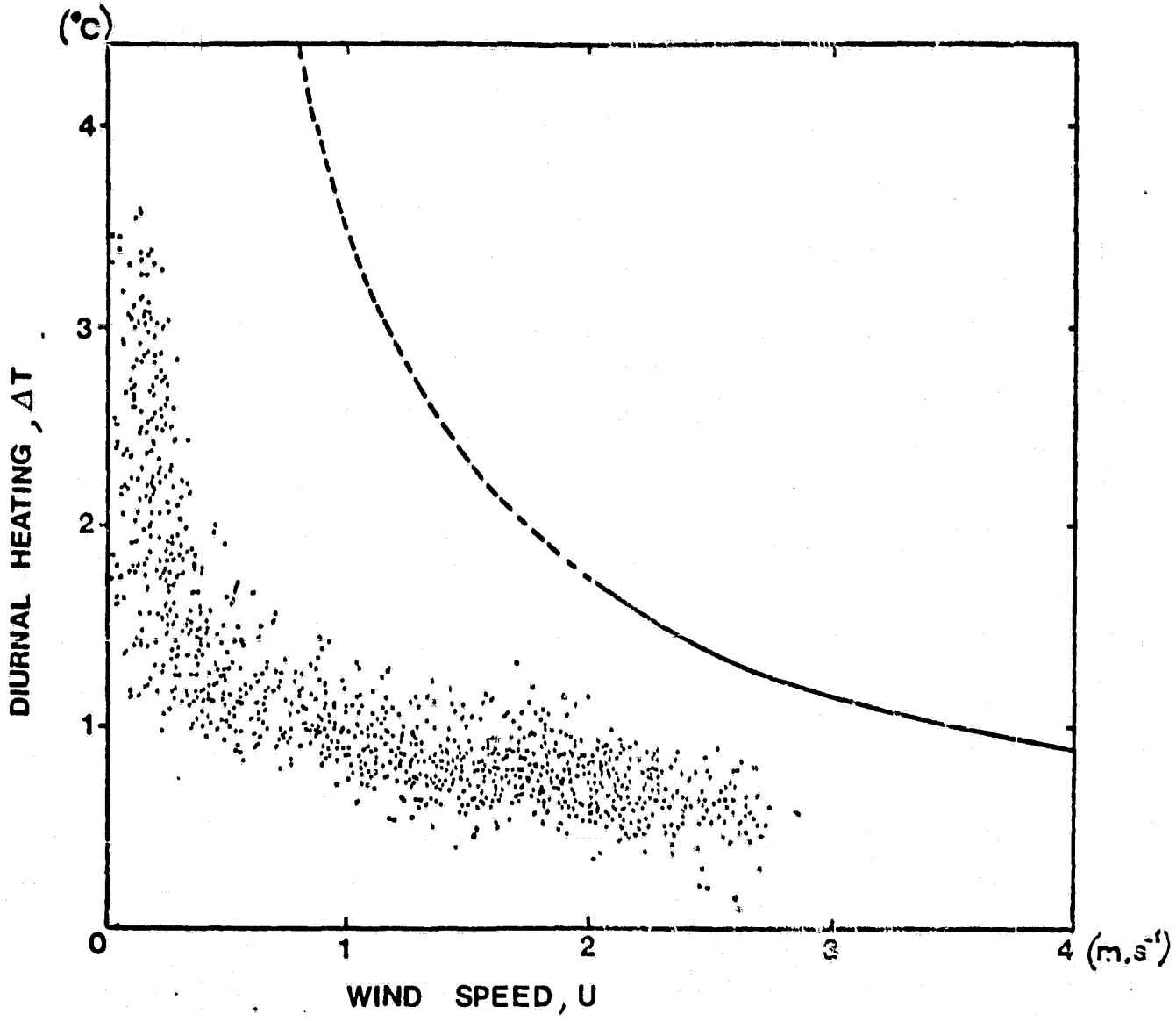

Figure 5 - Day-night temperature difference vs retrieved wind speed for the study area. The solid-dashed line shows the diurnal heating obtained from HASSE (1971), which is only valid at $U < 2$ m.s^{-1}.

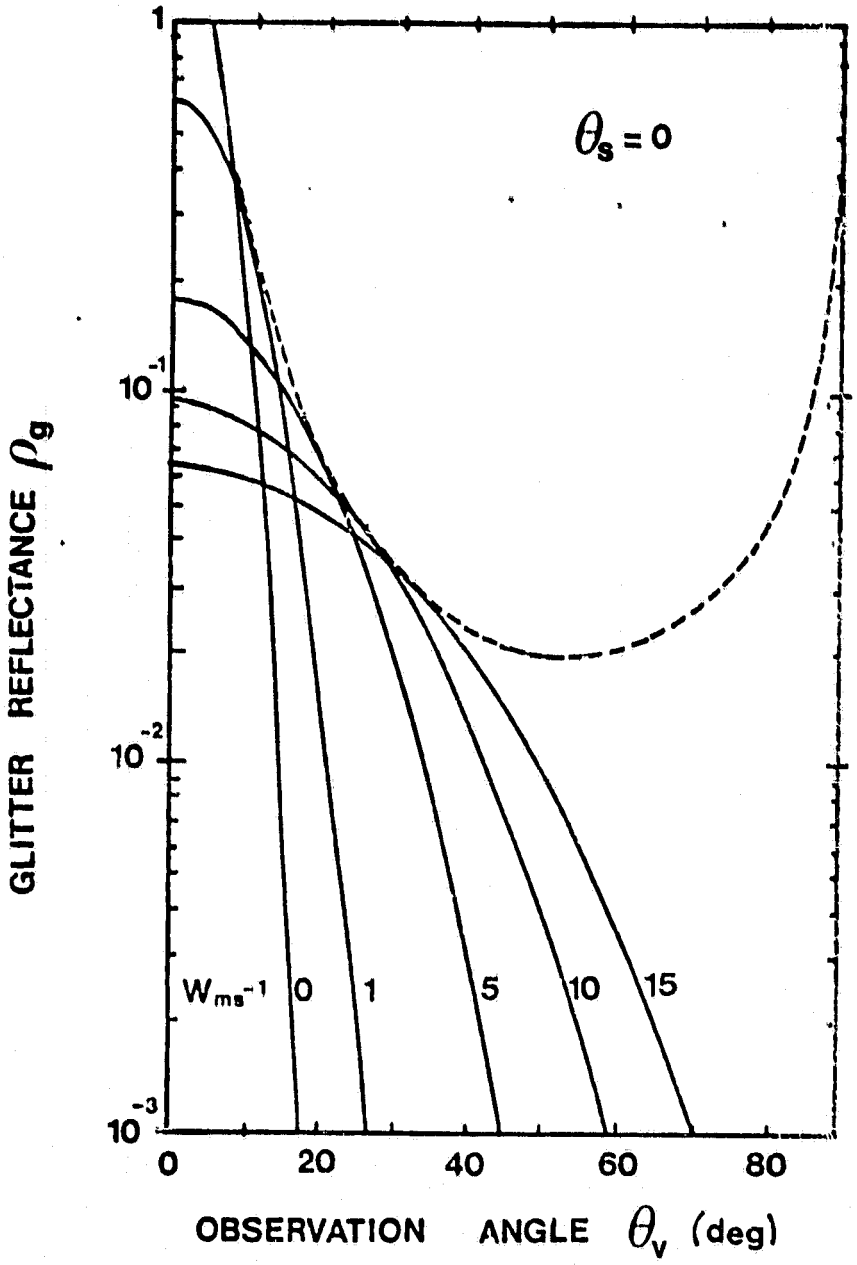

Figure 6 - Glitter reflectance vs zenithal viewing angle, for a sun at zenith, and several wind speeds from 0 to 15 $m.s^{-1}$. Maximum glitter reflectance is given by a dashed line.

Appendix F

SATELLITE EVIDENCE OF COLD WATER AREAS NEAR ISLANDS ALONG THE SOUTH BRITTANY SHORE

J. CASSANET

Laboratoire de Géographie de l'Ecole Normale Supérieure,
1, rue Maurice Arnoux, 92120 MONTROUGE, FRANCE.

ABSTRACT

From HCMM digital products processed at ENS, five scenes of high quality were selected for study because of their clear resolution of cold water areas around islands and shoals along the south Brittany shore. Tidal currents that induce turbulence in shallow depths and destroy the seasonal thermocline are responsible for the well-mixed cold coastal water that is separated from the warmer stratified offshore water by a transitional zone of high thermal gradient. Satellite measurements are compatible with ground truth data analysis.

I INTRODUCTION

Infrared satellite imagery (spectral band 10,5 µm - 12,5 µm)has been used to provide sea surface thermographies. For example, the HCMM and NOAA 5 imagery enabled the detection of the Ushant front which subsequently became the basis of various studies because of its importance in the distribution of phytoplancton.

The spatial and thermal resolution of the HCMM thermographies is more refined than that of the NOAA 5 thus providing better images of the frontal regions in the shallow shelf water along the coast of Brittany.

The thermal structure of these shallow coastal waters is not yet well-known. Cold water areas and high thermal gradients near reefs, shoals and Islands in the shelf region of the Bay of Biscay appeared several times in HCMM data. These areas are typified by their shapes and dimensions.

In this paper, they are described in relation to hydrological and meteorological conditions, and possible interpretations according with other observations are suggested.

II DATA ANALYSIS

Several HCMM photographic products (from May 1978 to November 1978) were studied because of their clear presentation of the existence and development of thermal boundaries and cold water areas. Due to the broad range in the dimensions of such phenomena (50 to 1000 square kilometers), digital products processing was applied.

Five scenes, to the area between Belle Ile, Yeu Island, and the Loire estuary, were selected for an in-depth study :

06/10/78	:	A-A0045-13160-2	: Day IR
08/19/78	:	A-A0115-02180-3	: Night IR
08/31/78	:	A-A0127-13380-2	: Day IR
09/15/78	:	A-A0142-13190-2	: Day IR
10/28/78	:	A-A0185-13180-2	: Day IR

Geometric correction, resampling for uniform scaling (1/500 000), and smoothing were applied to them before automatic sea surface temperature cartography. Results are given for three scenes in figures 1,2, and 3.

III HYDROLOGICAL AND METEOROLOGICAL CONDITIONS

HCMM scenes were registered from June to October 1978. During this period, the flow of the Loire river was not very strong. It fell from 800 m^3.s (06/10/1978) to 250 m^3/s during summer and autumn months. This last value is very weak considering that in the winter, the flow of the Loire can exceed 5000 m^3/s. Thus in all five cases, the influence of the river flow was trivial in comparison to the tidal stream, and could be neglected.

In the Bay of Biscay shelf region, the presence of bottom stress modifies direction and velocity of tidal currents. Thus the role of bathymetry in the dynamics of coastal currents is very important. For example, velocities near the shore are : 3 to 4 knots in the south of the "Presqu'île de Quiberon", in the "Passage de la Teignouse" ; 2 to 3 knots in the west of Noirmoutier island ; and 1 or 2 knots between Yeu island and Noirmoutier island. Spring to neap ratios vary from 1,6 to 2. The contribution by offshore tidal currents has not yet been established (about 0,5 to 1 knot between Belle Ile island and Yeu island) but should not be neglected.

In these five cases, meteorological conditions were very similar : Anticyclonic weather, high pressure, low pressure gradients, weak winds, low night-temperature, high day-temperature.

IV COLD WATER AREAS ; DESCRIPTION

On the five different scenes, two typical cold water areas can be seen :

- An important circular area east and north of Belle Ile Island in the "Passage de la Teignouse", and around Houat and Hoedic islands.
- The important area in the shape of an "S", between Yeu Island and Noirmoutier Island.

These two areas are surrounded by warm waters. We emphasize the similarity between the contouring of the cold water areas and the - 20 m isobath (see fig. 7).

FRACARTE - VERSION 1.1
LISSAGE 5x5 (2)
LIGNES 102 A 378 /1
COLONNES 102 A 338 /1
ECHELLE: 1/ 500000
REALISE EN NOVEMBRE 1980

Fig. 1 : Automatic cartography (06/10/78)
Sea surface temperature

IV.1 : 06/10/78 and 09/15/78

Thermal gradients near islands are important : 2°C/5 km. It is worth noting that the shapes of the cold water areas are very similar. However, the typical "S" which was very near Noirmoutier island on 09/15/78, one hour before high water (spring tide) is further off shore on 06/10/78, one hour after low water (neap tide). This corresponds to the dynamics of tidal currents which flow into the bay of Bourgneuf, north of the Noirmoutier island.

IV.2 : 08/19/78

The cold water area of Belle Ile island and the cold water area of Noirmoutier Island nearly join above shoals in front of the "Presqu'ile de Guérande". At the hour of the passage of the satellite pass occured during the high water of a spring tide (tidal coef : 1.06)

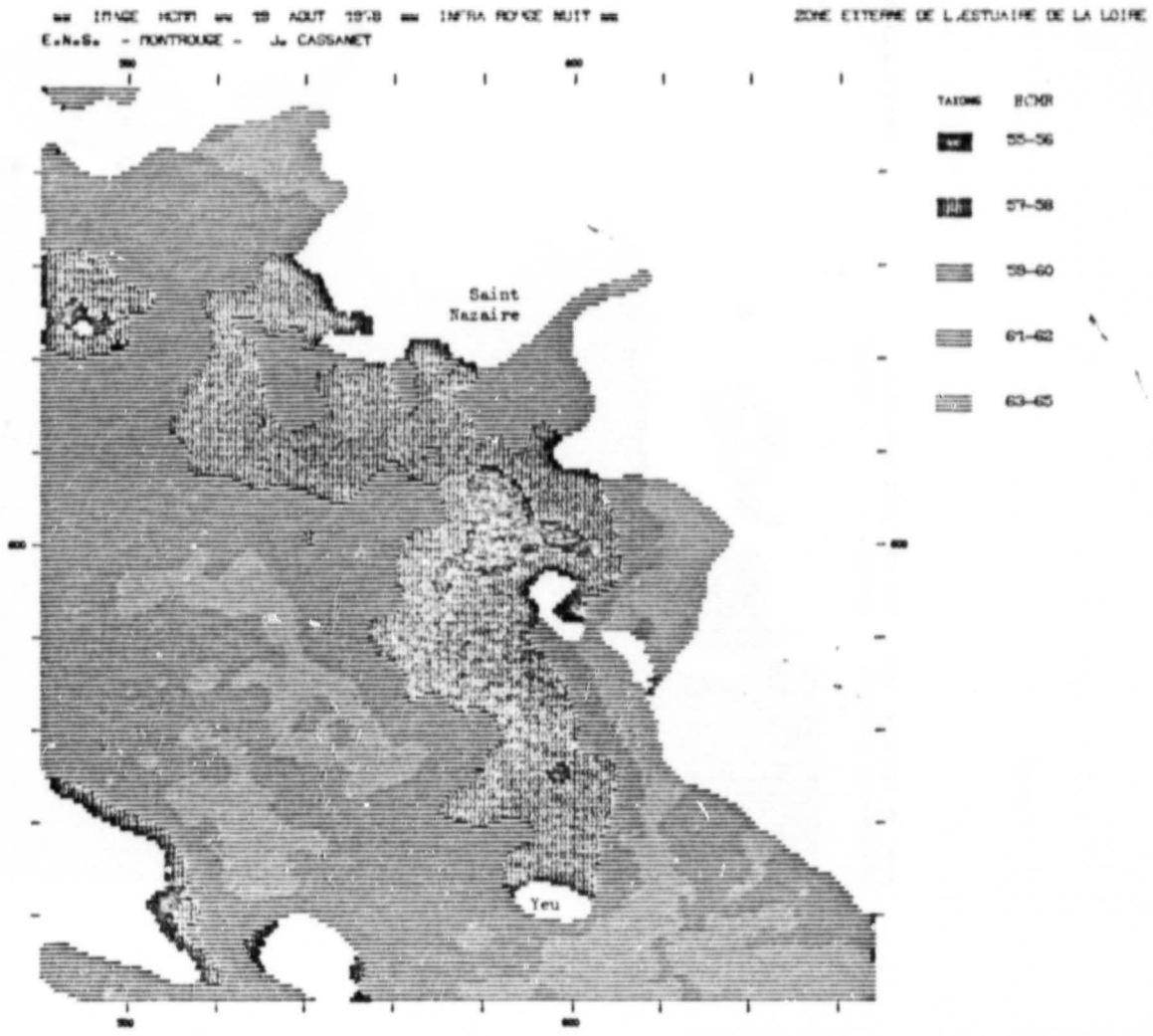

Fig. 2 : HCMM automatic cartography : sea surface temperature (08/19/78)

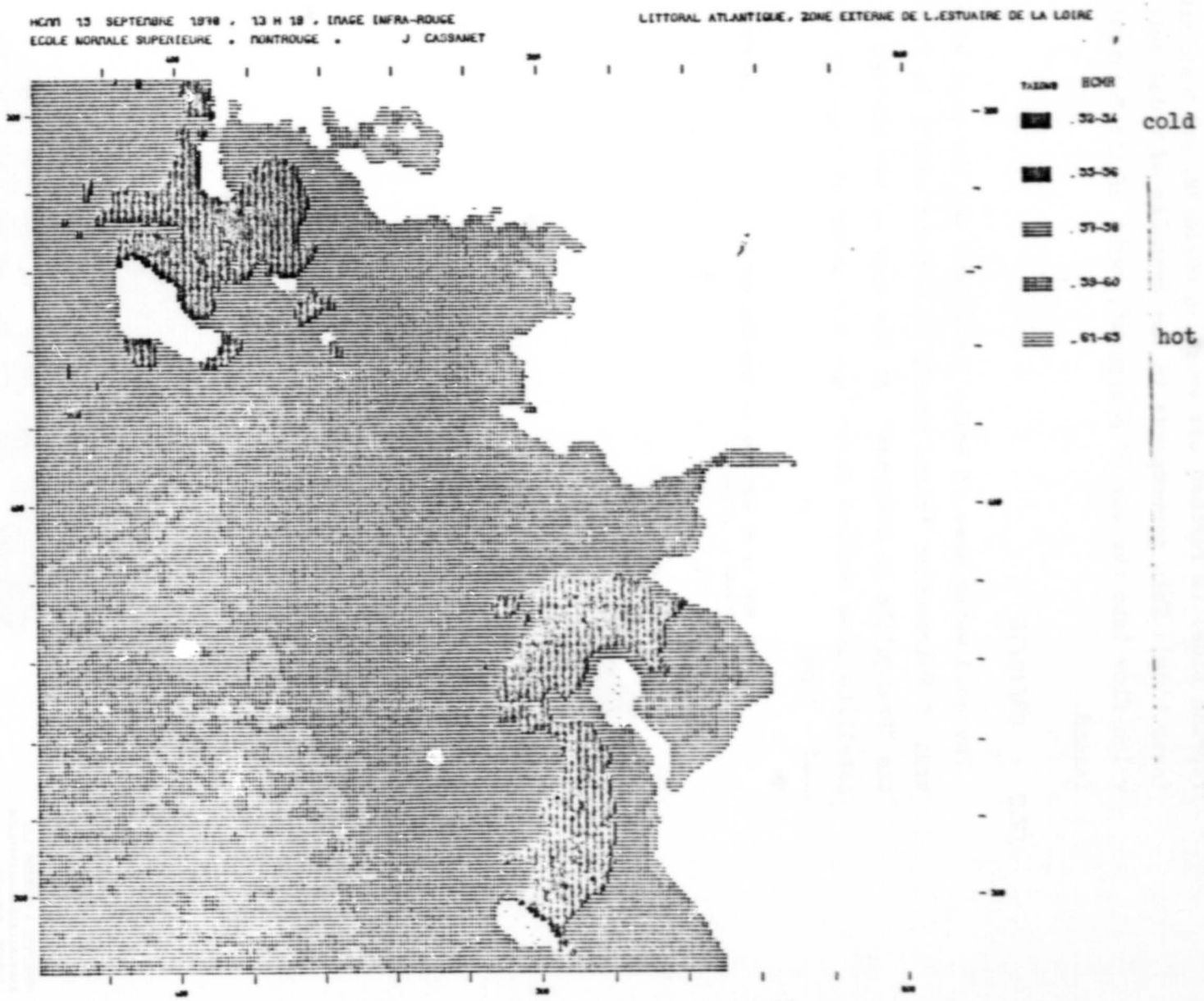

ORIGINAL PAGE IS
OF POOR QUALITY

F-6

Fig. 3 : Automatic cartography (09/15/78) Sea surface temperature

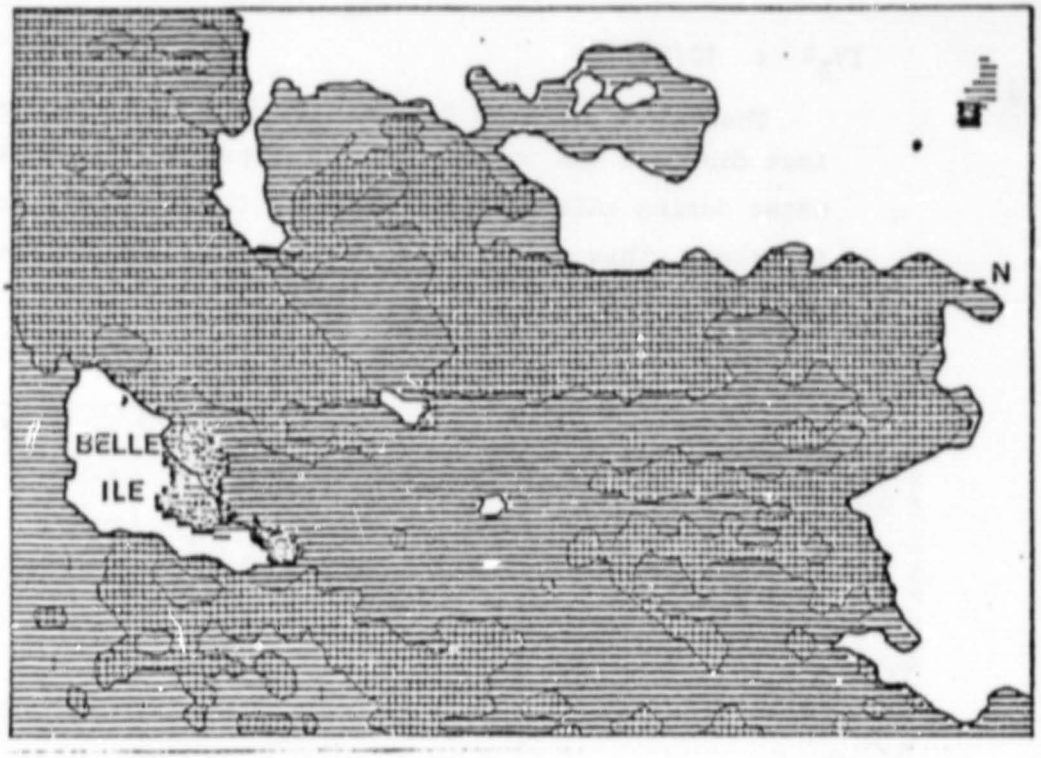

Fig. 4 : 08/31/78

Clouds over
Belle Ile

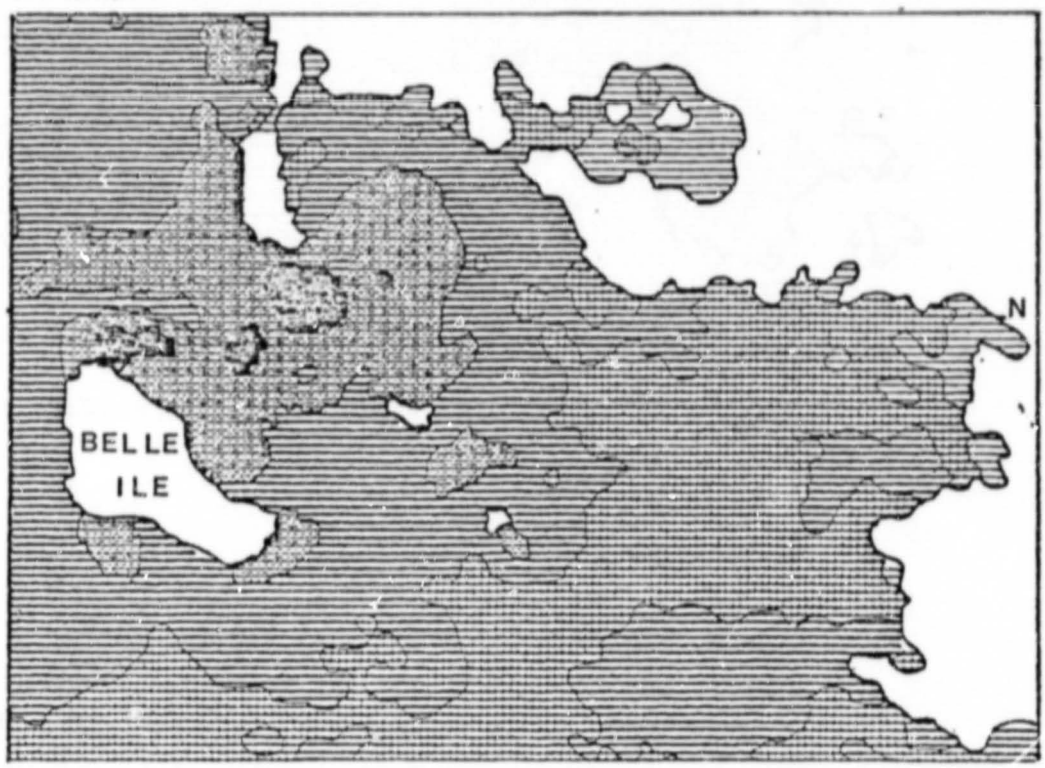

Fig. 5 : 09/15/78

IV.3 : 08/31/78 and 09/15/78

In both figures 4 and 5, the satellite pass occured approximately one hour prior to high water, but a difference appears in the tides :

08/31/78 : neap tides (coef. : 0,68)

09/15/78 : spring tides (coef. : 0,94)

Figures 4 and 5 show that cold water are particularly wide-spreading near islands during spring tides.

IV.4 : 10/28/78

Thermal structures are less visible and their contouring is less distinct due to the overriding presence of shallow coastal cold water during this season. However a thermal front is visible, parallelling the shore. This appears more clearly on HCMM pictures of Nov. 78 and Jan. 79.

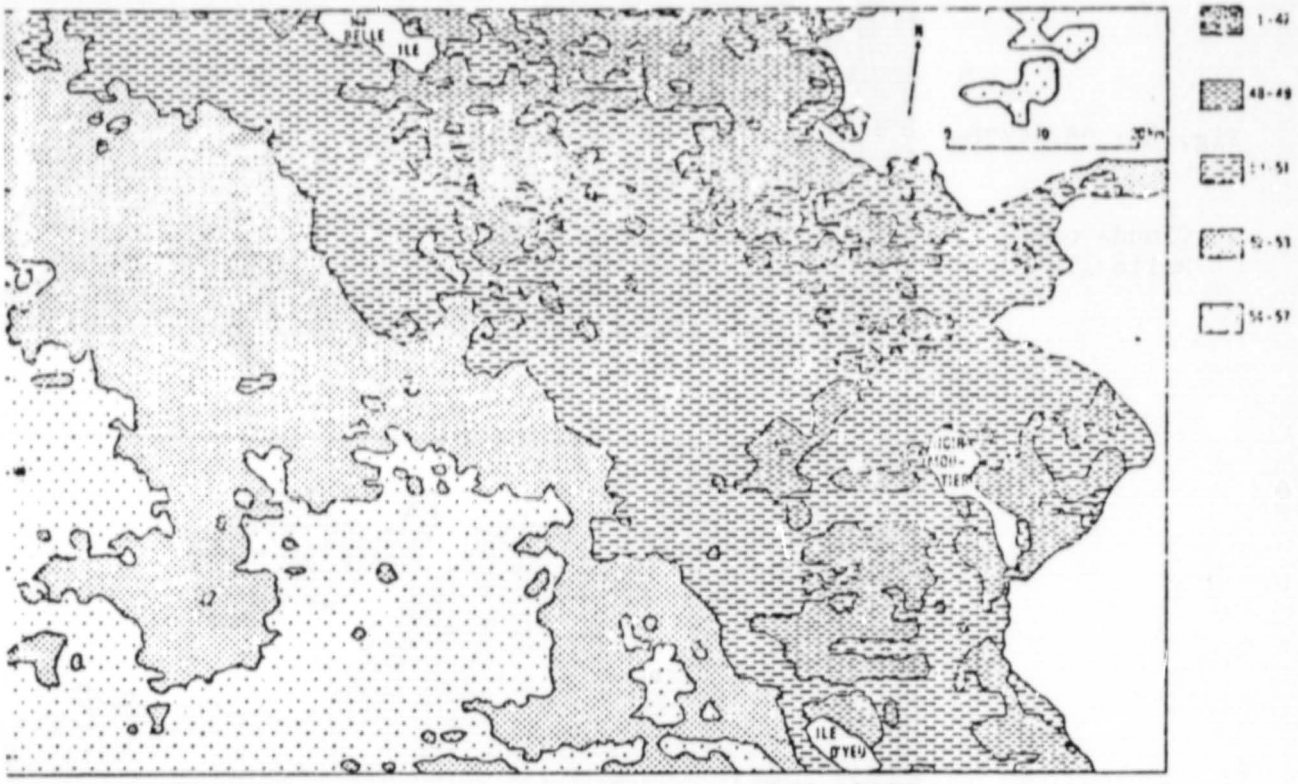

Fig. 6 : HCMM scene (10/28/78) ; sea surface temperature

V INTERPRETATION

Each studied scene shows that the contouring of cold water areas corresponds fairly well to the isobaths. These areas are situated in zones where tidal streams are important. The water depth and the current velocity have a fundamental part in spreading the cold water area.

Several authors have already emphasized the importance of tidal currents in the formation of thermal fronts separating two water masses with different temperatures, especially near shoals and islands (FEARNHEAD, 1974).

V.1 Formation of thermal fronts :

During spring and summer, in regions of sufficient depth and weak currents a seasonal thermocline is established offshore, separating warm sea surface waters and cold bottom waters.
In shallow waters more in shore, tidal currents create a turbulence which mixes the water column and presents the formation and development of the thermocline. It is for this reason that the sea surface temperature is colder in these shelf regions than it would be if thermocline existed.

The presence of this thermal front around British Isles, between stratified water and well mixed water has been studied by PINGREE and GRIFFITHS (1978). These authors have proposed a numerical model to determinate the position of the thermal fronts by the equation :

$S = \log \frac{h}{C_d u^3}$, where : h is the water depth
C_d is the bottom drag coefficient
u is the current velocity

They have predicted the position of the front in zones where $1 < S < 2$ and have proposed following classification :

$S > 2$: stratified water
$S = 1,5$: transitional Water
$S < 1$: well mixed water.

The importance of the term h/u^3 in the localisation of fronts on the continental shelf has been shown by SIMPSON, ALLEN and MORRIS (1978).

RAILLARD (1976) described the formation of Ushant front and GARZOLI proposed for this front, a critical value of the Richardson number for determining the boundary between stratified water and well mixed water. She has proposed : $h/u^2 < 1$ in well mixed water
$h/u^2 > 1$ in stratified water

V.2 Results :

We applied these numerical models to our study region, from Belle Ile island to Yeu island. Figure 7 shows stations where the water depth and currents were calculated. For each station, h, u, h/u^2 and S were calculated.

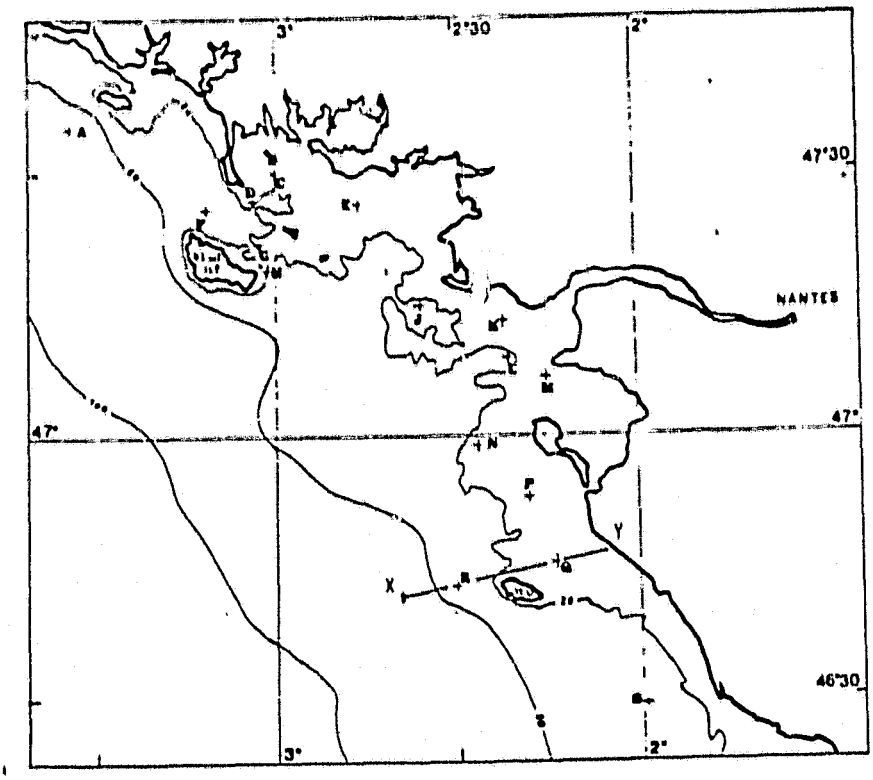

Fig. 7 : Current stations and sea surface temperature section XY

According to these numerical models, water should be stratified in stations A and S ($h/u^2 > 1$; $S > 2$).
Water should be well mixed in stations F,G,H, J,R, M,P,Q, where h/u^2 and S are less than 1.
h/u^2 and S reach critical values in stations E, L, N, R, in function of hydrological situations.
The boundaries between stratified and well mixed waters are shown in fig. 8. The $h/u^2 = 1$ limit presents the same shape as the - 20 m isobath. This result is in accordance with HCMM scenes.

Effects of diurnal heating are clearly visible on HCMM scenes, especially in the bay of Bourgneuf where water depth is less than 10 or 15 m.

Ground truth data and satellite measurements

Data collected from sea cruises (fig. 9) provide a picture of the vertical thermal structure near Yeu island. For example, during summers 1964 and 1965, the thermocline in B is situated between 18 and 30 m. This depth of thermocline seems to correspond with depth of transitional zone between stratified water and well mixed water.

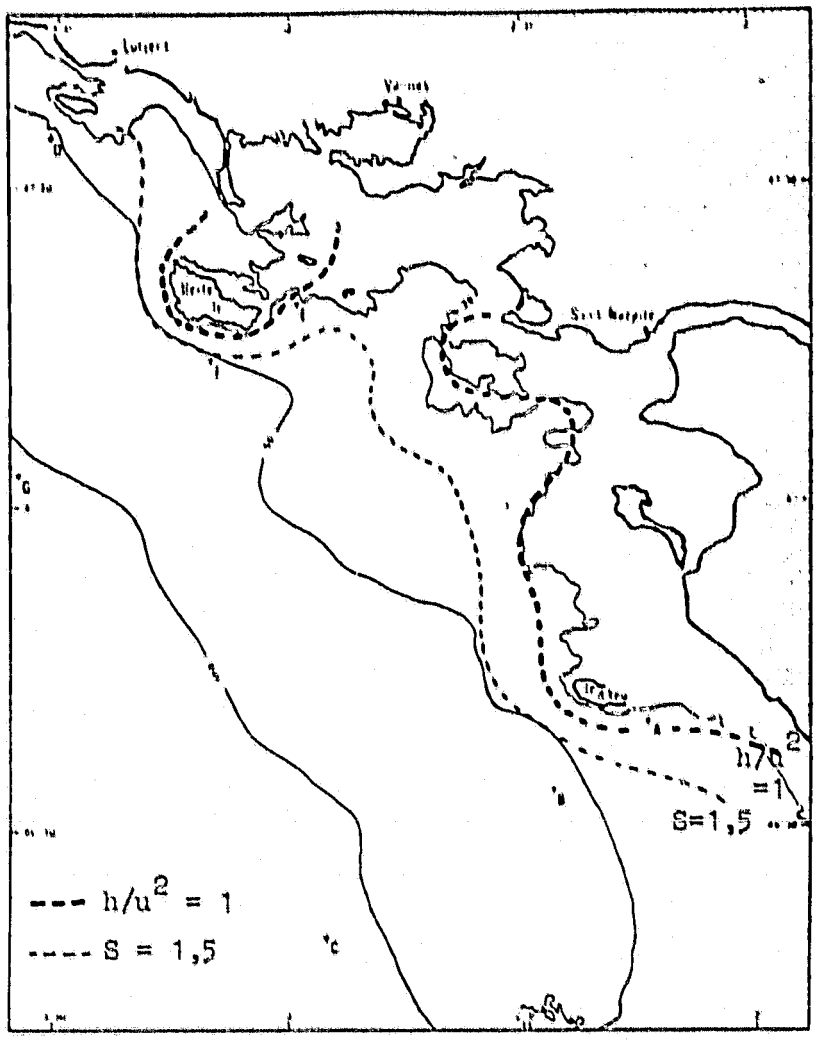

Fig. 8 : Thermal front near islands (average position)

A,B,C : N.N.D.O. data : coastal stations (1964,1965)

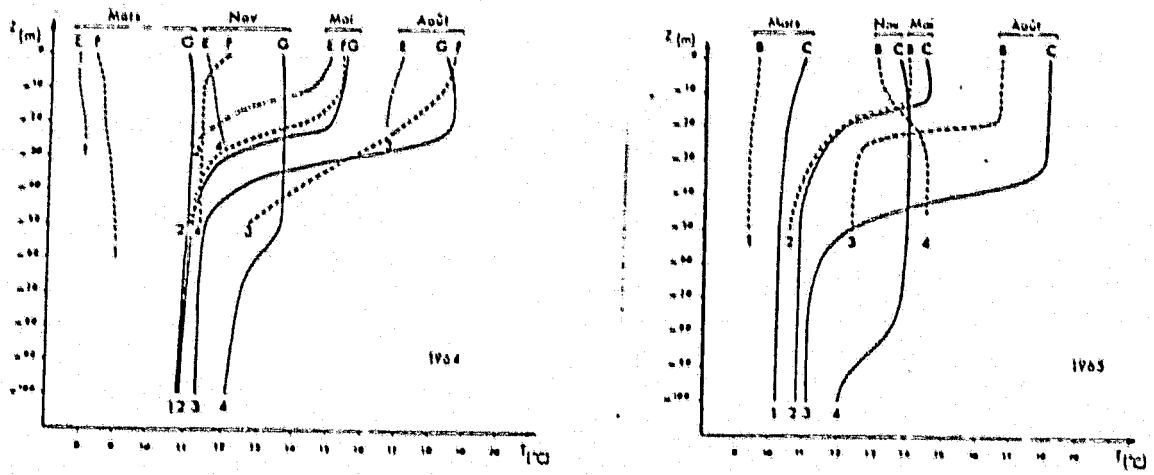

Fig. 9 : Vertical thermal structures in A,B, C (1964,1965)

This study suggests that three factors are important in the location of thermal fronts :

- depth of the water column,
- strength of the tidal currents,
- distance from the thermocline to the sea floor.

We proposed in Fig. 10 a shematic interpretation for cold water area observed near Yeu island (09/15/78), according to previous results and observations.

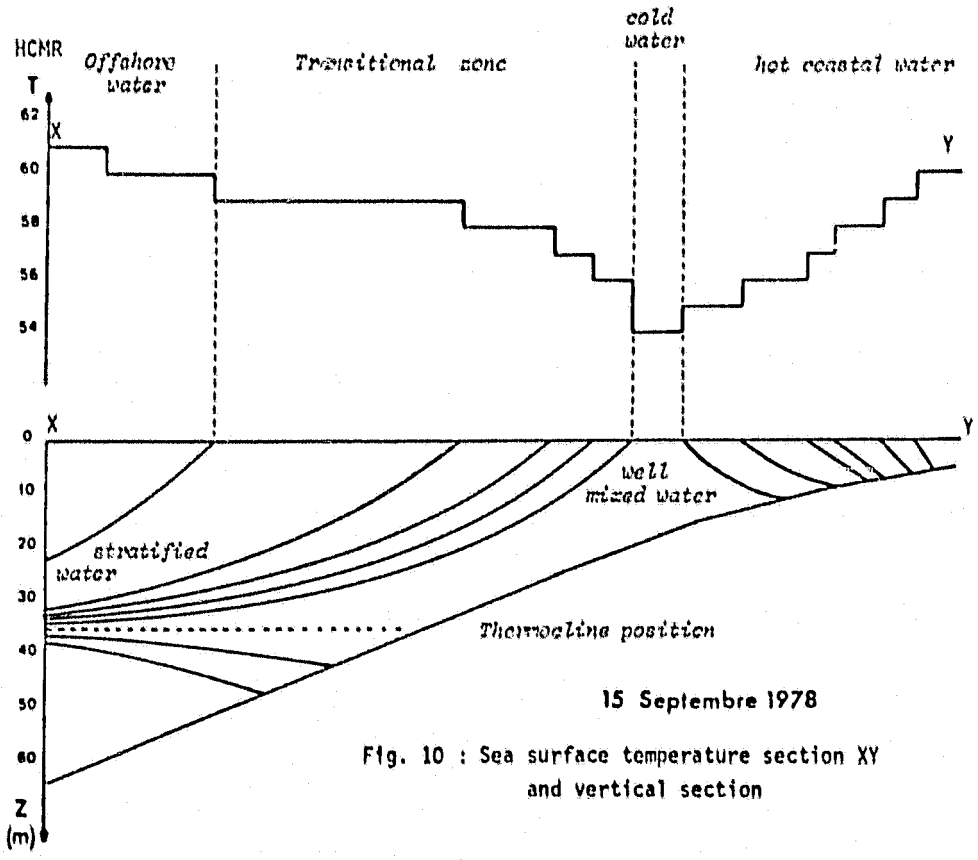

Fig. 10 : Sea surface temperature section XY and vertical section

CONCLUSION

In this investigation, sea surface temperature measurements from HCMR data were used for the examination local and coastal thermal structures which had not been observed before from other satellites. Cold water areas near shoals and islands were revealed. In these regions, tidal currents in shallow water create a turbulence which destroys the thermocline so that the sea surface of the well-mixed water is clearly visible by its cooler temperature, and is separated from stratified water by a transitional zone where the thermal gradients are two degrees higher. Numerical models proposed in the study of thermal fronts near Brittany and British Isles can be applied to this specific case with a fairly good fit.

REFERENCES :

1 - FEARNHEAD P. G. (1974) : On the formation of fronts by tidal mixing aroud the British Isles. *Deep-Sea Research, vol. 22 pp 311 to 321.*

2 - GARVINE R. W. (1973) : The effect of bathymetry on the coastal upwelling of homogeneous water. *Journal of Physical Oceanography, vol 3, pp 47 to 56.*

3 - GARZOLI S. L. (1978) : Contribution à l'étude de la formation et l'évolution du front thermique sur le plateau continental breton. *Annales Hydro., 5ème série, vol 7, fasc. 2, pp 5 à 24.*

4 - PINGREE R. D. and GRIFFITHS D. K. (1978) : Tidal fronts on the shelf seas around the British Isles. *Journal of Geo-physical Research, vol. 83, pp 4615 to 4622.*

5 - SIMPSON J. H, ALLEN C. M., and MORRIS N.C. G. (1978) : Fronts on the continental shelf. *Journal of Geophysical Research, vol. 83, 4607 to 4614.*

6 - NARAYANA PILLAI V., DICKSON R.R.? GURBUTT P. A. (1980) /: Satellite evidence of enhanced upwelling along the european continental slope. *Journal of Physical Oceanography, vol. 10, pp 813 to 819.*

Appendix G

MESOSCALE EDDIES DETECTED IN THE LIGURIAN SEA BY SATELLITE INFRARED RADIOMETERS - A STATISTICS THROUGH THE YEAR

L. WALD

Centre de Télédétection et d'Analyse des Milieux Naturels
Ecole Nationale Supérieure des Mines de Paris, Sophia-Antipolis
06560 Valbonne, France

Introduction

Recent AVHRR and HCMR infrared images of the Ligurian Sea have revealed, thanks to the improved radiometric performances of these instruments, a much more complex surface temperature field than one could infer from previous VHRR observations. The images exhibit mesoscale eddies and tongues of colder or warmer waters, which give a characteristic inhomogeneous aspect to the surface temperature field. This spatial variability captured on satellite imagery has already been reported by DAHME et al (1971) and STOCCHINO and TESTONI (1977) from in situ experiments.

NELEPO et al. (1978) argued that the temperature field in the homogeneous layer is, to a large extent, subordinated to the pattern of the eddy field of the mesoscale perturbations. Thus, the investigation and modelling of the processes generating the horizontal singularities in the homogeneous layer are an important and inseparable stage of the research into mesoscale variability of the ocean that has developed with the employment of remote sensing techniques .

With this in mind, and also with the intention to better assess the mooring positions during the DYOME in situ experiment (the DYOME experiment is a part of the GARP Med-Alpex program), the C.T.A.M.N. entered upon a statistical study of mesoscales eddies detected in the Ligurian sea.

Inventory of mesoscale eddies detected in the Ligurian Sea

AVHRR scenes were used, along with a few HCMR ones. All data were geometri-

cally corrected in order to obtain the same projection for the different images. No filtering or smoothing was applied to the data. By displaying the data on the interactive processing system TRIM of the C.T.A.M.N., the central axis and diameter of the eddies were determined, and stored with additional information concerning date and rotational direction (cyclonic, anticyclonic) of the eddies.

Out of seventy-five cloud-free images examined over the course of a year, thirty-nine exhibited mesoscale eddies (52 %) and the total number of eddies detected was eighty-nine (table 1). Note, that the frequency of anticyclonic eddies is three times more numerous than cyclonic ones. However except for May, June and July, the montly samples did not contain 'enough observations' to be representative of the situation. The diameter of the eddies ranged between 20 and 50 km with a mean value of 30 km, and was independent of the rotational direction. In figure 1, the central axes of the eddies are plotted. One can notice that most of the eddies are located south of the midline of the Ligurian Sea oriented NE-SW.

Discussion

In the Ligurian Basin (figure 2), the general circulation is cyclonic in the surface and intermediate waters. However currents from the east and west of Corsica merge north of Cape Corse creating instabilities in the mean flow. Eddies are generated to either side, with the predominant number being produced N.E. of a line joining Nice and Calvi. This result is close to SALUSTI's conclusions (1979) which were based on the work of Mc CREARY and WHITE (1979). It is likely that the presence of a sand bank in the trajectory of the mean flow contributes to the distribution and complexity of the eddy pattern. Unlike the Gulf Stream meanders which tend to produce

anticyclonic eddies north of the current and cyclonic ones south of the current, the mechanism generating eddies in the Ligurian basin appears more anomalous. To achieve a more complete understanding of the phenomenon, wind effect, residence time, and displacement speed of the eddies must be examined.

REFERENCES

STOCCHINO C., TESTONI A.,1977 - Nuove osservazioni sulla circulazione delle correctio nel mar Ligure - Ist. Idrogr. Mar. Genova.

DAHME A., CANARA A., PEDENOVI C.,1971 - The temperature structure within the first 150 m of depth of the Ligurian sea and its seasonal variation during the years 1960-1967 - Saclant ASW Research Center - Technical Memorandum 165.

NELEPO B.A., KUFTARKOV Y.M., KOSNYREV V.K., 1978 - Effect of mesoscale eddies on ocean surface temperature - Izv. Atm. Ocean. Phys., 14, 7, 545-550.

Mc CREARY J., WHITE W., 1979 - On the theory of Kuroshio meander - Deep-Sea Res., 24R, 317-320.

SALUSTI E., 1979 - Private communication.

WALD L., NIHOUS G., 1980 - Ligurian Sea : Annual variation of the sea surface thermal structure as detected by satellite NOAA-5 - Oceanol. Acta, 3, 4, 465-469.

Table 1 - Summary of mesoscale eddies detected through the year in the Ligurian Sea.

Month	Images analysed	Images with mesoscale eddies	Number of eddies		
			anticyclonic	cyclonic	total
January	1	0	0	0	0
February	7	5	1	7	8
March	8	3	5	0	5
April	6	1	1	0	1
May	13	5	7	4	11
June	5	3	4	0	4
July	9	7	13	3	16
August	9	6	15	2	17
September	7	5	11	9	20
October	3	2	4	0	4
November	2	0	0	0	0
December	3	1	3	0	3
Total	75	39	66	23	89

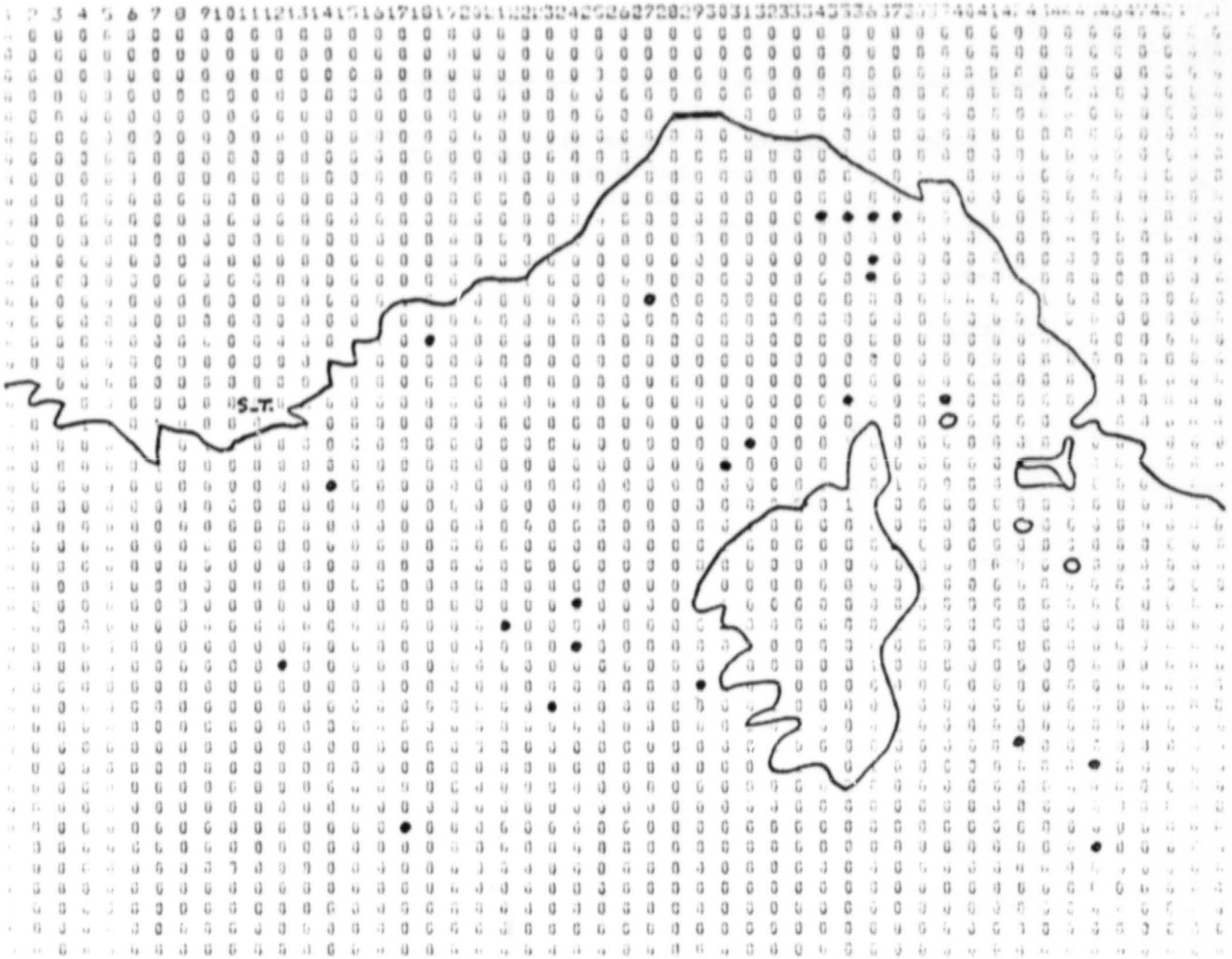

Fig. 1.a - Location of mesoscale cyclonic eddies

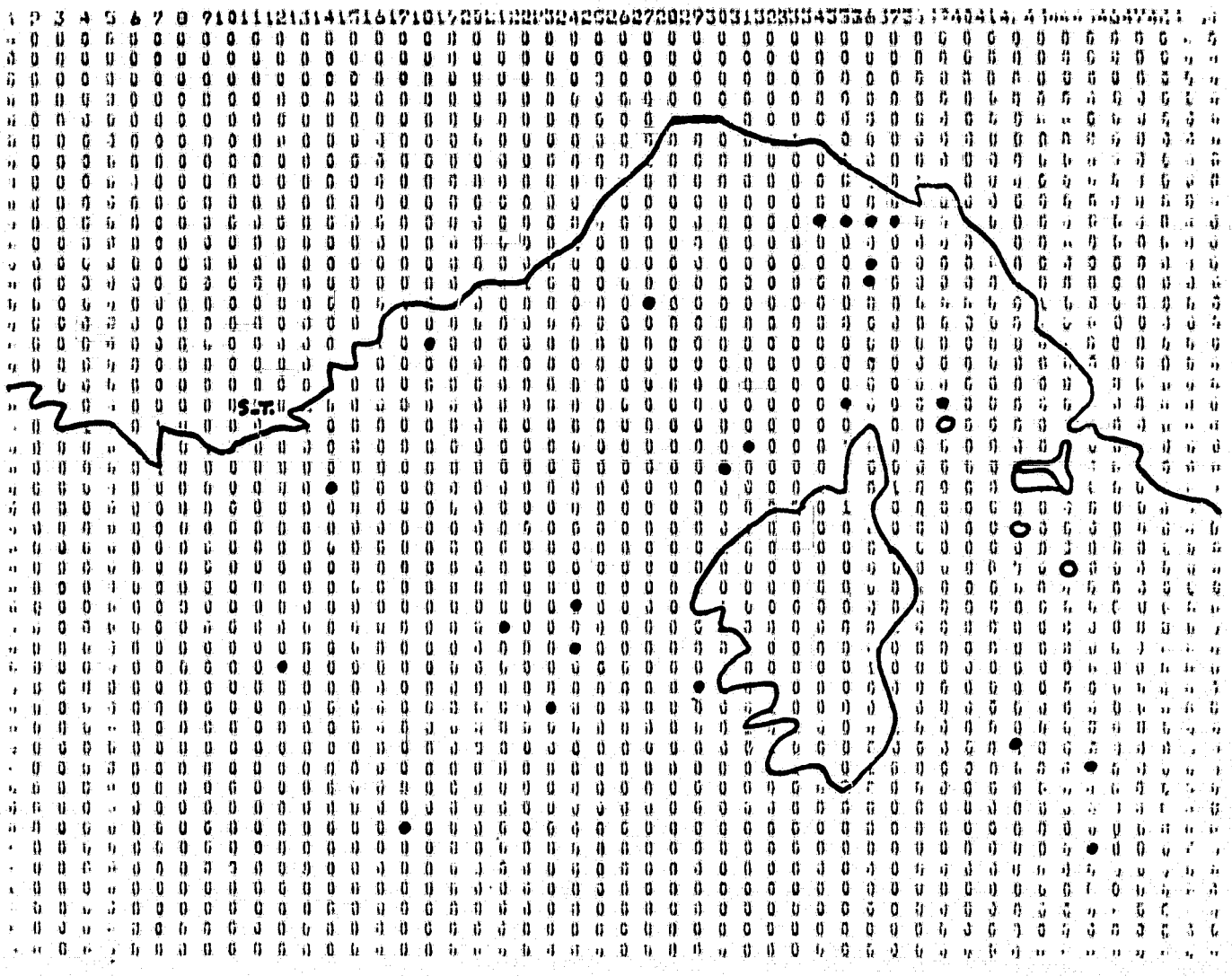

Fig. 1.a - Location of mesoscale cyclonic eddies

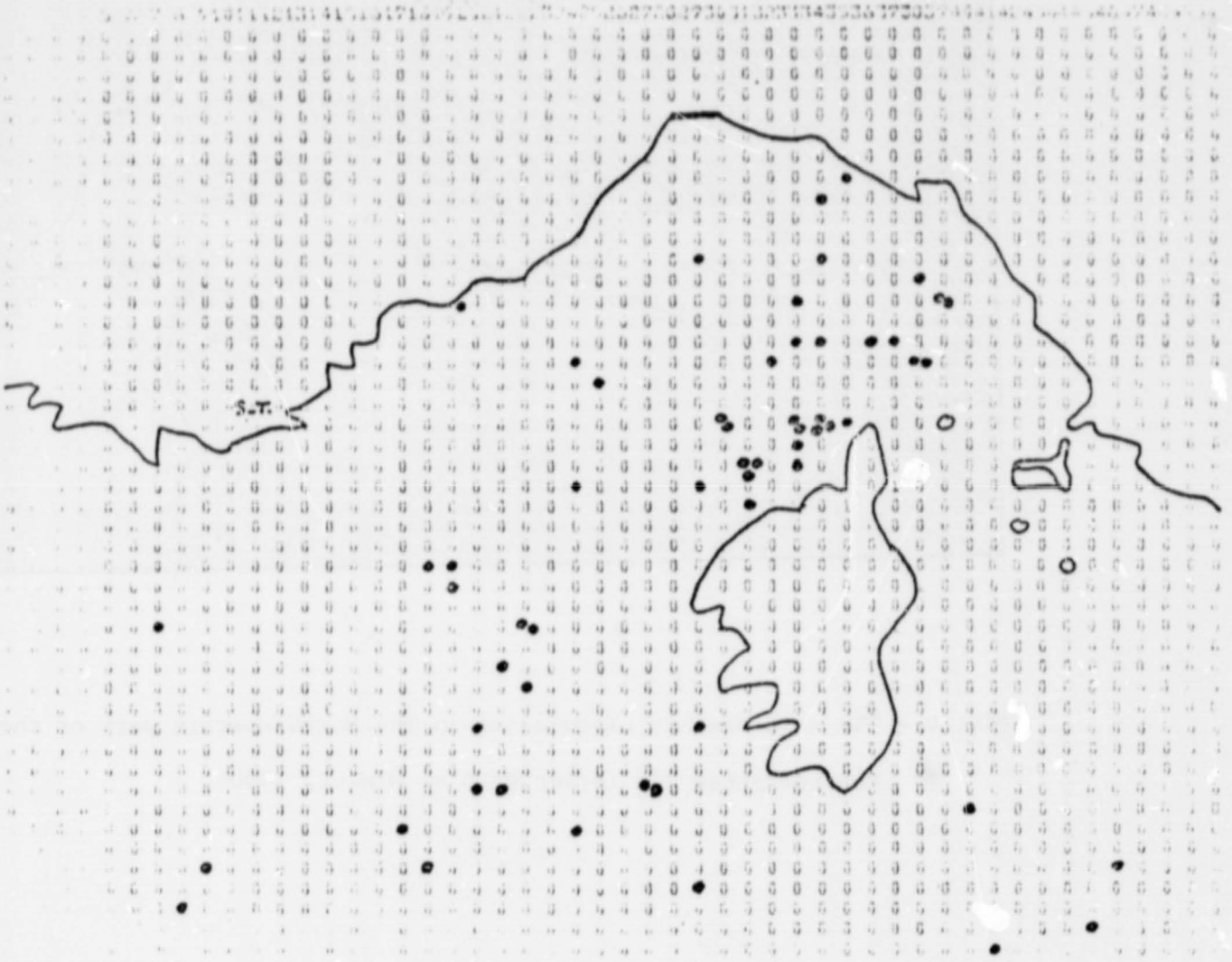

Fig. 1.b - Location of mesoscale anticyclonic eddies

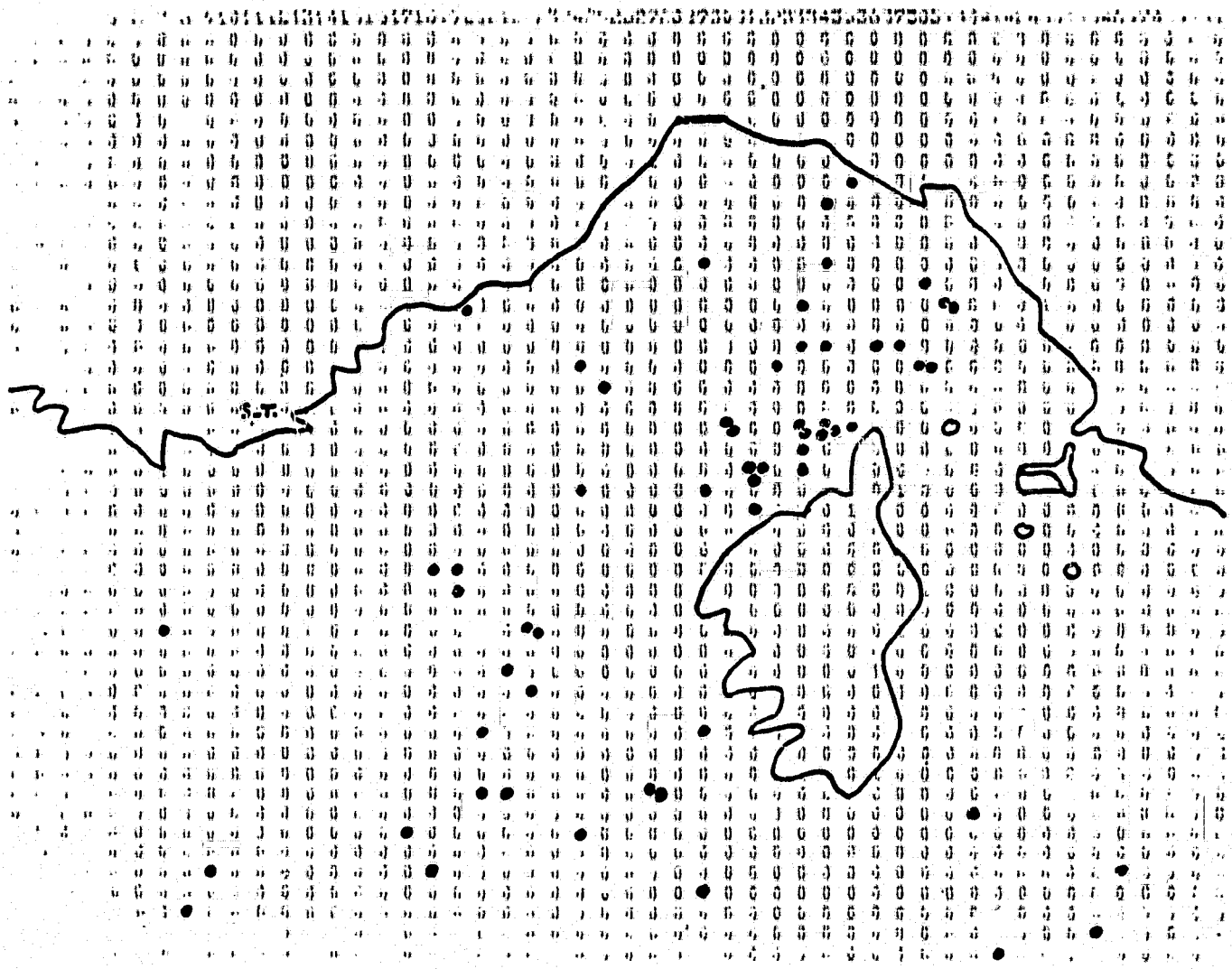

Fig. 1.b - Location of mesoscale anticyclonic eddies

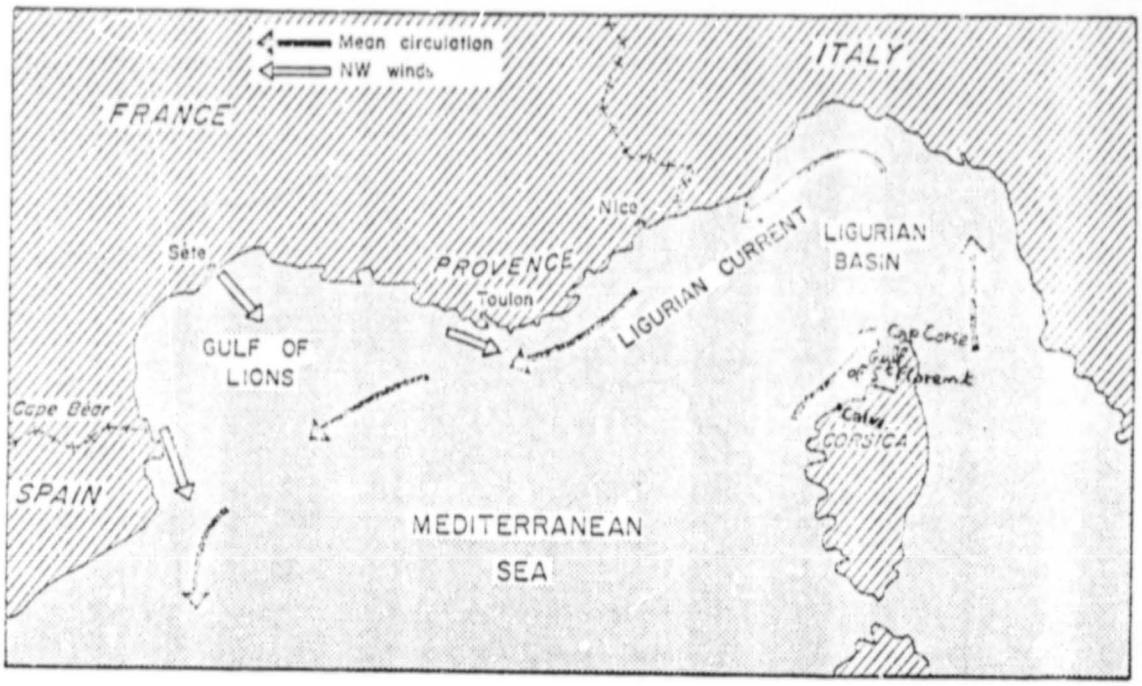

Fig. 2 - The mean oceanic circulation in the North Western part of the Mediterranean Sea (after WALD et NIHOUS, 1980).

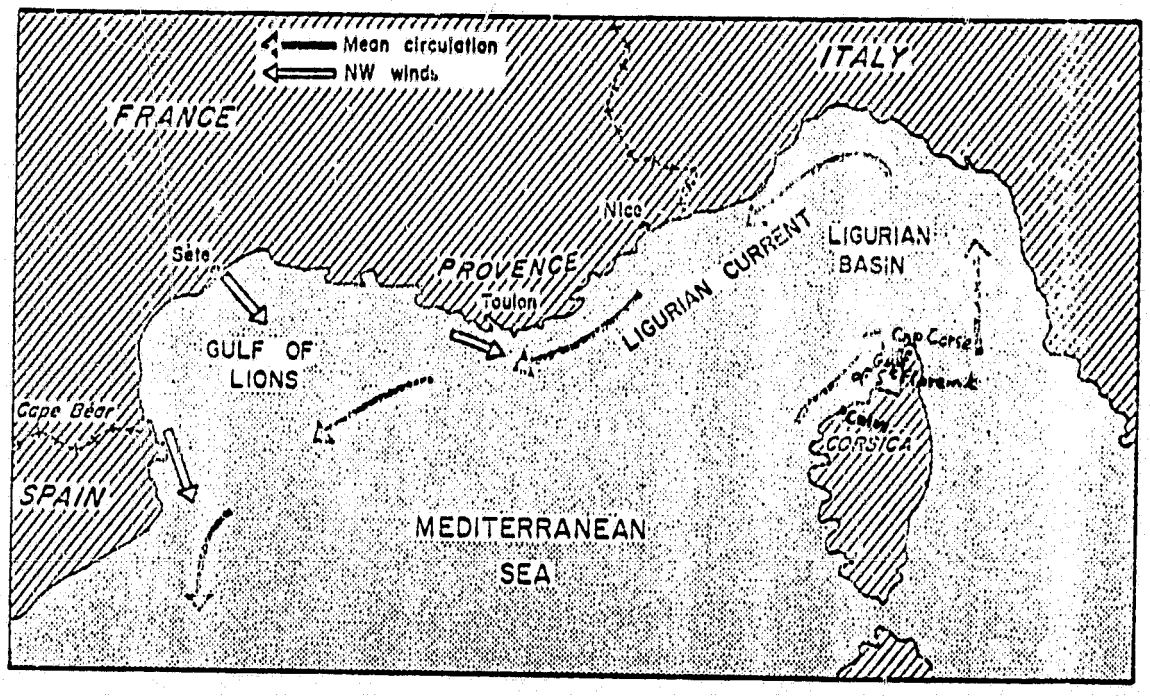

Fig. 2 - The mean oceanic circulation in the North Western part of the Mediterranean Sea (after WALD et NIHOUS, 1980).

Appendix H

The following listing give the date, identification and location of center of image of HCMM scenes received from NASA by the Principal Investigator. The last column "ETAT" give the status of the corresponding digital data :

- R : received
- IR : received but not readable
- C : requested but not received.

ORIGINAL PAGE IS
OF POOR QUALITY

NO	DATE	IDENTIFICATION	LOCATION		SYNE	BDE	STAT
1	11MAY78	15- 2540-3	53.32N	3.43W			
2	11MAY78	15- 2550-3	47.29N	6.08W		303	R
3	11MAY78	15- 2560-3	45.29N	6.08W		303	R
4	11MAY78	15- 2564-3	41.10N	8.45W			
5	11MAY78	15- 2570-3	41.26N	8.08W		303	R
6	11MAY78	15- 3000-3	52.50N	10.00W			
7	11MAY78	15-13510-1	40.35N	4.53W		318	R
8	11MAY78	15-13510-2	40.35N	4.53W		318	R
9	11MAY78	15-13530-1	46.38N	6.52W		318	R
10	11MAY78	15-13530-2	46.38N	6.52W		318	R
11	11MAY78	15-13550-1	52.40N	9.14W			
12	11MAY78	15-13550-2	52.40N	9.14W			
13	13MAY78	17- 1570-3	38.02N	5.56E		318	R
14	13MAY78	17-12510-1	41.29N	9.56E		318	R
15	13MAY78	17-12510-2	41.29N	9.56E		318	R
16	13MAY78	17-12540-1	53.34N	5.29E			
17	13MAY78	17-12540-2	53.34N	5.29E			
18	14MAY78	18- 2140-3	44.02N	3.10E			C
19	14MAY78	18- 2150-3	37.56N	1.19E			C
20	14MAY78	18-13080-1	39.07N	6.02E		312	R
21	14MAY78	18-13080-2	39.07N	6.02E		312	R
22	14MAY78	18-13100-1	45.11N	4.08E		312	R
23	14MAY78	18-13100-2	45.11N	4.08E		312	R
24	16MAY78	20- 2400-3	51.39N	3.11W		318	R
25	16MAY78	20- 2500-3	45.36N	5.28W		318	R
26	18MAY78	22- 3251-3	50.16N	12.55W			
27	18MAY78	22-12460-1	44.55N	10.11E			
28	18MAY78	22-12460-2	44.55N	10.11E			
29	18MAY78	22-12470-1	50.58N	7.57E		312	R
30	18MAY78	22-12470-2	50.58N	7.57E		312	R
31	19MAY78	23- 2050-3	55.24N	9.04E			
32	19MAY78	23- 2080-3	43.19N	4.20E			
33	19MAY78	23- 2100-3	57.13N	9.31E			
34	19MAY78	23-13050-2	50.25N	3.35E			
35	20MAY78	24-13200-1	58.07N	3.07E			
36	20MAY78	24-13200-1	56.32N	3.34E			
37	20MAY78	24-13200-2	58.07N	3.07E			
38	20MAY78	24-13200-2	56.32N	3.34E			
39	20MAY78	24-13220-1	44.11N	1.15E			
40	20MAY78	24-13220-2	44.11N	1.15E			
41	20MAY78	24-13230-1	48.40N	.19E		293	R
42	20MAY78	24-13230-1	50.13N	.56E		293	R
43	20MAY78	24-13230-2	48.40N	.19E		293	R
44	20MAY78	24-13230-2	50.13N	.56E		293	R
45	20MAY78	24-13250-1	54.40N	2.52W		293	R
46	20MAY78	24-13250-1	56.14N	3.37W		293	R
47	20MAY78	24-13250-2	54.40N	2.52W		293	R
48	20MAY78	24-13250-2	56.14N	3.37W		293	R
49	21MAY78	25-13380-1	55.53N	.52E			
50	21MAY78	25-13380-2	55.53N	.52E			

NO	DATE	IDENTIFICATION	LOCATION		SCENE	BDE	ETAT	C
51	21MAY78	25-13390-1	41.58N	2.38W				
52	21MAY78	25-13390-2	41.58N	2.38W				
53	21MAY78	25-13410-1	48.01N	4.41W		312	R	
54	21MAY78	25-13410-2	48.01N	4.41W		312	R	
55	21MAY78	25-13430-1	54.04N	7.08E				
56	21MAY78	25-13430-2	54.04N	7.08E				
57	22MAY78	26- 3000-3	52.30N	6.02W			C	
58	22MAY78	26- 3020-3	46.27N	8.23W			C	
59	23MAY78	27- 1440-3	42.47N	10.07E				
60	23MAY78	27- 1440-3	42.28N	10.01E				
61	23MAY78	27- 1450-3	36.40N	8.19E				
62	23MAY78	27- 1450-3	36.22N	8.14E				
63	23MAY78	27- 3180-3	52.55N	10.27W				
64	23MAY78	27- 3200-3	46.52N	12.50W		318	R	
65	24MAY78	28- 2020-3	43.47N	5.49E		320	R	
66	24MAY78	28- 2030-3	37.41N	3.58E				
67	24MAY78	28-12550-1	36.16N	9.35E				
68	24MAY78	28-12550-2	36.16N	9.35E				
69	24MAY78	28-12570-1	42.40N	7.47E		312	R	
70	24MAY78	28-12570-2	42.40N	7.47E		312	R	
71	25MAY78	29- 2210-3	39.37N	.02E		320	R	
72	25MAY78	29-13140-1	37.22N	4.40E				
73	25MAY78	29-13140-1	37.40N	4.35E				
74	25MAY78	29-13140-2	37.22N	4.40E				
75	25MAY78	29-13140-2	37.40N	4.35E				
76	25MAY78	29-13150-1	43.26N	2.50E			C	
77	25MAY78	29-13150-2	43.26N	2.50E			C	
78	25MAY78	29-13170-1	49.29N	.42E				
79	25MAY78	29-13170-1	49.47N	.35E		310	R	
80	25MAY78	29-13170-2	49.29N	.42E				
81	25MAY78	29-13170-2	49.47N	.35E		310	R	
82	26MAY78	30- 2370-3	48.31N	1.41W		320	R	
83	26MAY78	30- 2380-3	42.26N	3.45W		320	R	
84	26MAY78	30-13310-1	35.27N	.39E				
85	26MAY78	30-13310-2	35.27N	.39E				
86	26MAY78	30-13330-1	41.32N	1.06W				
87	26MAY78	30-13330-2	41.32N	1.06W				
88	26MAY78	30-13350-1	47.36N	3.08W			C	
89	26MAY78	30-13350-2	47.36N	3.08W			C	
90	26MAY78	30-13360-1	53.38N	5.34W				
91	26MAY78	30-13360-2	53.38N	5.34W				
92	27MAY78	31- 2540-3	50.25N	5.32W		320	R	I
93	27MAY78	31- 2560-3	44.21N	7.44W		320	R	I
94	27MAY78	31-13510-1	40.50N	5.28W				
95	27MAY78	31-13510-2	40.50N	5.28W				
96	27MAY78	31-13530-1	46.54N	7.27W			C	
97	27MAY78	31-13530-2	46.54N	7.27W			C	
98	27MAY78	31-13540-1	52.56N	9.50W				
99	27MAY78	31-13540-2	52.56N	9.50W				
100	28MAY78	32- 3120-3	53.05N	9.00W				

NO	DATE	IDENTIFICATION	LOCATION		SCENE	BDE	ETAT	D
101	28MAY78	32- 3180-3	47.02N	11.23W				
102	28MAY78	32-12350-1	50.08N	11.02E				
103	28MAY78	32-12350-1	51.38N	10.26E				
104	28MAY78	32-12350-2	50.08N	11.02E				
105	28MAY78	32-12350-2	51.38N	10.26E				
106	28MAY78	32-12360-1	56.08N	8.22E		320	R	
107	28MAY78	32-12360-2	56.08N	8.22E		320	R	
108	28MAY78	32-14110-1	46.49N	12.01W				
109	28MAY78	32-14110-2	46.49N	12.01W				
110	29MAY78	33- 1520-4	43.37N	8.47E		360	R	
111	29MAY78	33- 1520-5	43.37N	8.47E		362	R	
112	29MAY78	33- 1520-6	43.37N	8.47E		343	R	
113	29MAY78	33- 1520-7	43.37N	8.47E		343	R	
114	29MAY78	33- 1520-8	39.42N	5.56E		360	R	
115	29MAY78	33- 1550-3	43.35N	7.08E		303	R	
116	29MAY78	33- 1570-3	37.29N	5.18E				
117	29MAY78	33-12500-1	39.56N	9.57E		293	R	
118	29MAY78	33-12500-2	39.56N	9.57E		293	R	
119	29MAY78	33-12520-1	46.01N	7.59E		294	R	
120	29MAY78	33-12520-2	46.01N	7.59E		294	R	
121	29MAY78	33-12530-1	52.03N	5.40E		320	R	
122	29MAY78	33-12530-2	52.03N	5.40E		320	R	
123	30MAY78	34- 2120-3	50.41N	5.06E		303	R	
124	30MAY78	34- 2120-4	41.46N	4.47E		516	R	
125	30MAY78	34- 2120-4	43.32N	4.14E		328	R	
126	30MAY78	34- 2120-5	41.46N	4.47E		516	R	
127	30MAY78	34- 2120-5	43.32N	4.14E		328	R	
128	30MAY78	34- 2120-6	41.46N	4.47E		181	R	
129	30MAY78	34- 2120-6	43.32N	4.14E		333	R	
130	30MAY78	34- 2120-7	41.46N	4.47E		181	R	
131	30MAY78	34- 2120-7	43.32N	4.14E		333	R	
132	30MAY78	34- 2120-8	37.01N	.37E		516	R	
133	30MAY78	34- 2120-8	36.56N	.36E		328	R	
134	30MAY78	34- 2130-3	44.37N	2.53E		303	R	
135	30MAY78	34- 2130-3	50.05N	4.30E				
136	30MAY78	34- 2140-3	44.37N	2.53E			C	
137	30MAY78	34- 2150-3	38.31N	1.02E				
138	30MAY78	34- 2280-3	36.13N	3.00E			C	
139	30MAY78	34-13070-1	36.17N	6.25E				
140	30MAY78	34-13070-2	36.17N	6.25E				
141	30MAY78	34-13080-1	38.50N	5.41E		294	R	I
142	30MAY78	34-13080-2	38.50N	5.41E		294	R	I
143	30MAY78	34-13090-1	44.55N	3.47E		304	R	I
144	30MAY78	34-13090-1	42.22N	4.37E		304	R	I
145	30MAY78	34-13090-2	44.55N	3.47E		304	R	I
146	30MAY78	34-13090-2	42.22N	4.37E				
147	30MAY78	34-13100-1	48.26N	2.32E		303	R	I
148	30MAY78	34-13100-2	48.26N	2.32E		303	R	I
149	30MAY78	34-13110-1	50.58N	1.33E		321	R	I
150	30MAY78	34-13110-2	50.58N	1.33E		321	R	I

NO	DATE	IDENTIFICATION	LOCATION		SCENE	BDE	STAT	I
151	30MAY78	34-13120-1	54.27N	.01E		303	R	
152	30MAY78	34-13120-2	54.27N	.01E		303	R	
153	31MAY78	35- 2280-3	56.13N	3.00E		313	R	
154	31MAY78	35- 2300-3	50.47N	.34E		313	R	
155	31MAY78	35- 2300-3	50.11N	.19E			C	
156	31MAY78	35- 2310-3	44.43N	1.38W		299	R	
157	31MAY78	35- 2320-3	44.07N	1.50W			C	
158	31MAY78	35- 2330-3	38.01N	3.41W				
159	31MAY78	35- 2330-3	38.37N	3.30W				
160	31MAY78	35-21320-1	55.40N	119.30W		304	R	
161	31MAY78	35-21320-2	55.40N	119.30W		304	R	
162	1JUN78	36- 2480-3	51.25N	3.44W				
163	1JUN78	36- 2490-3	45.21N	6.00W				
164	1JUN78	36-13440-1	38.45N	3.23W		321	R	
165	1JUN78	36-13440-2	38.35N	3.23W		321	R	
166	1JUN78	36-13460-1	42.00N	4.25W				
167	1JUN78	36-13460-1	44.40N	5.17W		321	R	
168	1JUN78	36-13460-3	42.00N	4.25W				
169	1JUN78	36-13460-2	44.40N	5.17W		321	R	
170	1JUN78	36-13470-1	50.43N	7.31W				
171	1JUN78	36-13470-2	50.43N	7.31W				
172	2JUN78	37- 3060-3	51.12N	2.25W				
173	2JUN78	37- 3080-3	45.08N	10.41W				
174	3JUN78	38- 1490-4	43.39N	10.11E		197	R	
175	3JUN78	38- 1490-4	43.39N	10.11E		331	R	
176	3JUN78	38- 1480-5	43.39N	10.11E		194	R	
177	3JUN78	38- 1490-5	43.39N	10.11E		334	R	
178	3JUN78	38- 1480-6	43.39N	10.11E		182	R	
179	3JUN78	38- 1480-6	43.39N	10.11E		330	R	
180	3JUN78	38- 1480-7	43.39N	10.11E		182	R	
181	3JUN78	38- 1480-7	43.39N	10.11E		330	R	
182	3JUN78	38- 1480-8	54.57N	6.00E		182	R	
183	3JUN78	38- 1480-8	54.52N	5.59E		331	R	
184	3JUN78	38- 1490-3	41.46N	7.56E		294	R	
185	3JUN78	38- 1510-3	55.39N	6.11E				
186	3JUN78	38-12440-1	40.54N	11.04E		304	R	
187	3JUN78	38-12440-2	40.54N	11.04E			C	
188	3JUN78	38-12460-1	46.59N	9.04E		304	R	
189	3JUN78	38-12460-2	46.59N	9.04E		304	R	
190	3JUN78	38-12470-1	53.01N	6.40E		304	R	
191	3JUN78	38-12470-2	53.01N	6.40E		304	R	
192	4JUN78	39- 2040-3	55.46N	2.44E				
193	4JUN78	39- 2050-3	49.44N	6.06E				
194	4JUN78	39- 2070-3	43.39N	3.57E				
195	4JUN78	39- 2090-3	37.32N	2.07E			C	
196	4JUN78	39-13020-1	39.56N	6.47E			C	
197	4JUN78	39-13020-2	39.56N	6.47E			C	
198	4JUN78	39-13030-1	46.01N	4.49E				
199	4JUN78	39-13030-2	46.01N	4.49E				
200	4JUN78	39-13050-1	52.03N	2.29E			C	

NO	DATE	IDENTIFICATION	LOCATION		SCENE	ODE	STAT	D
201	4JUN78	39-13050-2	52.03N	2.29E			C	
202	5JUN78	40- 2220-3	55.30N	4.03E		354	R	
203	5JUN78	40- 2250-3	43.23N	.41E				
204	5JUN78	40- 2270-3	37.16N	2.30W				
205	5JUN78	40-13200-1	40.52N	1.56E				
206	5JUN78	40-13200-2	40.52N	1.56E				
207	5JUN78	40-13220-1	46.56N	.02E				
208	5JUN78	40-13220-2	46.56N	.02E				
209	5JUN78	40-13240-1	52.59N	2.26W				
210	5JUN78	40-13240-2	52.59N	2.26W				
211	6JUN78	41-13370-1	55.23N	1.05W			C	
212	6JUN78	41-13370-2	55.23N	1.05W			C	
213	6JUN78	41-13390-1	41.29N	2.51W				
214	6JUN78	41-13390-2	41.29N	2.51W				
215	6JUN78	41-13400-1	47.33N	4.53W			C	
216	6JUN78	41-13400-2	47.33N	4.53W			C	
217	7JUN78	42- 3020-3	42.24N	10.08W				
218	8JUN78	43- 3190-3	46.00N	13.32W				
219	8JUN78	43- 4110-1	33.25S	150.41E		363	R	
220	8JUN78	43- 4110-2	33.25S	150.41E		363	R	
221	8JUN78	43-12270-1	54.45N	14.15E				
222	8JUN78	43-12280-1	41.20N	12.20E		294	R	
223	8JUN78	43-12280-2	41.20N	12.20E		294	R	
224	9JUN78	44- 1590-3	50.04N	7.40E				
225	9JUN78	44- 2010-3	43.59N	5.30E				
226	9JUN78	44- 2020-3	37.53N	3.40E				
227	9JUN78	44-12250-1	58.41N	8.34E				
228	9JUN78	44-12550-2	38.41N	8.34E				
229	9JUN78	44-12570-1	44.46N	6.40E				
230	9JUN78	44-12570-2	44.46N	6.40E				
231	9JUN78	44-12580-1	50.50N	4.26E				
232	9JUN78	44-12580-2	50.50N	4.26E				
233	10JUN78	45-13130-1	36.36N	4.35E				
234	10JUN78	45-13130-2	36.36N	4.35E				
235	10JUN78	45-13140-1	42.41N	2.46E				
236	10JUN78	45-13140-2	42.41N	2.46E				
237	10JUN78	45-13160-1	48.46N	.40E		307	R	I
238	10JUN78	45-13160-2	48.46N	.40E		307	R	I
239	10JUN78	45-13180-1	54.47N	1.52W				
240	10JUN78	45-13180-2	54.47N	1.52W				
241	11JUN78	46-13310-1	35.45N	.16E		313	R	I
242	11JUN78	46-13310-2	35.45N	.16E		313	R	I
243	11JUN78	46-13320-1	41.50N	1.29E		363	R	
244	11JUN78	46-13320-2	41.50N	1.29W		363	R	
245	11JUN78	46-13340-1	47.55N	3.33W		313	R	I
246	11JUN78	46-13340-2	47.55N	3.33W		313	R	I
247	11JUN78	46-13360-1	53.57N	6.02W			C	
248	11JUN78	46-13360-2	53.57N	6.02W			C	
249	12JUN78	47-13500-1	42.12N	6.13W		355	R	
250	12JUN78	47-13500-2	42.12N	6.13W		355	R	

NO	DATE	IDENTIFICATION	LOCATION		SCENE	DDL	ETAT
251	12JUN78	47-13520-1	48.16N	8.17W		355	R
252	12JUN78	47-13520-2	48.16N	8.17W		355	R
253	13JUN78	48- 1370-3	41.36N	10.41E		354	R
254	13JUN78	48- 3110-3	52.49N	9.28W			
255	13JUN78	48- 3120-3	46.46N	11.51W			
256	13JUN78	48-12350-1	55.26N	8.24E			
257	13JUN78	48-12350-2	55.26N	8.24E			
258	14JUN78	49-12490-1	40.04N	9.38E			
259	14JUN78	49-12490-2	40.04N	9.38E			
260	14JUN78	49-12510-1	46.09N	7.40E			
261	14JUN78	49-12510-2	46.09N	7.40E			
262	14JUN78	49-12520-1	52.12N	5.20E			
263	14JUN78	49-12520-2	52.12N	5.20E			
264	15JUN78	50- 2090-3	55.49N	7.03E			
265	15JUN78	50- 2110-3	49.47N	4.25E			
266	15JUN78	50- 2120-3	43.42N	2.16E			
267	15JUN78	50- 2140-3	37.35N	.26E			
268	15JUN78	50-13070-1	40.05N	5.03E		355	R
269	15JUN78	50-13070-2	40.05N	5.03E		355	R
270	15JUN78	50-13100-1	52.13N	.46E			
271	15JUN78	50-13100-2	52.13N	.46E			
272	15JUN78	50-13120-2	58.14N	2.10W			
273	16JUN78	51- 2270-3	56.20N	2.44E			
274	16JUN78	51- 2320-3	58.07N	7.59W		307	R
275	16JUN78	51-13240-1	37.00N	1.23E			C
276	16JUN78	51-13240-2	37.00N	1.23E			C
277	16JUN78	51-13240-1	43.06N	.26E			
278	16JUN78	51-13260-2	43.06N	.26E			
279	16JUN78	51-13280-1	49.10N	2.34W			
280	16JUN78	51-13280-2	49.10N	2.34W			
281	17JUN78	52- 2450-3	55.38N	2.10W			
282	17JUN78	52- 2470-3	49.35N	4.47W			
283	17JUN78	52- 2490-3	43.31N	6.55W			
284	17JUN78	52-13430-1	37.35N	3.20W			
285	17JUN78	52-13460-1	49.45N	7.20W			
286	17JUN78	52-13460-2	49.45N	7.20W			
287	18JUN78	53- 3050-3	51.35N	8.33W		354	R
288	18JUN78	53- 3060-3	45.31N	10.50W		354	R
289	18JUN78	53-14030-1	46.05N	10.34W		305	R
290	18JUN78	53-14030-2	46.05N	10.34W		305	R
291	18JUN78	53-14050-1	52.09N	12.54W		305	R
292	18JUN78	53-14050-2	52.09N	12.54W		305	R
293	19JUN78	54- 1470-3	45.45N	8.58E		305	R
294	19JUN78	54- 1490-3	39.40N	7.02E		305	R
295	19JUN78	54-12430-1	42.46N	10.16E		294	R
296	19JUN78	54-12430-2	42.46N	10.16E		294	R
297	19JUN78	54-12450-1	48.51N	8.10E			
298	19JUN78	54-12450-2	48.51N	8.10E			
299	19JUN78	54-12470-1	54.53N	5.35E		321	R
300	19JUN78	54-12470-2	54.53N	5.35E		321	R

NO	DATE	IDENTIFICATION	LOCATION		SCENE	BDE	ETAT
301	20JUN78	55- 2030-3	52.43N	7.05E			
302	20JUN78	55- 2030-3	52.58N	7.11E		296	R
303	20JUN78	55- 2040-3	52.00N	6.46E			C
304	20JUN78	55- 2050-3	46.40N	4.43E			C
305	20JUN78	55- 2050-3	45.56N	4.27E			
306	20JUN78	55- 2050-3	46.54N	4.47E		296	R
307	20JUN78	55- 2070-3	40.48N	2.47E			
308	20JUN78	55- 2070-3	40.34N	2.43E			
309	20JUN78	55- 2070-3	39.49N	2.30E			C
310	20JUN78	55-13000-1	39.00N	6.50E		294	R
311	20JUN78	55-13000-2	39.00N	6.50E			C
312	20JUN78	55-13020-1	45.05N	4.55E		295	R
313	20JUN78	55-13020-2	45.05N	4.55E		295	R
314	20JUN78	55-13040-1	51.10N	2.39E		295	R
315	20JUN78	55-13040-2	51.10N	2.39E		295	R
316	21JUN78	56- 2210-3	56.11N	4.04E			
317	21JUN78	56- 2220-3	50.09N	1.26E			
318	21JUN78	56- 2240-3	44.04N	.43E			
319	21JUN78	56- 2260-3	37.58N	2.34W		295	R
320	21JUN78	56-13180-1	36.42N	2.55E		355	R
321	21JUN78	56-13180-2	36.42N	2.55E		355	R
322	21JUN78	56-13190-1	42.49N	1.07E		355	R
323	21JUN78	56-13190-2	42.49N	1.07E		355	R
324	22JUN78	57-13350-1	55.02N	1.10W		321	R
325	22JUN78	57-13350-2	55.02N	1.10W		321	R
326	22JUN78	57-13370-1	41.08N	2.56W			
327	22JUN78	57-13370-2	41.08N	2.56W			
328	22JUN78	57-13390-1	47.13N	4.58W			
329	22JUN78	57-13390-2	47.13N	4.58W			
330	22JUN78	57-13400-1	53.17N	7.23W			
331	22JUN78	57-13400-2	53.17N	7.23W			
332	23JUN78	58- 2590-3	47.49N	8.34W			
333	23JUN78	58-13550-1	41.11N	7.30W			
334	23JUN78	58-13550-2	41.11N	7.30W			
335	23JUN78	58-13570-1	47.17N	9.31W			
336	23JUN78	58-13570-2	47.17N	9.31W			
337	24JUN78	59- 1410-3	42.31N	9.22E		322	R
338	24JUN78	59- 1430-3	36.24N	7.35E		322	R
339	24JUN78	59- 3160-3	52.22N	11.20W			
340	24JUN78	59- 3180-3	46.18N	13.40W			
341	24JUN78	59-12370-1	42.34N	11.47E		322	R
342	24JUN78	59-12370-2	42.34N	11.47E		322	R
343	24JUN78	59-12400-1	54.41N	7.07E			
344	24JUN78	59-12400-2	54.41N	7.07E			
345	25JUN78	60- 1560-3	54.26N	9.19E			
346	25JUN78	60- 1580-3	48.23N	6.49E			
347	25JUN78	60- 2000-3	42.17N	4.45E			
348	25JUN78	60- 2010-3	36.11N	2.59E			
349	25JUN78	60-12540-1	41.16N	7.39E			
350	25JUN78	60-12540-2	41.16N	7.39E			

NO	DATE	IDENTIFICATION	LOCATION		SCENE	BDE	ETAT
351	25JUN78	60-12560-1	47.21N	5.38E			
352	25JUN78	60-12560-2	47.21N	5.38E			
353	26JUN78	61- 2160-3	49.14N	2.34E			
354	26JUN78	61- 2170-3	43.10N	.27E			
355	26JUN78	61- 2190-3	37.01N	1.20W		322	R
356	26JUN78	61-13110-1	56.55N	4.21E		322	R
357	26JUN78	61-13110-2	56.55N	4.21E		322	R
358	26JUN78	61-13130-1	43.01N	2.32E			
359	26JUN78	61-13130-2	43.01N	2.32E			
360	26JUN78	61-13150-1	49.06N	2.25E			
361	26JUN78	61-13150-2	40.06N	2.25E			
362	26JUN78	61-13160-1	55.08N	2.10W		358	
363	26JUN78	61-13160-2	55.08N	2.10W			
364	27JUN78	62-13290-1	35.01N	.19E		322	R
365	27JUN78	62-13290-2	35.01N	.19E		322	R
366	27JUN78	62-13300-1	41.08N	1.25W			
367	27JUN78	62-13300-2	41.08N	1.25W			
368	28JUN78	63- 2510-3	51.35N	5.36W			
369	28JUN78	63- 2530-3	45.32N	7.52W			
370	28JUN78	63-13490-1	43.33N	6.46W		323	R
371	28JUN78	63-13490-2	43.33N	6.46W		323	R
372	29JUN78	64-14080-1	44.41N	11.40W			
373	29JUN78	64-14080-2	44.41N	11.40W			
374	30JUN78	65- 1500-3	54.07N	10.39E			
375	30JUN78	65- 1530-3	41.59N	6.08E		305	R
376	30JUN78	65- 1550-3	55.53N	4.23E			
377	30JUN78	65-12470-1	59.22N	9.43E			
378	30JUN78	65-12470-2	59.22N	9.43E			
379	30JUN78	65-12490-1	45.29N	7.47E			
380	30JUN78	65-12490-2	45.49N	7.47E			
381	1JUL78	66-13050-1	58.10N	5.30E			C
382	1JUL78	66-13050-2	58.10N	5.30E			C
383	1JUL78	66-13080-1	50.21N	1.25E			
384	1JUL78	66-13080-2	50.21N	1.25E			
385	2JUL78	67- 2270-3	50.36N	.02E			
386	2JUL78	67- 2280-3	44.32N	2.09W			
387	2JUL78	67- 2300-3	58.26N	4.01W			C
388	4JUL78	69-14000-1	41.18N	9.05W			
389	4JUL78	69-14000-2	41.18N	9.05W			
390	4JUL78	69-14450-3	28.27S	162.05E		363	R
391	4JUL78	69-14470-3	28.27S	162.05E		363	R
392	5JUL78	70- 1460-3	43.16N	8.04E			
393	5JUL78	70- 1460-3	42.79N	7.49E			
394	5JUL78	70- 1470-3	57.10N	6.15E			
395	5JUL78	70- 1480-3	56.23N	6.02E			
396	5JUL78	70-12410-1	43.01N	10.08E		332	R
397	5JUL78	70-12410-1	43.34N	9.58E			
398	5JUL78	70-12410-2	43.01N	10.08E		332	R
399	5JUL78	70-12410-2	43.34N	9.58E			
400	5JUL78	70-12450-1	55.09N	5.25E			

NO	DATE	IDENTIFICATION	LOCATION		SCENE	ODE	ETAT
401	5JUL78	70-12450-1	55.41N	5.08E			
402	5JUL78	70-12450-2	55.09N	5.25E			
403	5JUL78	70-12450-2	55.41N	5.08E			
404	6JUL78	71- 2020-3	48.26N	5.17E			
405	6JUL78	71- 2040-3	42.22N	3.13E		305	R
406	6JUL78	71- 2060-3	36.16N	1.27E			
407	6JUL78	71-12570-1	36.10N	7.38E			
408	6JUL78	71-12570-2	36.10N	7.38E			
409	6JUL78	71-12590-1	42.16N	5.49E		323	R
410	6JUL78	71-12590-2	42.16N	5.49E		323	R
411	7JUL78	72- 2210-3	46.31N	.02E		295	R
412	7JUL78	72- 2230-3	40.25N	1.54W			
413	7JUL78	72-13170-1	40.08N	1.54E			
414	7JUL78	72-13170-1	40.05N	1.55E		295	R
415	7JUL78	72-13170-2	40.08N	1.54E			
416	7JUL78	72-13170-2	40.05N	1.55E		295	R
417	7JUL78	72-13180-1	46.14N	.03E			
418	7JUL78	72-13180-1	46.11N	.02E		295	R
419	7JUL78	72-13180-2	46.14N	.03E			
420	7JUL78	72-13180-2	46.11N	.02E		295	R
421	8JUL78	73- 2370-3	52.33N	2.10W			
422	8JUL78	73-13350-1	40.53N	2.50W			
423	8JUL78	73-13350-2	40.53N	2.50W			
424	8JUL78	73-13360-1	46.59N	4.51W		296	R
425	8JUL78	73-13360-2	46.59N	4.51W		296	R
426	10JUL78	75- 1390-3	42.20N	9.21E		296	R
427	10JUL78	75- 1410-3	36.14N	7.35E		296	R
428	10JUL78	75-12350-1	45.02N	11.01E		323	R
429	10JUL78	75-12350-2	45.02N	11.01E		323	R
430	10JUL78	75-12370-1	51.07N	8.46E			
431	10JUL78	75-12370-2	51.07N	8.46E			
432	11JUL78	76- 1540-3	52.29N	8.27E			
433	11JUL78	76- 1540-4	46.30N	5.57E		353	R
434	11JUL78	76- 1540-5	46.30N	5.57E		351	R
435	21JUL78	76- 1540-6	46.30N	5.57E		352	R
436	11JUL78	76- 1540-7	46.30N	5.57E		352	R
437	11JUL78	76- 1540-8	38.53N	3.44E		353	R
438	11JUL78	76- 1550-3	49.03N	7.04E			
439	11JUL78	76- 1560-3	46.26N	6.07E			
440	11JUL78	76- 1570-3	42.59N	4.58E		296	R
441	11JUL78	76- 1580-3	40.22N	4.10E		363	R
442	11JUL78	76- 1590-3	36.53N	3.10E		296	R
443	11JUL78	76-12520-1	40.33N	7.52E		323	R
444	11JUL78	76-12520-2	40.33N	7.52E		323	R
445	11JUL78	76-12530-1	46.40N	5.54E			
446	11JUL78	76-12530-2	46.40N	5.54E			
447	11JUL78	76-12550-1	52.43N	3.32E			
448	11JUL78	76-12550-2	52.43N	3.32E			
449	12JUL78	77- 2130-3	51.37N	3.33E			
450	12JUL78	77- 2140-3	45.34N	1.17E		296	R

NO	DATE	IDENTIFICATION	LOCATION	SCENE	BDE	CTAT
451	12JUL78	77- 2160-3	39.29N .37E		296	R
452	13JUL78	78- 2310-3	51.45N .56E			
453	13JUL78	78- 2320-3	45.42N 3.13W		322	R
454	16JUL78	81- 1500-3	45.08N 7.15E		323	R
455	16JUL78	81- 1510-3	39.04N 5.22E		323	R
456	17JUL78	82- 1540-3	.00N .00E			C
457	17JUL78	82- 2060-3	51.24N 5.02E			
458	17JUL78	82- 2080-3	45.21N 2.47E		297	R
459	17JUL78	82- 2090-3	39.17N .53E			
460	17JUL78	82-13020-1	39.22N 5.15E			C
461	17JUL78	82-13020-2	39.22N 5.15E			C
462	17JUL78	82-13040-1	45.29N 3.19E			C
463	17JUL78	82-13040-2	45.29N 3.19E			C
464	17JUL78	82-13060-1	51.33N 1.02E			
465	17JUL78	82-13060-2	51.33N 1.02E			
466	18JUL78	83- 2270-3	39.41N 3.39W			
467	18JUL78	83- 2440-3	51.22N .29E			
468	20JUL78	85- 3010-3	46.39N 10.22W			
469	21JUL78	86- 1450-3	56.18N 6.12E			
470	21JUL78	86-12380-1	42.55N 10.17E		297	R
471	21JUL78	86-12380-2	42.55N 10.17E		297	R
472	22JUL78	87- 2000-3	47.02N 4.59E			
473	22JUL78	87- 2020-3	40.50N 7.00E			C
474	23JUL78	88- 2200-3	40.08N 1.47W			
475	25JUL78	90- 2530-3	51.47N 6.47W		324	R
476	25JUL78	90- 2540-3	45.44N 9.04W		324	R
477	26JUL78	91- 1370-3	41.00N 9.14E		297	R
478	27JUL78	92- 1510-3	54.28N 9.41E			
479	27JUL78	92- 1530-3	48.27N 1.11E			
480	27JUL78	92- 1540-3	42.23N 5.07E		307	R
481	27JUL78	92- 1560-3	36.19N 7.20E			
482	24SEP78	93- 2080-4	41.41N 6.03E		329	R
483	24SEP78	93- 2080-5	41.41N 6.03E		329	R
484	24SEP78	93- 2080-6	41.41N 6.03E		326	R
485	24SEP79	93- 2080-7	41.41N 6.03E		326	R
486	28JUL78	93- 2080-8	41.08N .11E		329	R
487	28JUL78	93- 2100-3	50.54N 3.35E			
488	28JUL78	93- 2120-3	44.52N 1.22E			C
489	28JUL78	93- 2130-3	38.47N .30E			
490	28JUL78	93-13060-1	57.03N 4.29E		297	R
491	28JUL78	93-13060-2	57.03N 4.29E		297	R
492	28JUL78	93-13070-1	43.10N 2.40E		297	R
493	28JUL78	93-13070-2	43.10N 2.40E		297	R
494	28JUL78	93-13090-1	49.14N .33E		297	R
495	28JUL78	93-13090-2	49.14N .33E		297	R
496	28JUL78	93-13110-1	55.17N 2.01W			
497	28JUL78	93-13110-2	55.17N 2.01W			
498	29JUL78	94- 2280-3	51.50N .31E		324	R
499	29JUL78	94- 2290-3	45.48N 2.49W		324	R
500	29JUL78	94-13230-1	56.00N .16E			

NO	DATE	IDENTIFICATION	LOCATION	SCENE	BDE	ETAT
501	29JUL78	94-13230-2	56.00N .16E			
502	29JUL78	94-13250-1	42.07N 1.29W			
503	29JUL78	94-13250-2	42.07N 1.29W			
504	29JUL78	94-13270-1	48.11N 3.34W			
505	29JUL78	94-13270-2	48.11N 3.34W			
506	29JUL78	94-13280-1	54.14N 6.04W			
507	29JUL78	94-13280-2	54.14N 6.04W			
508	30JUL78	95- 2470-3	46.04N 7.16W			
509	30JUL78	95-13430-1	42.46N 6.16W			
510	30JUL78	95-13430-2	42.46N 6.16W			
511	30JUL78	95-13450-1	48.50N 8.22W			
512	30JUL78	95-13450-2	48.50N 8.22W			
513	31JUL78	96- 3040-3	51.54N 9.34W			
514	31JUL78	96- 3050-3	45.42N 11.52W			
515	31JUL78	96-12260-1	50.27N 10.45E			
516	31JUL78	96-12260-2	50.27N 10.45E			
517	31JUL78	96-12280-1	56.28N 8.01E			
518	31JUL78	96-12280-2	56.28N 8.01E			
519	31JUL78	96-14010-1	41.13N 10.17W			
520	31JUL78	96-14010-2	41.13N 10.17W			
521	31JUL78	96-14020-1	47.18N 12.19W			
522	31JUL78	96-14020-2	47.18N 12.19W			
523	1AUG78	97- 1470-3	43.46N 2.11E		298	R
524	1AUG78	97- 1490-3	37.42N 5.21E			
525	5AUG78	101- 2580-3	46.02N 10.08W			
526	7AUG78	103- 1580-3	42.59N 4.01E			
527	7AUG78	103- 1590-3	36.54N 2.12E			
528	7AUG78	103-12520-1	39.58N 6.54E			
529	7AUG78	103-12520-2	39.58N 6.54E			
530	8AUG78	104- 2140-3	49.55N 1.57E			
531	8AUG78	104- 2150-3	43.52N .12E			
532	8AUG78	104- 2170-3	37.47N 2.02W			
533	8AUG78	104-13100-1	39.41N 2.25E			
534	8AUG78	104-13100-2	39.41N 2.25E			
535	8AUG78	104-13120-1	45.46N .29E			
536	8AUG78	104-13120-2	45.46N .29E			
537	9AUG78	105-13290-1	44.46N 3.41W			
538	9AUG78	105-13290-2	44.46N 3.41W			
539	9AUG78	105-13310-1	50.50N 5.55W			
540	9AUG78	105-13310-2	50.50N 5.55W			
541	11AUG78	107- 1320-3	42.53N 10.11E			
542	11AUG78	107- 1340-3	36.48N 8.23E			
543	11AUG78	107- 3070-3	53.08N 10.17W			
544	11AUG78	107- 3090-3	47.07N 12.41W			
545	12AUG78	108- 1510-3	41.31N 5.13E			C
546	12AUG78	108- 1530-3	55.26N 3.28E			
547	12AUG78	108-12450-1	40.34N 8.19E		324	R
548	12AUG78	108-12450-2	40.34N 8.19E		324	R
549	12AUG78	108-12470-1	46.39N 6.21E		324	R
550	12AUG78	108-12470-2	46.39N 6.21E		324	R

NO	DATE	IDENTIFICATION	LOCATION		SCENE	DUE	ETAT
551	13AUG78	109- 2070-3	49.19N	3.22E			
552	13AUG78	109- 2080-3	43.17N	1.15E			
553	13AUG78	109- 2100-3	37.12N	.33E			
554	14AUG78	110- 2270-3	42.36N	3.29W			C
555	14AUG78	110-13210-1	40.07N	.34E			C
556	14AUG78	110-13210-2	40.07N	.34E			C
557	14AUG78	110-13220-1	46.11N	2.31W			C
558	14AUG78	110-13220-2	46.11N	2.31W			C
559	17AUG78	113-12380-1	40.49N	9.54E		325	R
560	17AUG78	113-12380-1	42.16N	9.27E		324	R
561	17AUG78	113-12380-2	40.49N	9.54E		325	R
562	17AUG78	113-12380-2	42.16N	9.27E		324	R
563	17AUG78	113-12390-1	46.53N	7.55E			
564	17AUG78	113-12390-2	46.53N	7.55E			
565	17AUG78	113-12410-1	52.55N	5.31E		298	R
566	17AUG78	113-12410-2	52.55N	5.31E		298	R
567	18AUG78	114-12550-1	37.48N	6.16E		325	R
568	18AUG78	114-12550-2	37.48N	6.16E		325	R
569	18AUG78	114-12570-1	43.53N	4.25E		298	R
570	18AUG78	114-12570-2	43.53N	4.25E		298	R
571	19AUG78	115- 2170-3	51.58N	1.35E			C
572	19AUG78	115- 2180-3	45.56N	.42E			
573	19AUG78	115- 2180-3	45.56N	.42E		307	R
574	19AUG78	115- 2200-3	39.52N	2.39W			
575	19AUG78	115-13130-1	37.32N	1.49E		325	R
576	19AUG78	115-13130-2	37.32N	1.49E		325	R
577	19AUG78	115-13140-1	43.37N	.00E		313	R
578	19AUG78	115-13140-2	43.37N	.00E		313	R
579	19AUG78	115-13160-1	49.40N	2.09W		313	R
580	19AUG78	115-13160-2	49.40N	2.09W		313	R
581	20AUG78	116- 2380-3	41.25N	6.43W			
582	20AUG78	116-13320-1	40.44N	3.38W			
583	20AUG78	116-13320-2	40.44N	3.38W			
584	20AUG78	116-13330-1	46.49N	5.37W			
585	20AUG78	116-13330-2	46.49N	5.37W			
586	20AUG78	116-13350-1	52.50N	8.00W			
587	20AUG78	116-13350-2	52.50N	8.00W			
588	21AUG78	117-13500-1	43.35N	9.04W		325	R
589	21AUG78	117-13500-2	43.35N	9.04W		325	R
590	21AUG78	117-13520-1	49.38N	11.13W		325	R
591	21AUG78	117-13520-2	49.38N	11.13W		325	R
592	22AUG78	118- 1350-3	45.16N	9.47E		298	R
593	22AUG78	118-12310-1	41.30N	11.21E		332	R
594	22AUG78	118-12310-2	41.30N	11.21E		332	R
595	22AUG78	118-12340-1	53.35N	6.53E			
596	22AUG78	118-12340-2	53.35N	6.53E			
597	23AUG78	119- 1510-3	54.52N	9.06E			
598	23AUG78	119- 1540-3	42.48N	4.26E			
599	23AUG78	119- 1560-3	56.43N	9.38E		307	R
600	24AUG78	120- 2110-3	47.10N	1.22E			

NO	DATE	IDENTIFICATION	LOCATION		SCENE	BDE	STAT.
601	24AUG78	120- 2120-3	41.06N	.37E			C
602	24AUG78	120-13060-1	40.34N	2.34E		307	R
603	24AUG78	120-13060-2	40.34N	2.34E		307	R
604	24AUG78	120-13080-1	46.38N	.36E		307	R
605	24AUG78	120-13080-2	46.38N	.36E		307	R
606	25AUG78	121-13240-1	40.43N	2.01W			C
607	25AUG78	121-13240-2	40.43N	2.01W			C
608	25AUG78	121-13260-1	46.47N	4.00W			C
609	25AUG78	121-13260-2	46.47N	4.00W			C
610	25AUG78	121-13280-1	52.49N	6.22W			
611	25AUG78	121-13280-2	52.49N	6.22W			
612	26AUG78	122-13440-1	43.50N	7.34W		357	R
613	26AUG78	122-13440-2	43.50N	7.34W		357	R
614	26AUG78	122-13450-1	49.53N	9.43W		357	R
615	26AUG78	122-13450-2	49.53N	9.43W		357	R
616	27AUG78	123- 1290-3	44.15N	10.58E			
617	27AUG78	123- 1300-3	38.10N	9.05E			
618	28AUG78	124- 1460-3	49.26N	8.13E			
619	28AUG78	124-12410-1	39.00N	9.00E			
620	28AUG78	124-12410-2	39.00N	9.00E			
621	28AUG78	124-12430-1	45.05N	7.07E		298	R
622	28AUG78	124-12430-2	45.05N	7.07E		298	R
623	28AUG78	124-12450-1	51.07N	4.52E		298	R
624	28AUG78	124-12450-2	51.07N	4.52E		298	R
625	30AUG78	126-13180-1	40.44N	.41E			C
626	30AUG78	126-13180-2	40.44N	.41E			C
627	30AUG78	126-13200-1	46.47N	2.40W			C
628	30AUG78	126-13200-2	46.47N	2.40W			C
629	30AUG78	126-13220-1	52.49N	5.02W			
630	30AUG78	126-13220-2	52.49N	5.02W			
631	31AUG78	127- 2401-3	50.15N	5.14W			C
632	31AUG78	127- 2421-3	44.12N	7.26W			
633	31AUG78	127-13380-1	45.05N	6.39W		308	R
634	31AUG78	127-13380-2	45.05N	6.39W		308	R
635	1SEP78	128-12220-1	56.23N	8.22E			
636	1SEP78	128-12220-2	56.23N	8.22E			
637	1SEP78	128-13550-1	41.23N	10.02W			
638	1SEP78	128-13550-2	41.23N	10.02W			
639	2SEP78	129- 1410-3	45.22N	8.06E		299	R
640	2SEP78	129- 1420-3	39.17N	6.11E			
641	2SEP78	129-12370-1	45.29N	8.19E			C
642	2SEP78	129-12370-2	45.29N	8.19E			C
643	3SEP78	130- 1590-3	42.55N	2.41E			
644	3SEP78	130-12540-1	38.57N	5.48E			
645	3SEP78	130-12540-2	38.57N	5.48E			
646	3SEP78	130-12550-1	45.01N	3.54E		308	R
647	3SEP78	130-12550-2	45.01N	3.54E		308	R
648	3SEP78	130-12570-1	51.04N	1.39E		308	IR
649	3SEP78	130-12570-2	51.04N	1.39E		308	R
650	4SEP78	131- 2150-3	51.40N	1.19E		308	R

NO	DATE	IDENTIFICATION	LOCATION		SCENE	BDE	ETAT
651	4SEP78	131- 2170-3	45.37N	.58E			
652	5SEP78	132- 2340-3	50.22N	3.49W			
653	5SEP78	132- 2350-3	44.18N	6.02W			
654	5SEP78	132-13300-1	59.34N	3.32W			
655	5SEP78	132-13300-2	59.34N	3.32W			
656	6SEP78	133-13490-1	43.30N	9.20W			
657	6SEP78	133-13490-2	43.30N	9.20W			
658	7SEP78	134- 1370-3	35.29N	6.31E			
659	7SEP78	134- 3090-3	53.38N	11.36W			
660	7SEP78	134-12300-1	43.44N	10.16E			
661	7SEP78	134-12300-1	43.29N	10.21E			
662	7SEP78	134-12300-2	43.29N	10.21E			
663	7SEP78	134-12300-2	43.44N	10.16E			
664	7SEP78	134-12340-1	55.32N	5.35E			
665	7SEP78	134-12340-1	55.47N	5.29E			
666	7SEP78	134-12340-2	55.47N	5.29E			
667	7SEP78	134-12340-2	55.32N	5.35E			
668	8SEP78	135- 1550-3	56.49N	2.15E			C
669	8SEP78	135-12470-1	57.32N	7.35E			C
670	8SEP78	135-12470-2	57.32N	7.35E			C
671	8SEP78	135-12490-1	43.37N	5.44E			C
672	8SEP78	135-12490-2	43.37N	5.44E			C
673	8SEP78	135-12500-1	49.40N	7.35E			
674	8SEP78	135-12500-2	49.40N	7.35E			
675	9SEP78	136- 2100-3	46.40N	.44E			
676	9SEP78	136- 2170-3	40.43N	1.14W			
677	9SEP78	136-13050-1	56.32N	2.17E			C
678	9SEP78	136-13050-2	56.32N	2.17E			C
679	9SEP78	136-13070-1	42.37N	1.29E			C
680	9SEP78	136-13070-2	42.37N	1.29E			C
681	9SEP78	136-13080-1	48.40N	.35E			
682	9SEP78	136-13080-2	48.40N	.35E			
683	10SEP78	137- 2290-3	44.37N	4.32W			
684	10SEP78	137-13240-1	40.06N	2.18W			
685	10SEP78	137-13240-2	40.06N	2.18W			
686	10SEP78	137-13260-1	46.10N	4.14W			C
687	10SEP78	137-13260-2	46.10N	4.14W			C
688	11SEP78	138- 2460-3	50.07N	7.07W			
689	12SEP78	139- 1290-3	42.43N	0.59E			
690	12SEP78	139-13000-3	56.41N	8.11E			
691	13SEP78	140- 1450-3	51.05N	8.26E			
692	14SEP78	141- 2050-3	41.38N	.28E		309	R
693	14SEP78	141-12580-1	56.02N	4.49E			
694	14SEP78	141-12580-1	56.10N	4.47E		309	R
695	14SEP78	141-12580-2	56.02N	4.49E			
696	14SEP78	141-12580-2	56.10N	4.47E		309	R
697	14SEP78	141-13000-1	42.07N	3.02E			
698	14SEP78	141-13000-1	42.15N	3.00E		309	R
699	14SEP78	141-13000-2	42.07N	3.02E			
700	14SEP78	141-13000-2	42.15N	3.00E		309	R

NO	DATE	IDENTIFICATION	LOCATION	SCENE	BDE	ETAT
701	14SEP78	141-13020-1	48.18N .56E		309	R
702	14SEP78	141-13020-1	48.11N .59E			
703	14SEP78	141-13020-2	48.11N .59E			
704	14SEP78	141-13020-2	48.18N .56E		309	R
705	14SEP78	141-13030-1	54.12N 1.30W			
706	14SEP78	141-13030-1	54.19N 1.33W			
707	14SEP78	141-13030-2	54.19N 1.33W			
708	14SEP78	141-13030-2	54.12N 1.30W			
709	15SEP78	142- 2210-3	52.02N .22E			
710	15SEP78	142- 2210-3	51.55N .25E		302	R
711	15SEP78	142- 2220-3	45.52N 2.43W			C
712	15SEP78	142- 2220-3	45.59N 2.41W			
713	15SEP78	142-13190-1	40.21N .58E		302	R
714	15SEP78	142-13180-2	40.21N .58E		302	R
715	15SEP78	142-13190-1	46.25N 2.55W		302	R
716	15SEP78	142-13190-2	46.25N 2.55W		302	R
717	15SEP78	142-13210-1	52.27N 5.16W			
718	15SEP78	142-13210-2	52.27N 5.16W			
719	16SEP78	143- 2390-3	52.49N 4.34W			
720	16SEP78	143- 2400-3	46.46N 6.57W			
721	17SEP78	144-12210-1	55.17N 8.33E			
722	17SEP78	144-12210-2	55.17N 8.33E			
723	17SEP78	144-13560-1	46.05N 11.58W			
724	17SEP78	144-13560-2	46.05N 11.58W			
725	17SEP78	144-13570-1	52.08N 14.17W			
726	17SEP78	144-13570-2	52.08N 14.17W			
727	18SEP78	145-12360-1	42.16N 9.00E		302	R
728	18SEP78	145-12360-2	42.16N 9.00E		302	R
729	18SEP78	145-12370-1	48.19N 6.56E			
730	18SEP78	145-12370-2	48.19N 6.56E			
731	18SEP78	145-12390-1	54.20N 4.26E			
732	18SEP78	145-12390-2	54.20N 4.26E			
733	19SEP78	146- 1570-3	50.44N 5.07E			C
734	19SEP78	146- 1580-3	44.41N 2.53E		354	R
735	19SEP78	146- 2000-3	38.35N .59E		354	R
736	21SEP78	148- 2340-3	45.48N 5.52W			
737	21SEP78	148-13280-1	36.19N 2.58W		357	R
738	21SEP78	148-13280-2	36.19N 2.58W		357	R
739	21SEP78	148-13300-1	42.25N 4.44W		357	R
740	21SEP78	148-13300-2	42.25N 4.44W		357	R
741	21SEP78	148-13320-1	48.28N 6.49W		357	R
742	21SEP78	148-13320-2	48.28N 6.49W		357	R
743	22SEP78	149- 2520-3	46.25N 10.13W		308	R
744	22SEP78	149-13480-1	40.49N 8.49W			C
745	22SEP78	149-13480-2	40.49N 8.49W			C
746	22SEP78	149-13490-1	46.53N 10.48W			C
747	22SEP78	149-13490-2	46.53N 10.48W			C
748	23SEP78	150-12300-1	46.19N 9.07E			
749	23SEP78	150-12300-2	46.19N 9.07E			
750	23SEP78	150-12320-1	52.22N 6.47E			

NO	DATE	IDENTIFICATION	LOCATION		SCENE	BDE	ETAT
751	24SEP78	151-12460-1	39.07N	6.50E			
752	24SEP78	151-12460-2	39.07N	6.50E			
753	24SEP78	151-12480-1	45.11N	4.56E			
754	24SEP78	151-12480-2	45.11N	4.56E			
755	24SEP78	151-12500-1	51.14N	2.41E			
756	24SEP78	151-12500-2	51.14N	2.41E			
757	25SEP78	152- 2080-3	50.33N	1.54E			C
758	25SEP78	152- 2100-3	44.28N	.18E		363	R
759	25SEP78	152- 2120-3	38.22N	2.11W			C
760	26SEP78	153-13220-1	37.49N	1.54W			
761	26SEP78	153-13220-2	37.49N	1.54W			
762	26SEP78	153-13240-1	43.54N	3.45W		310	R
763	26SEP78	153-13240-2	43.54N	3.45W		310	R
764	26SEP78	153-13260-1	49.57N	5.55W		310	R
765	26SEP78	153-13260-2	49.57N	5.55W		310	R
766	27SEP78	154- 2450-3	49.29N	7.38W			
767	27SEP78	154- 2460-3	43.25N	9.47W			
768	27SEP78	154-13420-1	43.26N	8.09W			C
769	27SEP78	154-13420-2	43.26N	8.09W			C
770	28SEP78	155- 1280-3	42.18N	9.35E			
771	28SEP78	155- 1290-3	36.11N	7.48E			
772	28SEP78	155-12230-1	42.50N	11.44E			
773	28SEP78	155-12230-2	42.50N	11.44E			
774	28SEP78	155-12260-1	54.55N	7.05E			
775	28SEP78	155-12260-2	54.55N	7.05E			
776	29SEP78	156- 1460-3	41.52N	4.53E			
777	29SEP78	156- 1480-3	55.45N	3.07E			
778	29SEP78	156-12400-1	37.51N	8.40E		358	R
779	29SEP78	156-12400-2	37.51N	8.40E		358	R
780	29SEP78	156-12410-1	43.56N	6.49E		358	R
781	29SEP78	156-12410-2	43.56N	6.49E		358	R
782	30SEP78	157- 2030-3	44.17N	1.04E			
783	30SEP78	157- 2040-3	43.11N	.43E			
784	30SEP78	157- 2050-3	37.04N	1.05W			
785	30SEP78	157- 2050-3	38.10N	.47E			
786	20CT78	159- 2400-3	44.11N	8.03W			
787	20CT78	159-13360-1	44.32N	7.01W			
788	20CT78	159-13360-2	44.32N	7.01W			
789	30CT78	160-13530-1	43.29N	11.13W			
790	30CT78	160-13530-2	43.29N	11.13W			
791	30CT78	160-13550-1	49.32N	13.21W			
792	30CT78	160-13550-2	49.32N	13.21W			
793	50CT78	162-12520-1	40.38N	4.49E			
794	50CT78	162-12520-2	40.38N	4.49E			
795	50CT78	162-12530-1	46.43N	2.50E			
796	50CT78	162-12530-2	46.43N	2.50E			
797	80CT78	165-13460-1	42.28N	9.23W			
798	80CT78	165-13460-2	42.28N	9.23W			
799	80CT78	165-13480-1	48.32N	11.27W			
800	80CT78	165-13480-2	48.32N	11.27W			

NO	DATE	IDENTIFICATION	LOCATION		SCENE	BDE	ETAT
801	90CT78	166-12270-1	41.44N	10.35E		364	R
802	90CT78	166-12270-2	41.44N	10.35E		364	R
803	90CT78	166-12290-1	47.49N	8.34E			
804	90CT78	166-12290-2	47.49N	8.34E			
805	90CT78	166-12300-1	53.52N	6.05E			
806	90CT78	166-12300-2	53.52N	6.05E			
807	100CT78	167-12450-1	39.56N	6.35E		299	R
808	100CT78	167-12450-2	39.56N	6.35E		299	R
809	100CT78	167-12460-1	46.02N	4.38E		299	R
810	100CT78	167-12460-2	46.02N	4.38E		299	R
811	110CT78	168-2050-3	55.40N	4.09E			
812	110CT78	168-2060-3	49.37N	1.30E			
813	110CT78	168-2080-3	43.32N	.38E			
814	110CT78	168-2100-3	37.26N	2.28W			
815	110CT78	168-13030-1	40.32N	1.52E			
816	110CT78	168-13030-2	40.32N	1.52E			
817	110CT78	168-13040-1	46.38N	.05E			
818	110CT78	168-13040-2	46.38N	.05E			
819	110CT78	168-13060-1	52.41N	2.27W			
820	110CT78	168-13060-2	52.41N	2.27W			
821	120CT78	169-13210-1	39.46N	2.26W			
822	120CT78	169-13210-2	39.46N	2.26W			
823	120CT78	169-13220-1	45.52N	4.22W			
824	120CT78	169-13220-2	45.52N	4.22W			
825	120CT78	169-13240-1	51.55N	6.40W			
826	120CT78	169-13240-2	51.55N	6.40W			
827	130CT78	170-13390-1	41.38N	7.32W			
828	130CT78	170-13390-2	41.38N	7.32W			
829	130CT78	170-13410-1	47.43N	9.34W			
830	130CT78	170-13410-2	47.43N	9.34W			
831	140CT78	171-12210-1	43.46N	11.31E			C
832	140CT78	171-12210-2	43.46N	11.31E			C
833	140CT78	171-12220-1	49.51N	9.22E			
834	140CT78	171-12220-2	49.51N	9.22E			
835	150CT78	172-12380-1	41.04N	7.50E			
836	150CT78	172-12380-2	41.04N	7.50E			
837	150CT78	172-12400-1	47.09N	5.50E			
838	150CT78	172-12400-2	47.09N	5.50E			
839	160CT78	173-12550-1	57.14N	4.24E			
840	160CT78	173-12550-2	57.14N	4.24E			
841	160CT78	173-12570-1	43.20N	2.35E			
842	160CT78	173-12570-2	43.20N	2.35E			
843	170CT78	174-13140-1	39.54N	.53E			
844	170CT78	174-13140-1	39.43N	.50E			
845	170CT78	174-13140-2	39.54N	.53E			
846	170CT78	174-13140-2	39.43N	.50E			
847	170CT78	174-13170-1	52.04N	5.08W			
848	170CT78	174-13170-1	51.53N	5.04W			
849	170CT78	174-13170-2	52.04N	5.08W			
850	170CT78	174-13170-2	51.53N	5.04W			

NO	DATE	IDENTIFICATION	LOCATION		SCENE	BDE	STAT
851	180CT78	175-13320-1	42.42N	6.16W			
852	180CT78	175-13320-2	42.42N	6.16W			
853	190CT78	176-12150-1	51.03N	10.30E			
854	190CT78	176-12150-2	51.03N	10.30E			
855	200CT78	177-12320-1	47.28N	7.21E			
856	200CT78	177-12320-2	47.28N	7.21E			
857	210CT78	178-12480-1	39.02N	5.32E			C
858	210CT78	178-12480-2	39.02N	5.32E			C
859	210CT78	178-12500-1	45.08N	3.38E			C
860	210CT78	178-12500-2	45.08N	3.38E			C
861	220CT78	178-13080-1	46.28N	1.20W			
862	220CT78	178-13080-2	46.28N	1.20W			
863	220CT78	179-13060-1	40.22N	.37E		358	R
864	220CT78	179-13060-2	40.22N	.37E			R
865	230CT78	180- 2270-3	52.22N	3.10W			
866	240CT78	181-13430-1	42.10N	8.57W		305	R
867	240CT78	181-13430-2	42.10N	8.57W		305	R
868	240CT78	181-13450-1	48.15N	11.01W		308	R
869	240CT78	181-13450-2	48.15N	11.01W		308	R
870	250CT78	182-12231-1	41.37N	10.58E			
871	250CT78	182-12231-2	41.37N	10.58E			
872	250CT78	182-12250-1	48.04N	8.48E			
873	250CT78	182-12251-1	47.42N	8.50E			
874	250CT78	182-12251-2	47.42N	8.56E			
875	250CT78	182-12270-1	54.07N	6.19E			
876	250CT78	182-12270-2	54.07N	6.19E			
877	250CT78	182-12271-1	53.46N	6.28E			
878	250CT78	182-12271-2	53.46N	6.28E			
879	260CT78	183-12410-1	38.50N	7.16E			
880	260CT78	183-12410-2	38.50N	7.16E			
881	260CT78	183-12420-1	44.57N	5.22E			
882	260CT78	183-12420-2	44.57N	5.22E			
883	270CT78	184-12530-1	55.14N	3.45E			C
884	270CT78	184-12580-2	55.14N	3.45E			C
885	270CT78	184-12590-1	41.22N	2.01E		358	R
886	270CT78	184-12590-2	41.22N	2.01E		358	R
887	270CT78	184-12590-3	40.45N	2.11E			C
888	270CT78	184-13010-1	47.28N	.00E			C
889	270CT78	184-13010-2	47.28N	.00E			C
890	270CT78	184-13010-3	46.51N	.13E			
891	270CT78	184-13020-3	52.55N	2.10W			
892	270CT78	184-13030-1	53.31N	2.26W			
893	270CT78	184-13030-2	53.31N	2.26W			
894	280CT78	185-13160-1	37.49N	1.26W		306	R
895	280CT78	185-13160-2	37.49N	1.26W			C
896	280CT78	185-13180-1	43.56N	3.17W		306	R
897	280CT78	185-13180-2	43.56N	3.17W		306	R
898	280CT78	185-13200-1	50.01N	5.27W		306	R
899	280CT78	185-13200-2	50.01N	5.27W		306	R
900	290CT78	186-13360-1	45.09N	8.13W			C

NO	DATE	IDENTIFICATION	LOCATION	SCENE	BDE	STAT
901	29OCT78	186-13360-2	45.09N 8.13W			C
902	29OCT78	186-13380-1	51.13N 10.28W			
903	29OCT78	186-13380-2	51.13N 10.28W			
904	30OCT78	187-12170-1	44.34N 11.44E		309	R
905	30OCT78	187-12170-2	44.34N 11.44E		309	R
906	30OCT78	187-12180-1	50.38N 9.31E			
907	31OCT78	188- 1370-3	49.13N 8.01E			
908	31OCT78	188- 1390-3	43.08N 5.53E			C
909	31OCT78	188- 1410-3	37.03N 4.04E			C
910	1NOV78	189- 1550-3	51.14N 4.19E			
911	1NOV78	189- 1560-3	45.10N 2.04E			C
912	1NOV78	189- 1580-3	39.05N .08E			C
913	1NOV78	189-12500-1	36.01N 5.17E			C
914	1NOV78	189-12500-2	36.01N 5.17E			C
915	1NOV78	189-12520-1	42.08N 3.31E			C
916	1NOV78	189-12520-2	42.08N 3.31E			C
917	1NOV78	189-12530-1	48.13N 1.28E			C
918	1NOV78	189-12530-2	48.13N 1.28E			C
919	1NOV78	189-12550-1	54.16N 1.02W			
920	1NOV78	189-12550-2	54.16N 1.02W			
921	2NOV78	190-13090-1	40.23N .26E			
922	2NOV78	190-13090-2	40.23N .26E			
923	2NOV78	190-13110-1	46.29N 2.24W		299	R
924	2NOV78	190-13110-2	46.29N 2.24W		299	R
925	2NOV78	190-13130-1	52.33N 4.46W			
926	2NOV78	190-13130-2	52.32N 4.46W			
927	3NOV78	191-13280-1	45.13N 6.28W			
928	3NOV78	191-13280-2	45.13N 6.28W			
929	5NOV78	193-12260-1	40.37N 10.16E			
930	5NOV78	193-12260-2	40.37N 10.16E			
931	5NOV78	193-12270-1	46.43N 8.17E			
932	5NOV78	193-12270-2	46.43N 8.17E			
933	5NOV78	193-12290-1	52.47N 5.55E			
934	5NOV78	193-12290-2	52.47N 5.55E			
935	6NOV78	194-12430-1	38.22N 6.25E			C
936	6NOV78	194-12430-2	38.22N 6.25E			C
937	6NOV78	194-12450-1	44.29N 4.34E			C
938	6NOV78	194-12450-2	44.29N 4.34E			C
939	6NOV78	194-12460-1	50.34N 2.21E			
940	6NOV78	194-12460-2	50.34N 2.21E			
941	7NOV78	195- 2050-3	48.22N .31E		310	R
942	7NOV78	195- 2050-3	48.50N .41E		310	IR
943	7NOV78	195- 2070-3	42.17N 1.33W		310	R
944	7NOV78	195- 2070-3	42.47N 1.24W		310	R
945	7NOV78	195- 2080-3	36.41N 3.13W			
946	7NOV78	195-13010-1	40.49N 1.13E			
947	7NOV78	195-13010-2	40.49N 1.13E			
948	7NOV78	195-13030-1	46.55N .45E			
949	7NOV78	195-13030-2	46.55N .45E			
950	7NOV78	195-13050-1	52.59N 3.09W			

NO	DATE	IDENTIFICATION	LOCATION		SCENE	BDE	ETAT
951	7NOV78	195-13050-2	52.59N	3.09W			
952	8NOV78	196- 2340-3	46.32N	4.36W			
953	9NOV78	197- 2400-3	52.53N	6.38W		306	R
954	9NOV78	197- 2420-3	46.52N	9.02W		363	R
955	10NOV78	198- 1240-3	40.59N	8.43E			
956	10NOV78	198-12190-1	42.10N	11.25E			
957	10NOV78	198-12190-2	42.10N	11.25E			
958	10NOV78	198-12210-1	48.14N	9.21E			
959	10NOV78	198-12210-2	48.14N	9.21E			
960	11NOV78	199- 1420-3	44.27N	5.11E			
961	11NOV78	199- 1430-3	38.22N	3.19E			
962	11NOV78	199-12360-1	56.19N	8.31E			
963	11NOV78	199-12360-2	56.19N	8.31E			
964	11NOV78	199-12370-1	42.25N	6.43E			
965	11NOV78	199-12370-2	42.25N	6.43E			
966	11NOV78	199-12390-1	48.31N	4.38E			
967	11NOV78	199-12390-2	48.31N	4.38E			
968	11NOV78	199-12410-1	54.33N	2.07E			
969	11NOV78	199-12410-2	54.33N	2.07E			
970	12NOV78	200- 2000-3	44.50N	.43E		299	R
971	12NOV78	200- 2010-3	38.46N	1.10W		299	R
972	12NOV78	200-12540-1	55.33N	4.07E			
973	12NOV78	200-12540-2	55.33N	4.07E			
974	12NOV78	200-12550-1	41.40N	2.21E			
975	12NOV78	200-12550-2	41.40N	2.21E			
976	12NOV78	200-12570-1	47.46N	.19E		300	R
977	12NOV78	200-12570-2	47.46N	.19E		300	R
978	14NOV78	202-13330-1	45.35N	8.06W		358	R
979	14NOV78	202-13330-2	45.35N	8.06W		358	R
980	15NOV78	203- 1180-3	42.13N	10.22E		363	R
981	15NOV78	203- 1200-3	56.08N	8.35E			C
982	16NOV78	204- 1340-3	49.53N	8.28E			
983	16NOV78	204- 1360-3	43.50N	6.17E		300	R
984	16NOV78	204- 1380-3	37.46N	4.26E			
985	17NOV78	205- 1520-3	51.40N	4.35E			
986	17NOV78	205- 1540-3	45.37N	2.17E		300	R
987	19NOV78	207- 2290-3	50.32N	5.04W			
988	19NOV78	207- 2310-3	44.29N	7.17W		354	R
989	21NOV78	209- 1310-3	59.49N	6.22E			
990	22NOV78	210- 1450-3	55.23N	7.38E			
991	22NOV78	210- 1470-3	49.23N	5.01E			
992	22NOV78	210- 1490-3	43.29N	2.52E			C
993	22NOV78	210- 1500-3	37.16N	1.02E			C
994	23NOV78	211- 2060-3	45.59N	.50E			C
995	23NOV78	211- 2080-3	39.55N	2.46W			
996	24NOV78	212- 2230-3	48.37N	4.27W			C
997	24NOV78	212- 2250-3	42.34N	6.32W			
998	28NOV78	216- 2020-3	57.38N	2.05W			
999	28NOV78	216-12540-1	56.58N	3.12E			
1000	28NOV78	216-12540-1	56.39N	3.17E			

NO	DATE	IDENTIFICATION	LOCATION		SCENE	BDE	ETAT
1001	28NOV78	216-12540-2	56.58N	3.12E			
1002	28NOV78	216-12540-2	56.39N	3.17E			
1003	28NOV78	216-12560-1	43.05N	1.18E			
1004	28NOV78	216-12560-1	42.47N	1.24E			
1005	28NOV78	216-12560-2	43.05N	1.18E			
1006	28NOV78	216-12560-2	42.47N	1.24E			
1007	28NOV78	216-12570-1	48.50N	.39E		300	R
1008	28NOV78	216-12570-2	48.50N	.39E		300	R
1009	28NOV78	216-12580-1	49.09N	.46E			
1010	28NOV78	216-12580-2	49.09N	.46E			
1011	28NOV78	216-12590-1	54.52N	3.12W			
1012	28NOV78	216-12590-2	54.52N	3.12W			
1013	30NOV78	218- 2340-3	52.04N	6.16W			
1014	30NOV78	218-13320-1	42.13N	7.32W			
1015	30NOV78	218-13320-2	42.13N	7.32W			
1016	30NOV78	218-13340-1	50.46N	10.33W		300	R
1017	30NOV78	218-13340-1	48.17N	9.35W		300	R
1018	30NOV78	218-13340-2	50.46N	10.33W		300	R
1019	30NOV78	218-13340-2	48.17N	9.35W		300	R
1020	5DEC78	223-13260-1	42.02N	6.01W			
1021	5DEC78	223-13260-2	42.02N	6.01W			
1022	6DEC78	224-12090-1	49.58N	10.45E			
1023	6DEC78	224-12090-2	49.58N	10.54E			
1024	6DEC78	224-12100-1	55.59N	8.14E			
1025	6DEC78	224-12100-2	55.59N	8.14E			
1026	6DEC78	224-13440-1	43.20N	11.02W			
1027	6DEC78	224-13440-2	43.20N	11.02W			
1028	6DEC78	224-13460-1	49.24N	13.10W			
1029	6DEC78	224-13460-2	49.24N	13.10W			
1030	7DEC78	225-12230-1	37.05N	10.32E			
1031	7DEC78	225-12230-2	37.05N	10.32E			
1032	7DEC78	225-12250-1	42.01N	9.05E		306	R
1033	7DEC78	225-12250-1	43.11N	8.44E			
1034	7DEC78	225-12250-2	42.01N	9.05E		306	R
1035	7DEC78	225-12250-2	43.11N	8.44E			
1036	7DEC78	225-12260-1	48.05N	7.02E			
1037	7DEC78	225-12260-2	48.05N	7.02E			
1038	7DEC78	225-12270-1	49.14N	6.37E			
1039	7DEC78	225-12270-2	49.14N	6.37E			
1040	7DEC78	225-12280-1	54.07N	4.34E		306	R
1041	7DEC78	225-12280-2	54.07N	4.34E		306	R
1042	8DEC78	226-12410-1	56.38N	6.06E			
1043	8DEC78	226-12410-2	56.38N	6.06E			
1044	9DEC78	227-12590-1	55.49N	1.46E			
1045	9DEC78	227-12590-2	55.49N	1.46E			
1046	9DEC78	227-13010-1	41.54N	.00E		301	R
1047	9DEC78	227-13010-2	41.54N	.00E		301	R
1048	9DEC78	227-13030-1	47.58N	2.01W		301	R
1049	9DEC78	227-13030-2	47.58N	2.01W		301	R
1050	9DEC78	227-13040-1	54.00N	4.29W			

NO	DATE	IDENTIFICATION	LOCATION		SCENE	BDE	ETAT
1051	9DEC78	227-13040-2	54.00N	4.29W			
1052	10DEC78	228-13170-1	54.58N	2.34W			
1053	10DEC78	228-13170-2	54.58N	2.34W			
1054	10DEC78	228-13190-1	41.04N	4.17W			
1055	10DEC78	228-13190-2	41.04N	4.17W			
1056	10DEC78	228-13220-1	53.10N	8.41W			
1057	10DEC78	228-13220-2	53.10N	8.41W			
1058	11DEC78	229-13400-1	50.35N	12.09W			
1059	11DEC78	229-13400-2	50.35N	12.09W			
1060	13DEC78	231-12350-1	38.01N	7.11E		359	R
1061	13DEC78	231-12350-2	38.01N	7.11E		359	R
1062	14DEC78	232-12530-1	35.27N	3.20E			
1063	14DEC78	232-12530-2	35.27N	3.20E			
1064	14DEC78	232-12540-1	41.33N	1.35E			
1065	14DEC78	232-12540-2	41.33N	1.35E			
1066	14DEC78	232-12560-1	47.37N	.25E			
1067	14DEC78	232-12560-2	47.37N	.25E			
1068	14DEC78	232-12580-1	53.38N	2.50W			
1069	14DEC78	232-12580-2	53.38N	2.50W			
1070	16DEC78	234-13320-1	48.27N	9.50W			
1071	16DEC78	234-13320-2	48.27N	9.50W			
1072	17DEC78	235- 2520-3	50.40N	11.35W			
1073	17DEC78	235- 2520-3	44.37N	13.49W			
1074	17DEC78	235-12120-1	42.37N	11.53E			
1075	17DEC78	235-12120-2	42.37N	11.53E			
1076	17DEC78	235-12130-1	48.41N	9.49E			
1077	17DEC78	235-12130-2	48.41N	9.49E			
1078	17DEC78	235-12150-1	54.42N	7.17E			
1079	17DEC78	235-12150-2	54.42N	7.17E			
1080	18DEC78	236-12280-1	36.24N	9.10E			
1081	18DEC78	236-12280-2	36.24N	9.10E			
1082	18DEC78	236-12310-1	48.32N	5.19E			
1083	18DEC78	236-12310-2	48.32N	5.19E			
1084	18DEC78	236-12330-1	54.34N	2.47E			
1085	18DEC78	236-12330-2	54.34N	2.47E			
1086	19DEC78	237-12460-1	36.07N	4.41E			
1087	19DEC78	237-12460-2	36.07N	4.41E			
1088	19DEC78	237-12480-1	42.12N	2.55E			
1089	19DEC78	237-12480-2	42.12N	2.55E			
1090	19DEC78	237-12490-1	48.16N	.52E			C
1091	19DEC78	237-12490-2	48.16N	.52E			C
1092	19DEC78	237-12510-1	54.16N	1.36W			C
1093	19DEC78	237-12510-2	54.16N	1.36W			C
1094	20DEC78	238-4380-2	37.20S	138.04E			
1095	21DEC78	239- 2290-3	44.08N	7.54W			
1096	21DEC78	239- 2290-3	43.49N	8.00W			
1097	21DEC78	239-13250-1	45.08N	7.04W			
1098	21DEC78	239-13250-2	45.08N	7.04W			
1099	22DEC78	240-13440-1	49.37N	13.16W			
1100	22DEC78	240-13440-2	49.37N	13.16W			

NO	DATE	IDENTIFICATION	LOCATION		SCENE	ODE	STAT
1101	23DEC78	241-12230-1	42.34N	8.55E			
1102	23DEC78	241-12230-2	42.34N	8.55E			
1103	24DEC78	242-12400-1	39.16N	5.22E			
1104	25DEC78	243- 2040-3	44.19N	1.42W		301	R
1105	25DEC78	243-12580-1	39.57N	.37E			
1106	25DEC78	243-12580-2	39.57N	.37E			
1107	25DEC78	243-13000-1	46.01N	1.18W		301	R
1108	25DEC78	243-13000-2	46.01N	1.18W		301	R
1109	25DEC78	243-13020-1	52.04N	3.36W			
1110	25DEC78	243-13020-2	52.04N	3.36W			
1111	26DEC78	244- 2210-3	45.24N	5.53W		301	R
1112	27DEC78	245- 2400-3	44.00N	10.55W			
1113	28DEC78	246- 1210-3	40.52N	7.52E			C
1114	28DEC78	246-12160-1	43.31N	10.11E		364	R
1115	28DEC78	246-12160-2	43.31N	10.11E		364	R
1116	29DEC78	247- 1400-3	37.10N	2.14E			
1117	29DEC78	247-12760-3	48.43N	3.51E			
1118	29DEC78	247-12770-3	54.44N	1.19E			
1119	30DEC78	248-12500-1	35.55N	3.20E			
1120	30DEC78	248-12520-1	42.01N	1.36E			
1121	30DEC78	248-12520-2	42.01N	1.36E			
1122	31DEC78	249- 2140-3	45.53N	4.07W			
1123	31DEC78	249-13110-1	45.41N	4.07W			
1124	31DEC78	249-13130-2	51.43N	6.24W			
1125	3JAN79	252- 1320-3	41.23N	8.07E			
1126	3JAN79	252- 1340-3	35.27N	3.22E			
1127	3JAN79	252-12260-1	39.56N	8.25E			
1128	3JAN79	252-12260-2	39.56N	8.25E			
1129	3JAN79	252-12280-1	46.00N	6.29E			
1130	3JAN79	252-12280-2	46.00N	6.29E			
1131	3JAN79	252-12290-1	52.02N	4.11E			
1132	3JAN79	252-12290-2	52.02N	4.11E			
1133	6JAN79	255- 2260-3	42.50N	8.04W			
1134	6JAN79	255-13210-1	44.07N	6.27W			
1135	6JAN79	255-13210-2	44.07N	6.27W			
1136	7JAN79	256- 1060-3	42.58N	11.44E			
1137	7JAN79	256- 2410-3	53.41N	8.29W			
1138	7JAN79	256-13390-1	43.02N	10.38W			
1139	7JAN79	256-13390-2	43.02N	10.38W			
1140	10JAN79	259- 1570-3	53.19N	2.31E			
1141	10JAN79	259- 2010-3	41.10N	1.55W			
1142	11JAN79	260- 2150-3	53.31N	1.49W			
1143	12JAN79	261- 2370-3	54.42N	5.48W			
1144	13JAN79	262- 1170-3	41.26N	8.50E	R	301	R
1145	13JAN79	262- 1190-3	35.19N	7.04E			
1146	13JAN79	262-12520-3	50.31N	12.05W			
1147	14JAN79	263- 1320-3	52.05N	8.13E		302	R
1148	14JAN79	263- 1360-3	39.55N	3.55E		302	R
1149	15JAN79	264- 1500-3	53.47N	4.25E			
1150	15JAN79	264- 1510-3	47.44N	1.57E		354	R

NO	DATE	IDENTIFICATION	LOCATION		SCENE	BDC	ETAT
1151	15JAN79	264-1530-3	41.39N	.00E		354	R
1152	16JAN79	265- 2090-3	48.14N	2.15W		301	R
1153	16JAN79	265- 2110-3	42.10N	4.20W		309	R
1154	17JAN79	266-2260-3	52.40N	4.57W			
1155	17JAN79	266- 2270-3	46.37N	7.20W		354	R
1156	17JAN79	266-13230-1	40.42N	5.56W			
1157	17JAN79	266-13230-2	40.42N	5.56W			
1158	17JAN79	266-13250-1	46.46N	7.55W			
1159	17JAN79	266-13250-2	46.46N	7.55W			
1160	17JAN79	266-13260-1	52.49N	10.18W			
1161	17JAN79	266-13260-2	52.49N	10.18W			
1162	18JAN79	267-13420-1	42.58N	11.08W			
1163	18JAN79	267-13420-2	42.58N	11.08W			
1164	19JAN79	268- 1290-3	35.34N	4.32E			
1165	21JAN79	270- 2010-3	51.18N	.36E			
1166	21JAN79	270-2010-3	51.18N	.36E			
1167	21JAN79	270- 2030-3	45.14N	1.40W			C
1168	21JAN78	270- 2040-3	39.08N	3.35W			
1169	21JAN79	270-13000-1	46.10N	1.36W			
1170	21JAN79	270-13000-2	46.10N	1.36W			
1171	21JAN79	270-13010-1	52.12N	3.56W			
1172	21JAN79	270-13010-2	52.12N	3.56W			
1173	23JAN79	272-12000-1	51.13N	11.05E			
1174	23JAN79	272-12000-2	51.13N	11.05E			
1175	23JAN79	272-13360-1	44.39N	10.47W			
1176	23JAN79	272-13360-2	44.39N	10.47W			
1177	23JAN79	272-13370-1	50.43N	13.01W			
1178	23JAN79	272-13370-2	50.43N	13.01W			
1179	24JAN79	273- 1210-3	41.20N	7.01E			C
1180	24JAN79	273- 1230-3	35.13N	5.16E			
1181	25JAN79	274-12340-2	40.39N	5.33E			
1182	25JAN79	274-12360-1	46.44N	3.34E			
1183	25JAN79	274-12360-2	46.44N	3.34E			
1184	25JAN79	274-12370-1	52.47N	1.11E			
1185	25JAN79	274-12370-2	52.47N	1.11E			
1186	26JAN79	275- 1590-3	58.33N	2.57W			
1187	26JAN79	275-12520-1	39.40N	1.14E			
1188	26JAN79	275-12520-2	39.40N	1.14E			
1189	26JAN79	275-12550-1	51.49N	2.58W			
1190	26JAN79	275-12550-2	51.49N	2.58W			
1191	27JAN79	276- 2140-3	50.40N	3.29W			
1192	28JAN79	277- 2330-3	47.36N	0.16W			
1193	28JAN79	277-13300-1	44.39N	9.26W			
1194	28JAN79	277-13300-2	44.39N	9.26W			
1195	28JAN79	277-13320-1	50.33N	11.39W			
1196	28JAN79	277-13320-2	50.33N	11.39W			
1197	29JAN79	278- 1170-3	56.12N	6.51E			
1198	30JAN79	279- 1330-3	43.00N	4.16E			C
1199	30JAN79	279- 1350-3	36.54N	2.28E			C
1200	30JAN79	279-12280-1	40.38N	6.51E			

NO	DATE	IDENTIFICATION	LOCATION	SCENE	BDE	ETAT
1201	30JAN79	279-12280-2	40.38N 6.51E			
1202	31JAN79	280-1490-3	51.37N 2.49E			C
1203	31JAN79	280-1510-3	45.33N .31E			C
1204	31JAN79	280-1530-3	39.28N 1.23W			C
1205	1FEB79	281-2080-3	51.26N 1.50W			
1206	1FEB79	281-2090-3	45.23N 4.07W			
1207	2FEB79	282-2261-3	49.15N 7.19W			
1208	3FEB79	283-1090-3	42.47N 10.08E			
1209	3FEB79	283-1110-3	36.41N 8.20E			C
1210	4FEB79	284-1250-3	50.26N 8.16E			
1211	4FEB79	284-1270-3	44.22N 6.04E			C
1212	4FEB79	284-1290-3	38.16N 4.11E			C
1213	4FEB79	284-12220-1	39.01N 8.41E			C
1214	4FEB79	284-12220-2	39.01N 8.41E			C
1215	5FEB79	285-1430-3	50.50N 3.50E			
1216	5FEB79	285-1450-3	44.46N 1.37E			
1217	5FEB79	285-1470-3	38.41N .16E			
1218	5FEB79	285-12400-1	38.01N 4.24E			C
1219	5FEB79	285-12400-2	38.01N 4.24E			C
1220	5FEB79	285-12430-1	50.11N .22E			
1221	5FEB79	285-12430-2	50.11N .22E			
1222	6FEB79	286-2010-3	53.41N .23E			C
1223	6FEB79	286-2020-3	47.38N 1.59W			C
1224	6FEB79	286-12570-1	56.03N .20E			
1225	6FEB79	286-12570-2	56.03N .20E			
1226	7FEB79	287-13160-1	39.37N 5.13W			
1227	7FEB79	287-13160-2	39.37N 5.13W			
1228	7FEB79	287-13180-1	45.43N 7.08W			
1229	7FEB79	287-13180-2	45.43N 7.08W			
1230	10FEB79	290-1370-3	49.51N 5.27E			
1231	14FEB79	294-12090-1	42.04N 11.14E			
1232	14FEB79	294-12090-2	42.04N 11.14E			
1233	15FEB79	295-12260-1	38.46N 7.40E			
1234	15FEB79	295-12260-2	38.46N 7.40E			
1235	16FEB79	296-12450-1	40.41N 2.32E			
1236	17FEB79	297-13090-1	38.04N 1.13W			
1237	17FEB79	297-13090-2	38.04N 1.13W			
1238	17FEB79	297-13040-1	44.10N 3.04W			
1239	17FEB79	297-13040-2	44.10N 3.04W			
1240	20FEB79	300-12190-1	38.49N 9.13E			
1241	20FEB79	300-12190-2	38.49N 9.13E			
1242	20FEB79	300-12210-1	44.55N 7.20E			
1243	20FEB79	300-12210-2	44.55N 7.20E			
1244	20FEB79	300-12230-1	50.59N 5.05E			
1245	20FEB79	300-12230-2	50.59N 5.05E			
1246	21FEB79	301-12380-1	41.35N 3.53E			C
1247	21FEB79	301-12380-2	41.35N 3.53E			C
1248	21FEB79	301-12400-1	47.40N 1.50E			C
1249	21FEB79	301-12400-2	47.40N 1.50E			C
1250	22FEB79	302-12550-1	38.53N .08E			

NO	DATE	IDENTIFICATION	LOCATION		SCENE	BDE	ETAT
1251	22FEB79	302-12550-2	38.53N	.08E			C
1252	22FEB79	302-12590-1	51.04N	4.00W			C
1253	22FEB79	302-12590-2	51.04N	4.00W			
1254	23FEB79	303-13150-1	44.11N	6.00W			C
1255	23FEB79	303-13150-2	44.11N	6.00W			C
1256	23FEB79	303-13160-1	50.16N	8.12W			C
1257	23FEB79	303-13160-2	50.16N	8.12W			C
1258	24FEB79	304-11580-1	52.42N	10.33E			
1259	24FEB79	304-11580-2	52.42N	10.33E			
1260	24FEB79	304-13330-1	44.39N	10.40W			
1261	24FEB79	304-13330-2	44.39N	10.40W			
1262	25FEB79	305-12130-1	42.46N	9.42E			
1263	25FEB79	305-12130-2	42.46N	9.42E			
1264	25FEB79	305-12150-1	48.52N	7.36E			
1265	25FEB79	305-12150-2	48.52N	7.36E			
1266	25FEB79	305-12160-1	54.54N	5.02E			
1267	25FEB79	305-12160-2	54.54N	5.02E			
1268	26FEB79	306-12300-1	39.14N	6.16E			
1269	26FEB79	306-12300-2	39.14N	6.16E			
1270	26FEB79	306-12320-1	45.20N	4.21E			
1271	26FEB79	306-12320-2	45.20N	4.21E			
1272	26FEB79	306-12330-1	51.24N	2.04E			
1273	26FEB79	306-12330-2	51.24N	2.04E			
1274	27FEB79	307- 1530-3	45.35N	.51E			C
1275	27FEB79	307- 1550-3	39.30N	2.46W			
1276	27FEB79	307-12480-1	38.01N	2.06E			
1277	27FEB79	307-12480-2	38.01N	2.06E			
1278	27FEB79	307-12490-1	44.07N	.14E		359	R
1279	27FEB79	307-12490-2	44.07N	.14E		359	R
1280	27FEB79	307-12510-1	50.11N	1.56W			C
1281	27FEB79	307-12510-2	50.11N	1.56W			C
1282	1MAR79	309-13250-1	45.01N	9.03W			
1283	1MAR79	309-13250-2	45.01N	9.03W			
1284	14MAR79	322-12270-1	38.42N	6.07E			C
1285	14MAR79	322-12270-2	38.42N	6.07E			C
1286	14MAR79	322-12290-2	44.47N	4.13E			C
1287	15MAR79	323-12460-1	39.55N	1.08E			
1288	15MAR79	323-12460-2	39.55N	1.08E			
1289	16MAR79	324-13040-1	39.04N	3.11W			
1290	16MAR79	324-13040-2	39.04N	3.11W			
1291	16MAR79	324-13050-1	45.09N	5.05W			C
1292	16MAR79	324-13050-2	45.09N	5.05W			C
1293	17MAR79	325-13230-1	41.02N	8.20W			
1294	17MAR79	325-13230-2	41.02N	8.20W			
1295	17MAR79	325-13240-1	47.07N	10.20W			
1296	17MAR79	325-13240-2	47.07N	10.20W			
1297	18MAR79	326-12040-1	43.29N	10.35E			C
1298	18MAR79	326-12040-2	43.29N	10.35E			C
1299	18MAR79	326-12080-1	55.34N	5.50E			
1300	18MAR79	326-12080-2	55.34N	5.50E			

NO	DATE	IDENTIFICATION	LOCATION		SCENE	BDE	ETAT
1304	19MAR79	327-12210-1	37.19N	7.52E			C
1305	19MAR79	327-12210-2	37.19N	7.52E			C
1303	19MAR79	327-12220-1	43.25N	6.03E			
1304	19MAR79	327-12220-2	43.25N	6.03E			
1305	19MAR79	327-12260-1	55.30N	1.17E			
1306	19MAR79	327-12260-2	55.30N	1.17E			
1307	20MAR79	328-12390-1	36.41N	3.28E			C
1308	20MAR79	328-12390-2	36.41N	3.28E			C
1309	20MAR79	328-12400-1	42.47N	1.40E			C
1310	20MAR79	328-12400-2	42.47N	1.40E			C
1311	20MAR79	328-12420-1	48.51N	.25E			C
1312	20MAR79	328-12420-2	48.51N	.25E			C
1313	21MAR79	329-12570-1	38.56N	1.43W			
1314	21MAR79	329-12570-2	38.56N	1.43W			
1315	21MAR79	329-12590-1	45.01N	3.37W			
1316	21MAR79	329-12590-2	45.01N	3.37W			
1317	21MAR79	329-13010-1	51.04N	5.51W			
1318	21MAR79	329-13010-2	51.04N	5.51W			
1319	23MAR79	331-11580-1	43.29N	12.02E			
1320	23MAR79	331-11580-2	43.29N	12.02E			
1321	23MAR79	331-11590-1	49.32N	9.53E			
1322	23MAR79	331-11590-2	49.32N	9.53E			
1323	23MAR79	331-12010-1	55.34N	7.16E			C
1324	23MAR79	331-12010-2	55.34N	7.16E			C
1325	24MAR79	332-12150-1	39.07N	8.49E			C
1326	24MAR79	332-12150-2	39.07N	8.49E			C
1327	24MAR79	332-12160-1	45.12N	6.56E			C
1328	24MAR79	332-12160-2	45.12N	6.56E			C
1329	24MAR79	332-12180-1	51.15N	4.41E			C
1330	24MAR79	332-12180-2	51.15N	4.41E			C
1331	25MAR79	333-12330-1	38.09N	4.32E			
1332	25MAR79	333-12330-2	38.09N	4.32E			
1333	26MAR79	334-12530-1	46.59N	2.47W			
1334	26MAR79	334-12530-2	46.59N	2.47W			
1335	27MAR79	335-13090-1	39.46N	5.00W			
1336	27MAR79	335-13090-2	39.46N	5.00W			
1337	30MAR79	338-12260-1	38.02N	6.10E			
1338	30MAR79	338-12260-2	38.02N	6.10E			
1339	30MAR79	338-12270-1	44.07N	4.19E			
1340	30MAR79	338-12270-2	44.07N	4.19E			
1341	1APR79	340-13010-1	57.32N	2.13W			
1342	1APR79	340-13010-2	57.32N	2.13W			
1343	1APR79	340-13030-1	43.37N	4.04W			
1344	1APR79	340-13030-2	43.37N	4.04W			
1345	1APR79	340-13050-1	49.40N	6.14W			
1346	1APR79	340-13050-2	49.40N	6.14W			
1347	2APR79	341-13210-1	41.59N	8.05W			
1348	2APR79	341-13210-2	41.59N	8.05W			
1349	2APR79	341-13220-1	48.03N	10.08W			
1350	2APR79	341-13220-2	48.03N	10.08W			

#NO#	DATE	IDENTIFICATION	LOCATION		SCENE		EDGE	ETAT
1351	7APR79	346-13130-1	43.41N	7.21W				
1352	7APR79	346-13130-2	43.41N	7.21W				
1353	7APR79	346-13150-1	49.45N	9.31W				
1354	7APR79	346-13150-2	49.45N	9.31W				
1355	8APR79	347- 590-3	41.38N	10.23E			302	R
1356	8APR79	347-13330-1	49.01N	13.43W				
1357	8APR79	347-13330-2	49.01N	13.43W				
1358	10APR79	349-12290-1	39.14N	4.48E				
1359	10APR79	349-12290-2	39.14N	4.48E				
1360	10APR79	349-12320-1	51.22N	.37E				C
1361	10APR79	349-12320-2	51.22N	.37E				C
1362	11APR79	350-12460-1	39.40N	.11E				
1363	11APR79	350-12460-2	39.40N	.11E				
1364	11APR79	350-12480-1	45.45N	1.44W				
1365	11APR79	350-12480-2	45.45N	1.44W				
1366	12APR79	351-13050-1	39.13N	4.18W				
1367	12APR79	351-13050-2	39.13N	4.18W				
1368	12APR79	351-13060-1	45.17N	6.12W				C
1369	12APR79	351-13060-2	45.17N	6.12W				C
1370	13APR79	352-11490-1	50.39N	11.28E				
1371	13APR79	352-11490-2	50.39N	11.28E				
1372	13APR79	352-11500-1	53.04N	10.26E				
1373	13APR79	352-11500-2	53.04N	10.26E				
1374	13APR79	352-11510-1	56.40N	8.43E				
1375	13APR79	352-11510-2	56.40N	8.43E				
1376	17APR79	356-13000-1	39.13N	3.11W				C
1377	17APR79	356-13000-2	39.13N	3.11W				C
1378	17APR79	356-13010-1	45.17N	5.06W			359	R
1379	17APR79	356-13010-2	45.17N	5.06W			359	R
1380	17APR79	356-13030-1	51.20N	7.22W			359	R
1381	17APR79	356-13030-2	51.20N	7.22W			359	R
1382	18APR79	357-13200-1	45.06N	9.41W				
1383	18APR79	357-13200-2	45.06N	9.41W				
1384	19APR79	358-12000-1	41.25N	11.10E				
1385	19APR79	358-12000-2	41.25N	11.10E				
1386	19APR79	358-12030-1	53.30N	6.43E				
1387	19APR79	358-12030-2	53.30N	6.43E				
1388	21APR79	360-12370-1	40.30N	2.10E				
1389	21APR79	360-12370-2	40.30N	2.10E				
1390	23APR79	362-13160-1	49.34N	10.08W				
1391	23APR79	362-13160-2	49.34N	10.08W				
1392	25APR79	364- 1160-3	50.47N	8.08E				
1393	25APR79	364- 1180-3	44.43N	5.56E				C
1394	26APR79	365- 1350-3	48.31N	2.40E				
1395	26APR79	365- 1370-3	42.26N	.35E				
1396	26APR79	365-12310-1	40.06N	3.28E				C
1397	26APR79	365-12310-2	40.06N	3.28E				C
1398	26APR79	365-12330-1	46.10N	1.32E				
1399	26APR79	365-12330-2	46.10N	1.32E				
1400	26APR79	365-12340-1	52.13N	.47E				

NO	DATE	IDENTIFICATION	LOCATION	SCENE	ODE	ETAT
1401	29APR79	368- 540-3	43.11N 11.18E			
1402	1MAY79	370- 1310-3	41.56N 1.40E		364	R
1403	1MAY79	370-12250-1	37.28N 5.29E		332	R
1404	1MAY79	370-12250-2	37.28N 5.29E		332	R
1405	1MAY79	370-12260-1	43.34N 3.38E		332	R
1406	1MAY79	370-12260-2	43.34N 3.38E		332	R
1407	2MAY79	371- 1480-3	46.58N 1.15W			
1408	2MAY79	371- 1500-3	40.53N 3.14W			
1409	3MAY79	372- 2040-3	55.53N 2.08W			
1410	3MAY79	372- 2060-3	49.50N 4.47W			
1411	5MAY79	374- 1060-3	45.37N 8.46E			C
1412	6MAY79	375- 1230-3	50.43N 6.04E			
1413	6MAY79	375- 1250-3	44.38N 3.51E			C
1414	6MAY79	375-12200-1	39.50N 6.04E		332	R
1415	6MAY79	375-12200-2	39.50N 6.04E		332	R
1416	6MAY79	375-12210-1	45.56N 4.08E			
1417	6MAY79	375-12210-2	45.56N 4.08E			
1418	7MAY79	376- 1420-3	46.56N .01E			C
1419	7MAY79	376- 1440-3	40.50N 1.57W			
1420	7MAY79	376-12380-1	41.03N 1.09E			C
1421	7MAY79	376-12380-2	41.03N 1.09E			C
1422	8MAY79	377- 2000-3	48.56N 3.50W			
1423	10MAY79	379- 1010-3	41.32N 8.46E			C
1424	11MAY79	380- 1180-3	45.22N 5.26E			C
1425	11MAY79	380-12130-1	38.41N 7.46E			C
1426	11MAY79	380-12130-2	38.41N 7.46E			C
1427	11MAY79	380-12150-1	44.46N 5.53E			C
1428	11MAY79	380-12150-2	44.46N 5.53E			C